ASSEMBLY OF SEPTINS ON CURVED MEMBRANES: FROM SINGLE MOLECULES TO HIGHER-ORDER STRUCTURES

Kevin S. Cannon

A dissertation submitted to the faculty at the University of North Carolina at Chapel Hill in partial fulfillment of the requirements for the degree of Doctor of Philosophy in the Department of Biology in the College of Arts and Sciences

Chapel Hill
2020

Approved by:

Amy Gladfelter

Kevin Slep

Patrick Brennwald

Paul S. Maddox

Harold Erickson

ABSTRACT

Kevin S. Cannon: ASSEMBLY OF SEPTINS ON CURVED MEMBRANES: FROM SINGLE MOLCEULES TO HIGHER-ORDER STRUCTURES
(Under the direction of Amy S. Gladfelter)

The septin cytoskeleton is a highly conserved family of filament-forming, GTP-binding proteins found in yeast through humans. Septins were first discovered during the cell division cycle (*cdc*) mutagenesis screens in budding yeast, where they were shown to be essential for cytokinesis. Despite their discovery in the 1970's, comparatively little is known about septin structure, function, and mechanisms of assembly when compared to other cytoskeletal polymers such as actin, microtubules, and intermediate filaments. In cells, septins are often found associated on membranes, both flat and curved, where they function in cell cycle progression, cell migration, and degradation of invading microorganisms into host cells. Septin assembly onto membranes begins with the binding of short nanometer-sized rod complexes which diffuse and anneal to form filaments and higher-order structures including filament pairs, rings, and gauzes. Despite our current knowledge, it is unclear how septins associate with membranes, especially in a geometry-dependent manner. Moreover, it is unclear if/how the step-wise septin assembly process is sensitive to changes in membrane shape. In this dissertation we find that septins contain a highly conserved amphipathic helix, a structural motif essential for preferential assembly of septins onto curved membranes. Interestingly, we find that single septin octamers are capable of sensing membrane curvature on the nanometer scale, however, this does not explain the micrometer-scale curvature preference of septins able to polymerize. We find that

septins must polymerize to stably associate with membranes and that septin filaments are longer on micrometer-scale membrane curvatures. Collectively, our data shows that curvature sensing by septins operates on multiple length scales, at the level of individual protein domains through filament formation.

For Laura:
Your love spirals outward.

For Mom, Dad, and Chris:
Thank you for always being proud of me, no matter what.

ACKNOWLEDGEMENTS

The lab. This lab has been an interesting amalgam of people. Everyone is so different from one another, yet you all come together to create this harmony that sounds beautiful. I know that it's not uncommon for a lab to be like this, but I had never been a part of such a collective before, so just being here always felt special to me. I wish labs were only additive, but they're not. You join a lab, work for some amount of time, and then you watch these people you talk to every day just disappear. I hate that. Most of the people from the lab that I'd like to hear this aren't even here. You know, sometimes at night when I'm in bed, I swear I can hear all of you arguing through my window, though, I'm never quite sure who is who. This always makes me smile. All of you have influenced how I think about, just about everything. I look forward to all of your continued successes as you all grow older and continue to change the scientific landscape. It has been truly wonderful to grow next to each and every one of you. Thank you for that.

Amy, no different from a mother, you can always recognize my desperate displays. Thank you taking in an invisible boy from a translational medicine lab and always seeing him for who he was: a directionless kid from Jersey who grew up on Billy Joel songs and lived a trial and error kind of life. You are so vibrant and passionate about your science, so just talking to you has always been a breath of fresh air. Most importantly though, you care about your students as people. It's wonderful to watch your face when someone new joins the lab and asks a really good question. I'll never forget the day I told you I hadn't written my qualifying exam- three days before it was due. In all our conversations together, I'd never seen your jaw drop like that. So,

you chewed me out and I submitted my crumbled thoughts the next day. It's worth noting that you weren't mad because you'd thought I'd fail (well maybe you were), but more in a way that you were upset that I didn't take the opportunity to really grow from the experience. I like to think that you thought I had all the right pieces but couldn't put them together. I feel that way a lot these days. I always say the right thing, but act the wrong way. I guess at the end of the day, all you really need is one great person to believe in you. Thank you for letting me join you in the sun, even if it was only for a little while. These years working in your lab have been a gift, and I leave your lab with a heavy heart. I will carry this time in my life with me, always.

Mom, Dad, and Chris. I know these years have been long for you, especially after my first try at graduate school. They've been long for me too. I'm getting better on dealing with science and the emotions that come with it, but I've still got a long way to go. Chris, you're tragically flawed, but you have a really big heart. You should embrace this heart of yours more often than you do. I'm sorry I still embarrass you when I'm weird at family events. It's thoughtful when you invite me to hang out with your friends when I'm home and have nothing to do, fully knowing I'll never actually accept the invitation. I know I push your buttons, and you never had to do that, but I appreciate it and I love you. You just bought a house and I'm proud of you. Mom and Dad, thank you for loving me, thank you for always being there, thank you for raising a man who knows how to feel. I know I've put you both through a lot and I'm sorry about that. It takes an ocean for me to be happy and I know that you both have come to have mercy on my rough and rowdy ways. "The only true currency in this bankrupt world is what you share with someone else when you're uncool". Around you guys, I have been forever uncool and you've loved me just the same. I appreciate that and I love you both.

Steve, "in Santa Barbara Hannah cried and missed those freezing beaches. I walked into town to buy some kindling for the fire. Hannah tore the New York Times up into pieces." Thank

you for always taking care of me and making sure I'm doing okay, even when I feel like Hannah, as I so often do. You can always find some kind of good in anything, even in a world littered in Alt-right opium and popup war emporia. Thank you for making me laugh, for giving me a place to crash in Manhattan, and for always picking up a Martin or Gibson whenever I want to jam. You have a profound ability to care for others, and I thank you for making the New York times some of the best of my life. You're a good person Steve and I hope you let yourself know that.

Ant, you're usually quiet when the everyone is talking about heavier things, but I think that's just because you're listening. And when you finally do open up, it's obvious that you have the biggest heart of all of us. I think you should let that heart of yours out more often than you do; it makes us all feel better. From the hours spent aimlessly driving around Marlton, to those spent on that futon playing Call of Duty in college, or those stumbling around Philadelphia, Manhattan, and Lisbon you've always had the right words to keep me smiling. I need that Ant, I really do.

Vinny, you're leaving UNC in a couple of days (May 30th 2019) and that makes me sad. I attribute our friendship to our common interests and vices. Some of my favorite days in Chapel Hill were spent in the Post Doc office on the third floor of Fordham, either talking deeply about our data or drinking beer at noon when we wanted to forget about life on any given Tuesday. Fordham has been colorless and empty since you left. I guess I just miss my friend. Some Sundays, I sneak back into that room just to drink a beer and either laugh or just sit and wonder where the time has gone. I think when this whole things is over, I'll sign my name on the ceiling tile on the 5th floor, right next to yours. You're a good man Vinny and I'm lucky to have spent time with you.

Therese, it's 4 pm on a Thursday, we're sitting at TRU and you're three tonic and gins in. We're planning our experiments for a summer at Woods Hole and you're frustrating me by

proposing 8 month long genetic screens. It's okay though, you're still one of my favorite scientists. I swear that by listening to the questions you ask make me a better scientist. I knew I wanted to join this lab during my rotation when during some late-night science you and I got hammered on Rolling Rock and Sam Adams IPAs, we and tried to look at the effects of yeast extracts on recombinant septin filaments. By the time we were imaging I couldn't type, so you did, and I operated the TIRF (April 2016). This is one of my favorite memories as a graduate student, and I will never forget what I remember of it.

Ross, we grew up doing karate together, and because of that, we have all these memories and inside jokes from when we were kids. Like how our childhood role models turned out to be very, very human as we grew up. I think we can laugh a little harder now, considering we grew up and aren't really any different. Whenever I'm in Marlton, I drive by your old house in Westbury Chase and smile. I can't be home and not think of all our laughter when we'd lock ourselves in your parent's basement and be idiots. I swear I can still hear the echoes of those laughs, and it makes me smile knowing that they have stood the test of time.

Dan, Delaware was really, really tough for both of us. We'd stay up late with cheap beer, cigarettes, science, rock and roll, and some Simon and Garfunkel, which in time, put a lot of things in my mind. You are hands down the most thoughtful and insightful person I've ever met. Our Bud light Platinum daydreams and conversations in that windowless room somewhere in Delaware fundamentally changed me as a person. I don't know where I'd be if I didn't have you to lean on during the most difficult time in my life. I genuinely love you Dan. There is nobody in this world like you, and I'm lucky to know you. Wasn't D.C. beautiful in April of 2015? I think part of the reason I left Delaware was that you were leaving it too. I didn't know what to do without you there. When I came to Manhattan in March 2019 we all went out, and after the night was over you reached over to me and said that when we were in Delaware (sometime in 2015)

the two of us had a conversation about where we thought we'd be in five years. Then, you smiled as you reminded me that we both ended up exactly where we said we would. I'm getting this Ph.D. because of you. I just wanted you to know that.

To my wife Laura, I missed you for twenty-five years, but by way of a green line bus and an actin biochemistry lab, I found you. Not long after that, we were dancing in your kitchen in that apartment on Lyme road as we cooked dinner on any freezing New England evening. You live a life of patience, warmth, intelligence, beauty, bad ass-ness, humor, and kindness every single day. I love the way you drive your truck; I love the way you pour concrete; I love watching you thoroughly analyze a restaurant menu before we decide to go there for dinner. Being a part of your life has made these past few years some of the best of mine, and all of your moments have made me a better person. I got through this Ph.D. because of you, but you already know that. When I look forward in time, I see you coming home from work and I'm there to kiss you on the forehead. I ask how your day was, but you don't hear me because you're too excited, as it's been so long since the kids came home for dinner. So I set the table, you put some kindling in the fire, and we wait for the doorbell to ring as we sit in the garden we planted and think about everything we've grown.

PREFACE
(One More Thing/I Am Easy To Find)

I was here and now I'm not

In the land of the lotus eaters, time's arrow breaks and bends in unusual ways. I used to drive down the New Jersey Turnpike thinking about how it would feel to get a Ph.D. Five years later, I don't drive the turnpike anymore, but I'm finally getting my degree. It's funny how all the little things that used to make me nervous seemed to just disappear with the weather now that this whole thing is over. I knew what it was going to be like from the start though; I had been to this Lemon-world before, but I dropped out, and I've been trying to disconnect those dots ever since. I've been standing in this ether for so long, and now I think I'm almost afraid to leave. But I guess that's just the way the weather works here. I know that my prose might seem a little too purple, but as I've aged I've become increasingly more sentimental. It's only half my fault, so half forgive me. But that's okay. That means I've probably captured this experience as I truly felt it, and I think can live with that.

It was the best of times, it was the worst of times, and everyone told me it would be this way. Now I know. Mistakes were made, hearts were broken, harsh lessons learned. My friends and family went on without me, as I drowned in an ocean of rate constants, helices, and pixels. Still, here I stand, melting away in the warm Carolina sun, if only for a little while longer. One day I'll live in that city I love and I'll take the F-train to get back home.

I write this at the end of it all; a requiem for a graduate student. I'm a little lost, a little flustered, and a lot relieved that this is finally over. I think the funniest thing is that I spent so many years writing down the things that this experience has brought to my attention, and all I've

written in the past week is this preface. This makes my last few days here among the happiest I'll probably ever ignore. It's hard to believe that I'm leaving something like this behind. I put my whole heart into this work for what feels like a very long time, and I'm supposed to just walk away and not rock the casbah?

If you're actually reading this, you're probably a graduate student or post doc that is building on this work. I just want you to know that the septins are some of the most gorgeous and complicated proteins in biology. Like most pillars of beauty, they don't give up their secrets to most people, and when they do, it's not easily. So during your trip from Providence to Phoenix and back again, make sure to persevere and work hard when things fall apart, step outside of what's comfortable, break the rules, and be kind. There's a million little battles that you're never going to win in this place, but in the end, you always end up becoming yourself. During your time here I hope that you find some kind of happiness, learn what it really means to persevere, and grow into the scientist you always wanted to be. I wish you the best. Go and push the field forward, like all of us who have tried before your time. Good luck.

Hysteresis (Graduate School)

How long have I been here? I'm underwater again. I think about you way more than anything else. Breathe in our iodine baby! On, off, diffuse, collide, fall apart. Over and over again. It's in your head, it's in your head, it's in your head. It's getting cold, but New York's gorgeous. I don't believe in god, I still go out to department stores. I've forgotten what I'm supposed to do today. Who even are you? I'm breaking wine glasses in the middle of the street and I have trouble remembering people. Vilify. You're thinking too fast again, you're like marbles on glass. Not what I really wanted. Why can't I just be here? Kinetics. The elevators make me nervous. Sleep on the floor. Annie, why are you here? You got tired of yourself on a turnpike exit. I've had too much to drink again and you're probably on pills. Do you still love the

natural light when it's captured in black and white? We both can feel the walls filling with molasses. The floors are falling out from everybody I know. What you think I am, it isn't me**.** Exile. There's so much sun where I'm from. Give me a time and a place to be. *I am easy to find.* Maybe I'll run away again and you'll forget about me. This time I'll end up in the valley, somewhere near Calabasas, or maybe on a lea in Eden. One day, *I'll be hard to find.* Exile. Gasoline. Give up. Another week indoors. Hospital gowns don't really fit like they should. Is this the best I'm ever going to be? I've never lived without a sad, jealous eye. I've never been away this long. One day I'll get money and I'll get funny again. I can be happy. Did you dreams come true, now that it's over, Kevin? Yeah. I think so. I just didn't expect to feel so tired when they did.

Random access memories

I wanted to walk around Chapel Hill today (July 2019). I haven't really seen it in a while. I was just in Woods Hole for a couple of weeks, and I don't really have the desire to go out in Carolina anymore, mostly because I get so nostalgic. I have laughed in almost every building on Franklin Street and Carrboro, and now walking by those storefronts just makes me miss people who aren't around anymore. But that day I wanted to walk around. It was two in the afternoon and I should have been doing experiments or analyzing data, but I love being in places when I'm not supposed to be there. So I walked around Franklin street for a little while. Everything started to look the same after a couple of minutes, it always does. All these places and their bars where I once dreamt I would think; Marlton, Hanover, Manhattan, Berlin, Philadelphia, Lisbon, Newark, Lucerne, and Chapel Hill are all on this single street in this continuous memory of mine.

Annie always walks past me in front of Linda's on the corner of Franklin and Henderson Street, but our glances are never timed right, so she's left thinking it was someone else, but I know, and I'm left to internalize it. My grandfathers, Otto and Dudley, can always be found

through the window of some bar in Barrio Alto, but they're flirting with the bartender and don't notice me knocking at the glass. My best friends laugh loudly when they start their ride on the Empire Corridor from upstate New York into Manhattan, but I always get off at the halfway mark, knowing I'll miss them as they ride the remaining 230 miles into the city. I see my second love jogging towards the New Jersey side of the Benjamin Franklin Bridge, but I can't roll down my car window fast enough to ask what music she's listening to, or if the red light on the Christiana tower is still blinking. I'm always seeing these people in the wrong places, mostly because they're not really there at all. My brain is constantly playing these films about ghosts, leaving me to think that the weather must be too much for a kid who wears a black hoodie and black jeans year round. I guess there's still room to grow.

Today, I'm in Woods Hole again. Another year gets away, another summer of love. I think I really love this place, going to talks and learning something new every day, pushing myself intellectually, but all the gossip in the grain makes me dizzy. I don't know why I care; I guess I've always been a delicate kid. So I often find myself hiding in the bathroom because it's the only place I can be by myself and breathe for a minute. I've been hyperventilating in the bathrooms here for 3 years now (from the leftmost seat at the bar at Captain Kidd 2018). This is my relationship with science; I get so sick of it at times; I always find myself consistently frustrated, lost, and uncomfortable, only to find myself in love with it again the next day. The feelings and challenges that come with science, the ones that wake me up in the middle of the night and always seem to cause strain, still get me out of bed in the morning and relieve me of all the other air-conditioned stresses of everyday life. Science does that a lot for me, and it makes me scared to think of what could ever take its place.

Some kind of clarity (Nash equilibrium)

Getting to do science has been beautiful, challenging, downright brutal, and one of the most rewarding experiences of my life. It's something I've found love in and even found love through. It also made me realize the outright disillusionment, frustration, sacrifice, and sadness that can come with pursuing something that is an absolute truth. Now that it's over, I think that my biggest regret is not taking my time. I wasted so many years being stressed because I wanted to produce as all this data so I could be on as many papers as I possibly could. I thought that there wasn't any other way to be. To be honest, I lost sight of why I got into science in the first place. That's not how it should be. I remember the day when my first data paper got accepted and I was proud of myself for a couple of hours. I've never felt more proud of anything in my life, and yet I never really think about it. I wish I could just be proud of myself for more than a minute. I guess I thought that being the best would bring me happiness; I never got to that point but I'm pretty sure if I had, it wouldn't make me happy when my bright future finally leaves me and my hair starts to go grey. I guess what I wanted myself to be, it was never really me.

Transatlanticism

Home's face, how ages when you're away. All the small ephemera that you think will be there forever kind of just disappears once you decide to leave it behind. And I'll come home and drive all those bends I've known my whole life, past the department stores I never went into on Route 73, the SugarHouse Casino I never gambled in, the wind in the New Jersey wheat, and the whole thing. But I wanted to disappear from these places so badly when I was younger, and *it's so easy to become hard to find* if that's what you really want. So I left. These days, I find myself on Google's street view virtually driving down streets where I grew up, pausing at the loading zones where I used to do stupid shit with my friends, the graduate school I mastered out of, or the freezing beaches where I'd wade in waist high water when I was a kid, actively looking for

places where I used to spend my time. If I went back to those places today, everything I used to know would probably be *hard to find*.

What nobody tells you that when you actually do leave home, it's not just the fronts to the outlet stores that change, but it's the relationships you've built entire life with your family and friends that become completely different. I'm nostalgic all the time, I have to go out of my way to visit my best friends in Manhattan, most of the people I knew in college don't remember me, and I miss being my mother's son. I guess everything that feels permanent is pretty easily lost in sock drawers. And every time I come back home everyone will remind me that look gossamer thin and tired. Don't you all think I know that? I'm doing the best I can. Don't you know how fucking hard it is to build something back up with worn out tools? (December 2018)

I remember driving around Marlton with one of my best friends' Ant after getting back from Lisbon (May 2019). I was staying in New Jersey for a couple days before I went back to North Carolina so I could breathe. It felt so good to be in my old home. It always makes me sentimental when I run my hand over the railing as I walk up the stairs to my old room, see the pawprint of my childhood dog on the refrigerator, or look at the New Jersey sky I condemn so often, only to feel of the wind in my hair as Ant and I drove down the roads that will always feel familiar. Maybe I should have stayed; I could have sold apples and lemonade at the church on Sundays; I would have worked with my dad; I should have bought a house close to my parents and brother by the time I turned thirty; I could see my best friends every weekend. Was this Ph.D. was really worth missing out on all this? Would I have been happier if I stayed? But at the end of the day, somethings always feel like home, no matter how far away you actually are.

I guess home can be a room in a building, or on a road in some map that's in a dusty atlas. I'm home when I visit New Jersey over the Holidays and I sleep for 13 hours a day; I'm home when I stumble into a ticker tape parade in Manhattan with my best friends; I'm home

when I walk through a freezing Philadelphia by myself every December 27th with my headphones in; I'm home when I'm dancing in the processing room by myself; I'm home when I watch Laura tending to the garden we planted; I'm home when I walk in the scope room and turn on the TIRF. All of these people, places, and things have become home and I am grateful for that (January 2018).

One More Thing

Okay, it's finally over, so I'll say a couple more things. Science is really hard, it is a labor of love and you have to use your entire heart to get you through. Be understanding, humble, and kind. Always build people up; never put them down. There's no shade in the shadow of other graduate students, so just do the best you can. Spend time in Manhattan. Visit Philadelphia, but only when it's sunny. Always do a little more than what's expected of you. Don't be afraid to appear stupid, fall and figure out what to do on the way down. Change your brain chemistry every now and then. If you can give yourself to something, then you should. One More Thing, once you lose that absurd idea of being perfect, you can be good.

TABLE OF CONTENTS

LIST OF FIGURES

LIST OF TABLES

LIST OF ABBREVIATIONS

AH	Amphipathic helix
A. aceri	*Ashbya aceri*
A. gossypii	*Ashbya gossypii*
BAR	Bin-amphiphysin-Rvs
B. subtilis	*Bacillus subtilis*
BME	β-mercaptoethanol.
C. elegans	*Caenorhabditis elegans*
$CaCl_2$	Calcium chloride
Cdc	Cell division cycle
CTE	C-terminal extension
D. melanogaster	*Drosophila melanogaster*
DIC	Differential interference contrast
DOPC	1,2-Dioleoyl-sn-glycero-3-phosphocholine
DOPE	1,2-Dioleoyl-sn-glycero-3-phosphoethanolamine
DOPS	1,2-Dioyleoyl-sn-glycero-3-phospho-L-serine
DMPC	1,2-Dimyristol-sn-glycero-3-phosphocholine
ER	Endoplasmic reticulum
GFP	Green fluorescence protein
GUV	Giant unilamellar vesicle
GTP	Guanine triphosphate
HIS	Histidine
HS-AFM	High speed- atomic force microscopy

H. sapiens	*Homo sapiens*
IPTG	Isopropyl β-d-1-thiogalactopyranoside
K_a	Association rate
K_{off}	Disassociation rate
K_d	Equilibrium disassociation constant
$MgCl_2$	Magnesium chloride
MSD	Mean-sqaured displacement
PI	Phosphatidylinositol
PI(3,5)P2	Phosphatidyltidylinositol 3,5-bisphosphate
PI(4,5)P2	Phosphatidyltidylinositol 4,5-bisphosphate
PEG	Polyethylene glycol
PTM	Post-translational modification
Rh-PE	1,2-dioleoyl-sn-glycero-3-phosphoethanolamine-N-(lissamine rhodamine B sulfonyl)
S. cerevisiae	*Saccharomyces cerevisiae*
S. pombe	*Schizosaccromyces pombe*
SDS-PAGE	Sodium dodecyl sulfate polyacrylamide gel electrophoresis
SEM	Scanning electron microscopy
SLB	Supported planar bilayer
SUV	Small unilamellar vesicle
TIRF	Total internal reflection fluorescence
TEM	Transmission electron microscopy
T. thermophilia	*Tetrahymena thermophila*

CHAPTER 1
INTRODUCTION

1.1 Evolution of septin protein domains throughout the eukaryotic tree of life

Septins were first discovered in the fungus *Saccharomyces cerevisiae* as essential gene products for cytokinesis (Hartwell *et al.*, 1973). Since then, septins have been identified throughout the eukaryotic tree of life in both opisthokonts (animals, fungi, choanoflagellates, and microsproidia) and non-opisthokonts (chlorophyte algae, ciliates, cryptophytes, and dinoflagellates) alike, suggesting septins were present in an early eukaryotic ancestor. The number of septin genes within an organism ranges from 1 (i.e. *Chlamydomonas reinhardtii*) to 13 (i.e. *Homo sapiens)*. Sequence analysis across opisthokonts and non-opisthokonts have shown two major identifying characteristics of septin sequences including the G1, G3, and G4 core GTPase binding domains, as well as the septin unique element (Pan, Malmberg and Momany, 2007; Nishihama, Onishi and Pringle, 2011) (Figure 1.1). Guanine nucleotide binding has been shown to be important for assembly of septin polypeptides into the characteristic heteromeric rod-shaped protofilament (Weems and McMurray, 2017), whereas the septin unique element has been suggested to play a role in septin polymerization into filaments (Sirajuddin *et al.*, 2007; Nishihama, Onishi and Pringle, 2011). Interestingly, the well-known polybasic region and the C-terminal coiled-coil regions present in many opisthokont septins are notably absent in most, if not all non-opisthokont sepins (Pan, Malmberg and Momany, 2007; Nishihama, Onishi and Pringle, 2011). Polybasic regions, or short stretches of positively charged amino acids have been long suggested

to be important for septin-membrane interactions (Casamayor and Snyder, 2003; Aurélie Bertin *et al.*, 2010), whereas the function of the coiled-coil regions have remained mysterious, but have been suggested to participate in septin-septin pairing interactions (Aurélie Bertin *et al.*, 2010; Finnigan, Takagi, *et al.*, 2015). Interestingly, regions in the predicted coiled-coil element of several septin polypeptides including Cdc12 in budding yeast and Sept6 in humans, are actually amphipathic helices, which are important for septin membrane binding (Cannon *et al.*, 2019). Interestingly, instead of a polybasic region or coiled-coil element, several non-opisthokont septins, including those in chlorophyte-algae, brown algea and *T. thermophilia* have a conserved hydrophobic patch in their C-termini (Nishihama, Onishi and Pringle, 2011). It is tempting to speculate that this hydrophobic patch serves a similar function to the membrane binding domains of those found in opisthokont septins. The sequence and phylogenetic analysis of septins by Momany, Onishi, and Pringle have provided invaluable clues into the origins of the septin cytoskeleton. However, there is much left to be done, as a better understanding of how septin protein domains have evolved in different organisms over time will better elucidate their mysterious and pleiotropic functions.

Figure 1.1 Schematic of septin protein domain structures across eukaryotes
(A) Typical protein domain structure for opisthokont septins. 1.) Disordered N-terminal region; 2.) Polybasic region; 3.) GTP-binding domain; 4.) Septin unique element; 5.) C-terminal extension; 6.) Predicted coiled-coil region within the C-terminal extension. (B) Typical protein domain structure for non-opisthokont septins. 1.) Disordered N-terminal region; 3.) GTP-binding domain; 4.) Septin unique element; 5.) C-terminal extension; 7.) Predicted transmembrane domain within the C-terminal extension.

1.2 Septin ultrastructure and assembly into higher-order structures on membranes

Septin polypeptides are arranged into a heteromeric rod-shaped complex (Field *et al.*, 1996b; John *et al.*, 2007; Sirajuddin *et al.*, 2007; A. Bertin *et al.*, 2008) (Figure 1.2). Several ultrastructural studies have shown that the number of septins and length of given rod varies with the organism; *S. cerevisiae* septin rods consist of two copies of four different polypeptides to form a 32 nm-long hetero-octamer, whereas *C. elegans* rods are built from two copies of two different polypeptides to form a 16 nm-long hetero-tetramer (John *et al.*, 2007; A. Bertin *et al.*, 2008). Septin rods are nonpolar along the long axis of the rod, as the individual polypeptides are arranged in a palindromic fashion (Sirajuddin *et al.*, 2007; A. Bertin *et al.*, 2008), with the C-terminal extensions (CTEs) extending out from the globular region.

Septin rods assemble into filaments in a process that is intimately tied to membrane binding (Figure 1.2A). Interestingly, in fungal cells, septin filaments are only found on the plasma membrane, whereas septin rods are only detectable in the cytoplasm (Bridges *et al.*, 2014). However, in mammalian cells septin filaments are also found on actin and microtubule cytoskeletons (Kinoshita *et al.*, 2002; Hu *et al.*, 2012). The current model for septin filament formation on membranes begins with septin rods from the bulk (cytoplasm) binding to a phospholipid bilayer. Membrane-bound octamers will then diffuse and collide with one another via their terminal subunits (i.e. Cdc11 in *S. cerevisiae*) to form filaments in a process termed diffusion-driven annealing. Septin filaments can either fragment or connect interact to with nearby filaments to form higher-order structures including pairs, layers, and rings (Figure 1.2B-F).

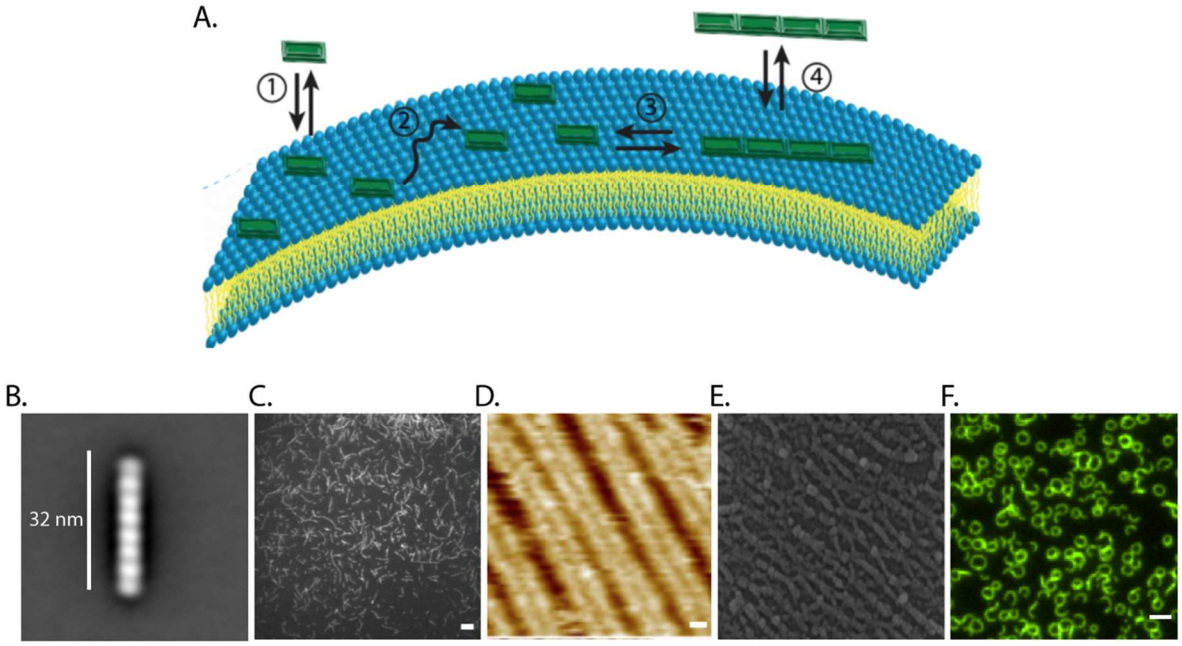

Figure 1.2 Septin assembly on membranes and the variety of septin structures

(A) The current model for septin assembly onto membranes. 1.) Rod complexes from the bulk can bind or unbind the membrane with specific rate constants; 2.) Septin rods diffuse laterally along the membrane. (3) Diffusing rods can collide with one another to form filaments. Alternatively, filaments can fragment anywhere along their length to generate septins rods or shorter filaments.(4) Septin filament dissociation from the membrane. Although it hasn't been observed, septin filaments formed in bulk can potentially interact with membranes. (B) Class averaged *S. cerevisiae* septin rod complex imaged by transmission electron microscopy (TEM). (In collaboration with Neil Billington, NIH). (C) *S. cerevisiae* septin filaments imaged by total internal reflection fluorescence (TIRF) microscopy. Scale bar 4µm. (D) High-speed atomic force micrograph of septin filament pairs. Scale bar 4 µm. (In collaboration with Simon Scheurring, Cornell). (E) Dense septin filament layers imaged using scanning electron microscopy (SEM). (F) *S. cerevisiae* septins forming rings on planar supported lipid bilayers. Scale bar 2 µm. (Image courtesy of Ben Woods).

1.3 Septin function in cells

In cells, septins are found associated with membranes (Bridges and Gladfelter, 2015), as well as actin (Kinoshita *et al.*, 2002) and microtubule cytoskeletons (Hu *et al.*, 2012), where they help regulate multiple processes including cell cycle progression (Shulewitz, Inouye and Thorner, 1999; M. S. Longtine *et al.*, 2000), migration (Dolat *et al.*, 2014), and vesicular

trafficking (Dolat and Spiliotis, 2016; Krokowski *et al.*, 2018). At these sites, septins function as signaling platforms by localizing suites of proteins to discrete locations within cells (Gladfelter, Pringle and Lew, 2001), provide a lateral diffusion barrier for select membrane-anchored proteins (Luedeke *et al.*, 2005; Chao *et al.*, 2014), and influence the rigidity of the cortex (Gilden *et al.*, 2012). These diverse functions are associated with a wide array of septin higher-order structures (Figure 1.3).

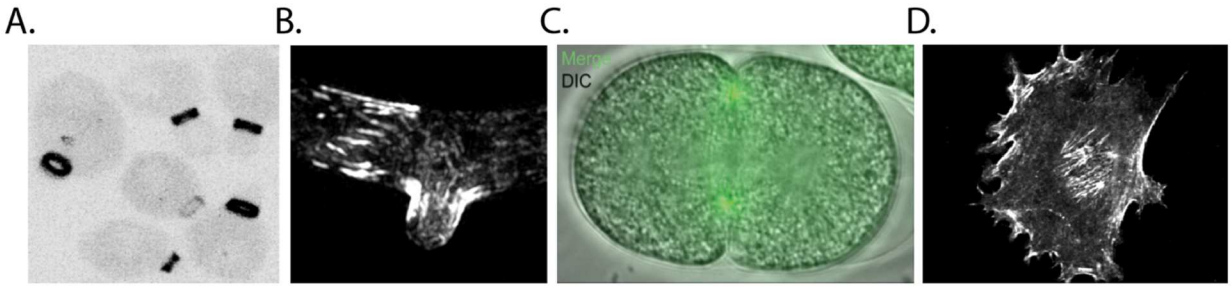

Figure 1.3 Septin localization in fungi through humans
(A) Septin nascent rings and hourglass structures in *S. cerevisiae* (Image courtesy of Ben Woods). (B) Septin inter-region ring and curvature-localized structures in the filamentous fungus *Ashbya gossypii*. (C) Septin localization (green) at the cytokinetic furrow in the developing C. elegans embryo (Image courtesy of Amy Maddox lab). (D) Septin localization in a migrating NIH 3T3 fibroblast cell. Strong septin localization is observed at the leading edge of the plasma membrane as well as at the perinuclear region. (Image courtesy of Patrick Oakes).

In budding yeast, septins undergo multiple structural rearrangements over the course of the cell cycle. For example, the septin filaments comprising the hour-glass structure formed at S/G2 run parallel to the mother-bud axis where they align with the positive principle curvature on the cortex; however just before cytokinesis, the hour-glass structure splits into double rings where septin filaments run perpendicular to the mother-bud axis (Ong *et al.*, 2014). Hourglass-structures recruit effector proteins such as Hsl1, Elm1, and Hsl7 to facilitate the degradation of Swe1 (a wee1 homologue) to allow progression through the cell cycle (Shulewitz, Inouye and Thorner, 1999; M. S. Longtine *et al.*, 2000; Cid *et al.*, 2001; Sakchaisri *et al.*, 2004; Asano *et al.*, 2005; Raspelli *et*

al., 2011; Kang, Tsygankov and Lew, 2016). In the pathogenic rice blast fungus, *M. oryzae,* septins form a ring at the base of infectious peg structures to promote infection into host plant cells (Dagdas *et al.*, 2012). Additionally, septins will form cages around *Shigella flexneri* upon infection in mammalian cells to facilitate the degradation of the virulent bacteria (Krokowski *et al.*, 2018). The variety of septin structures observed in cells is remarkable, however there is much work left to be done to understand their functions. In the next section, we will focus on how septins localize to specific membrane geometries and the functional implications that this has in cells.

1.4 Micron-scale membrane curvature sensors

Adapted from a review article published in *Trends in Biochemical Sciences*, October 2017

AUTHORS: Kevin S. Cannon, Benjamin L. Woods, Amy S. Gladfelter

1.4.1 Cellular membranes and curvature

Shape is a common feature used to describe cells. Consider the transformation of a platelet from a smooth disc to a protrusion-rich, activated state; the distinct morphologies of cells such as neurons and podocytes; and the variety of cell shapes found in the microbial world. The ability to make and change shapes is central to specialized cell functions and adaptations of cells to changing environments. This link between form and function is exemplified in a dendritic spine or the dramatic switches between budding and filamentation of pathogenic fungi in hosts. Shape depends on cells spatially controlling networks of proteins and regulating the physical properties of membranes. While it is somewhat understood how cells generate different shapes, comparatively little is known about how cells recognize their own shape and use information about their geometry.

One way cell shape can be described is in terms of membrane curvature. Cell membranes are thin, lipid-protein mosaics that function primarily to compartmentalize the cell and provide a selective barrier to the extracellular environment (Singer and Nicolson, 1972) . Additional functions of membranes include responding to physical forces, serving as signaling platforms, regulating the transport of nutrients and ions into the cell, and the storage of lipids and proteins(Walker, Willingham and Zuker, 2000; Bretscher, 2003; Fujimoto and Parton, 2011; Brown, 2012). Membrane composition between cell and organelle membranes can vary extensively, with differences arising from the combinations of particular lipid species, fatty acyl chains and saturation. *In vitro* studies have shown that these differences can alter membrane physicochemical characteristics such as thickness, curvature, fluidity, surface charge and what proteins reside in or on specific membranes (Lewis and Engelman, 1983; Szule, Fuller and Peter Rand, 2002; Zhang *et al.*, 2011; Budvytyte *et al.*, 2013). Ultimately, cell and organelle shape can be influenced by properties of the membrane.

Cellular membrane curvature can span from nanometer to micrometer scales (Figure 1A). Membrane curvature sensing is best understood for nanometer-sized molecules binding nanometer curvatures such as ArfGAP1(Bigay *et al.*, 2005; Drin *et al.*, 2007; Vanni *et al.*, 2014), α-synuclein (Pranke *et al.*, 2011), and BAR proteins(Peter *et al.*, 2004; Simunovic *et al.*, 2016). When compared to typical globular proteins, curvatures at the micron scale would have a thousand-fold larger area (Figure 1A*).* How do nanometer sized proteins perceive membrane curvatures that are several orders of magnitude their scale?

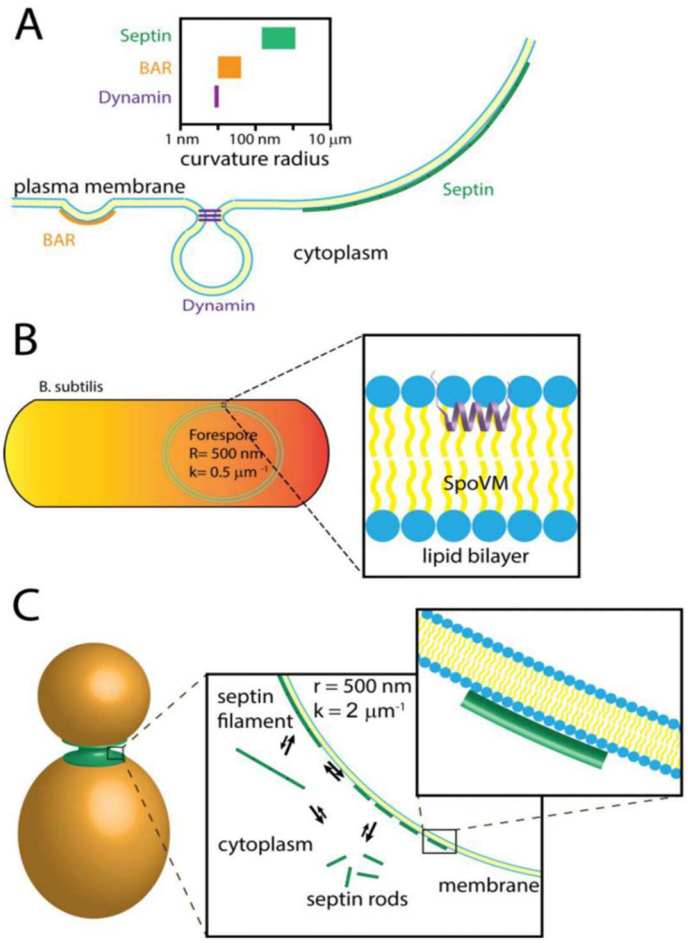

Figure 1.4 | The disparity between nanometer-scaled molecules and micrometer-scale curvature at the membrane.
(A) Cells possess a variety of proteins that can bind and recognize curved biological membranes. Some of the best understood membrane curvature "sensors" are BAR domain proteins (left) and dynamin (center), which recognize steep, nanometer-scale curvatures. Comparatively, the septin cytoskeleton (right) recognizes much shallower curvatures at a micron-scale. The range of curvatures recognized by these proteins are depicted above.
(B) During sporulation in the bacterium *Bacillus subtilis* SpoVM preferentially binds to the forespore membrane, the only site of positive curvature in the cell, which has a curvature of about 4 μm^{-1} (or a radius of 500 nm). The amphipathic helix of SpoVM is thought to insert into the lipid bilayer of the forespore membrane (inset). Across the length of SpoVM (~ 4 nm), the perceived membrane curvature is nearly flat.
(C) After bud emergence in the budding yeast *Saccharomyces cerevisiaie,* septins are localized to the mother-bud neck, which is the only area of continuous positive curvature at the plasma membrane. Septins are thought to be in an equilibrium between soluble and assembled states at the plasma membrane (first inset). Septins may cooperatively associate with lipid supported bilayers on beads *in vitro* suggesting that septin polymerization into filaments stabilizes their association to the membrane. Across the length of septin rod (17-32 nm), the perceived membrane curvature is nearly flat (second inset).

To date, only SpoVM and the septins have been identified to be able to sense positive micron-scale membrane curvature. SpoVM was identified in the bacterium *Bacillus subtilis* as essential for spore formation (Levin *et al.*, 1993). Septins were identified in the budding yeast as essential gene products during cytokinesis, and have since been found to be conserved throughout eukaryotes but missing from land plants(Hartwell *et al.*, 1973; Pan, Malmberg and Momany, 2007; Mostowy and Cossart, 2012; Onishi and Pringle, 2016). For both SpoVM and septins, the ability to sense curvature at this scale is central to their biological function. In the case of SpoVM, curvature sensing is likely essential for spore maturation (Ramamurthi *et al.*, 2009). For septins, their best-established curvature role is in the morphogenesis checkpoint where they act to sense the presence of a bud in yeast to coordinate cell shape with cell cycle progression(M. S. Longtine *et al.*, 2000; Kang, Tsygankov and Lew, 2016). Before elaborating on these cell biological functions, we will discuss experiments that established these proteins as micron-scaled curvature sensors, and the current thinking on how these relatively small proteins recognize such shallow curvatures.

1.4.2 SpoVM, a prokaryotic micron-scale curvature sensor

In response to environmental stresses, *B. subtilis* sporulate to generate a dormant endospore (Tan and Ramamurthi, 2014). The endospore is metabolically inactive and can withstand harsh environmental conditions (Henriques and Moran, 2007; Mckenney, Driks and Eichenberger, 2013). Sporulation is dependent on the formation of an intracellular double membrane structure called the forespore. At 1-micron in diameter, the forespore is the only site of shallow positive membrane curvature in the cell (Figure 1B) (Higgins and Dworkin, 2012). SpoVM, a 26 amino acid polypeptide, localizes to the forespore where it recruits SpoIVA(Ramamurthi, Clapham and Losick, 2006; Ramamurthi *et al.*, 2009). SpoIVA can then recruit a network of forespore proteins necessary for forespore maturation. *spoVM* mutants form

very thin, immature spores that are not resistant to environmental stresses (Levin *et al.*, 1993). This indicates SpoVM is essential for proper *B. subtilis* sporulation. However, the possibility remained that some other protein is the true curvature sensor, and not SpoVM.

To determine whether SpoVM can distinguish between different curvatures, recombinant SpoVM was incubated with lipid bilayers supported on spherical silica beads of defined curvatures (Ramamurthi *et al.*, 2009; Gill, J.-P. Castaing, *et al.*, 2015). Saturation binding curves for SpoVM adsorption onto 2 μm and 8 μm diameter surfaces revealed that at low concentrations, SpoVM preferentially binds the 2 μm beads. Increasing the SpoVM concentration showed binding to both bead sizes; however, SpoVM adsorption onto 2 μm beads occurred more rapidly. Saturation binding curves for both bead sizes further revealed that although the number of binding sites for SpoVM were similar on both curvatures, SpoVM had a threefold-higher affinity for the 2 μm-sized beads compared to 8 μm-sized beads. ese current data suggest that SpoVM has intrinsic, micron-scale curvature sensing abilities. Interestingly, replacing the proline as the 9th residue with an alanine ($SpoVM^{P9A}$) abolishes its curvature preference to 2 μm beads, leading to equal binding to both bead sizes, with a two-fold *increase* in affinity when compared to wild-type SpoVM. This raises the question; how does a single amino acid residue contribute to curvature sensitivity?

Analysis of the primary sequence followed by solution state NMR of SpoVM revealed that an amphipathic helix extends from amino acid residues 11 to 23, flanked by flexible N and C termini (Ramamurthi *et al.*, 2009; Gill, J. P. Castaing, *et al.*, 2015). Amphipathic helices harbor hydrophobic and polar regions on opposite faces of the helix and are a recurring theme of membrane curvature sensors. Interestingly, in contrast to SpoVM, $SpoVM^{P9A}$ was helical along the entire length of the protein and had an increase in positive charge along its polar face.

Probing the interaction of SpoVM with the membrane identified that the helical residues of SpoVM were less accessible to a water-soluble probe than the N or C termini. Molecular dynamics (MD) simulations show that both SpoVM and SpoVM^{P9A} may submerge within the bilayer, well below the phospholipid head groups, oriented parallel to the membrane. Although the wild-type SpoVM N terminus was found to be highly flexible, the SpoVM^{P9A} N terminus was more rigid. It was proposed that the flexible N terminus is important for recruiting additional SpoVM molecules and other forespore proteins to positively curved membranes in a cooperative manner, consistent with the obtained Hill coefficients from saturation binding curves. Cooperativity may emerge from oligomerization and thus it will be important to determine if SpoVM can oligomerize (perhaps mediated by its flexible N-terminus), and if oligomerization is critical for membrane curvature sensing. It will also be important to determine the specificity of SpoVM membrane curvature recognition between nanometer and micrometer-scale curvatures.

Interestingly, similar themes emerge for a sensor of negative membrane curvature from prokaryotes, DivIVA. This protein preferentially assembles at sites of micron-scale, negative membrane curvature and binds membranes using an amphipathic helix (Lenarcic *et al.*, 2009) . Several prokaryotic proteins, including DivIVA localize to sites of membrane curvature (Table 1), however, their intrinsic curvature sensing capacity in vitro remains to be determined.

Table 1.41 | A subset of prokaryotic membrane curvature sensors and their properties

Protein	Curvature localized to in vivo	Membrane binding motif	Deform liposomes in vitro?	Formation of higher order structures	Primary Function
FtsZ	Negative	-	+ when complexed with FtsA* or when fused to a membrane targeting sequence	+	Cytokinesis
FtsA	Negative	Amphipathic helix	+ when complexed with FtsZ	+	Tether FtsZ to the membrane, Z-ring assembly
MreB	Negative and Positive	Amphipathic Helix	+	+	Cell shape maintenance/ cell wall synthesis
CrvA	Low positive to negative	Unknown. Data suggests CrvA localizes in the periplasm	Unknown. Shown in vivo	+	Cell wall insertion, generates cell curvature
CreS	Positive	-	Unknown. Shown in vivo	+	Cell shape maintenance, surface colonization

1.4.3 Septins as a micron-scale curvature sensor in eukaryotic cells

Septins are filament forming, GTP-binding proteins conserved from yeast to humans. Recombinant and immunoprecipitated septins from budding yeast form octameric rod complexes, as seen using negative stain transmission electron microscopy (TEM) (Aurelie Bertin *et al.*, 2008). Structural analysis of septins from worms, and mammalian cells show that rod complex formation is an intrinsic feature of septins (John *et al.*, 2007; Sirajuddin *et al.*, 2007). The septin rod contains two copies of each septin polypeptide, and depending on the organism, can vary in length from ~ 17 nm in *C. elegans* (John *et al.*, 2007) to ~32 nm in *S. cerevisiae* (A. Bertin *et al.*, 2008). Septin rods can associate and diffuse at the membrane, where they can bind end-on to one another to form micron-scaled filaments as demonstrated by total internal reflection fluorescence (TIRF) microscopy (Bridges *et al.*, 2014). Septin filaments can be arranged to a variety of higher-order structures, some of which are at sites of micron-scale membrane curvature, including at the bud-neck in *S. cerevisiae*, and at the bases of dendritic

spines and hyphal branches in neurons and filamentous fungi, respectively (MARK S Longtine *et al.*, 2000; DeMay *et al.*, 2009; Cho *et al.*, 2011; Bridges *et al.*, 2016). At these sites, septins coordinate cell cycle progression (MARK S Longtine *et al.*, 2000), influence the organization of actin (Mavrakis *et al.*, 2014) and microtubules (Nölke *et al.*, 2016), and may function as a lateral diffusion barrier in the membrane(Barral *et al.*, 2000; Luedeke *et al.*, 2005; Hu *et al.*, 2010). The fact that septin structures are often localized to sites of micron-scale membrane curvature suggested that the septins might be able to "sense" these shallow curvatures.

To test if septins could sense curvature, recombinant septins were incubated with supported lipid bilayers on beads of different diameters, similar to experiments done with SpoVM detailed above. Purified septins from *S. cerevisiae* and mammals preferentially bound to membranes with micron-scale curvatures, comparable to what is seen at the bud neck and at the cytokinetic furrow (Bridges *et al.*, 2016). Specifically, septins were enriched on 1 μm and 3 μm beads, and less so on beads above and below these sizes (Figure 2) Furthermore, time-lapse microscopy showed that septins accumulated faster onto 1 μm beads than 5 μm beads, suggesting that differences in maximum adsorption alone cannot explain preferential septin binding to different curvatures. Interestingly, septin binding to 5 μm beads had a bimodal distribution such that some beads were coated with septins while other beads were devoid of septins, suggestive of a cooperative mechanism for septin adsorption. These data suggest that membrane affinity and binding cooperativity - rather than the number of available membrane binding sites - are what determine septin binding preference to curved membranes, akin to SpoVM.

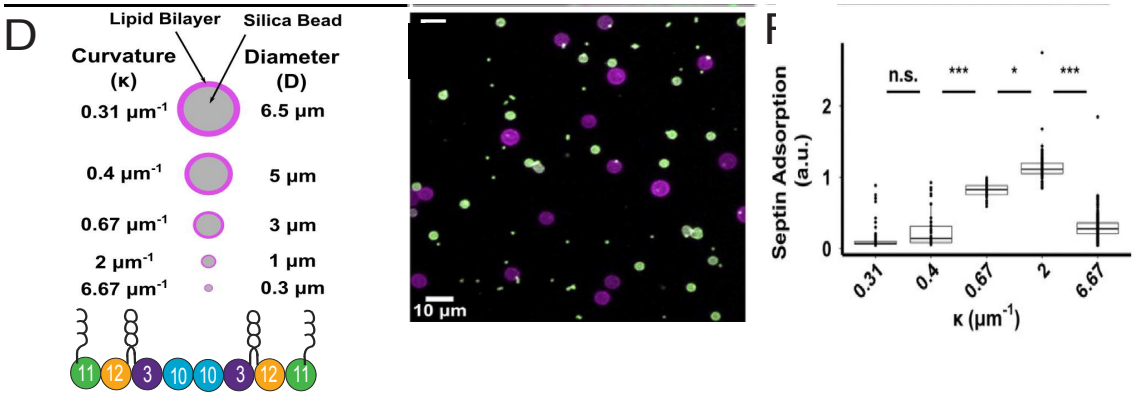

Figure 1.5 Septins preferentially adsorb onto micrometer scale membrane curvature in vitro. (A-C) A minimal in vitro reconstitution system consisting of silica beads of different diameters coated in a lipid bilayer and purified septin proteins. (A) Cartoon of membrane coated silica beads of different diameters with cartoon of septins representing purified recombinant proteins Cdc11, Cdc12, Cdc3, and Cdc10. (B) Maximum intensity projection showing septin binding (green) to specific micrometer-scale membrane curvatures. Magenta represents the lipid bilayer. (C) Quantification measuring septin adsorption onto tested membrane curvatures. (Bridges et. al., 2016)

How do septins distinguish different curvatures? Is septin filament polymerization required to sense micron-scale curvature? Or can a single septin rod sense shallow membrane curvature? It is tempting to speculate that membrane curvature is recognized at the level of the septin filament which can extend hundreds of nanometers, and not necessarily at the level of the rod. To test this hypothesis, Bridges et al. assessed whether individual, non-polymerizable mutant septin rods preferentially associated to supported lipid bilayers on beads of varying sizes (Bridges *et al.*, 2016). Non-polymerizable rods did not stably associate to beads of any size, indicating septin association with membranes is likely driven by the collective and cooperative affinity of many subunits of a filament. To bypass this limitation, histidine-tagged, non-polymerizable septin rods were recruited to lipid coated beads containing Ni^{2+}-NTA headgroups. Remarkably, these rods preferentially adsorbed onto 1 μm diameter beads, albeit much less well than the filament-forming septins. These data suggest that at some level a single septin rod can recognize micron scale curvature, possibly through the flexibility of the rod itself (Sirajuddin *et*

al., 2007; A. Bertin *et al.*, 2008). Future work should address how the length scale of septin filaments affects curvature sensing, what surface of the septin binds to curved surfaces, and whether lateral interactions (bundling) of septin filaments and different membrane curvatures affect septins' cooperative affinity to the membrane.

1.4.4 Sensing micron-scale curvature in the cell: An open question

How might SpoVM or septins "detect" micron-scale membrane curvature at the individual protein level? To address this question, we will discuss mechanisms employed by nanometer-scale curvature sensors and how those mechanisms may relate to micron-scale curvature sensors. Nanometer-scale curvature sensors utilize amphipathic helices (Drin *et al.*, 2007), tune protein-membrane affinity through electrostatic interactions (Takemura *et al.*, 2017), and formation of polymeric scaffolds (Simunovic *et al.*, 2016) to sense curvature (a subset of curvature sensors summarized in Table 1.42). Interestingly, some evidence suggests that both SpoVM and septins might also use amphipathic helices and electrostatic interactions.

Table 1.42 | A subset of membrane curvature sensors and their properties

Protein	Curvature localized to in vitro	Scale	BAR domain	Insertional amphipathic helix	Deform liposomes in vitro?	Formation of higher ordered structures	Membrane binding sensitive to electrostatics	Membrane binding sensitive to lipid packing defects	PTM	Primary Function
Endophilin	Positive	nm	+ N-BAR	+	+	+	+	+	+	Endocytosis
Amphiphysin	Positive	nm	+ N-BAR	+	+	+	+	Unknown	Unknown	Endocytosis
IRSp53	Negative	nm	+ I-BAR	_	+	Unknown	+	Unknown	Unknown	Filopodia formation
ESCRT-III	Negative	nm	-	+	+	+	+	Unknown	Unknown	Multivesicular body formation
ArfGAP1	Positive	nm	-	+	Unknown	Unknown	-	+	+	Vesicular trafficking
SpoVM	Positive	µm	-	+	Unknown	Unknown	Unknown	Unknown.	-	Forespore formation in *B. subtilis*
DivIVa	Negative	µm	-	+	-	+	Unknown	Unknown	-	Cell division site selection
Septin	Positive	µm	-	Unknown	+	+	+	Unknown	+	Cytokinesis

How are amphipathic helices utilized to "sense" curvature? The expanding leaflet of a membrane in response to high curvature at the nanometer scale can drive phospholipid head groups apart (Hatzakis *et al.*, 2009). This reveals open sites for amphipathic helix insertion into

the membrane. On the micron-scale, defects in lipid packing are likely to manifest differently, and *may* be at the level of the fatty acyl chain rather than with the phospholipid head group. This could explain why SpoVM penetrates the bilayer and likely localizes well below the phospholipid head group (Gill, J.-P. Castaing, *et al.*, 2015). Altering the charge of an amphipathic helix affects both nanometer and micrometer curvature sensing. Increasing positive charge on the polar face of the SpoVM^{P9A} helix resulted in increased affinity for lipid-coated beads and impaired curvature sensing. Similarly, adding only two lysine residues to the polar face of the otherwise uncharged amphipathic helix of ArfGAP1, a nanometer-scale curvature sensor, increased membrane binding and completely abolished curvature sensitivity (Drin *et al.*, 2007). We speculate amphipathic helices may be a conserved feature for both nanometer- and micrometer-scale membrane curvature recognition.

Another common feature among nanometer-scale curvature sensors is their cooperative association with curved membranes. Cooperativity could arise through oligomerization of proteins. For example, the H0 amphipathic helix of endophilin is important in forming lateral contacts with neighboring endophilin molecules to form scaffolds/lattices on lipid tubules in vitro (Mim *et al.*, 2012). Alternatively, cooperativity could arise through protein-mediated changes in the membrane, thereby favoring the recruitment of additional proteins. For example, coarse-grained simulations of an N-BAR domain on flat membranes show additional protein recruitment upon the initial adherence and curvature induction via individual proteins (Simunovic, Srivastava and Voth, 2013). On the micron scale, both SpoVM and septin adsorption onto micron-scale curvatures seem to be reliant on effective affinity differences for various curved surfaces and cooperativity in binding. Adjusting cooperativity and affinity in Monte Carlo simulations of SpoVM adsorption onto beads highlighted how these two parameters

synergistically combine to affect curvature sensitivity. Small differences in affinity combined with modest cooperativity alterations yield clear curvature preferences for SpoVM. For septins, filament polymerization is essential for its stable association to membranes; its bimodal adsorption onto 5 μm beads suggest a cooperative mechanism is particularly important on curved surfaces (Bridges *et al.*, 2016).

Although additional work needs to be done on the molecular basis of cooperativity, it seems central feature of micron-scale curvature recognition. Could the local curvature regulate the recruitment of proteins on the membrane through some cooperative mechanism? It is tempting to speculate that the local curvature could promote the formation of different higher-ordered septin structures. However, this is a hypothesis that remains to be tested. The knowledge of nanometer curvature sensors can serve as a powerful guide for understanding micrometer-scale sensing but further work will be required to determine how the mechanisms established for nanometer perception are also exploited for micrometer sensing. Many questions remain regarding how these mechanisms first described at the nanometer scale transfer to the micron scale, if at all. The depth and breadth of these questions reveal what a ripe problem this is for further study.

1.4.5 Curvature sensing vs. curvature induction

Curvature sensing is often linked to curvature induction, however, the degree to which the two are separable can be challenging to study. For the BAR-domain protein amphiphysin, it has been seen that at low protein densities the proteins are generally in a curvature sensing regime and at high protein densities crowding and potentially lateral associations that build a rigid scaffold then induce membrane curvature (Sorre *et al.*, 2012). Similar density-sensitive behavior has also been seen for dynamin that also can assemble and act in a curvature-sensitive

manner (Roux *et al.*, 2010). Thus, the role of a protein as a sensor vs an inducer may be highly dependent on the concentration of protein.

Septins can bind and tubulate giant unilamellar vesicles (GUV) to micron-scale tubules (Tanaka-Takiguchi, Kinoshita and Takiguchi, 2009). This work suggests that curvature sensing and induction could be tightly connected for septins and potentially sensing the local geometry can be used to recruit more protein and drive membrane bending. However, artificially recruiting high concentrations of his-GFP to Ni^{2+}-NTA containing GUVs also results in tabulation (Stachowiak *et al.*, 2012) suggesting that protein crowding alone can drive membrane bending. Thus, whether tubulation is a specific function or by-product of crowding is not clear.

The fact that septins induce micron-scale tubules as opposed to highly variable or nanometer-scale tubules would support that induction of curvature may be physiologically relevant but it would be useful to assess septin curvature sensing and induction of a range of protein densities as has been done with amphiphysin and dynamin. Septin recruitment to cell blebs in mammalian cells (Gilden *et al.*, 2012) may be a context where septins both sense and induce curvature changes. In the case of experiments with SpoVM and septins using beads, induction is not possible because the bilayers are supported and similarly in fungal cells, the cell wall limits the role of septins in inducing curvature (Bridges *et al.*, 2016). In cells without such rigid extracellular domains, further work is required to disentangle the relationship between micron scale-curvature sensing and induction.

1.4.6 How cells use micron-scale membrane curvature

1.4.6a Micron scale curvature throughout the cell cycle

One of the best examples of a cell using information about its shape to inform a decision is the morphogenesis checkpoint in budding yeast. The morphogenesis checkpoint effectively

monitors whether the cell has bud, delaying nuclear division until after bud emergence (Lew, 2003). However, this raises the question: how does the cell "know" whether it has a bud? Stresses that prevent bud formation lead to an increase and stabilization in the levels of the inhibitory kinase, Swe1 (wee1 homologue), which phosphorylates the mitotic CDK, delaying the cell cycle (Sia, Herald and Lew, 1996; Sia, Bardes and Lew, 1998; McMillan *et al.*, 2002). After bud emergence, the septin collar at the mother-bud neck recruits a series of effectors (Hsl1, Elm1, and Hsl7) that lead to the hyperphosphorylation and degradation of Swe1 (Shulewitz, Inouye and Thorner, 1999; M. S. Longtine *et al.*, 2000; Cid *et al.*, 2001; Sakchaisri *et al.*, 2004; Asano *et al.*, 2005; Raspelli *et al.*, 2011; Kang, Tsygankov and Lew, 2016).The point at which Hsl1, Elm1, and Hsl7 are localized to the septin collar coincides with when septin filaments are arranged in a parallel array aligned with the positive membrane curvature of the bud neck (Ong *et al.*, 2014; Kang, Tsygankov and Lew, 2016). In cells that have not properly formed a bud, septins are unable to stably recruit Hsl1, Elm1, and Hsl7, thus allowing Swe1 levels to rise (Figure 3A). Thus, the ability of septins to recognize the positive membrane curvature of the mother-bud neck is critical to the morphogenesis checkpoint.

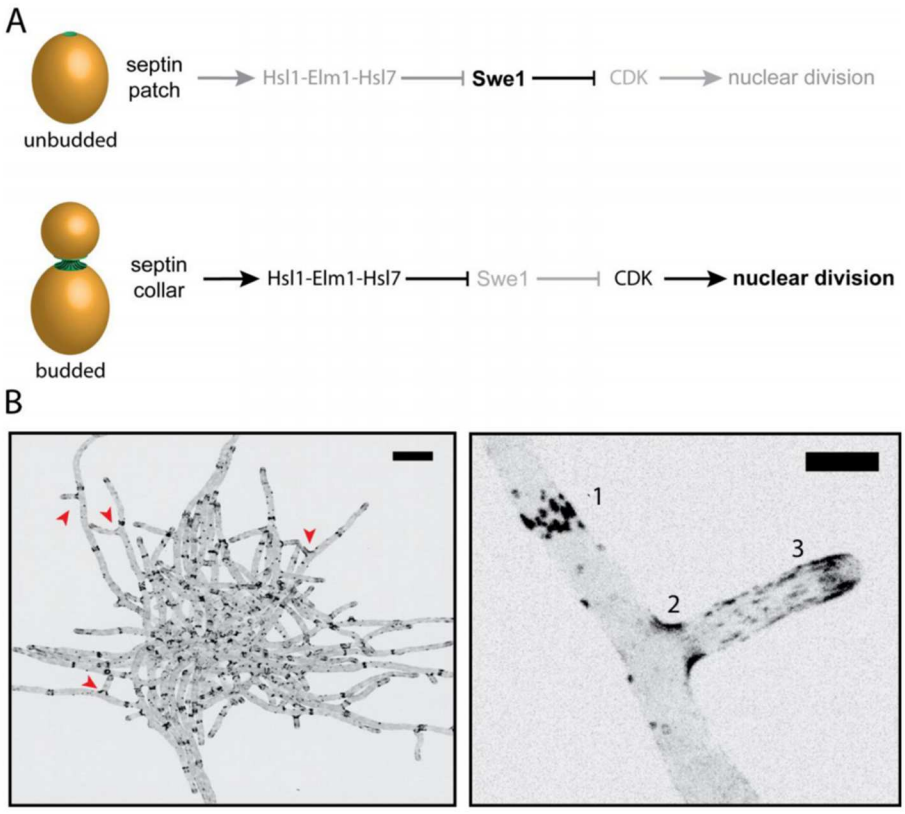

Figure 1.6 | Septin structures and localization in budding yeast and *Ashbya gossypii*
(A) Morphogenesis checkpoint in S. cerevisiae: Hsl1-Elm1-Hsl7 are not recruited to the septin patch in unbudded cells, thereby allowing the CDK-inhibitor Swe1 levels to rise. As soon as the bud emerges, septin localization transitions to an hourglass shape coincident with the generation of micron-scale curvature. Swe1-regulators are recruited after this transition to initiate the degradation of Swe1 and promote progression through the cell cycle. (B) An inverted, maximum z-stack projection of a A. gossypii cell expressing Cdc11-GFP. Scale bar, 20 µm. (Bottom right) Zoomed-in image of A. gossypii hyphae expressing Cdc11- GFP from above. Septins are organized into various higher-ordered structures in Ashbya: [1] Thick bars structures, [2] basal collars at branch points, and [3] thin, flexible filaments. Scale bar 5 µm.

Septins also localize to the developing forespore membranes during sporulation in both *S. cerevisiae* (Fares, Goetsch and Pringle, 1996) and *S. pombe* (Onishi *et al.*, 2010). During sporulation, membranous structures engulf and partition nuclear material into four separate haploid nuclei spores (Neiman, 2011). These spores display curvatures from approximately 1 μm^{-1} - 0.5 μm^{-1} (compared to 2 μm^{-1} at the mother-bud neck, Figure 1C). During spore formation expression of spore specific septins, *SPR3* and *SPR28* increase (Kaback and Feldberg, 1985). An

analogous process occurs within *S. pombe* (Mata *et al.*, 2002; Onishi *et al.*, 2010) (Onishi *et al.*, 2010; Heasley and Mcmurray, 2016). These spore specific septins are essential for sporulation, as mutants for either of these genes have misshapen forespore membranes, their forespore membranes fail to encapsulate nuclei, and cell walls do not mature properly. Mechanistically, how septins contribute to sporulation, remains unclear, but is presumably related to micron-scale membrane shape changes. It is interesting to note that spore-specific septins and mitotic-specific septins appear recognize different membrane curvatures (the forespore membrane vs. the bud neck), possibly owing a different composition of the respective septin oligomer. This would suggest that different septin complexes may have different intrinsic curvature preferences, a possibility that is also interesting to consider in mammalian cells where a more diverse suite of septin proteins and isoforms can coexist in the same cell. The problems of how septin curvature sensing is tuned developmentally and via expression of distinct heteromeric complexes is wide open for exploration.

Closely related to budding yeast, the filamentous fungus, *Ashbya gossypii,* has been a powerful, emerging model to examine the varied forms and functions of the septin cytoskeleton. During hyphal growth septins polymerize at the plasma membrane where they can form three distinct higher-ordered structures: 1) interregion rings, which are straight septin bundles organized as bars circumferentially around hyphae, 2.) basal collars that localize to newly emergent hyphae, 3.) thin, flexible filaments that run parallel to the hyphal axis (Figure 3B). Septin accumulation to the base of branches suggested their preferential localization to saddle points or sites of positive curvature. When quantified, it became clear that septins are recruited in proportion to the degree of local positive curvature. In contrast, both the thick bars and thin flexible septin filaments align along the hyphal tube, as to seemingly avoid the negative

curvature that exists orthogonal to the hyphal long axis (DeMay *et al.*, 2009). Interestingly, Hsl7, was found to localize exclusively to the septin bar structures and not curved structures. This suggests that the local geometry of the membrane may dictate the local organization of septin filaments, which in turn could control recruitment of downstream signaling proteins.

Septins are also found at the cleavage furrow of most dividing animal cells (Spiliotis, Kinoshita and Nelson, 2005). Loss of septins leads to varying degrees of cytokinesis defects, depending on the organism and distinct septin complexes that participate in early cytokinesis and abscission (Estey *et al.*, 2010). In many cells, septin enrichment is coincident with ingression, where the membrane curvature is increasing. This raises the possibility that as a cleavage furrow ingresses, septin recruitment is enhanced in a curvature-dependent manner, potentially to stabilize or regulate the actomyosin contractile ring. In this scenario membrane curvature might supply a source of positive feedback in septin recruitment during cytokinesis. Interestingly, there are also F-BAR proteins found to associate with the cytokinetic furrow in a variety of systems (Takeda *et al.*, 2013; Arasada and Pollard, 2015). During cytokinesis, some F-BAR proteins are thought to target vesicles from the late secretory pathway, whereas others are thought to participate in membrane curvature induction. It is worth investigating whether F-BAR proteins and septins coordinate the different length scales of curvature changes at the plasma membrane during cytokinesis.

1.4.6bMicron scale curvature in autophagy and lipid droplets

Autophagy is a cellular process where cytoplasmic components are degraded. During autophagy aggregated protein complexes, ribosomes (Kraft *et al.*, 2008), organelles including mitochondria (Kanki *et al.*, 2009) and invading microorganisms including *Listeria monocytogenes* (Yoshikawa *et al.*, 2009) and *Shigella flexneri* (Mostowy *et al.*, 2010) can be

targeted for degradation suggesting broad size distribution among autophagosomes. Indeed, these structures have been observed to range in curvature from 2.2 μm^{-1} to 4 μm^{-1} in yeast and 1.6 μm^{-1} to 4 μm^{-1} in mammalian cells (Baba *et al.*, 1997; Fengsrud *et al.*, 2000; Nguyen, Shteyn and Melia, 2017). Recent studies showed that septins assemble into cage-like structures around intracellular bacteria in a manner promoted by mitochondria (Mostowy *et al.*, 2010; Sirianni *et al.*, 2016). The topology and positive membrane curvature of rod-shaped bacteria and mitochondria are ideal for septins, raising the possibility that a septin-mediated immune response is induced by this ideal curvature.

Another subcellular structure with a wide variety of curvatures are lipid droplets. Lipid droplets (LD), amalgams of neutral lipids surrounded by a phospholipid monolayer, have been shown to contribute to lipid and membrane homeostasis in several organisms and cell types including *S. cerevisiae* (Yang *et al.*, 2016), adipocytes (Heid *et al.*, 2014) and hepatocytes (Ajat *et al.*, 2017). Lipid droplets display curvatures ranging from 0.4 μm^{-1} to 50 μm^{-1} in non-adipocytes (Fujimoto and Parton, 2011). Knockdown of Sept9 in Huh7 cells resulted in a decrease in LD number and size (Akil *et al.*, 2016). Additionally, Sept9 was found to colocalize with neutral lipid biosynthetic enzyme, diacylglycerol acyltransferase-1 (DGAT-1), further supporting that septins may be involved in regulating lipid and membrane homeostasis. Further work needs to be done to determine whether septins are in fact directly binding to and sensing the curvature of the surface of lipid droplets, or whether septins are recruited by other factors to the surface of droplets.

1.4.6cMicron scale curvature and lateral compartmentalization and function of membrane-interacting proteins

Biological membranes can be compartmentalized into specific domains with distinct protein compositions. One way to compartmentalize membranes is through membrane diffusion

barriers (Gehlen *et al.*, 2011; Boettcher *et al.*, 2012; Trimble and Grinstein, 2015). Diffusion barriers have been postulated at the base of cilia (Hu *et al.*, 2010), dendritic spines (Ewers *et al.*, 2014) and at the tip of mating projections during chemotropism (J. B. Kelley *et al.*, 2015), at the mother-bud neck in *S. cerevisiae* (Barral *et al.*, 2000; Chao *et al.*, 2014), and the annulus in spermatozoa. Interestingly, septins localize to each of these structures, and have been proposed to contribute to the membrane diffusion barrier (Caudron and Barral, 2009).

In the budding yeast, there is even evidence that septins act as a diffusion barrier for membranes that are adjacent to the plasma membrane. A septin-ER tether limits the diffusion of ER transmembrane proteins Pho88 and Ist2 between the mother and bud (Luedeke *et al.*, 2005; Chao *et al.*, 2014). One component of the barrier appears to be through a formation of a sphingolipid-dependent compartment at the mother-bud neck. This is thought to create a specialized membrane domain to restrict the mobility of transmembrane proteins (Clay *et al.*, 2014a).

Interestingly, septins were shown to induce local domains of supported lipid bilayers consisting of dimyristol- and dioylphosphatidylcholne (DMPC and DOPC, respectively) and phosphatidylinositol (PI) (Yamada *et al.*, 2016). It has been postulated that septins can act as a membrane diffusion barrier either by acting as physical hindrance for other membrane associated proteins, through altering the lipid abundance, by affecting lipid localization, or by some combination of the three. Future work is needed to understand the mechanisms by which septins influence mobility in membranes and the degree to which this function is due to the local topology of the membrane.

1.4.7 Regulation of micron-scale curvature sensors

Given the possibility of electrostatics driving curvature recognition, a potential way for cells to tune curvature preferences is through post-translational modifications that modulate the affinity of protein complexes for the membrane. Genetic and biochemistry experiments have

revealed numerous potential septin regulatory mechanisms, including direct protein-protein interactions, post-translational modifications (PTMs) and lipid-protein interactions (Versele and Thorner, 2004; Egelhofer *et al.*, 2008; DeMay *et al.*, 2009; DeMay, Bai, *et al.*, 2011; Garcia *et al.*, 2011a; Meseroll, Occhipinti and Gladfelter, 2013a; Suetsugu, Kurisu and Takenawa, 2014; S. W. Kim *et al.*, 2017). Septin filaments can be assembled into a variety of different organizations and patterns as higher-order structure. It is tempting to speculate that septins are tightly regulated to specify different higher-order organizations of septin filaments and possibly even fine tune septin membrane curvature recognition. Although very little is known regarding how septins or other micron-scale curvature sensors are regulated, next we will discuss what is known about septin regulation as it pertains to their ability to sense micron-scale membrane curvature.

1.4.7a Post-translational modifications as a means to regulate protein localization to micron scale membrane curvature

Proteins often undergo dynamic transitions between an insoluble membrane bound state and soluble cytoplasmic state. Post-translational modifications (PTMs) of proteins is an attractive mechanism to spatiotemporally control the localization and functions of proteins, including those that act on micron-scale membrane curvatures. Throughout the cell cycle of *S. cerevisiae,* the septin cytoskeleton is subject to changes in organization (DeMay, Bai, *et al.*, 2011; DeMay, Noda, *et al.*, 2011; Ong *et al.*, 2014). Not surprisingly, all five mitotic septins can be phosphorylated at multiple sites (Egelhofer *et al.*, 2008; Meseroll, Occhipinti and Gladfelter, 2013a). Septin-associated kinases Gin4, Elm1, and Cla4 have been shown to be important for regulating higher-order septin structures. Cla4 is required for septin collar formation in *S. cerevisiae* (Versele and Thorner, 2004), whereas loss of either Gin4 or Elm1 in *A. gossypii*

results in a loss of thick septin bar structures (DeMay *et al.*, 2009). Nonetheless, septin localization to sites of positive curvature still persist. This suggests that straight septin bars require phosphorylation whereas assembly on curved membranes does not. However, a direct a link between septin phosphorylation and curvature sensing has yet to be established. Recently, Shen et. al. showed that phosphorylation within the GTP-binding domain of Sept12 abolished septin ring formation at the annulus in sperm (Shen *et al.*, 2017), further highlighting the importance of septin regulation by phosphorylation. Interestingly, an acetylation/SUMO-ylation switch was found to regulate Cdc11 localization from the bud scar to the new incipient bud site in *S. cerevisiae* (S. W. Kim *et al.*, 2017). Despite this, it is still unclear whether septin phosphorylation, acetylation, and SUMO-ylation contribute to curvature sensing. We speculate that cells may tune the specific curvature preference of septins using PTMs that change the affinity of septins for different membrane shapes.

1.4.7b The role of the membrane composition in regulating micron scale membrane curvature

Lipid asymmetry across the bilayer is an inherent feature of cellular membranes; phosphatidylcholine and sphingolipids are predominately localized to the outer leaflet of lipid bilayers, whereas phosphatidylserine, phosphatidylethanolamine, phosphoinositols and their phosphoinositide derivatives localize to the inner leaflet (Suetsugu, Kurisu and Takenawa, 2014). This provides a means to localize membrane binding proteins to particular compartments on the basis of electrostatics, lipid packing, and local geometry. Phosphoinositides (PI) in particular, seem to have an emerging role in regulating cellular processes where micron-scale curvature is present including forespore membrane extension in *S. pombe* (Onishi *et al.*, 2010), autophagy (Tan *et al.*, 2016), and micropinocytosis (Dolat and Spiliotis, 2016) in mammalian cells. Septins may be locally recruited to membranes based on the local lipid composition.

Mammalian septin filaments comprised of, Sept2, Sept6, and Sept7 were found to localize to mature macropinocytic vesicles in a PI(3,5)P2-dependent manner and septins are found in what are thought to be PI(4,5)P2-rich sites in yeast at mating projections and the neck (Garrenton *et al.*, 2010; Dolat and Spiliotis, 2016). PI(4,5)P2-containing lipid monolayers were shown to drive septin filament assembly even in high salt conditions where septin polymerization is perturbed in solution (Aurélie Bertin *et al.*, 2010). These data suggest that phosphoinositides play a key role in regulating protein adsorption onto a wide range of membrane curvatures and may play a role in modulating curvature preferences.

1.4.8 Discussion

How do SpoVM and septins recognize micron-scale positive membrane curvature? Interestingly, both SpoVM and the septins cooperatively associate membranes with shallow positive curvature; hinting that polymerization may be important. Septins are known to polymerize into filaments hundreds of nanometers to micrometers in length. For septins it is tempting to speculate that membrane curvature is recognized at the level of the filament, and not necessarily at the level of the rod. Nonetheless, even non-polymerizable septin mutants preferentially associate with shallow curved membranes, albeit much weaker than septins that can polymerize. How then might SpoVM and septins sense shallow curvature at the protein level? Many nanometer-scale curvature sensors utilize an amphipathic helix that inserts into the lipid bilayer. SpoVM, and possibly septins, also have amphipathic helixes. Perhaps both insertion of an amphipathic helix to the membrane is conserved mechanism for sensing curvature, even at shallow curvatures.

The fact that individual septin rods can intrinsically detect shallow membrane curvature raises an interesting question. If septin filament polymerization is unnecessary for curvature

sensing, why polymerize at all? To answer this question, first consider the kinetics of an individual septin rod on and off the membrane (Figure 1C). Free septin rods that are not incorporated into filaments are favored to dissociate from the membrane (high k_{off} relative to k_{on}). Stable septin association to the membrane depends whether it is incorporated into a polymerized septin filament. This is likely critical for septins to reliably and correctly "sense" *persistent* micron-scale curvature. Otherwise, if individual septin rods could tightly associate with shallow curved membranes without polymerizing, septins would presumably localize to dispersed regions across the cortex, anywhere shallow curvature might incidentally arise (such as a relatively flat, yet slightly undulating membrane). Thus, septin filament polymerization at the membrane ensures that septins curvature recognition is limited only to persistent, shallow membrane curvatures that define cellular shapes at the micron scale.

We are just beginning to understand how cells perceive cellular membrane curvature, and by extension how cells "sense" their shape (see Outstanding Questions). It will be interesting to determine whether there are analogous proteins to SpoVM that can recognize shallow positive membrane curvature in other prokaryotes. Despite their variety of shapes and forms, both animal and fungal cells utilize the same cytoskeletal proteins, the septins, to sense micron-scale cellular membrane curvature. Oligomeric septin rods can assemble into micron-scaled filaments at the membrane, and these filaments can then assemble into various larger structures depending where they polymerize in cell. Interestingly, the organization of these larger assemblies appear to be dependent on the local membrane curvature. In budding yeast, the ability of septins to "sense" positive curvature at the mother-bud neck is critical to ensure that both the mother and future daughter cell inherit a nucleus before cytokinesis. In many different cell types, septins localize to the cytokinentic furrow and are required for cytokinesis. Further work will hopefully elucidate

roles of septins in different cell types, and determine whether the ability of septins to recognize membrane curvature is essential for these cell types.

CHAPTER 2

AN AMPHIPATHIC HELIX ENABLES SEPTINS TO SENSE MICRON-SCALE MEMBRANE CURVATURE

Published in the *Journal of Cell Biology*, January 2019

AUTHORS: Kevin S. Cannon, Benjamin L. Woods, John M. Crutchley, and Amy S. Gladfelter

2.1 Introduction

Shape is a fundamental feature in cell biology and can be thought in terms of membrane curvature (Zimmerberg and Kozlov, 2006; Cannon, Woods and Gladfelter, 2017). Cellular membrane curvature is a continuum, spanning nanometer to micrometer scales. How do cells use nanometer-sized components to perceive micron-scale changes in shape? Septins, are filament-forming, GTP-binding proteins that localize to sites of micron-scale membrane curvature from yeast to humans (Field *et al.*, 1996a; Pan, Malmberg and Momany, 2007; Bridges *et al.*, 2016). Examples of curvature-associated localizations include the bud-neck in *S. cerevisiae* (Byers and Goetsch, 1976; Haarer and Pringle, 1987; Ford and Pringle, 1991), bases of dendritic spines in neurons (Cho *et al.*, 2011), branches in filamentous fungi (Westfall and Momany, 2002; DeMay *et al.*, 2009; Bridges *et al.*, 2016), and the cytokinetic furrow (Spiliotis, Kinoshita and Nelson, 2005; Joo, Surka and Trimble, 2007; Maddox *et al.*, 2007). At these sites, septins coordinate cell cycle progression (M. S. Longtine *et al.*, 2000; Sakchaisri *et al.*, 2004), influence diffusion in the membrane (Clay *et al.*, 2014a; Yamada *et al.*, 2016), and act as a scaffold to recruit proteins

required for chromosome segregation (Spiliotis, Kinoshita and Nelson, 2005) and cytokinesis (Meitinger *et al.*, 2011; Finnigan, Booth, *et al.*, 2015).

Septins carry out these functions by assembling into heteromeric, rod-shaped, non-polar complexes which can anneal end-on to polymerize into filaments at the plasma membrane (Field *et al.*, 1996a; John *et al.*, 2007; Sirajuddin *et al.*, 2007; A. Bertin *et al.*, 2008). Budding yeast possess five mitotic septins that assemble into hetero-octamers in which the terminal subunit is either Cdc11 or Shs1(Garcia *et al.*, 2011; Khan *et al.*, 2018). Purified recombinant septins from yeast and humans preferentially adsorb onto micrometer curvatures in the absence of any cellular factors (Bridges *et al.*, 2016) indicating that curvature sensing is a conserved feature of the septin cytoskeleton. The mechanism underlying how septins sense micron-scale membrane curvature is unclear.

Most of what we know about curvature sensing comes from nanometer-sized molecules interacting with nanometer-scale curvatures. Proteins containing BAR domains and/or amphipathic helices (AH) utilize combinations of membrane insertion (Drin and Antonny, 2010), oligomerization, and scaffolding mechanisms (Simunovic, Srivastava and Voth, 2013; Simunovic *et al.*, 2015) to either sense or deform the local curvature. Membrane curvature generates lipid packing defects, providing binding sites for AHs (Hatzakis *et al.*, 2009). Proteins such as α-synuclein (Pranke *et al.*, 2011), Opi1 (Hofbauer *et al.*, 2018), and ArfGAP1 (Drin *et al.*, 2007) employ this mechanism to sense curvature. Interestingly, known micrometer-scale curvature sensors including SpoVM (Ramamurthi *et al.*, 2009), MreB (Ursell *et al.*, 2014; Hussain *et al.*, 2018) contain AHs.

In this study, we investigate the mechanisms of septin curvature sensing. We discovered that septins vary in their affinity for different curvatures, that single septin oligomers bind with

different association rates depending on the curvature and that a conserved AH is both necessary and sufficient for curvature sensing by septins. This study provides the first insights into the molecular basis for how septins sense curvature.

2.2 Materials and Methods

Yeast septin purification

BL21 (DE3) *E. coli* cells were transformed using a duet expression system (*Bridges et al.* 2016) and selected with ampicillin and chloramphenicol. Selected cells were cultured to an $O.D._{600\ nm}$ between 0.6 and 0.8 and induced with 1 mM of IPTG. Induced cultures were grown for 24 hours at 22^{o} C (3 hours for Cdc12 amphipathic helix construct) before harvesting. Cultures were pelleted at 10,000 RCF for 15 min. Pellets were resuspended in lysis buffer (1M KCl, 50 mM, Hepes pH 7.4, 1 mM $MgCl_2$, 10% glycerol, 1% Tween-20, and 1x protease inhibitor tablet (Roche), 20 mM Imidazole, 1 mg/mL lysozyme) for 30 minutes on ice with intermittent vortexing. The lysate was sonicated twice for 10 seconds and clarified by centrifugation using an SS-34 rotor at 20,000 RPM for 30 minutes. Clarified supernatant was filtered using 0.44 μm filter, then incubated with equilibrated Nickel-NTA^{2+} or Cobalt resin (Thermo Fisher Scientific; 2 mL resin per liter of *E.* coli culture) at 4^{o}C for 1 hour. Resin and lysate were added to a gravity flow column. Bound protein was washed four times with 5x the column volume with wash buffer (1M KCl, 50 mM Hepes pH 7.4, 20 mM Imidazole), and then eluted in elution buffer (300mM KCl, 50 mM Hepes pH 7.4, 500 mM Imidazole). Eluted protein was then dialyzed into septin storage buffer (300 mM KCl, 50 mM Hepes pH 7.4, 1 mM BME) for 24 hours in two steps (Slide-A-Lyzer G2 20K MWCO, Thermo Fisher Scientific; 10K MWCO for amphipathic helix constructs). During dialysis, 60 μg of TEV protease (Sigma) was added to cleave the 6x-histidine tag on Cdc12. 24 hours later, the protein was run over a second column (either Ni-NTA or cobalt

resin) to remove the protease, the poly-histidine tag, and additional contaminants. Protein purity was determined via SDS-PAGE and protein concentration was determined via Bradford assay. Purification of the Cdc12-6 complexes and AH domain constructs were purified as described above. However, for AH domain purifications, cells were induced for 4 hours at 37^{o} C and harvested for protein purification.

Amphipathic helix construct sequences

2x-AH-GFP construct has the following sequence followed by a GFP tag: LEEIQGKVKKLEEQVKSL-GSGSRSGSGS-LEEIQGKVKKLEEQVKSL-GSGSSR-GFP tag, where the underlined sequences are the AH domains within Cdc12 and the serine-glycine repeats constitute the linker regions between tandem AH domains and the GFP tag. Similarly, the 1x-AH construct has the following sequence: LEEIQGKVKKLEEQVKSL-GSGSSR-GFP tag.

Lipid mix preparation

All septin binding experiments were done using supported lipid bilayers consisting of 75 mol % dioleoylphosphatidylcholine (DOPC) Avanti Polar Lipids, 25 mol % PI (Liver, Bovine) sodium salt, and trace amounts (less than 0.1%) of phosphatidylethanolamine-N-(lissamine rhodamine B sulfonyl) (Rh-PE) (ammonium salt) Egg-Transphosphatidylated, Chicken) (Avanti Polar Lipids 810146) unless otherwise mentioned. All lipid compositions were made the same way. Lipids were mixed in chloroform solvent, and dried by a stream of argon gas to generate a lipid film. Remaining solvent was evaporated by placing the lipid film under a vacuum for at least 6 hours. Lipids were rehydrated in supported lipid bilayer buffer (300 mM KCl, 20 mM Hepes pH 7.4, 1 mM $MgCl_2$) for 30 minutes at 37^{o}C to give a final concentration of 5 mM. Hydrated lipids were subject to vortex for 10 seconds, every 5 mins for 30 mins bath sonicated in 2 minute intervals until clarification to yield small unilamellar vesicles (SUVs).

Preparation of supported lipid bilayers on silica microspheres

SUVs were adsorbed onto silica microspheres (Bangs laboratories) of various curvatures by mixing 50 nM lipids with 440 um^2 of silica microsphere surface area or 10 uL of rods in a final volume of 80 uL for 1 hour on a roller drum at room temperature. Unbound lipid was washed away by pelleting lipid-coated beads at the minimum force required to pellet each bead size using pre-reaction buffer (33.3 mM KCl, 50 mM Hepes pH 7.4) (See http://www.bangslabs.com/ for sedimentation speeds). Washes were preformed 4 times.

Measuring protein adsorption onto silica microspheres

To examine septin adsorption onto different membrane curvatures, 25 µL of septins in septin storage buffer were added to 75 µL of a bead-buffer solution of 5 mm^2 total lipid-bead surface area to give a final buffer composition of 100 mM KCl, 50 mM Hepes pH 7.4, 1 mM BME, 0.1% methylcellulose, and 0.1% bovine serum albumin (fatty acid free- Sigma). Saturation binding curves were obtained using several different septin concentrations in simple mixtures, containing only one bead size per reaction volume. Amphipathic helix adsorption was measured in mixtures containing protein and various bead diameters. Each reaction was incubated in a plastic chamber (Bridges methods paper) glued to a polyethyleneglycol (PEG)-passivated coverslip for 1 hour (to allow the reaction to reach equilibrium). Beads were imaged using either a wide-field microscope with a Ti-82 Nikon stage a 100x Plan Apo 1.49 NA oil lens, and Zyla sCMOS (Andor) (saturation binding curves) or a spinning disc (Yokogawa) confocal microscope (Nikon Ti-82 stage) using a 100x Plan Apo 1.49 NA oil lens, and a Prime 95B CMOS (Photometrics) (amphipathic helix and Cdc12-6 septin complex adsorption experiments). For analysis of septin binding, raw images were exported into Imaris 8.1.2 (Bitplane AG, Zurich, Switzerland). Each image was background subtracted in both channels using the software's

Gaussian filter for background determination (width 31.4 μm). The surface of each bead was defined using the lipid channel. Using the surface generate on each bead, sum intensity values from lipid and septin channels were exported from Imaris into Microsoft Excel. Septin adsorption was calculated by dividing the multiple sum intensity values from the septin channel over the sum intensity values from the lipid channel as to control for surface area for each bead size. Boxplots were generated through exporting intensity sum values from both channels into R version 3.2. 2 (R Foundation for Statistical Computing, Vienna, Austria, using RStudio 0.99.467, Boston, MA, USA). Boxplots were generated using ggplot2 package (Wickham, 2007; Wickham, 2009; Winston, 2014).

Generation and preparation of septin-rod supported lipid bilayer mixture.

Borosilicate rods were obtained from Glass Microfiber filters, GFC, 42.5 mm (Whatman). A single filter was torn up into small pieces into a beaker with 60 mL of 100% ethanol and sonicated until the solution became opaque. The solution was stored at room temperature overnight. The next day, 10 μL of rods were taken from the solution after thorough mixing. 70 uL of SLB buffer was added to the rods and spun down at top speed to dilute the ethanol in the solution. This step was repeated 4 additional times. 5 mM of SUVs (75% DOPC, 25% PI, trace Rh-PE, as described above) were added to the polycarbonate rods and allowed to incubate for 1 hour at room temperature. Unbound lipid was washed away pelleting lipid-coated beads at top speed (16.1 RCF) using pre-reaction buffer. The mixture of septin-lipid-coated rods were added to a circular 12mm (PEG)-coated coverslips and incubated at room temperature for 1 hour and then and prepared for scanning electron microscopy.

Scanning electron microscopy

The septin-rod mixture onto a circular PEG-coated 12mm coverslip, was fixed in 2.5% glutaraldehyde in 0.05 M sodium cacodylate (NaCo) pH 7.4 for 30 minutes followed by 2x washes in 0.05 M NaCo (5 min each wash). Samples were post-fixed in 0.5% OsO_4 Cacodylate buffer for 30 minutes and washed 3x in NaCo (5 minutes each wash). Samples were then incubated with 1% tannic acid for 15 minutes followed by 3x washes in NaCo. 0.5% OsO_4 was added for 15 minutes followed by 3x washes in NaCo. Samples were then dehydrated with increasing ethanol concentrations: (30% EtOH for 5 minuets, 2x; 50% EtOH for 5 minutes; 75% EtOH for 5 minutes; 100% EtOH for 5 minuetes, 2x followed by another 10 minute incubation). Samples were incubated in transition fluid (hexamethyldisilazane) 3x; (incubation times: 5 minutes, 10 minutes, 5 minutes) and were allowed to airdry and then placed in a desiccator until sputter coating. Samples were coated in a gold/palladium alloy and then imaged on a Zeiss Supra 25 Field Emission Scanning Electron Microscope.

Kinetics of single septin complex onto lipid-coated beads

Two PEG-passivated coverslips were sandwiched together using double-coated pressure sensitive adhesive tape (Nitto product:5015ELE) to make narrow (~20 μL flow chambers). A mixture of septins and lipid-coated beads of a given diameter were then flowed through the chamber and imaged using near-total internal reflection fluorescence microscopy. The number and duration of binding events were performed manually. Association-rate was quantified by calculating the number of binding events over the product of septin concentration, time, and binding area. To ensure the off rates were not dominated by bleaching, we generated bleach profiles (Supplemental fig.1). The amount of time it took to bleach single septin complexes is much higher than the observed dwell time (~ 1.5 seconds). Bleach steps were also used to calibrate intensity so that scored puncta were single septin complexes. As a control,

we measured the dwell time of single septin molecules that localized to areas of the coverslip that did not contain any beads and measured a dwell time of 0.062 seconds (data not shown), ensuring that our measured dwell times on beads reflect accurate association dynamics of single septin molecules on lipid-coated beads.

Generation of helical wheel diagrams

Helical wheels and the calculation of net charge and hydrophobic moment were generated using Heliquest (http://heliquest.ipmc.cnrs.fr).

Ashbya gossypii strain construction, culture and imaging

We generated an analogous *cdc12-6* allele (LEEVQAKVKKLEEQVRALQLRKH* → LEEVQAKVKN*) with GFP tag for integration at the endogenous locus by cloning a FragmentGENE (Genewiz) (637bp) harboring the mutation into AGB260 (*pCDC12*-GFP:*GEN*) (Meseroll, Occhipinti and Gladfelter, 2013b) via the restriction enzymes *BspEI* and *BsrGI* yielding AGB1209 (*pcdc12-6*-GFP:*GEN*). AGB1209 was linearized by digestion with *SphI* for targeted integration at the *CDC12* locus, and transformed into the wild-type *A. gossypii* strain (Altmann-Jöhl and Philippsen, 1996) to generate AG884 (*Agcdc12-6*-GFP:GEN *leu2*Δ *thr4*Δ). AG384 (*AgCDC11a*-GFP:*GEN leu2*Δ *thr4*Δ) is described in (Meseroll, Occhipinti and Gladfelter, 2013b). *A. gossypii* strains were grown from spores in full medium at either 24°C (*cdc12-6*) for 24 h or 30°C (wt) for 16 h before harvesting mycelial cells. Cells were mounted onto Low Fluorescence medium pads solidified with 2% agarose for imaging. Images were acquired using a spinning disc (Yokogawa) confocal microscope (Nikon Ti-82 stage) using a 100x Plan Apo 1.49 NA oil lens, and a Prime 95B CMOS (Photometrics).

2.3 Results and Discussion

2.3.1 Analysis of septin saturation binding to different curvatures

We first generated saturation binding isotherms from which affinity, maximal binding and cooperativity can be estimated for septins on different curvatures. We used a minimal reconstitution system consisting of recombinant yeast septin complexes (Cdc11-GFP, Cdc12, Cdc3, and Cdc10) and supported lipid bilayers (SLBs) formed on silica beads of different curvatures (Gopalakrishnan *et al.*, 2009; Bridges *et al.*, 2016). We measured septin binding onto SLB-coated beads at a range of concentrations with different bead sizes using quantitative microscopy. We found that septins have the strongest affinity for 1 μm beads (curvature, κ= 2 μm^{-1}, K_d 13.5 nM), followed by 3 μm beads (κ= 0.67 μm^{-1}, K_d 18.5 nM), and 0.5 μm beads (κ= 4 μm^{-1}, K_d 34.3 nM) (Fig.1, Table 1). Additionally, the difference in maximal binding capacity (B_{max}) is dramatically different for tested bead sizes, indicating that there are curvature-dependent differences in the number of effective binding sites for septins (Fig.1, Table 1). This is not due to differences in surface area on different bead sizes, as we normalized for surface area. At high septin concentrations, filaments formed in solution at curvature κ= 4 μm^{-1}, indicating excess complex is available for polymerization, suggesting the number of binding sites is limiting at this curvature (Fig.1). Hill coefficients of 2.6 (κ= 4 $\mu m^{-1}$and κ= 0.67 μm^{-1}) and 2.9 (κ= 2 μm^{-1}), indicated septin adsorption on all tested membrane curvatures is cooperative, consistent with the observation that some beads are fully bound by septins whereas others have none.

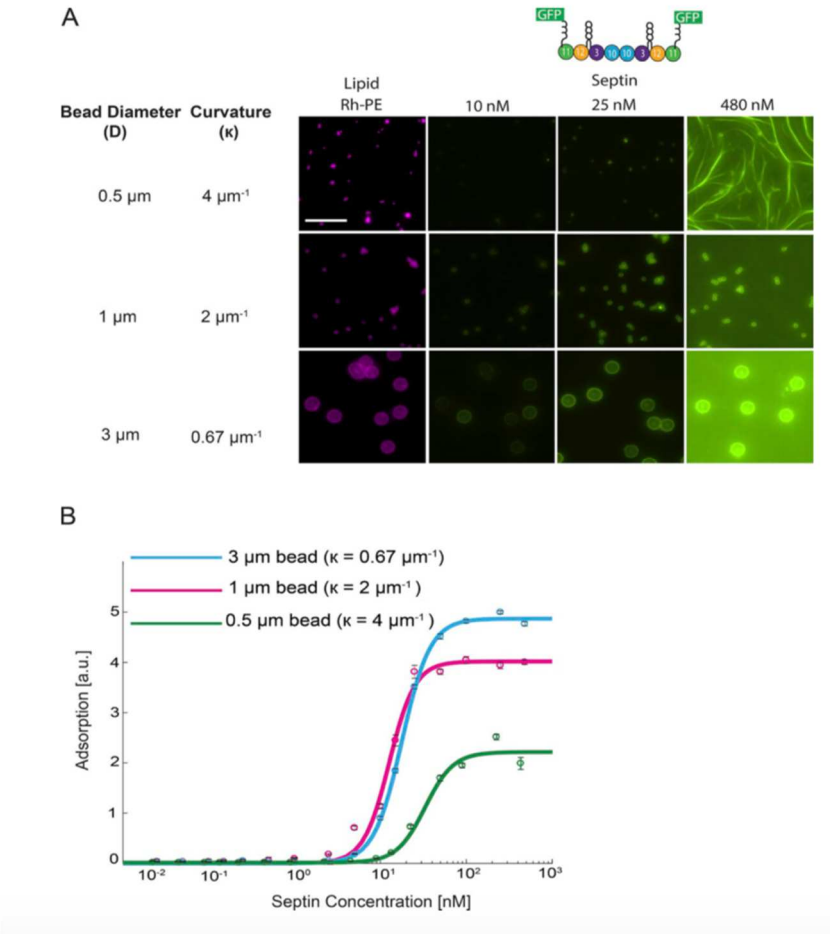

Figure 2.1 Septins bind cooperatively to curved membranes with differences in affinity and maximal binding
SLBs (75% DOPC, 25% (PI), and trace amounts of Rh-PE) were reconstituted on silica beads. Purified septins were added at several concentrations through saturation. (A) Representative images are maximum intensity projections. Scale bar 10 μm. (B) Quantification of septin adsorption at equilibrium onto SLBs of varying curvature. Each data point represents the mean intensity for 98-600 beads. Error bars are SEM, N=3.

We predict that affinity is a major driver of curvature sensing at low septin concentrations and at high concentrations how dense filaments can arrange on different curvatures becomes important. Collectively, these data suggest that differences in septin affinity and the number of available binding sites can drive preferential assembly of septins onto specific curvatures in a cooperative fashion. Cooperativity in assembly could arise at filament formation, lateral associations between filaments and/or other higher-order structures including layers of filaments.

2.3.2 Septin filament orientation is dependent on membrane curvature

To evaluate how cooperativity may arise at the level of polymerization, we asked how long a septin filament must be to align along optimum curvature. We adapted the SLB assay to rods of different diameters to visualize filaments using scanning electron microscopy (SEM). We scored the length and orientation of filaments on a range of rod diameters binned to three categories (100-400 nm, 401-600 nm, and 601-1000 nm). For all three categories, we found that single septin octamers (32 nm in length) sampled a variety of orientations as each image is a snapshot at the time of fixation (Fig.2E-G, orange boxes, Table 2). For rod diameters of 600-1000 nm, filaments 64 nm long tend to align along the axis of principal curvature (Fig.2G, green boxes). On rod diameters from 401-600 nm, septin filaments up to 128 nm long (four annealed octamers) had a wide distribution of orientations (Fig.2F). In contrast, for the smallest rods with diameters spanning 100-400 nm, 64 nm filaments begin to align along the long-axis (axis of zero curvature) of the rod to avoid the higher positive curvature (Fig.2E). For longer filaments, this alignment is even more evident (Fig.2E and G, pink and blue boxes). These data suggest even short septin filaments align along positive curvature.

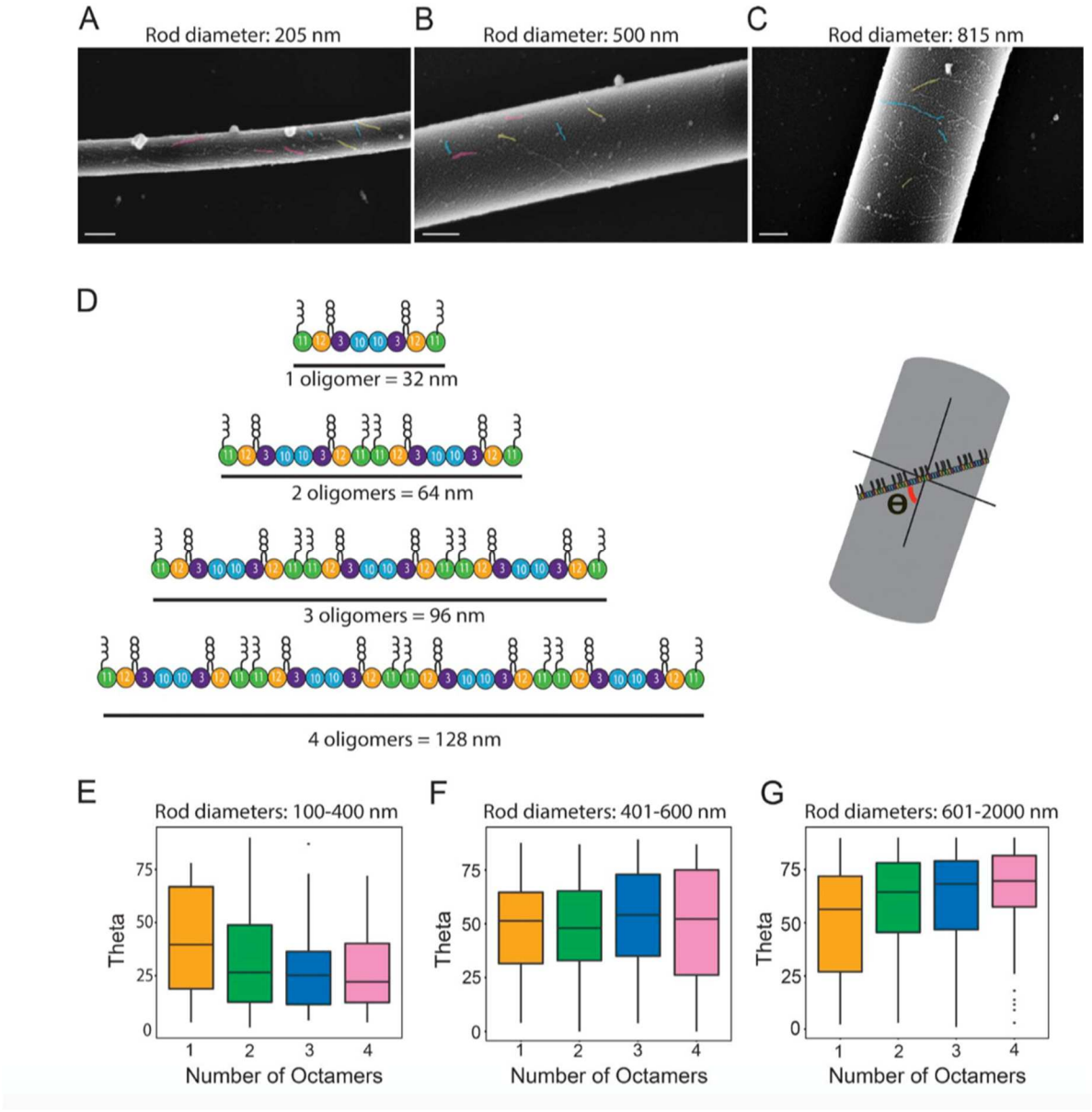

Figure 2.2 Septin filament alignment towards the axis of principal curvature is dependent on filament length

SLBs (75% DOPC, 25% PI, and trace amounts of Rh-PE) were reconstituted on borosilicate rods of different diameters ranging from approximately 100 nm to 2300 nm.(A-C) Representative images of septin filament alignment on rods from the three different categories. Scale bar 200 nm. A subset of filaments was false colored to depict alignments; pink are parallel to the long axis of curvature; yellow are oriented at ~ 45°; blue are aligned to the axis of principal curvature. (D) Schematic of septin filament length in terms of the number of octamers and a cartoon depicting how filament orientation relative rod was measured. (E-G) Box and whisker plot quantifying septin filament alignment on various rod diameters as a function of filament length binned to three diameter ranges. Black bars represent the median. Error bars are standard

deviation (E) 100-400 nm rods. N= 23 rods and 193 filaments (F) 401-600 nm rods. N= 15 rods and 189 filaments. (G) 601-2000 nm rods. N= 24 rods and 491 filaments.

We predicted that with longer septin filaments and/or lateral interactions that a tighter distribution of orientations would be seen. Indeed, on narrow and wide diameter rods (Fig.3E, pink and blue) with septins at high concentrations (50-500 nM) filaments are well aligned with one another and tightly packed. On rod diameters from ~400 nm through ~ 630 nm, septin filaments exhibit a wide range of orientations (Fig.3E, yellow). However, neighboring filaments have a tendency to align with one another. Septin filament orientation is very similar on other lipid compositions including DOPS, DOPE, PI $(4,5)P_2$, showing that septins can sense curved membranes on a variety of lipid compositions (Supplemental Fig.2). Thus, at high density, septin filaments more closely match the curvature of the rod than septin filaments at a low-density.

These data suggest that the ability of septins to perceive micron-scale curvature may be in part driven by septin filament density and filament length. Both length and packing may contribute to the cooperativity detected in the saturation binding curves (Fig.1B). Aligned septin filaments in close proximity to each other might be stabilized by lateral interactions with one another as has been noted previously (Frazier *et al.*, 1998; A. Bertin *et al.*, 2008; Sadian *et al.*, 2013) (Fig.3D). We also imagine that tightly packed septins might sterically hinder one another, thus "enforcing" alignment along the optimal curvature through transient interactions while diffusing on the membrane. At higher septin concentrations, filaments are also longer on rods than at low concentrations so it is possible that filament length is also a driving factor in this assay.

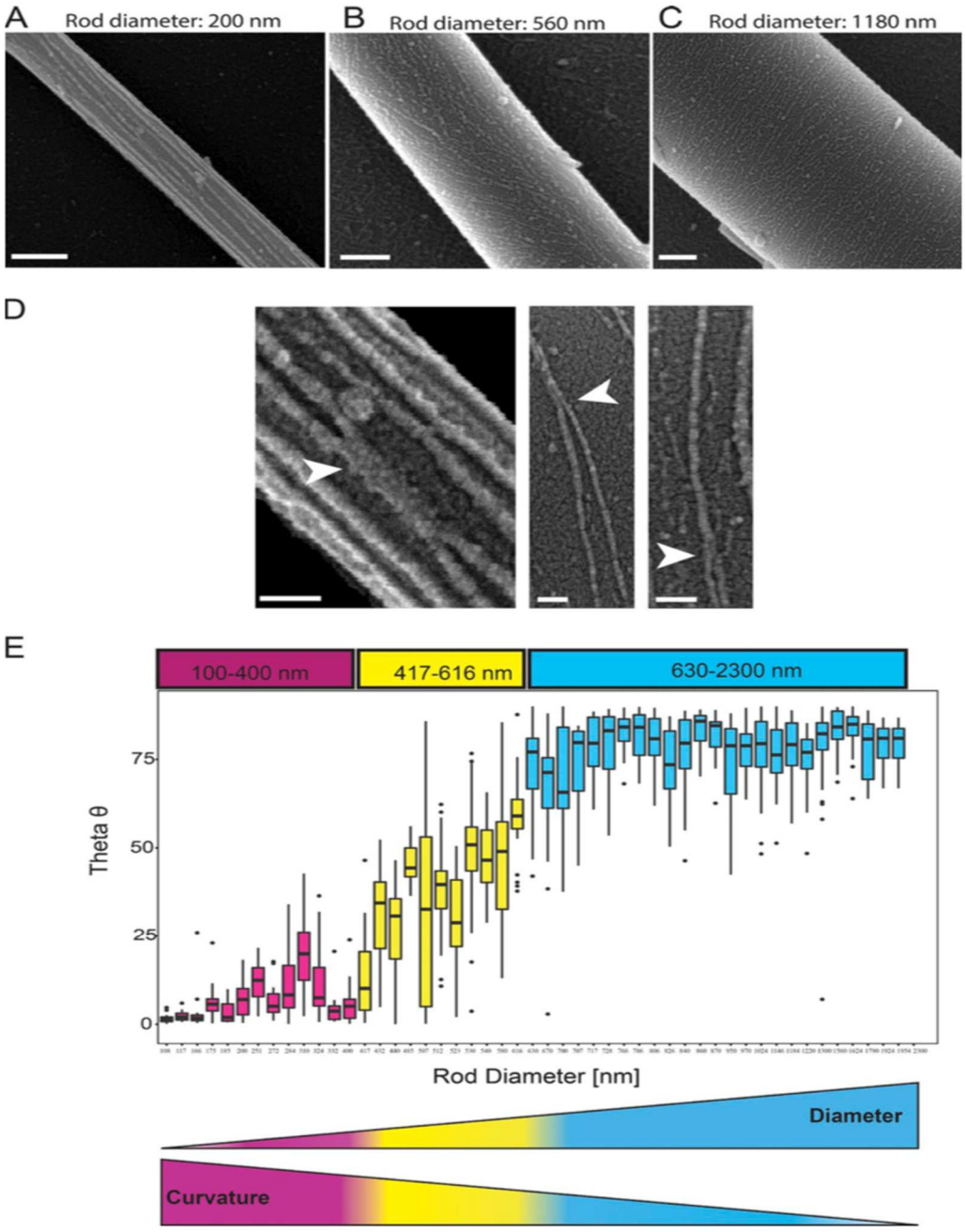

Figure 2.3 Septin filament orientation is dependent on membrane curvature
SLBs (75% DOPC, 25% PI, and trace Rh-PE) were generated on borosilicate rods of different diameters (100- 2300 nm). Purified septins were added to SLBs at saturating concentrations (from 50 nM to 500 nM) and imaged using SEM. (A-C) Representative images of septin filament alignment on rods from the three different categories at 50 nM septin concentration. (D) Example septin bundling (white arrows). Scale bar 50 nm. (E) Box and whisker plots of septin filament orientation on measured rod diameters at several septin concentrations (50 nM, 100 nM, 250 nM, and 500 nM). The number of filament orientations measured per rod ranged > 10 filaments. Quantification is from 49 rods. Measured filaments were greater than 100 nm (~3 octamers) in length. Black bars represent the median. Error bars are standard deviations.

2.3.3 Association rates of single septin complex are curvature sensitive

We next examined curvature-dependent septin affinity differences. We measured the number and duration of binding events to calculate association and off rates for single septin complexes on curvatures of 2 μm^{-1} and 0.67 μm^{-1} (Fig.4, Supplemental Fig.1). Histograms of dwell times for single septin-complex binding events were fit to a single exponential decay function. The measured dwell times for these curvatures were 0.21s ± 0.019 and 0.21 ± 0.023, for $\kappa = 2\ \mu m^{-1}$ and $\kappa = 0.67\ \mu m^{-1}$, respectively ($N_{particles\ per\ curvature} > 150$). Dwell times correspond to a high off-rate, supporting previous observations that a single septin octamer does not stably associate with membranes (Bridges *et al.*, 2016). Notably, the measured dwell times were the same on both curvatures tested, suggesting that curvature does not influence the off rate. Next, association rates were quantified by calculating the number of binding events over the product of septin concentration, time, and binding area. We found that single septin octamers show differences in the association rate as a function of membrane curvature (Fig.4, $\kappa = 2\ \mu m^{-1}$ was 0.061 $\mu m^{-2}s^{-1}nM^{-1}$and $\kappa = 0.67\ \mu m^{-1}$was 0.025 $um^{-2}s^{-1}nM^{-1}$).

The ~2.5-fold difference in association rate between these two curvatures was striking, given that our saturation binding isotherms show K_d values so close to one another (13.5 and 18.5 nM, respectively). This could be explained by the fact that our binding curve data is a summation of several reactions: initial binding, septin annealing and fragmentation events, and lateral interactions, all of which may be influenced by curvature and contribute to the K_d values. These results suggest that even a single septin octamer can detect curvature differences through the initial association with the curved membrane and curvature-dependent bilayer defects are perceptible on micron-scale curvature.

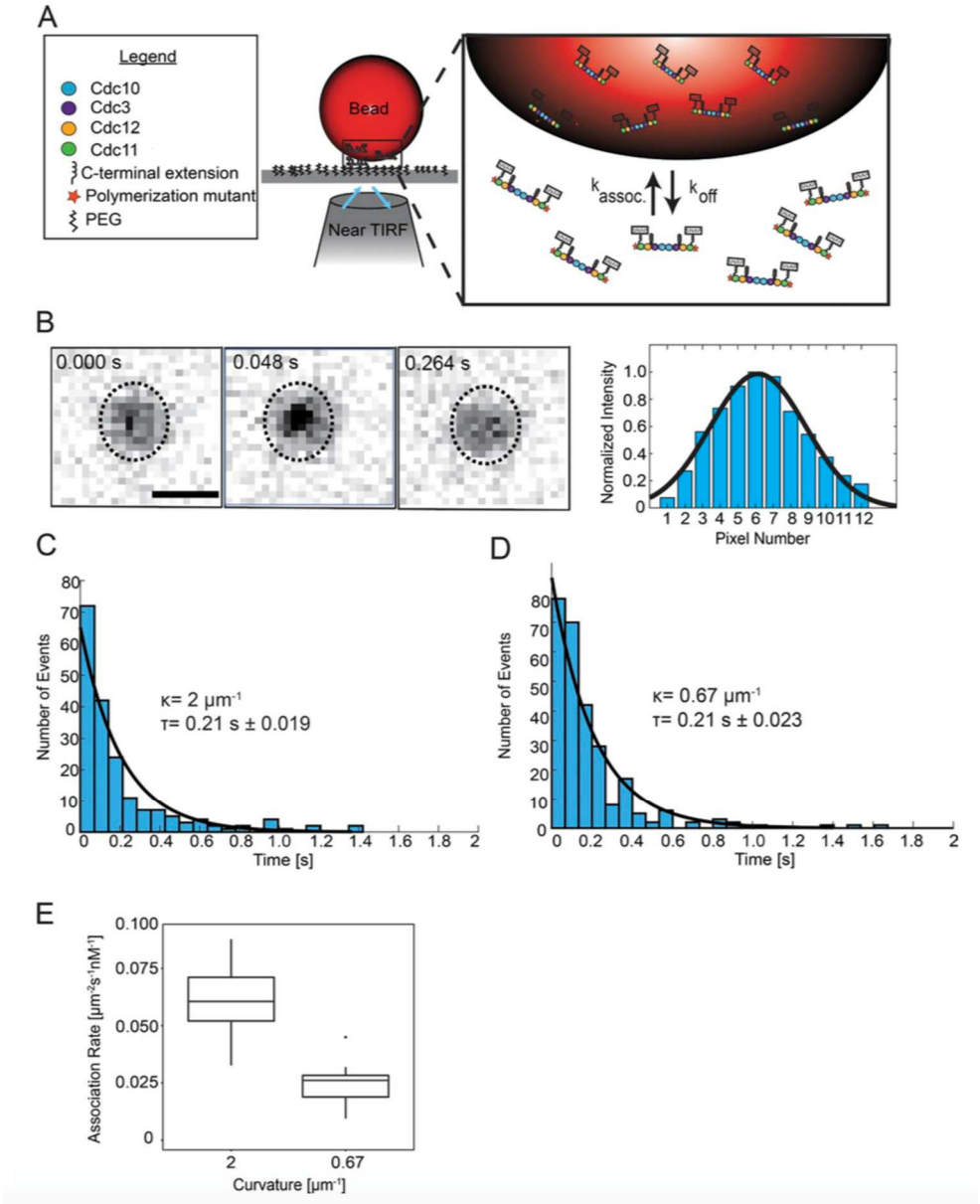

Figure 2.4 Single septin complexes have a higher association rate for optimal membrane curvatures

(A) SLBs (75% DOPC and 25% PI) were reconstituted on curvatures of 2 μm^{-1} or 0.67 μm^{-1} and flowed between two polyethylene-glycol (PEG, black) coated coverslips (top coverslip not shown). Non-polymerizable septin complexes were then flowed into the chamber and septin binding and unbinding events were observed using near-TIRF microscopy. (B) Representative images of a binding event on κ= 2 μm^{-1} (1 μm bead). Line scan through the particle shows signal intensity fit to a Gaussian function. (C-D) Dwell time histograms for membrane curvature of 2 μm^{-1} and 0.67μm^{-1}, respectively. (E) Box and whisker plot quantifying association rate of non-polymerizable septin complexes onto both curvatures (κ =2μm^{-1} and 0.67μm^{-1}). Black bars

represent the median. Error bars are standard deviations. N_{beads} = 10 (for κ =2μm^{-1} and 0.67μm^{-1}) $N_{binding\ events}$ = 844 and 315 for for κ =2μm^{-1} and 0.67μm^{-1}, respectively.

2.3.4 An amphipathic helix domain in septins is necessary and sufficient for curvature sensing

How can the association rate of a single septin octamer be sensitive to curvature on the micron scale? Many proteins that sense nanometer scale curvatures contain membrane-binding amphipathic helices (Drin *et al.*, 2007; Drin and Antonny, 2010). Interestingly, another micron scale curvature sensor, SpoVM, a 26-amino acid polypeptide, utilizes an 11-residue amphipathic helix to sense curvature (Gill, J.-P. Castaing, *et al.*, 2015) and also shows curvature-dependent association rates (E. Y. Kim *et al.*, 2017). We manually searched for AH motifs in septin sequences using Heliquest (Gautier *et al.*, 2008) to screen primary sequences for α-helical properties and found conserved, predicted amphipathic helices at the C-termini of a subset of septins (Fig.5). Despite differences in amino acid composition, septin AH motifs are similarly situated within the primary sequence and have similar lengths, net charges, and hydrophobic moments, suggesting that the physicochemical properties of the AH domains are highly conserved across multiple species (Supplemental Fig.3).

We asked if the septin AH domain confers specificity for curved membranes. Interestingly, the AH domain of Cdc12 is truncated in a well characterized temperature sensitive septin mutant, *cdc12-6* (Adams and Pringle, 1984; Johnson *et al.*, 2015) (Fig.5). In these mutants, septins localize normally to the bud-neck at permissive temperature, but rapidly disassemble at restrictive temperature (Amy S Gladfelter *et al.*, 2005). First, we evaluated whether the AH was necessary for curvature sensing using recombinant septin complex with the cdc12-6 protein. Interestingly, we found that cdc12-6 mutant complexes bound all tested membrane curvatures indiscriminately in contrast to wild-type septins (Fig.5C and D). This

suggests that AH of Cdc12 is not required for septin membrane association, but rather it specifies septin preference for membrane-curvature.

Next, we asked if the AH of Cdc12 was sufficient to distinguish membrane curvature. We purified a polypeptide with two copies of the AH to mimic the stoichiometry of the intact septin complex which has two copies of Cdc12. This tandem AH polypeptide adsorbed onto membrane curvatures of 2 μm^{-1} (albeit significantly less than septin complexes), while showing reduced binding to other tested membrane curvatures of 6.67 μm^{-1} ,4 μm^{-1}, 0.67 μm^{-1} and 0.4 μm^{-1} (Fig.5E). The reduced binding onto beads of κ= 0.67 μm^{-1} was surprising, given the robust binding of septin complexes to this curvature (Fig. 1). We suspect that the spacing between tandem AH domains is an important factor in tuning the curvature preference as the spacing between AH domains in this construct is only 9 amino acids, whereas the spacing within a septin complex is approximately 24 nm (A. Bertin *et al.*, 2008). Interestingly, a single AH-GFP adsorbed onto a range of more highly curved surfaces (κ=6.67, 4, and 2 μm^{-1}) but less so on shallower curvatures (κ = 0.67 and 0.4 μm^{-1}) (Supplemental Fig.2). However, we observed filament-like structures forming within both 2x AH-GFP and 1x AH-GFP constructs (Fig.5E and Supplemental Fig.2K, white arrows), suggesting that AH domains are capable of oligomerizing at the membrane, which might be expected given the small size of the domains (Huang and Ramamurthi, 2010). We see identical behavior with a tandem construct lacking a GFP tag and visualized by dye labeling showing that the preference and any oligomerization is not an artifact of the tag (unpublished result). Collectively, this data suggests that the spatial arrangement of AH domains and the capacity to self-assemble likely tune curvature sensitivity.

There is strong evidence that AH domains demonstrate lipid-specific binding (Vanni *et al.*, 2014; Hofbauer *et al.*, 2018) . Similarly, septins preferentially bind membranes containing

phosphatidylinositol (4,5) bis-phosphate ($PI_{4,5}P_2$), which may be dependent on the presence of polybasic regions within individual septin polypeptides (Casamayor and Snyder, 2003; Akil *et al.*, 2016). However, the polybasic motifs are potentially buried within a septin oligomer (Sirajuddin *et al.*, 2007; Aurélie Bertin *et al.*, 2010) and mutations within these regions could affect the assembly of septins into octamers and/or filaments and have downstream consequences that potentially impact septin-membrane interactionsWe probed the AH domain lipid-specificity by measuring adsorption onto both optimum ($\kappa = 2\ \mu m^{-1}$) and non-optimum ($\kappa = 0.4\ \mu m^{-1}$) membrane curvatures with varying lipid compositions while keeping the global charge across the membrane equivalent. There are, local differences in charge of the lipids used with $PI_{4,5}P_2$ (-3 at pH 7.4) greater than PI or PS (both -1 at pH 7.4) (Tsui, Ojcius and Hubbell, 1986; Beber *et al.*, 2018). We found that curvature sensitivity remained intact on the different lipids, however, we observed increased binding of the 2x-AH domain, the single AH-GFP and the full septin complex to $PI_{4,5}P_2$containing membranes over membranes containing either phosphatidylinositol (PI) or phosphotidylserine (PS) (Fig. 5F, Supplemental Fig.2K,L,M and N). Interestingly, we observed stronger binding of the 2x-AH to PI over PS, despite their equal charge, suggesting that either the molecular shape of the lipid or the different fatty acyl chain environment influences AH adsorption.

Finally, we assessed the functionality of the Cdc12 AH in live cells using *Ashbya gossypii*, a filamentous fungus which displays prominent septin assemblies at sites of micron-scale curvature (DeMay *et al.*, 2009; Bridges *et al.*, 2016). We generated a *cdc12-6* mutant allele in *Ashbya*, similar to the *S. cerevisiae* allele. In *cdc12-6* mutants, septins rarely assemble at branches (17%; n=104 branches;12 cells), but still assembled into tightly-bundled filaments, septation site rings and thin filaments at hyphal tips (Fig. 5G). The few branch assemblies

detected were aberrant, with low signal intensity and only at the base of newly formed branches. This shows that the amphipathic helix in Cdc12 is required for septin localization at curved membranes in cells.

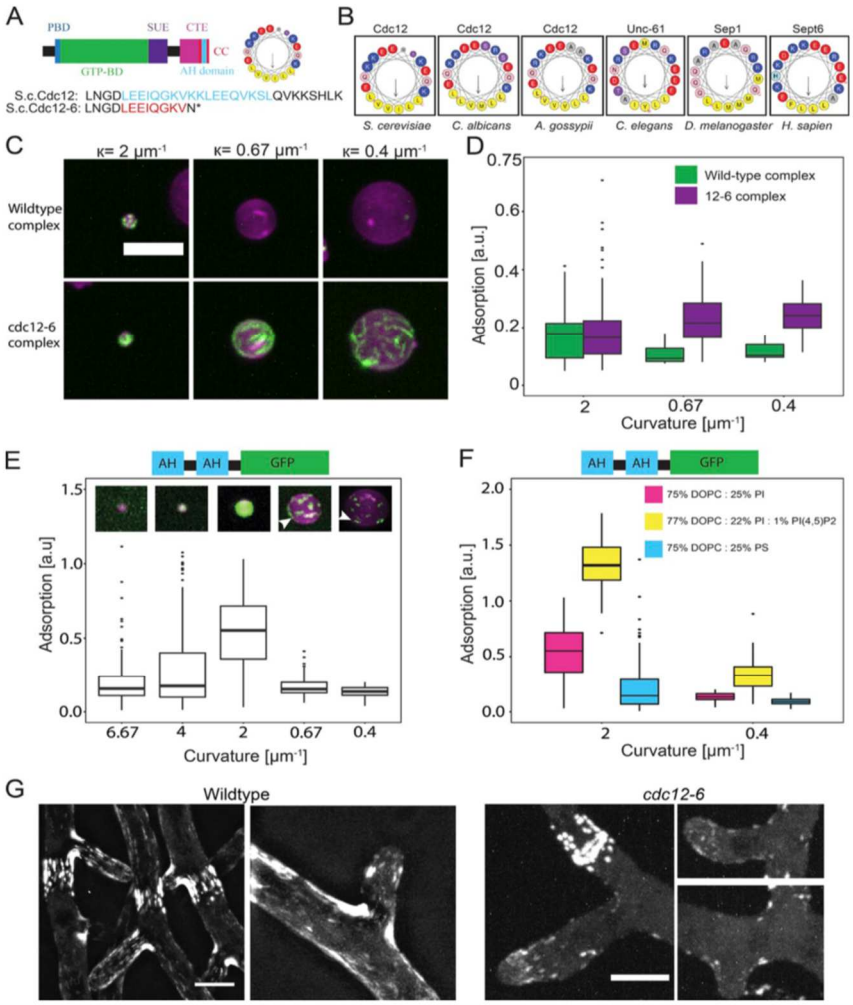

Figure 2.5 Septins have conserved amphipathic helices at their C-termini
(A) Domains within the yeast septin, Cdc12. PBD (blue): polybasic domain; GTP-BD (green): GTP-binding domain; SUE (purple): Septin unique element; CTE(pink): C-terminal extension; CTE(magenta): coiled-coil domain (red); AH domain (cyan). The AH domain is shown as a helical wheel corresponding primary sequences for wild-type Cdc12 and Cdc12-6 (below). (B) Amphipathic helices found in the C-terminal extensions of septins in multiple species represented through helical wheel diagrams. (C) 1 nM of purified wild-type septin complexes (panel 1) and *cdc12-6* septin complexes (panel 2) adsorption (green) onto SLBs (magenta) with different curvatures. (D) Box and whisker plot quantifying adsorption of wild-type or cdc12-6 septin complexes onto SLBs of various curvature. Black bars represent the median. Error bars represent the standard deviation. n > 50 beads for each curvature. (E) Representative images of 1 μM of 2x-Cdc12 AH-GFP binding onto SLBs on beads with curvatures. Arrows highlight

filament-like structures. (F) Box and whisker plot of 2x-Cdc12 AH-GFP adsorption onto different membrane compositions and curvatures. Black bars represent the median. Error bars at each curvature are standard deviations for n> 100 beads. (G) Septins assemble at the base hyphal branches in wild-type cells (wildtype; Cdc11a-GFP), but rarely assemble in *cdc12-6* mutants (cdc12-6-GFP) at permissive temperature

Conclusion 2.4

We identify a mechanism that uses both affinity and the number of available binding sites to drive cooperative, curvature-specific accumulation of septins. Even a single septin octamer is capable of detecting changes micrometer scale curvatures, manifested as differences in association rate. An amphipathic helix located at the very C-terminus of Cdc12 is necessary and sufficient for septins to distinguish different lipid compositions and curvatures. It is now clear that AH domains are not just useful for sensing nanometer-scale curvature but also to detect micrometer-scale curvature. The ability of septins to bind membranes in the absence of the AH domain suggests that there are additional curvature-independent septin-membrane interaction motifs. What septin amphipathic helices sense in the local lipid environment will be an exciting area of future investigation

Supplementary Material 2.6

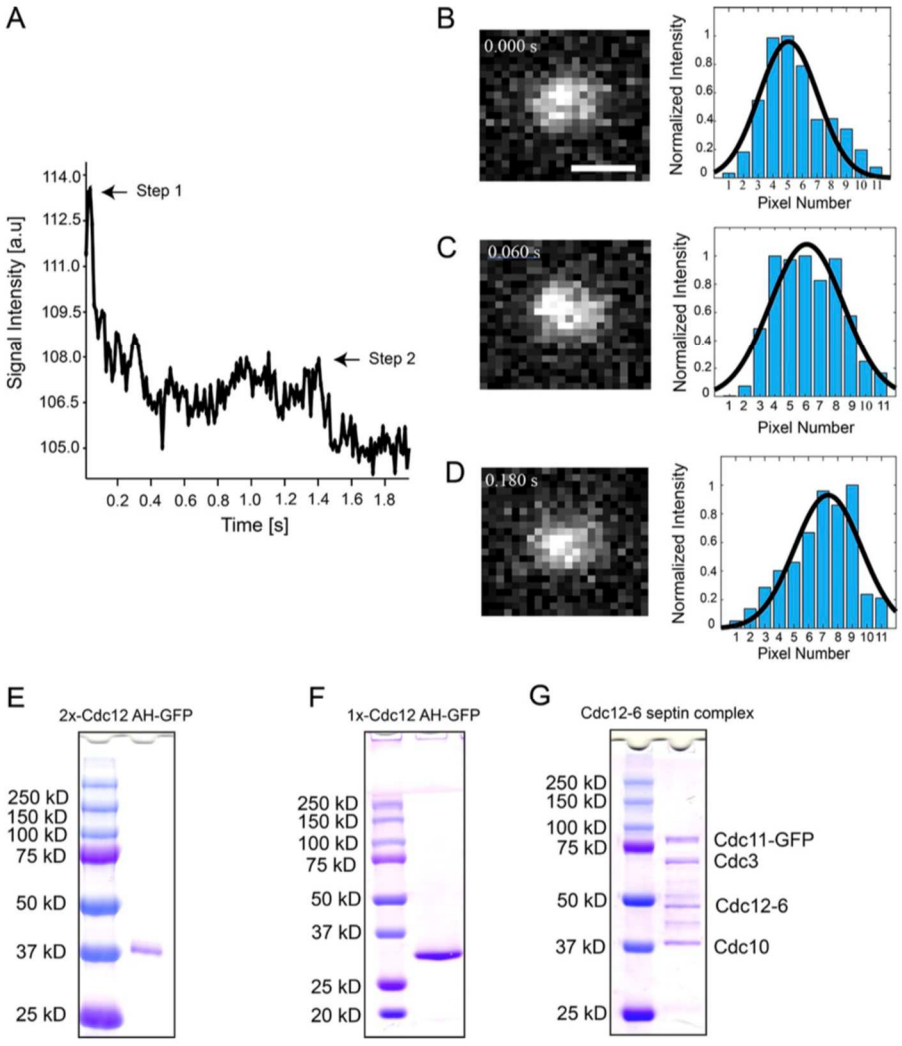

Figure 2 S1. Single-molecule photobleaching profiles and protein purification. (A) Two-step photobleaching profile for a single septin complex. (B–D) Time lapse imaging of single septin molecules binding to a 1-μm bead (B). A single-septin complex is bound to the bead. Bar, 1 μm. (C) A second septin com- plex binds to the bead, adjacent to the initially bound septin particle. (D) A single-septin particle disassociates from the bead. Signal intensity profiles for B–D were all fit to Gaussian distributions. (E–G) Coomassie staining of recombinantly expressed 2× Cdc12-AH-GFP, 1× Cdc12 AH-GFP, and yeast septins Cdc11- GFP, Cdc3, Cdc12-6, and Cdc10, after cleavage of 6×-histidine tag via Tobacco etch virus protease, respectively

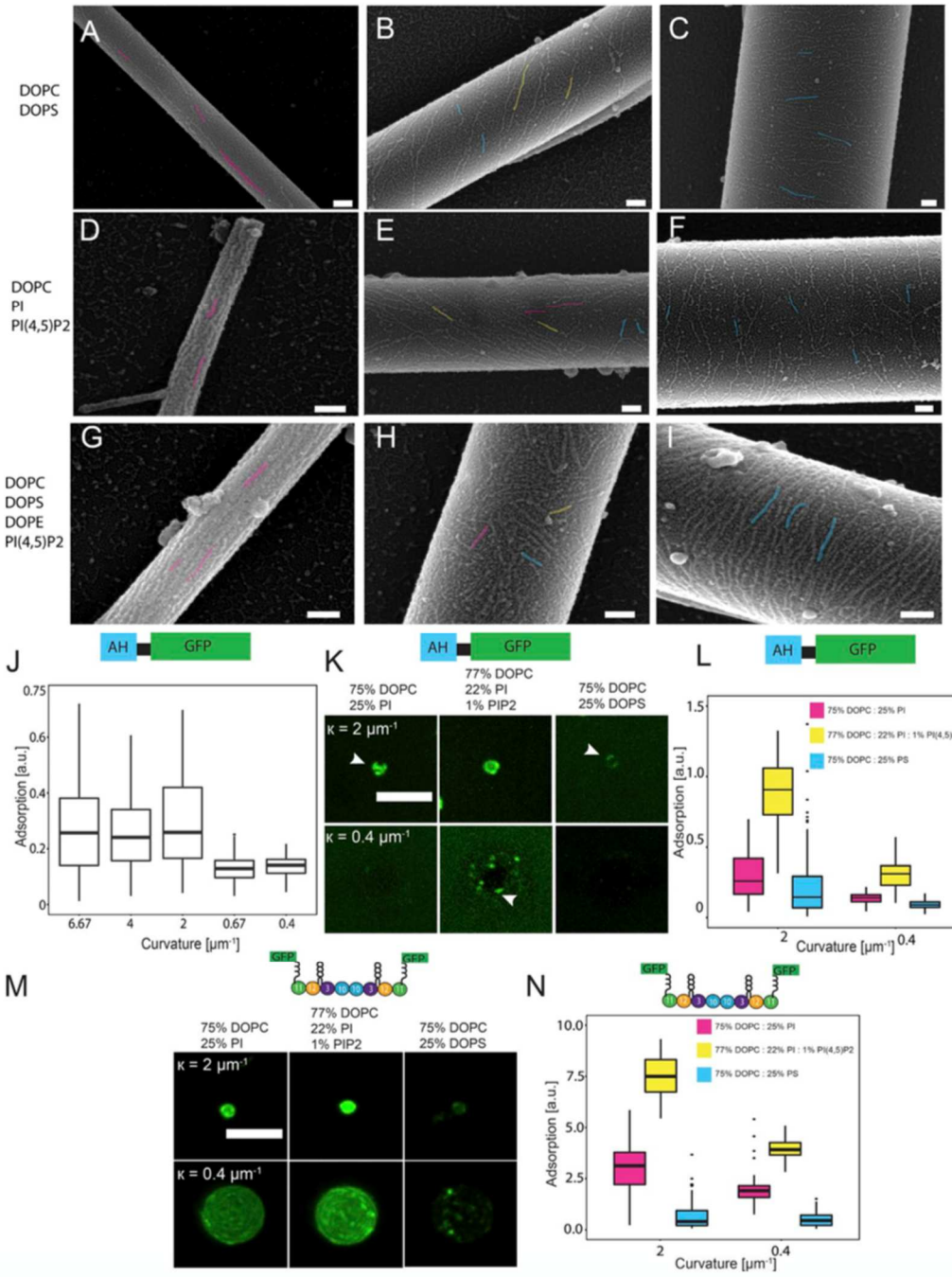

Figure 2 S2. The effects of lipid composition on septin filament orientation and binding of 1× AH domain and septin complexes onto curved membranes. SLBs of various lipid compositions were generated onto borosilicate rods. 50 nM purified septins were added to SLBs, and images were acquired using a scanning electron microscope. Representative images were selected from three different categories (100–400 nm, 401–600 nm, and 601–2,300 nm. A subset of filaments were false colored; pink filaments are more parallel to the long axis of curvature; yellow filaments are oriented at ~45°; blue filaments are aligned to the axis of principal curvature. (A–C) Representative images of septin filament alignment on DOPC (75%)- and DOPS (25%)-coated rods. Rod diameters are 195 nm, 470 nm, and 1,096 nm (left to right). (D–

F) Representative images of septin filament alignment on DOPC (75%)-, PI (20%)-, and PI(4,5)P_2 (5%)-coated rods. Rod diameters are 95 nm, 494 nm, and 1,006 nm (left to right). (G–I) Representative images of septin filament alignment on DOPC (70%)-, DOPS (10%)-, DOPE (10%)-, and PI(4,5)P_2 (10%)-coated rods. Rod diameters are 189 nm, 519 nm, and 1803 nm, respectively. Bars, 100 nm. (J) Box and whisker plot quantifying adsorption of 1 μM 1× AH-GFP onto various membrane curvatures with a lipid composition of 75% DOPC, 25% PI, and trace Rh-PE. n > 74 beads per curvature. Black bars represent the median, and error bars represent the standard deviation. (K) Binding of 1 μM 1× AH-GFP (green) to either $\kappa = 2\ \mu m^{-1}$ or $0.4\ \mu m^{-1}$ membrane curvatures with various lipid compositions. All images are contrasted identically. White arrowheads highlight filament-like structures. Bar, 5 μm. (L) Box and whisker plot quantifying adsorption of 1× AH-GFP onto membrane curvatures with various lipid compositions from K. n > 74 beads per condition. Black bars represent the median, and error bars represent the standard deviation. (M) Adsorption of 15 nM septin complex (green) to either $\kappa = 2\ \mu m^{-1}$ or $0.4\ \mu m^{-1}$ membrane curvatures with various lipid compositions. All images are contrasted identically. Bar, 5 μm. (N) Box and whisker plot quantifying adsorption of septin complexes onto membrane curvatures with various lipid compositions from M. n > 36 beads per condition. Black bars represent the median and error bars represent the standard deviation.

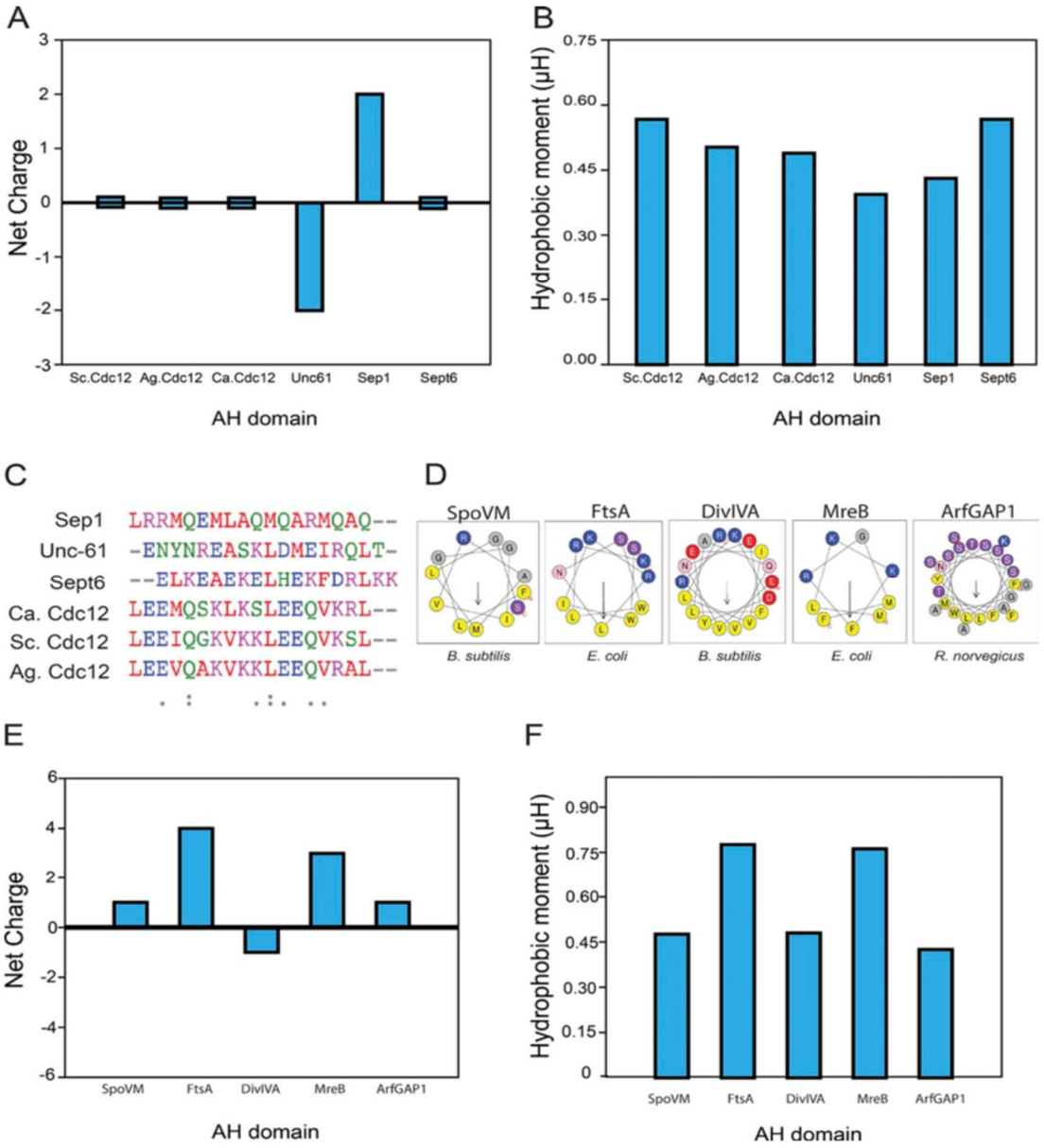

Figure 2 S3. **Septin AHs net charge and hydrophobicity.** (A and B) Net charge and hydrophobic moment of selected septin AHs, respectively. (C) Primary sequence alignment of septin AHs. (D) Helical wheel diagrams for selected membrane binding and/or curvature-sensing AHs. (E and F) Net charge and hy- drophobic moment of selected AHs. Interestingly, AH domains with a net charge of zero (S. cerevisiae, Candida albicans, A. gossypii, and Homo sapiens) have higher hydrophobic moments than AH domains that are charged (C. elegans and Drosophila melanogaster). The properties of the AH domain might be tuned to reflect differences in lipid compositions across species, yet still localize to similar membrane geometries. The septin AH hydrophobic moments closely match SpoVM and DivIVA, other micrometer-scale sensors from bacteria.

CHAPTER 3

INTERPLAY OF SEPTIN AMPHIPATHIC HELICES IN SENSING MEMBRANE CURVATURE AND REGULATING FILAMENT BUNDLING

AUTHORS:, Benjamin L. Woods*, Kevin S. Cannon*, Ellysa Vogt, and Amy S. Gladfelter

- Denotes co-authorship

Currently under revision at *Molecular Biology of the Cell,* 2020

3.1 Introduction

Cell shape is critical for function and can be thought of in terms of membrane curvature. Cell membranes range in curvatures from nanometer to micron scales. How cells use nanometer sized proteins to sense micron-scale membrane curvature is not well understood. One way cells solve this problem is through a class of cytoskeletal proteins called septins, which are conserved from yeast to humans (Field *et al.*, 1996a; Pan, Malmberg and Momany, 2007) . Septins are GTP-binding proteins that form heteromeric complexes(Versele and Thorner, 2004; Low and Macara, 2006; Sirajuddin *et al.*, 2007; A. Bertin *et al.*, 2008). These complexes associate with the plasma membrane, where they can polymerize into filaments and higher order assemblies such as bundles and rings (Rodal *et al.*, 2005; John *et al.*, 2007; Sirajuddin *et al.*, 2007; A. Bertin *et al.*, 2008; DeMay *et al.*, 2009; DeMay, Bai, *et al.*, 2011). Higher order septin assemblies can act as scaffolds for signaling proteins, organize membrane properties and influence the organization of other cytoskeletal elements (Lew and Reed, 1995; M. S. Longtine *et al.*, 2000; Gladfelter, Pringle and Lew, 2001; Hu *et al.*, 2010; Gilden *et al.*, 2012; Clay *et al.*, 2014b;

Bridges *et al.*, 2016). . In many of these functions, higher order septin assemblies are built in the context of micron-scale curvature.

Septins can distinguish positive membrane curvatures at the micron-scale without any other cellular factors (Bridges *et al.*, 2016). When purified septins are mixed with membranes at a range of different curvatures, septins polymerize into aligned filaments wrapped at an optimal curvature (Tanaka-Takiguchi, Kinoshita and Takiguchi, 2009; Beber *et al.*, 2019; Cannon *et al.*, 2019). However, individual septin complexes can distinguish membranes with micron-scale curvature which manifests through septin-membrane binding kinetics (Cannon *et al.*, 2019). Septins, like other curvature sensitive proteins, possess an amphipathic helix (AH) domain (Drin *et al.*, 2007; E. Y. Kim *et al.*, 2017; Cannon *et al.*, 2019). AH domains function by binding to lipid packing defects within curved membranes. In the budding yeast *Saccharomyces cerevisiae*, the amphipathic helix at the C-terminus of Cdc12 is necessary and sufficient for septins to distinguish between different curvatures of the plasma membrane. Thus, the ability of septins to sense membrane curvature occurs at multiple scales.

Here we report that Shs1, a non-essential mitotic septin, also has an AH domain within its C-terminal extension (CTE). Shs1 occupies the terminal position at either end of a subset of heteromers, adjacent to Cdc12, the only essential septin subunit to possess an AH domain in yeast (Garcia *et al.*, 2011b; Finnigan, Booth, *et al.*, 2015; Cannon *et al.*, 2019). Like the Cdc12 AH domain, the Shs1 AH domain recognizes membrane curvature. In the absence of the Cdc12 AH domain, the Shs1 AH domain restores the ability of septins to distinguish between different curvatures. Moreover, Shs1 and its CTE are indispensable in mutants harboring an incomplete Cdc12 AH domain in cells. This suggests septin complexes can contain different numbers of curvature sensitive AH domains, which may allow for another layer of control of higher order septin assemblies.

3.2 Materials and Methods

Yeast strain construction and culturing

Standard molecular genetic techniques were used to generate and culture yeast strains in this study. All yeast strains used in this study are listed in Supplemental table 3S1. The temperature sensitive *cdc12-6* mutant was used assess the function of Shs1 truncations. We received a *bar1Δ* strain and a diploid strain heterozygous for *shs1Δ* and *cdc12-6* as gifts (D. Lew, Duke University). We generated the untagged Shs1 truncations (Shs1$^{\Delta 341\text{-}551}$, Shs1$^{\Delta 488\text{-}551}$, Shs1$^{\Delta 488\text{-}507}$, Shs1$^{\Delta 506\text{-}551}$, Shs1$^{\Delta 508\text{-}551}$, and Shs1$^{\Delta 523\text{-}551}$) and GFP-tagged Shs1 constructs (Shs1-GFP, Shs1$^{\Delta 341\text{-}551}$-GFP, Shs1$^{\Delta 488\text{-}551}$-GFP, Shs1$^{\Delta 506\text{-}551}$-GFP) using the PCR-based C-terminal modification method (Longtine et al., 1998). We generated Cdc12-6, Cdc12$^{\Delta AH}$ AH-chimeric (SpoVM^{AH}, Shs1$^{488\text{-}505}$, Shs1$^{488\text{-}507}$, Rvs161^{AH}, Rvs167^{AH}, *S. pombe* Rit1^{AH}) and Cdc12$^{\Delta 400\text{-}407}$ constructs with an HA-tag using the PCR-based C-terminal modification method mentioned above. PCR vectors were integrated at their endogenous loci (*SHS1* or *CDC12,* respectively) to generate heterozygous diploids. All transformants were verified for targeted integration by PCR amplification of genomic DNA.

Cells were grown to mid-log phase at 24°C in Complete Synthetic Medium (CSM, Sunrise Science Products) supplemented with 0.67% yeast nitrogen base, 2% dextrose, and 0.01% adenine, then harvested. Cells were mounted onto CSM + 2% dextrose agarose (2%) pads prior to imaging. For experiments using yeast pheromone, mid-log phase cultures of *bar1Δ* cells were treated with 50 nM α-factor (GenWay Biotech) for two hours at 24°C before fixation with 3.7% formaldehyde for 10 minutes at room temperature before imaging.

Ashbya gossypii culturing

The *A. gossypii* strain harboring the *cdc12-6*-GFP allele at the endogenous *CDC12* locus (AG884; *AgCDC12:cdc12-6*-GFP:*GEN leu2Δ thr4Δ*) was described before. *A gossypii* was grown

from spores in full medium for 16 hours at 24°C before harvesting mycelial cells unless otherwise indicated. Cells were mounted on Low Fluorescence medium agarose (2%) pads for imaging.

Cell microscopy

Confocal images were acquired using a spinning disc (Yokogawa W1) confocal microscope (Nikon Ti-82 stage) using a 100x Plan Apo 1.49 NA oil lens and a Prime 95B CMOS camera (Photometrics). Differential interference contrast (DIC) images were acquired on a custom-built microscope with an inverted Olympus IX-83 body equipped with an Olympus 60x 1.3 NA lens and an EMCCD camera (Andor iXon-888). Live cell microscopy images were prepared using ImageJ (FIJI).

Immunoblotting

For Western blot analysis, ~$2x10^7$ cells were harvested from mid-log phase cultures grown at 24°C and total protein was extracted by TCA precipitation as previously published. Electrophoresis and Western blotting were performed as previously described. A polyclonal rabbit α-HA epitope antibody preparation was used at 1:2000 dilution (Rockland Immunochemicals). A monoclonal mouse α-Cdc42 antibody preparation (gift from P. Brennwald, UNC) was used at 1:500 dilution. Polyclonal goat antibodies against rabbit (Goat anti-Rabbit IgG DyLight 680 conjugated, Rockland Immunochemicals) and mouse (Goat anti-Mouse IgG DyLight 800 conjugated, Rockland Immunochemicals) were used at 1:10,000 dilution as secondary antibodies. Blots were imaged with an ODYSSEY infrared laser scanner (LI-COR Biosciences).

Protein purification

Recombinant *S. cerevisiae* septin protein complexes were expressed from a duet expression system in BL21 (DE3) *E. coli* cells and purified as previously described (Supplemental table 3S2). The Shs1 amphipathic helix conjugated to GFP was purified with a

similar protocol as septins, however induced cultures were grown for four hours at 37°C instead of 24 hours at 22°C.

Amphipathic helix constructs

The 2x AH(Shs1)-GFP construct has the primary sequence: KELQKRIQELERKAHELK-GSGSRSGSGS KELQKRIQELERKAHELK-GSGSSR-GFP tag. The underline sequence represents the AH domain from Shs1. The glycine-serine repeats represent linker sequences between the AH domains and the GFP tag.

Lipid mix preparation

Lipids (from Avanti Polar Lipids) were mixed in chloroform solvent at a ratio of 75 mole percent dioleoylphosphatidylcholine (DOPC) and 25 mole percent PI (liver, bovine) sodium salt in a glass cuvette. For lipid mix preparations to incubated on silica microspheres, trace amounts (>0.1%) of phosphatidylethanolamine-N-(lissamine rhodamine B sulfonyl) (RH-PE) were added. Lipid mixtures were then dried with argon gas to create a lipid film and stored under negative vacuum pressure overnight to evaporate trace chloroform. Lipids were rehydrated in Supported Lipid Bilayer buffer (300 mM KCl, 20 mM Hepes pH 7.4, 1 mM $MgCl_2$) at 37°C to a final lipid concentration of 5 mM. Lipids were then resuspended over the course of 30 minutes at 37°C, with vortexing for 10 seconds every five minutes. Fully resuspended lipids were then bath sonicated at 2-minute intervals until solution clarified to yield small unilamellar vesicles (SUVs).

Preparation of supported lipid bilayers

Lipid bilayers supported on silica microspheres were prepared as previously described. SUVs were adsorbed onto silica microspheres (Bangs Laboratories) by incubating 50 nM of lipid with different bead sizes (with a summed surface area of 440 mM^2) for hour at room temperature with gentle rotation. Microspheres were pelleted, then resuspended in in Pre-Reaction buffer (33

mM KCl, 50 mM HEPES pH 7.4) to wash away excess SUVs. This wash step was repeated four additional times.

Planar supported lipid bilayers were prepared in a similar process as reported previously. No. 1.5 coverslips were first cleaned with oxygen plasma (PE25-JW, Plasma Etch). Chambers for lipid bilayers cut from PCR tubes were glued (Norland optical adhesive, Thor Labs) onto cleaned coverslips. SUVs were incubated at 37°C in chambers on coverslips suspended in Supported Lipid Bilayer buffer with additional 1 mM $CaCl_2$ for 20 minutes (1 mM final lipid concentration in 50 µl solution). After vesicle fusion, lipid bilayers were washed six times with 150 µl of Supported Lipid Bilayer buffer to rinse away excess SUVs. Immediately prior to adding septins, bilayers were further washed with a 150 µl of buffer containing 50 mM Hepes pH7.4, 1 mM BME, and 0.01% BSA six times.

Measuring protein adsorption on lipid bilayers supported on silica microspheres

Experiments measuring the adsorption of septins and AH domains on different curvatures were performed as previously published. Reactions (with a final buffer composition of 100 mM KCl, 50 mM Hepes pH 7.4, 1 mM BME, 0.1% methyl-cellulose, and 0.01% BSA) were incubated in a plastic chamber glued onto a polyethylene glycol (PEG)-coated passivated coverslip for one hour to reach equilibria. Confocal images of fluorescent-tagged protein adsorbed onto curved supported bilayers on microspheres were acquired using a spinning disc (Yokogawa W1) confocal microscope (Nikon Ti-82 stage) using a 100x Plan Apo 1.49 NA oil lens and a Prime 95B CMOS camera (Photometrics). Raw images were analyzed using Imaris 8.1.2 software (Bitplane AG) as previously described. Boxplots were generated using R version 3.2.2 (R Foundation for Statistical Computing; R studio 0.99.467) with ggplot2 package (Wickham et al., 2007, 2015).

Total internal reflection fluorescence microscopy

Experiments in which septin filaments were polymerized in solution, reactions were incubated in plastic chambers were glued onto PEG-coated passivated coverslips for one hour to reach equilibria. Recombinant protein was diluted to 250 nM final concentration in reaction buffer (75 mM KCl, 50 mM Hepes pH 7.4, 1 mM BME, 0.1% methyl-cellulose, and 0.01% BSA). For experiments on planar supported lipid bilayers, recombinant septins were incubated to a final concentration of 3 nM in buffer with 50 mM KCl, 50 mM Hepes pH 7.4, 1 mM BME, and 0.01% BSA. On lipid bilayers, septin polymerization was imaged immediately upon incubation. Images were acquired utilizing a Nikon TiE TIRF system equipped with a solid-state laser system (15 mW, Nikon LUn-4), a Nikon Ti-82 stage, a 100x Plan Apo 1.49 NA oil lens, and Prime 95B CMOS camera (Photometrics). TIRF microscopy images were processed and analyzed using ImageJ (FIJI).

Persistence length measurements

The cosine correlation of tangent angles along the filament lengths were assembled from single time points and fitted to an exponential to determine the persistence length using a MATLAB GUI previously published.

Helical diagram generation

Amphipathic helical wheels were generated, and their net charge and hydrophobicity were determined using Heliquest.

3.3 Results and Discussion

3.3.1 A predicted AH domain of Shs1 can distinguish between different membrane curvatures in vitro

We reported previously that septin complexes harboring Cdc12 mutant protein, cdc12-6, where the AH domain is truncated, no longer could distinguish between different membrane

curvatures (Cannon *et al.*, 2019). In *cdc12-6* mutants, septins quickly disassemble from the bud neck at restrictive temperature. However, at permissive temperature septins remain localized to bud neck, which is a site of positive micron-scale membrane curvature in cells (Amy S. Gladfelter *et al.*, 2005). We reasoned that another, unidentified AH domain might enable septins to localize in these mutants at permissive temperature. Screening through protein sequences of all mitotically expressed septins in ascomycetes including *S. cerevisiae*, *A. gossypii*, and *K. lactis* revealed an AH domain within the CTE of Shs1 (Figure 3.1, B and C). Interestingly, the ascomycetes *N. crassa*, *S. pombe*, and *A. nidulans* lack an Shs1 homolog all together, whereas *C. albicans* Shs1 does not have an AH. Despite sharing relatively low homology (~65%) among AH-containing Shs1 polypeptides (Figure 3.1, A), AH domains are nearly identical (Figure 3.1 B-D**).** The physicochemical properties of AH domains have been shown to affect membrane binding and curvature sensing (Drin *et al.*, 2007; Drin and Antonny, 2010). Interestingly, the charge and hydrophobic moment of the Shs1 AH are different than the Cdc12 AH (Figure 3.1, A and B). Together, these data suggest that the Shs1 AH domain might impart a distinct curvature preference when combined with Cdc12 in the same septin complex.

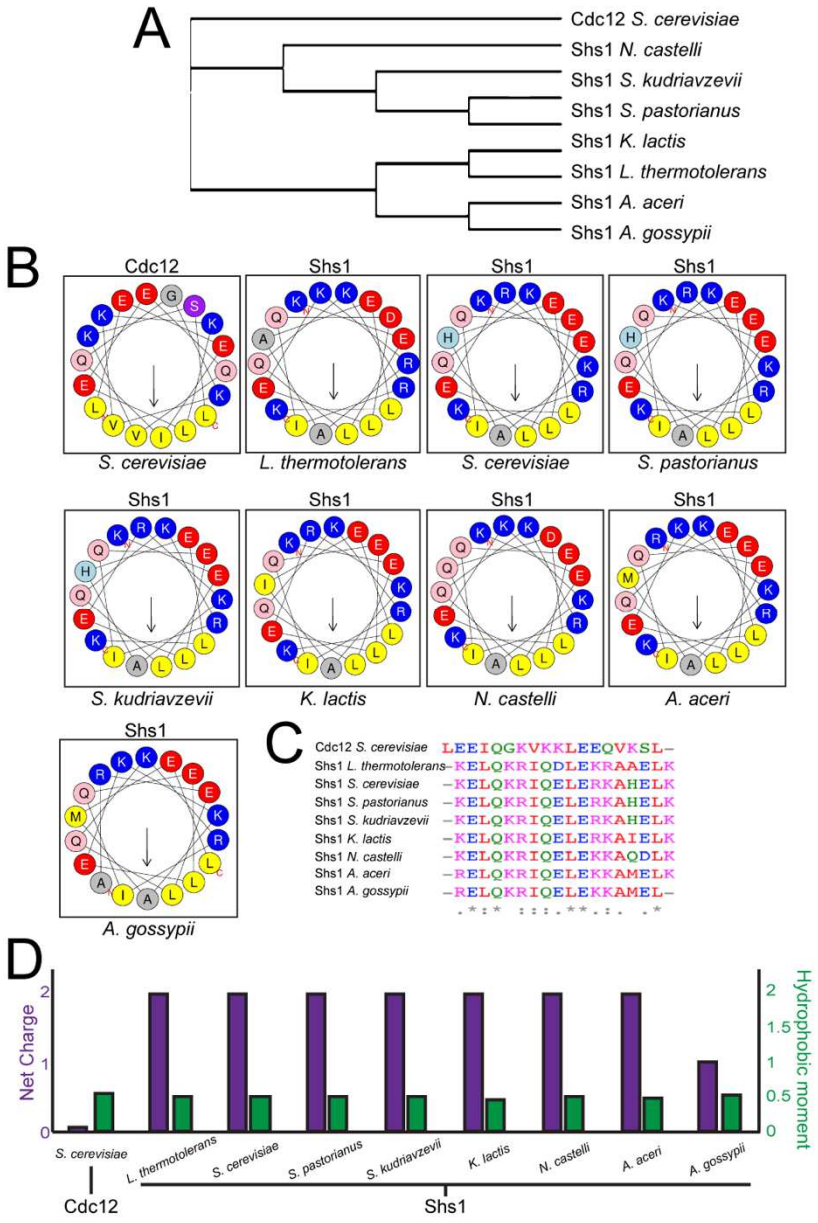

Figure 3.1 Shs1 contains a highly conserved amphipathic helix within its C-terminal domain. (A) Cladogram constructed from multiple alignments of Shs1 primary sequences from various ascomycetes. (B) Helical wheels representing amphipathic helices present in septin polypeptides screened ascomycetes. (C) Sequence alignment of amphipathic helices.(D) Net charge and hydrophobic moment of septin amphipathic helices.

To assess whether the *S. cerevisiae* Shs1 AH domain can distinguish between membrane curvatures, we purified a polypeptide with 2 copies of the AH of Shs1 to mimic the stoichiometry of the septin complex and mixed it with membrane-coated, silica beads ranging in

diameter from 300 nm to 5 μm (curvatures of $\kappa = 6.67\ \mu m^{-1}$ to $\kappa = 0.4\ \mu m^{-1}$ respectively). The Shs1 AH domain adsorbed best to higher curvatures (although the preference between curvatures of $6.67\ \mu m^{-1}$ and $2\ \mu m^{-1}$ were not statistically significant), with almost no binding at lower curvatures (Figure 3.2A). Thus, the Shs1 AH can distinguish different curvatures and - despite the different chemical properties - has a similar membrane curvature preference to the Cdc12 AH (Cannon *et al.*, 2019).

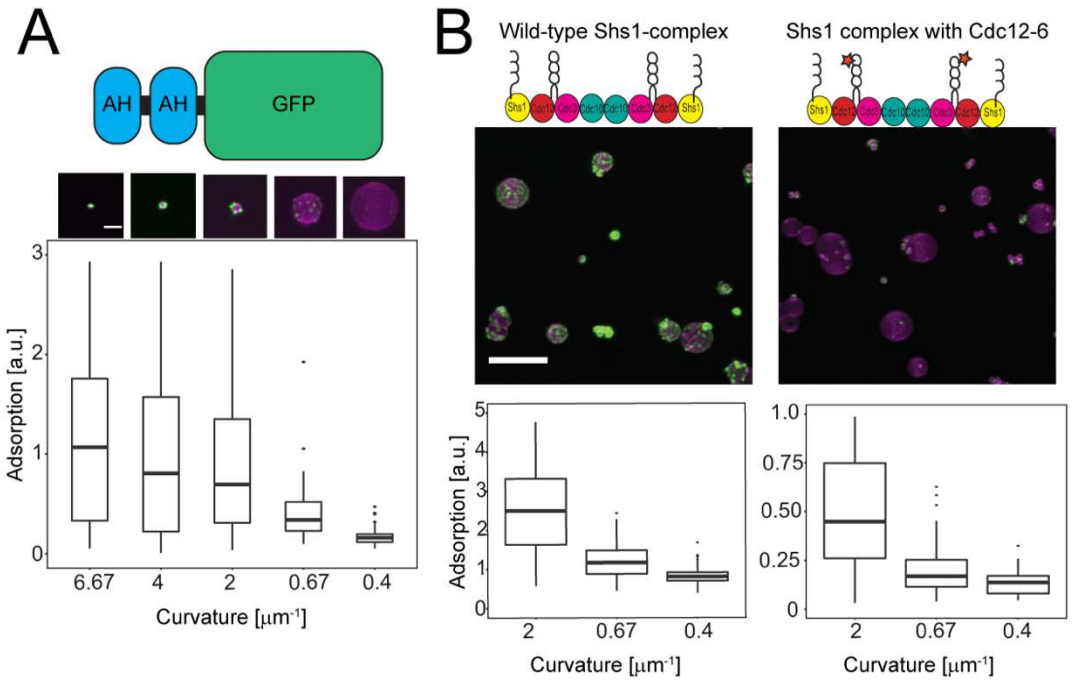

Figure 3.2 Shs1's amphipathic helix is capable of binding micrometer-scale membrane curvatures. (A) (Top) Maximum projection images of 2 μM 2x-Shs1AH-GFP (green) adsorbed onto curved supported lipid bilayers (magenta). Scale bar, 2 μm. Images contrasted identically. (Bottom) Box and whisker plot of 2x-Shs1AH-GFP adsorption onto different membrane curvatures. Black bars represent the median. Error bars are the standard deviation for N >10 beads at each curvature. (B) (Top) Maximum projection images of 100 nM wild-type Shs1 complex (green, panel 1) or Shs1-Cdc12-6 complex (green, panel 2) on curved supported lipid bilayers (magenta). Scale bar, 10 μm. Images are contrasted identically. (Bottom) Box and whisker plot quantifying adsorption onto different curvatures. Black bars represent the median. Error bars are the standard deviation for N >70 beads at each curvature

Why does Shs1 harbor a curvature-sensing AH domain? Within the septin complex Cdc12 resides at the penultimate position, with the terminal subunit being either Cdc11 or Shs1

and there is no evidence of "chimeric" octamers with Cdc11/Shs1 on either end(Garcia *et al.*, 2011b; Weems and McMurray, 2017; Khan, Newby and Gladfelter, 2018). Thus, Cdc11-capped complexes possess two AH domains, spaced apart by ~24 nm (the distance between the Cdc12 subunits) while Shs1-capped complexes have four AH domains, altering the valency and spacing of AHs within assemblies. This raises the possibility that septin curvature preference could be different when both AHs are combined in the same complex.

To test whether the Shs1 AH domain alters the curvature preference of septins, we purified Shs1-capped octamers and mixed them with different-sized membrane coated beads. Shs1-capped octamers displayed a similar membrane curvature preference to that of Cdc11-capped octamers with the highest adsorbance on beads 1 μm in diameter ($\kappa = 2\ \mu m^{-1}$) (Figure 3.2B) (Cannon *et al.*, 2019). This is consistent with the behavior of tandem AH domains (Figure 3.2A and Cannon et al., 2019) and our previous observation where Cdc11- and Shs1-capped octamers were mixed and preferentially adsorbed onto membrane curvatures 1 μm in diameter (Khan, Newby and Gladfelter, 2018). It was unclear why addition of two more AH domains did not alter membrane-curvature sensitivity. One possibility is that the second pair of AHs in the complex help stabilize membrane interactions, while not changing the curvature preference. This makes sense as Shs1 complexes have diminished ability to form filaments to provide avidity in membrane association.

Next, we tested if Shs1-capped complexes could restore membrane curvature sensitivity of cdc12-6 heteromeric-complexes in which the AH domain is truncated. Consistent with the Shs1 AH having a similar curvature preference as the Cdc12 AH, septin complexes harboring cdc12-6 and capped with Shs1 preferentially adsorbed onto similar membrane curvatures as complexes harboring wild-type Cdc12 (Figure 3.2B). Collectively, these data suggest that within

a septin complex, the AH domains of Shs1 and Cdc12 sense membrane curvature at the same scale.

Despite restoration of curvature sensing, the adsorption of cdc12-6 Shs1-capped octamers were substantially lower than Cdc12-wt Shs1-capped octamers. This contrasts with cdc12-6 Cdc11-capped octamers which lack curvature sensitivity, adsorbing nonspecifically to all curvatures tested (Cannon *et al.*, 2019). The differential adsorption of cdc12-6 octamers with either Cdc11 or Shs1 has several implications. First, it suggests the enhanced, non-specific binding of cdc12-6 complexes is dependent on Cdc11, suggesting a strong membrane-interaction surface in Cdc11. Second, given Shs1's limited ability to polymerize, cdc12-6 Shs1-capped complexes may be less stably associated with the membrane and with an even greater handicap to form filaments, further reducing overall adsorption. Nonetheless, these data suggest that the Shs1 AH is a functional curvature sensor.

3.3.2 The Shs1 CTE and AH domain are required for normal septin function in the cdc12-6 mutant

As Shs1 harbors an AH domain, it is possible that Shs1 becomes critical for septin localization at the bud neck in *cdc12-6* strains at permissive temperature. If the ability of septins to differentiate membrane curvatures is essential, and either the Cdc12 or Shs1 AH domain can mediate curvature sensing, then compromising both would be synthetic lethal. Consistent with this hypothesis, it had been previously reported that deletion of *SHS1* in a *cdc12-6* background is inviable (Finnigan, Booth, *et al.*, 2015), which was corroborated by tetrad dissection in our strain background at 24°C (Figure 3.3B). To distinguish whether it was the Shs1 AH domain that was essential in *cdc12-6* mutants, we generated a panel of C-terminal Shs1 truncations in the *cdc12-6* background (Figure 3.3A). C-terminal truncations of Shs1 that begin immediately *after* the AH

domain (*shs1*$^{\Delta 506\text{-}551}$ and *shs1*$^{\Delta 508\text{-}551}$) were viable in the *cdc12-6* background at 24°C (Figure 3.3B). However, some double mutants had classic septin mutant phenotypes with elongated buds and often failed to separate from the mother (Fig 3.2C). This may be due to the proximity of the truncation to the AH domain. *cdc12-6* mutants expressing Shs1 truncation beginning 15 residues *after* the AH domain were fully viable without septin defects (Figure 3.3, B and C). *cdc12-6* mutants expressing a more extensive Shs1 truncation (*shs1*$^{\Delta 488\text{-}551}$) or an AH deletion (*shs1*$^{\Delta AH}$) were sick, displaying fully penetrant septin defects at 24°C (Figure 3.3, B and C). Truncating the entire Shs1 CTE (*shs1*$^{\Delta 341\text{-}551}$) was synthetic lethal with *cdc12-6* (Figure 3.3B). These data indicate that the AH domain within the CTE is necessary for proper septin function in *cdc12-6* mutants but that the full CTE is required for viability.

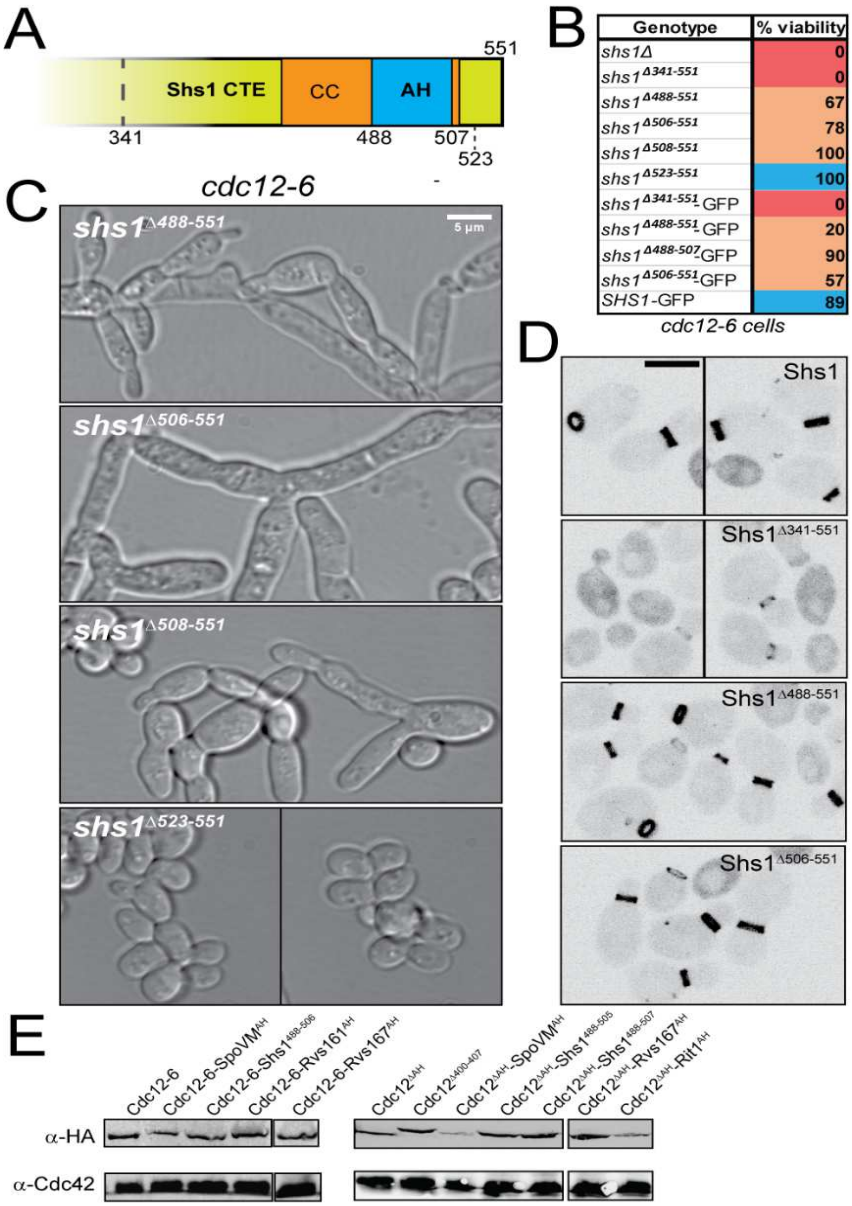

Figure 3.3 Genetic analyses of Shs1 and Cdc12 AH domains

(A) *S. cerevisiae* Shs1 CTE with a predicted AH domain within the coiled coil. Truncation sites within Shs1 CTE demarcated. (B) Viability of *cdc12-6* cells expressing indicated *SHS1* alleles expressed from the endogenous locus based on tetrad dissections at permissive temperature (24°C). Genotypes labeled in blue appeared normal, without obvious septin defects. Genotypes in orange were sick, with partially or fully penetrant septin defects. Genotypes in red were inviable. (C) DIC images of *cdc12-6 shs1* mutants (see B) at 24°C. Scale bar, 5 µm. (D) Heterozygous diploids expressing the indicated Shs1 protein fused to GFP from the *SHS1* locus. Scale bar, 5 µm. (E)Western blot comparing expression of indicated Cdc12 chimeras fused to 3xHA epitope in heterozygous diploids.

It was possible that truncating Shs1 reduced Shs1 incorporation into septin complexes. To rule this out, we generated GFP tagged Shs1 truncations expressed from the endogenous *SHS1* locus to assess Shs1 expression and localization. In wild-type *CDC12* cells Shs1 truncations (with the exception of Shs1$^{\Delta 341\text{-}551}$-GFP) were expressed at similar levels to wild-type Shs1-GFP and localized to the bud neck normally (Figure 3.3D). This suggests these truncations do not interfere with Shs1 incorporation. Shs1$^{\Delta 341\text{-}551}$-GFP, in which the entire CTE is truncated, was expressed normally in wild-type cells, but localized predominantly in the cytoplasm with reduced signal at the bud neck (Figure 3.3D). The increased cytoplasmic distribution of Shs1$^{\Delta 341\text{-}551}$-GFP provides an explanation for the observed synthetic lethality with *cdc12-6* mutants. In sum these data suggest that removal of the AH does not block Shs1 incorporation into septin complexes.

We reasoned that if the main function of the Cdc12 AH domain is to sense membrane curvature, then swapping it with other AH domains might be sufficient to restore cdc12-6 function. We generated chimeric strains where different AH domains were fused to the C-terminus of either cdc12-6 or Cdc12 lacking its entire AH domain (Cdc12$^{\Delta AH}$). Chimeric Cdc12 included AH domains from Shs1, Rvs161, Rvs167, *S. pombe* RitC, and *B. subtilus* SpoVM (Youn *et al.*, 2010; Bendezú *et al.*, 2015; Gill, J.-P. Castaing, *et al.*, 2015). Surprisingly, none of these chimeric strains were viable even at permissive temperature as assessed by tetrad dissection. This is despite that Cdc12 AH domain chimeras were expressed normally relative to wild-type Cdc12 (Figure 3.3E). Moreover, we could discount the possibility that the 3xHA tag adjacent to the AH domain was responsible for the lethality since the 3xHA tag adjacent to the Cdc12 AH domain (Cdc12$^{\Delta 400\text{-}407}$) had no effect on viability (Figure 3.3B). These data indicate

that the Cdc12 AH domain cannot be simply swapped for another AH domain, even if chimeric AH domain recognizes similar curvatures (Figure 3.2A).

Why are *cdc12$^{\Delta AH}$* mutants inviable even in the presence of wild-type *SHS1*? It is possible that cdc12-6 containing octamers *in vivo* maintain some minimal ability to localize to membrane curvature that can be supplemented by Shs1. Although this contrasts with the *in vitro* data. Another possibility is that cdc12$^{\Delta AH}$ does not fold properly or incorporate into octamers efficiently, rendering it non-functional. However, cdc12$^{\Delta AH}$ was expressed at wild-type levels (Figure 3.2E) suggesting it is not degraded and that is incorporated into septin complexes. A third possibility is that Shs1 does not efficiently cap cdc12$^{\Delta AH}$ septin oligomers.

3.3.3 The Cdc12 AH domain inhibits septin bundling

Why are Cdc12-AH domain chimeras non-functional? And why are *cdc12-6* mutants sensitive to Shs1 CTE truncations, including ones that maintain the Shs1 AH? We reasoned there might be an additional, essential function to the Cdc12 AH domain or a gain-of-function that occurs when the curvature sensitivity of the AH domain is lost. A clue comes from yeast cells exposed to pheromone, where in *cdc12-6* mutants septins no longer localize into filaments in the shmoo, and typically remain cytoplasmic (Giot and Konopka, 1997; Longtine, Fares and Pringle, 1998). In a subset of cells, we observed aberrant septin structures that appeared to be bundled "needles" and not in association with the cortex (Figure 3.4A). Needles were not observed in cycling, heterozygous diploids (*cdc12-6/CDC12*), possibly indicating that ectopic bundled needles are a recessive phenotype of *cdc12-6* mutants.

In *Ashbya cdc12-6* mutants, bundled needle-like structures were detectable in the cytoplasm of vegetatively growing cells, with some needles extending the entire length of hyphae (Figure 3.4B). Interestingly, *cdc12-6* septin needles are temperature sensitive and quickly

disassemble when *Ashbya* mutants are shifted to 37°C (Figure 3.4C). Curiously, after shifting down from 37°C to 22°C, septins did not immediately reform into needles, but instead localized to hyphal tips (Figure 3.4C). This is consistent with a previous observation in budding yeast *cdc12-6* mutants in which after shifting down to permissive temperature, septins did not localize to the bud neck, but instead localized to the bud where polarity factors are localized (Amy S. Gladfelter *et al.*, 2005).

The existence of naturally occurring bundled septin structures in cells suggest that cdc12-6 bundles are not necessarily only a gain-of-function mutation but that the C-terminus of Cdc12 could be relevant for bundling septins under certain contexts (DeMay *et al.*, 2009; Liu *et al.*, 2019). However, given their abundance in *cdc12-6* mutants, the needles could act like a sponge, sequestering septin complexes from the cytoplasm into "function-less" structures. Consistent with this, recombinant cdc12-6 septin complexes (capped with Cdc11) form needles in solution that were less flexible than wild-type filaments (Figure 3.4, D and E). This indicates formation of needle-like structures is an intrinsic feature of cdc12-6 septin complexes and is not dependent on other cellular factors. Interestingly, when added on supported planar lipid bilayers, cdc12-6 octamers did not form bundled needles (Figure 3.4F), suggesting that membranes may play an inhibitory role in bundling. This is supported by the observation that needles in cells appeared to be within the cytosol away from the cortex.

The needle-like septin structures in *cdc12-6* mutants suggest the AH domain of Cdc12 may also have a role in septin bundling (Figure 3.4G). Truncation of the Cdc12 AH domain is predicted to misfold the coiled-coil element at the C-terminus of Cdc12 (*MultiCoil*). Within the septin complex, the coiled-coil element of Cdc12 (Wolf, Kim and Berger, 1997) is thought to associate with the coiled-coil element of Cdc3 in parallel (Versele and Thorner, 2004; Aurélie

Bertin *et al.*, 2010). Homologous coiled-coil elements can dimerize or even oligomerize into larger coiled-coil structures in the absence of the preferred binding partner (Harbury *et al.*, 1993; Lupas and Bassler, 2017). We speculate that free Cdc3 coiled-coil elements could oligomerize in the absence of the Cdc12 coiled-coil elements to promote bundling. If coiled-coil misfolding is exacerbated in mutants lacking the AH, it could be another explanation as to why *cdc12*$^{\Delta AH}$ mutants are inviable. In *Ashbya*, dispersed septin filaments near the tips of hyphae coalesce into discrete bundled structures along the hyphal body. This transition is dependent on the kinase Gin4, which is predicted to interact with the coiled-coil element of Cdc3 and phosphorylates Shs1 in *S. cerevisiae* (Longtine, Fares and Pringle, 1998; Mortensen *et al.*, 2002). The Cdc3/Cdc12 coiled-coil may act like togglable switch, whose disassembly - either through phosphorylation or Cdc12 AH domain sequestration - could promote septin bundling through Cdc3 coiled-coil oligomerization.

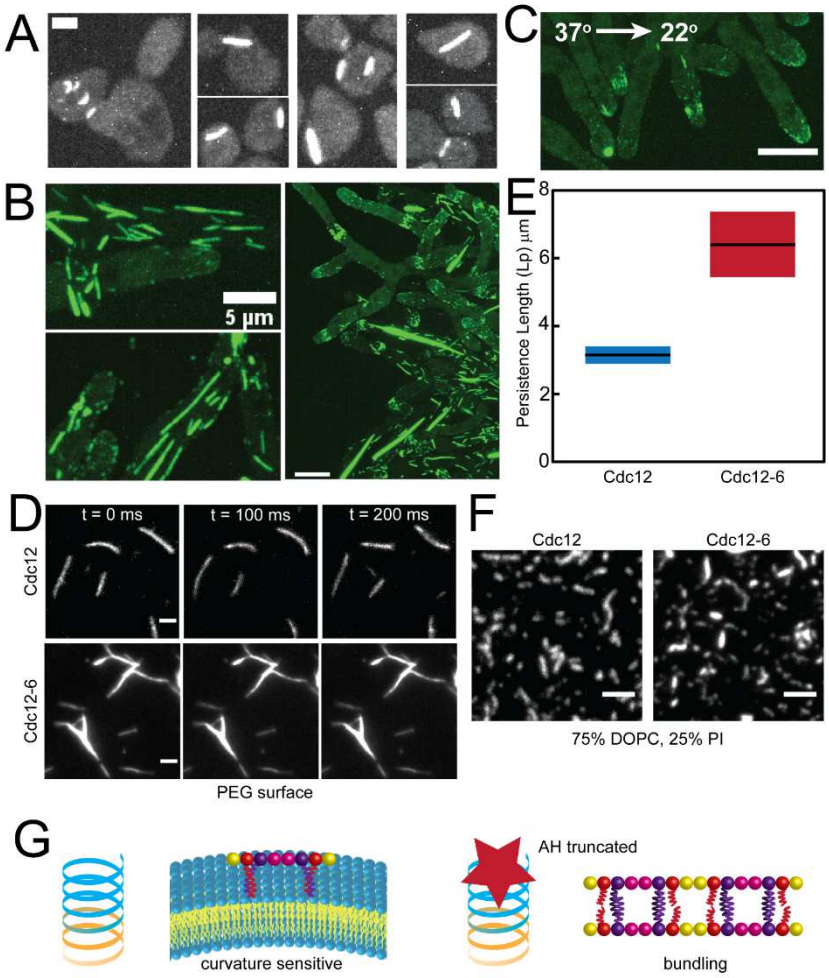

Figure 3.4 The Cdc12 AH domain inhibits septin bundling
(A) Maximum projections (contrasted identically) of fixed cells with bundled "needles" in *cdc12-6 S. cerevisiae* mutants expressing Cdc3-mCherry treated with pheromone . Scale bar, 2 µm. (B)Maximum projections of bundled "needles" in *A. gossypii* expressing Cdc12-6-GFP at 22°C. Scale bars, 5 µm (left panels) and 10 µm (right). (C)Maximum projection of a *cdc12-6 A. gossypii* mutant at 22°C immediately after being shifted down from 37°C for one hour. Scale bar, 10 µm. (D) TIRF images of wild-type (top) and cdc12-6 (bottom) septin filaments formed in solution. Scale bar, 10 µm. (E) Persistence length as determined by the cosine correlation of wild-type and Cdc12-6 filament tangent angles in solution. Lines represent mean, bars represent range. (F) TIRF images of 3 nM wild-type and cdc12-6 septins polymerized into filaments on planar supported lipid bilayers. Scale bar, 2 µm. (G) The Cdc12 AH domain enables septins to discriminate micron-scale membrane curvature. Blocking the AH domain promotes septin bundling.

3.4 Conclusion

Here we report that an additional AH domain in the non-essential septin, Shs1, can recognize membrane-curvature. Shs1 and its CTE harboring the AH domain become essential in mutants lacking a fully functional AH domain in Cdc12 (*cdc12-6*). cdc12-6 induces filament bundling into non-physiological needle-like structures, possibly exacerbating its phenotype. This may indicate a role for the AH domain in septin bundling. Future research should investigate how the Shs1 AH domain might influence septin-membrane binding affinity and diffusion in the membrane. The role of AH domains in septin biochemistry and biology is only beginning to be understood and is an exciting area of future study.

Supplemental table 3S1. Yeast strains used in this study.

STRAIN	RELEVANT GENOTYPE	SOURCE
AGY411	MATa/α *shs1::HIS3/SHS1 cdc12-6/CDC12 CDC3-mCherry:LEU2/CDC3 BEM1-GFP:LEU2/BEM1*	Daniel Lew
AGY436	MATa/α *shs1$^{\Delta 488-551}$*-GFP:*HIS3/SHS1 cdc12-6/CDC12*	This study
AGY441	MATa/α *SHS1*-GFP:*HIS3/SHS1*	This study
AGY444	MATa/α *shs1$^{\Delta 341-551}$*-GFP:*HIS3/SHS1*	This study
AGY450	MATa/α *shs1$^{\Delta 488-551}$*-GFP:*HIS3/SHS1*	This study
AGY453	MATa/α *shs1$^{\Delta 506-551}$*-GFP:*HIS3/SHS1*	This study
AGY460	MATa/α *SHS1*-GFP:*HIS3/SHS1 cdc12-6/CDC12*	This study
AGY462	MATa/α *shs1$^{\Delta 341-551}$*-GFP:*HIS3/SHS1 cdc12-6/CDC12*	This study
AGY463	MATa/α *shs1$^{\Delta 488-551}$*-GFP:*HIS3/SHS1 cdc12-6/CDC12*	This study
AGY464	MATa/α *shs1$^{\Delta 506-551}$*-GFP:*HIS3/SHS1 cdc12-6/CDC12*	This study
AGY478	MATa/α *cdc12-6*-3xHA*:TRP1/CDC12*	This study
AGY479	MATa/α *cdc12-6-(SpoVM-AH)*-3xHA*:TRP1/CDC12*	This study
AGY481	MATa/α *cdc12-6-(SHS1$^{488-505}$)*-3xHA*:TRP1/CDC12*	This study
AGY482	MATa/α *cdc12-6-(RVS161-AH)*-3xHA*:TRP1/CDC12*	This study
AGY484	MATa/α *cdc12-6-(RVS167-AH)*-3xHA*:TRP1/CDC12*	This study
AGY493	MATa/α *shs1$^{\Delta 523-551}$:HIS3/SHS1 cdc12-6/CDC12*	This study
AGY494	MATα *shs1$^{\Delta 523-551}$:HIS3 cdc12-6*	This study
AGY496	MATa/α *shs1$^{\Delta 341-551}$:HIS3/SHS1 cdc12-6/CDC12*	This study
AGY498	MATa/α *shs1$^{\Delta 488-551}$:HIS3/SHS1 cdc12-6/CDC12*	This study
AGY500	MATa/α *shs1$^{\Delta 506-551}$:HIS3/SHS1 cdc12-6/CDC12*	This study
AGY502	MATa/α *shs1$^{\Delta 508-551}$:HIS3/SHS1 cdc12-6/CDC12*	This study
AGY508	MATα *shs1$^{\Delta 488-551}$:HIS3 cdc12-6*	This study
AGY512	MATα *shs1$^{\Delta 506-551}$:HIS3 cdc12-6*	This study
AGY516	MATα *shs1$^{\Delta 508-551}$:HIS3 cdc12-6*	This study
AGY524	MATa *cdc12-6 CDC3-mCherry:LEU2 bar1::URA3*	This study
AGY533	MATa/α *cdc12$^{\Delta AH}$*-3xHA:*TRP1/CDC12*	This study
AGY534	MATa/α *cdc12$^{\Delta 400-407}$*-3xHA:*TRP1/CDC12*	This study
AGY537	MATa/α *cdc12$^{\Delta AH}$-(SpoVM-AH)*-3xHA:*TRP1/CDC12*	This study
AGY538	MATa/α *cdc12$^{\Delta AH}$-(SHS1$^{488-505}$)*-3xHA:*TRP1/CDC12*	This study
AGY540	MATa/α *cdc12$^{\Delta AH}$-(RVS167-AH)*-3xHA:*TRP1/CDC12*	This study
AGY541	MATa/α *cdc12$^{\Delta AH}$-(*S.p.*RITC-AH)*-3xHA:*TRP1/CDC12*	This study
AGY542	MATa/α *cdc12$^{\Delta AH}$-(SHS1$^{488-507}$)*-3xHA:*TRP1/CDC12*	This study
AGY548	MATa/α *shs1$^{\Delta 488-507}$*-GFP:*HIS3/SHS1 cdc12-6/CDC12*	This study

Yeast strains were in the YEF473 genetic background (*his3-Δ200, leu2-Δ1, lys2-801, trp1-Δ63, ura3-5*)

Supplemental table 3S2. Plasmids used in this study

NAME	DESCRIPTION	SELECTION MARKER
AGB 548	pMVB133 ScCDC3/ ScSHS1-GFP	CAM
AGB 710	pMVB128 6-HIS-TEV-ScCDC12/ScCDC10	AMP
AGB 1084	pUC57 2xScShs1AH-GFP	AMP
AGB 1204	pET-duet-6HIS-TEV-ScCDC12-6/ScCDC10	AMP

CHAPTER 4

THE PHYSICAL BASIS OF CURVATURE SENSING BY SEPTINS

AUTHORS: Kevin S. Cannon, Wenzheng Shi, Ehssan Nazockdast, and Amy S. Gladfelter

Note: This is a collaboration between myself, Amy, and applied physcists Wenzheng and his advisor Ehssan. I am responsible for the experimental data and intellectual contributions for the physical models below. Wenzheng is responsible for the mathematical formulations and simulations.

4.1 Introduction

Cells and their internal compartments take on a spectacular array of shapes. How cells generate and utilize their shape to best suit their functions has been a central question in biology since the advent of the light microscope. Since then, much has been learned about how cells generate and sense their complex shapes (Rodal *et al.*, 2005; Simunovic *et al.*, 2015). Most of the work done on cell shape sensing has been done in the context of endocytosis (Gallop *et al.*, 2006; Lai *et al.*, 2012; Sorre *et al.*, 2012) and vesicle trafficking (Drin *et al.*, 2007; Roux *et al.*, 2010; Colom *et al.*, 2017), where nanometer-scaled proteins containing BAR domains or amphipathic helices are used by the cell to assemble onto nanometer-scaled membrane curvatures. Nanometer scale curvature sensors that contain amphipathic helices often utilize lipid packing defects, or exposed regions of hydrophobicity between lipid species, generated by the high curvatures as sites to interact with- and bind to the membrane (Hatzakis *et al.*, 2009). Other proteins, including those containing BAR domains utilize combinations of electrostatics, scaffolding, and even amphipathic helices to either sense or deform membrane curvature (Simunovic *et al.*, 2015). Collectively, the

physiochemical landscape of nanometer-scale membrane curvatures, including the shape of lipid headgroups, length of fatty acyl chains, and electrostatics are all important features used by cells to drive preferentially assembly of proteins onto curved surfaces (Cannon, Woods and Gladfelter, 2017).

Despite the breadth of knowledge about nanometer-scale curvature sensors, comparatively, much less is known about how cells use nanometer-scaled assemblies to detect changes in membrane curvature on the micrometer scale. This physical disparity is striking, as a micrometer-scale curvature is essentially a flat surface for a typical globular protein. However, these shallow curvatures are found throughout the cell at autophagosomes, lipid droplets, and the plasma membrane, suggesting cells must have a means to detect structures of this magnitude.

Septins are GTP-binding proteins that localize to sites of micrometer scale membrane curvature in yeast through humans (Bridges *et al.*, 2016; Cannon *et al.*, 2019). At these sites, septins coordinate cell cycle progression, cell migration, and aid in the degradation of invading microorganisms in host cells. Septin function is crucial for cellular homeostasis, as deleterious mutations within septin genes have been implicated in various cancers and neurodegenerative diseases. The four essential mitotic septin polypeptides from *Saccharomyces cerevisiae,* namely Cdc3, Cdc10, Cdc11, and Cdc12 are assembled into rod shaped, hetero-octameric complexes and constitute the minimal septin subunit (Hartwell *et al.*, 1973; Frazier *et al.*, 1998; A. Bertin *et al.*, 2008). Septin assembly at sites of membrane curvature begins with the binding of the septin octamer complexes to the membrane. Membrane-bound octamers will then diffuse and collide with one another to form filaments in a process termed diffusion-driven annealing (Bridges *et al.*, 2014). Septin filaments can either fragment or connect interact to with nearby filaments to form higher-order structures including pairs, rings, and gauzes seen in cells (Garcia *et al.*, 2011b; Ong

et al., 2014; Jiao *et al.*, 2020). Understanding the stages of the septin-membrane and septin-septin interaction are influenced by membrane curvature will be essential for elucidating the mechanisms by which septins sense micrometer-scale membrane curvature.

In this study we utilized a combination of single molecule imaging, scanning electron microscopy, time-lapse confocal microscopy, and modeling and simulation to probe the multiple scales at which curvature sensing by septins occurs. We show that single septin octamer kinetics and diffusion are sensitive to membrane curvature. Both of these processes are dependent on the septin interaction with lipid packing defects present in the membrane. Interestingly, we find that septin filament length is dependent on membrane curvature, yet the curvature of septin filaments is independent of membrane geometry. Lastly, the septin assembly process on curved membranes operates in two regimes: 1.) Through competition 2.) Through total adsorption at steady state. These data show that curvature-dependent assembly by septins functions at multiple scales.

4.2 Materials and Methods

Yeast septin purification

BL21 (DE3) *E. coli* cells were transformed using a duet expression system (*Bridges et al.* 2016) and selected with ampicillin and chloramphenicol. Selected cells were cultured to an $O.D._{600\ nm}$ between 0.6 and 0.8 and induced with 1 mM of IPTG. Induced cultures were grown for 24 hours at 22^{o} C (3 hours for Cdc12 amphipathic helix construct) before harvesting. Cultures were pelleted at 10,000 RCF for 15 min. Pellets were resuspended in lysis buffer (1M KCl, 50 mM, Hepes pH 7.4, 1 mM $MgCl_2$, 10% glycerol, 1% Tween-20, and 1x protease inhibitor tablet (Roche), 20 mM Imidazole, 1 mg/mL lysozyme) for 30 minutes on ice with intermittent vortexing. The lysate was sonicated twice for 10 seconds and clarified by centrifugation using an SS-34 rotor at 20,000 RPM for 30 minutes. Clarified supernatant was filtered using 0.44 μm

filter, then incubated with equilibrated Cobalt resin (Thermo Fisher Scientific; 2 mL resin per liter of *E.* coli culture) at 4ºC for 1 hour. Resin and lysate were added to a gravity flow column. Bound protein was washed four times with 5x the column volume with wash buffer (1M KCl, 50 mM Hepes pH 7.4, 20 mM Imidazole), and then eluted in elution buffer (300mM KCl, 50 mM Hepes pH 7.4, 500 mM Imidazole). Eluted protein was then dialyzed into septin storage buffer (300 mM KCl, 50 mM Hepes pH 7.4, 1 mM BME) for 24 hours in two steps (Slide-A-Lyzer G2 20K MWCO, Thermo Fisher Scientific; 10K MWCO for amphipathic helix constructs). During dialysis, 60 μg of TEV protease (Sigma) was added to cleave the 6x-histidine tag on Cdc12. 24 hours later, the protein was run over a second column (either Ni-NTA or cobalt resin) to remove the protease, the poly-histidine tag, and additional contaminants. Protein purity was determined via SDS-PAGE and protein concentration was determined via Bradford assay.

Lipid mix preparation

All septin binding experiments were done using supported lipid bilayers consisting of 75 mol % dioleoylphosphatidylcholine (DOPC) Avanti Polar Lipids, 25 mol % PI (Liver, Bovine) sodium salt, and trace amounts (less than 0.1%) of phosphatidylethanolamine-N-(lissamine rhodamine B sulfonyl) (Rh-PE) (ammonium salt) Egg-Transphosphatidylated, Chicken) (Avanti Polar Lipids 810146) unless otherwise mentioned. All lipid compositions were made the same way. Lipids were mixed in chloroform solvent, and dried by a stream of argon gas to generate a lipid film. Remaining solvent was evaporated by placing the lipid film under a vacuum for at least 6 hours. Lipids were rehydrated in supported lipid bilayer buffer (300 mM KCl, 20 mM Hepes pH 7.4, 1 mM $MgCl_2$) for 30 minutes at 37ºC to give a final concentration of 5 mM. Hydrated lipids were subject to vortex for 10 seconds, every 5 mins for 30 mins bath sonicated in 2 minute intervals until clarification to yield small unilamellar vesicles (SUVs).

Preparation of supported lipid bilayers on silica microspheres

SUVs were adsorbed onto silica microspheres (Bangs laboratories) of various curvatures by mixing 50 nM lipids with 440 um^2 of silica microsphere surface area or 10 uL of rods in a final volume of 80 uL for 1 hour on a roller drum at room temperature. Unbound lipid was washed away by pelleting lipid-coated beads at the minimum force required to pellet each bead size using pre-reaction buffer (33.3 mM KCl, 50 mM Hepes pH 7.4) (See http://www.bangslabs.com/ for sedimentation speeds). Washes were preformed 4 times.

Kinetics of single septin complex onto lipid-coated beads

Two PEG-passivated coverslips were sandwiched together using double-coated pressure sensitive adhesive tape (Nitto product:5015ELE) to make narrow (~20 µL flow chambers). A mixture of septins and lipid-coated beads of a given diameter were then flowed through the chamber and imaged using near-total internal reflection fluorescence microscopy. The number and duration of binding events were performed manually. Association-rate was quantified by calculating the number of binding events over the product of septin concentration, time, and binding area.

Single molecule diffusion analysis

Single septin octamer binding to beads of various membrane curvature was performed as described above. Using the FIJI plugin, Trackmate (Tinevez *et al.*, 2017), we were able to identify and track the position of single septin molecules over time. Using this information we generated plots showing mean-squared displacement (MSD) as a function of time (in log-log space) using a custom code. MSD and anamolous diffusion exponents were calculated using the following equations:

$$< X^2 > = \frac{1}{N-i+1} \sum_{n=0}^{N-i} (X_{n+i} - X_n)^2 \qquad \text{(Eq.M1)}$$

$$< X^2 >= 4Dt^{\alpha} \quad \text{(Eq.M2)}$$

Where X_i is the positin of the single septin octamer after ith time step, D is the diffusion coefficient, T is the total time of septin octamer diffusion and α is the anomalous diffusion exponent.

Generation and preparation of septin-rod supported lipid bilayer mixture.

Borosilicate rods were obtained from Glass Microfiber filters, GFC, 42.5 mm (Whatman). A single filter was torn up into small pieces into a beaker with 60 mL of 100% ethanol and sonicated until the solution became opaque. The solution was stored at room temperature overnight. The next day, 10 µL of rods were taken from the solution after thorough mixing. 70 uL of SLB buffer was added to the rods and spun down at top speed to dilute the ethanol in the solution. This step was repeated 4 additional times. 5 mM of SUVs (75% DOPC, 25% PI, trace Rh-PE, as described above) were added to the polycarbonate rods and allowed to incubate for 1 hour at room temperature. Unbound lipid was washed away pelleting lipid-coated beads at top speed (16.1 RCF) using pre-reaction buffer. The mixture of septin-lipid-coated rods were added to a circular 12mm (PEG)-coated coverslips and incubated at room temperature for 1 hour and then and prepared for scanning electron microscopy.

Scanning electron microscopy

The septin-rod mixture onto a circular PEG-coated 12mm coverslip, was fixed in 2.5% glutaraldehyde in 0.05 M sodium cacodylate (NaCo) pH 7.4 for 30 minutes followed by 2x washes in 0.05 M NaCo (5 min each wash). Samples were post-fixed in 0.5% OsO_4 Cacodylate buffer for 30 minutes and washed 3x in NaCo (5 minutes each wash). Samples were then incubated with 1% tannic acid for 15 minutes followed by 3x washes in NaCo. 0.5% OsO_4 was added for 15 minutes followed by 3x washes in NaCo. Samples were then dehydrated with

increasing ethanol concentrations: (30% EtOH for 5 minuets, 2x; 50% EtOH for 5 minutes; 75% EtOH for 5 minutes; 100% EtOH for 5 minuetes, 2x followed by another 10 minute incubation). Samples were incubated in transition fluid (hexamethyldisilazane) 3x; (incubation times: 5 minutes, 10 minutes, 5 minutes) and were allowed to airdry and then placed in a desiccator until sputter coating. Samples were coated in a gold/palladium alloy and then imaged on a Zeiss Supra 25 Field Emission Scanning Electron Microscope.

Measuring protein adsorption on lipid bilayers supported on silica microspheres

Experiments measuring the adsorption of septins on different curvatures were performed as previously published. Reactions had a final buffer composition of 100 mM KCl, 50 mM Hepes pH 7.4, 1 mM BME, 0.1% methyl-cellulose, and 0.01% BSA). Membrane coated beads allowed to settle by gravity in a plastic chamber glued onto a polyethylene glycol (PEG)-coated passivated coverslip for 30 minutes. Fluorescently tagged septins at a desired concentration were genetly added to these chambers and confocal images were acquired every 30 seconds for 1.5 hours to measure septin adsorbtion onto curved supported bilayers on microspheres over time. Images were acquired using a spinning disc (Yokogawa W1) confocal microscope (Nikon Ti-82 stage) using a 100x Plan Apo 1.49 NA oil lens and a Prime 95B CMOS camera (Photometrics). Raw images were analyzed using Imaris 8.1.2 software (Bitplane AG) as previously described. Plots were generated using a custom Python code.

4.3 Results and Discussion

4.3.1 Single septin complexes can detect changes in membrane curvature through the association rate

First, we examined if the kinetics of single septin octamers binding to membranes is influenced by membrane curvature (Figure 4.1A). To do so, we utilized a previously developed assay where recombinantly purified septin octamers, that are unable to polymerize, are mixed with

membrane-coated beads of different curvatures (radii). The number of binding events and the dwell times for single octamers are, then, measured using near-TIRF microscopy and different bead radii, from which association (k_{on}) and dissociation rates (k_{off}) are calculated as a function of curvature and octamer's concentration in the bulk (Figure 4.1B-D). Our previous studies on only two bead sizes suggested differences in ka as a function of curvature but from two bead sizes we could not infer the trend over many curvatures. We observed that at bulk concentrations lower than 1 nM, the association rate of octamers with membranes increases linearly with bulk concentration (Figure 4.1D, Note that the y-axis is the adsorption divided by the area of the bead and the bulk concentration.). We also observed that, at a given concentration, the association rate increases superlinearly with curvature (Figure 4.1C). Differences in association rates are consistent with previous studies on two different bead sizes (Cannon *et al.*, 2019), however by extending these experiments across a range of bead sizes, it becomes clear that while ka changes with different curvatures, the superlinear increase with increasing curvature cannot account for the curvature sensitivity seen by septins, which display an optimum curvature sensitivity rather than an increasing adsorption on higher curvatures.

Similarly, we previously measured the dwell times for only two curvatures and therefore we next measured the dwell times of single septin octamers on a broader range of various curved membranes. To calculate the dissociation rate (k_{off}) from this data we assumed that the dissociation is a Poisson process, and the normalized probability distribution of dwell times is $P(\tau) = \frac{1}{k_{off}} exp^{(-k_{off}\tau)}$. This expression was fitted against the experimentally measured distribution of dwell times (see the distribution around each datapoint in Figure 4.1E) to compute k_{off}. The average dwell times were calculated using $\tau_{avg} = \frac{1}{k_{off}}$ (Figure 4.1E). Consistent with our previous results, the dwell times, k_{off} remain nearly constant with variations of membrane curvature. This

is demonstrated more clearly in Figure 4.1F, where the cumulative probability distribution of dwell times at different curvatures are shown to superimpose and are not statistically different.

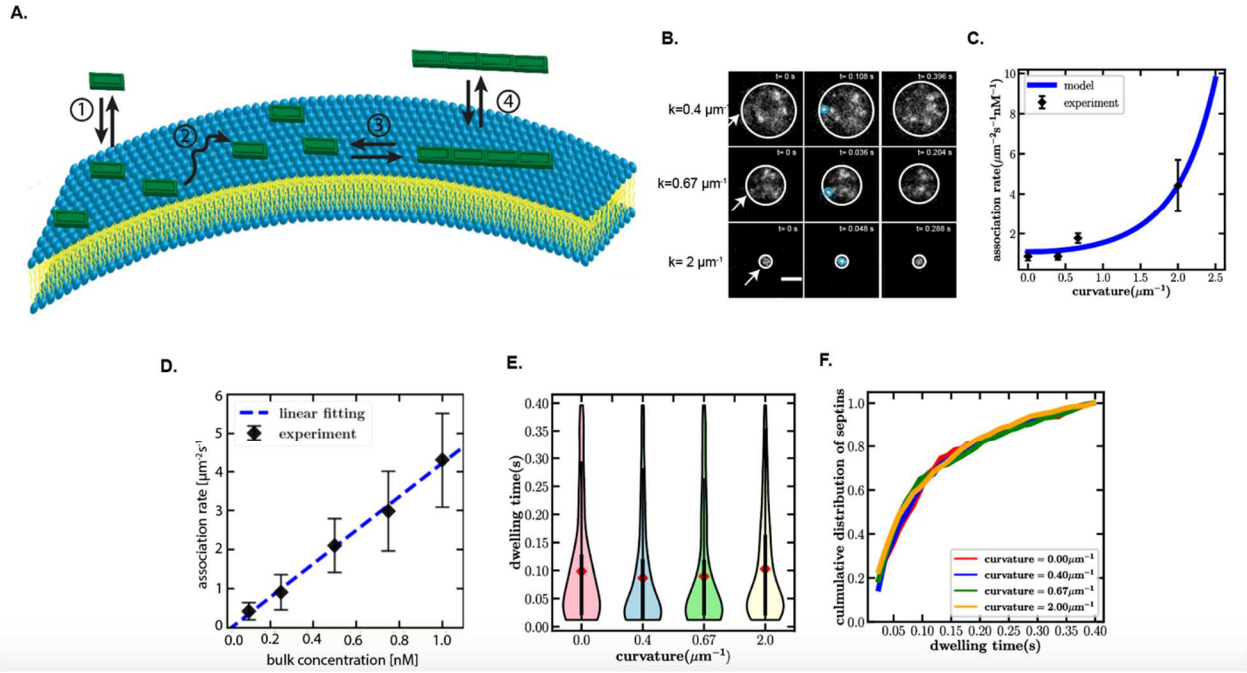

Figure 4.1 **Single septin complexes can detect changes in membrane curvature through the association rate. A.)** Schematic of the septin assembly process on membranes. 1.) Single septin octamers from the bulk interact with the membrane; 2.) Membrane-bound septin octamers diffuse and collide with nearby octamers; 3.) Septin octamers in close proximity to one another will interact end-on to form filaments. Filaments can interact with other filaments or fragment into smaller filaments/octamers; 4.) Septin filaments can associate or disassociate from the membrane. **B.)** Representative near-TIRF images showing single octamer binding and unbinding events on various membrane curvatures. Scale bar is 2μm. **C.)** Measured association rates for single octamer binding onto various membrane curvatures. N> 100 particles per curvature. Error bars represent the standard deviation. Measured association rates were fit to our lipid packing defect energy model, blue line. **D.)** Measured association rates of single septin octamers onto membrane curvature k= 2μm^{-1} at various septin concentrations. N>100 particles for each concentration. Error bars represent the standard deviation. **E.)** Violin plots highlighting the distribution of measured dwell times for single septin octamers on various membrane curvatures. N> 100 particles per curvature. Red triangles highlight the mean. **F.)** Cumulative distribution of septin octamers as a function of dwell time for various curvatures. Red line:planar membranes; blue line: k=0.4 μm^{-1};green line: k=0.67 μm^{-1};yellow line: k= 2 μm^{-1}

4.3.2 A mechanochemical model for interactions of octamers with the membrane

We turn to modeling to understand the interactions of septin octamters with the membrane and curvature sensing in single octamer length scale. As septins contain a curvature sensitive amphipathic helix (AH) (Cannon *et al.*, 2019), we reasoned that septin adsorption onto curved membranes begins through intercalation of AH domain into the membrane's outer leaflet. We assume the intercalations of the AH domain occur when the lipid bilayers are locally strained due to thermal energy, such that AH domains can penetrate into the membrane. We refer to these local openings as lipid defects. The schematic of this model is shown in Figure 4.2D.

The adsorption/desorption process of an octamer in our model is divided into two steps: i.) formation and healing of lipid packing defects (Eq. 1). ii.) association and disassociation of septin octamers (via AH domain insertion) on and off the membrane (Eq. 2). Following this, the kinetic equations describing septin's adsorption with time (n_s) are expressed as:

$$\frac{dn_d}{dt} = k_{on}^d - k_{off}^d n_d - k_{on}^s n_b n_d \qquad \text{(Eq.1)}$$

$$\frac{dn_s}{dt} = k_{on}^s n_b n_d - k_{off}^s n_s \qquad \text{(Eq. 2)}$$

where subscripts d, s, and b, respectively, refer to defects, membrane-bound septins, septins in the bulk, whereas n denotes number density. At steady state ($\frac{dn_d}{dt}$ and $\frac{dn_s}{dt}$ both equal zero) we can show the relationship between the number of bound septins and the rates of lipid packing defect formation/healing and septin association/disassociation (Eq. 3).

$$N^s = \frac{k_{on}^d k_{on}^s n_b}{k_{off}^s (k_{off}^d + k_{on}^s n_b)} \qquad \text{(Eq.3)}$$

Note the values reported in Figures 4.1D is the net measured association rate, k_{on}^{exp} with the defect dynamics embedded in it, while the dissociation rates in the model and experiments have the same physical definitions, $k_{off}^{exp} = k_{off}^{s}$. Given that the adsorption can be defined as Eq.3 we can express the measured association rate as

$$k_{on}^{exp} = \frac{k_{on}^{d} k_{on}^{s}}{k_{off}^{d} + k_{on}^{s}} \qquad \text{(Eq. 4)}$$

When the rate of adsorption of octamers to defects is significantly smaller than the healing rate of defects, such that $k_{on}^{s} n_b \ll k_{off}$,the steady-state adsorption simplifies to:

$$N^{s} = \left(\frac{k_{on}^{d} k_{on}^{s}}{k_{off}^{s}}\right) n_b \qquad \text{(Eq.5)}$$

This is in agreement with the linear scaling of the association rate with bulk concentration (Figure 4.1D) at very small values of bulk concentrations ($n_b < 1\ nM$). Additionally, Eq.5 also shows that the measured association rate is proportional to the equilibrium constant that controls number of defects in the membrane (See Eq. 6 for rearrangement of variables from Eq. 5)

$$k_{on}^{exp} \sim N_d = \frac{k_{on}^{d}}{k_{off}^{d}} = K^{d} \qquad \text{(Eq. 6)}$$

As membranes bend, the spacing between neighboring lipids increases (on the leaflet undergoing expansion), thereby increasing the probability of lipid packing defect formation. In other words, the energy barrier of defects formation gets reduced. Therefore, we expressed number of defects present in terms of the free energy of the membrane:

$$K^d = k_{on}^{do} e(-\frac{Ed-2GmK^2}{kbT}) \qquad \text{(Eq.7)}$$

Where k_{on}^{do} represents the defect healing rate, E_d is the membrane bending energy, G_m is the splay modulus of the membrane, K is the curvature of the membrane, and kbT is Boltzmann's constant. Therefore, by combining Eqs. 5 and 7 (Eq. 8) we can see a superlinear relationship between the association rate of septin octamers as a function of curvature as well as a linear relationship between bulk concentration and the association rate, consistent with our experimentally measured observations (Figure 4.1C).

$$k_{on}^{s} = k_{on}^{do} e\left(-\frac{Ed}{kbT}\right) e(\frac{2Gm}{kbT}K^2) k_{on}^{s0} n_b \quad \text{(Eq.8)}$$

Collectively, we've shown that the association rate of single septin octamers is dependent on the formation of lipid packing defects, which are influenced by membrane properties including curvature and bending rigidity. Moreover, the association rate continues to increase superlinearly with curvature and linearly with the bulk concentration of octamers. These data suggest that single septin octamers alone cannot account for the non-monotonic preference of septins for a membrane curvature of k= 2μm^{-1} previously observed by Bridges et. al., 2016 and Cannon et. al., 2019.

4.3.3 Single septin complexes display sub-diffusive behavior on curved membranes

After the initial binding, a septin oligomer may rapidly unbind or has the opportunity to diffuse and collide end-on to form a filament in a process referred to as "diffusion-driven annealing" (Figure 4.1A,1-3). How the diffusive state of a protein can be influenced to change the probability of collisions and promote filament formation could be an important process in driving a cooperative and preferential assembly of septins onto curved membranes. Using our single

molecule TIRF assay and particle tracking software (Tinevez *et al.*, 2017) we were able to examine the lateral mobility of single septin octamers on curved membranes (Figure 4.2A) from which mean squared displacement could be measured. The mean squared displacement is described by $MSD = 4Dt^{\alpha}$,where alpha, the anomalous diffusion exponent, can be used to describe the diffusive state of the particle whether it be Brownian (alpha =1), sub-diffusive (alpha < 1), or super-diffusive (alpha >1). We found that on membrane curvatures (k=0.4 μm^{-1} and 0.67 μm^{-1}), septin octamers exhibit sub-diffusive behavior with alpha values ranging from 0.68-0.01 (Figure 2B, C). Interestingly, we noticed that as the dwell time of single octamers increased, the alpha exponent decreased. Unfortunately, given the small diameter of beads where k= 2μm^{-1} we were unable to make faithful estimates of mobility on this curvature.

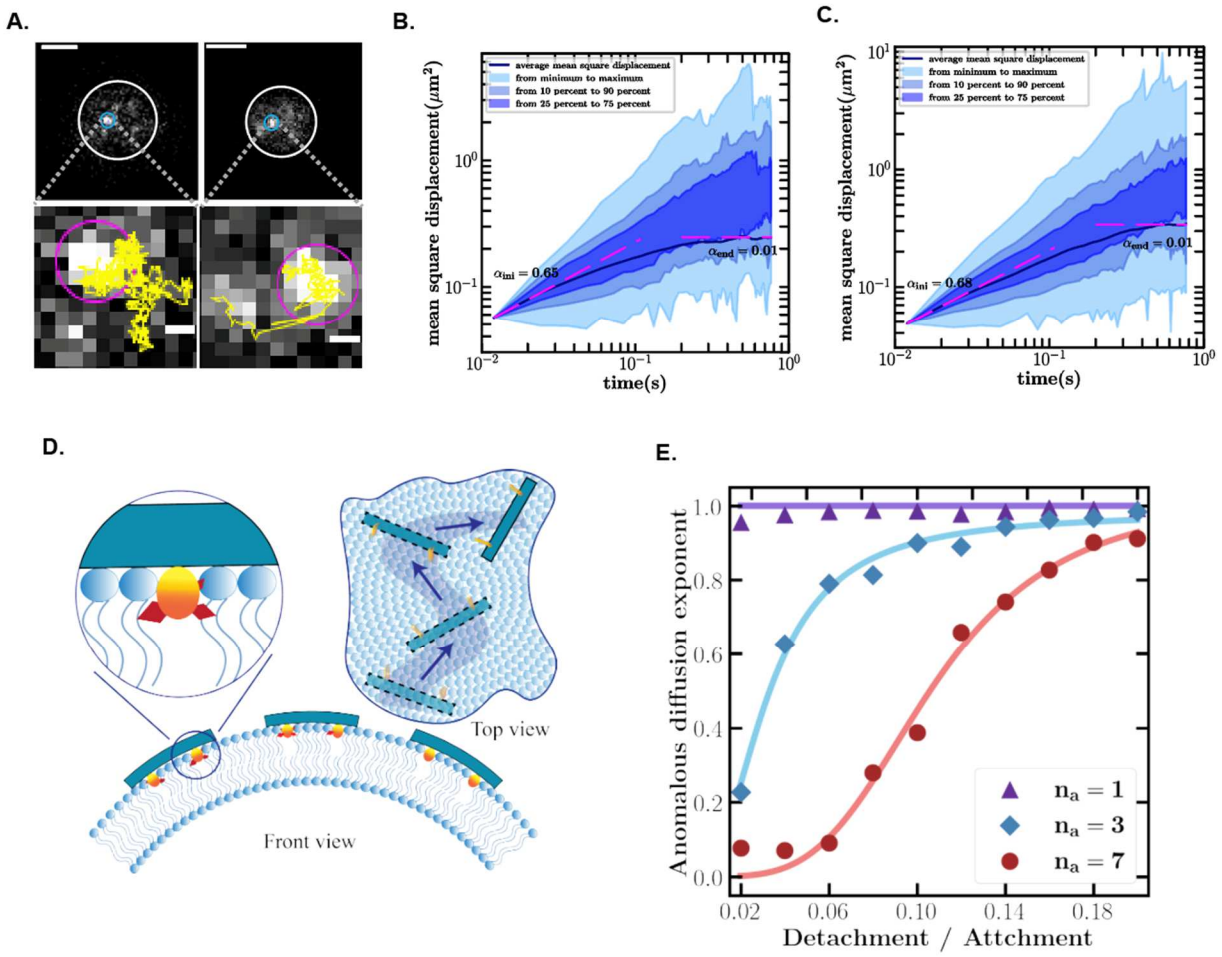

Figure 4.2 Single septin complexes display sub-diffusive behavior on curved membranes Representative TIRF images of single septin complexes on membrane curvatures k=0.4 μm^{-1} and k=0.67μm^{-1},respectively (Top panel). Scale bar: 2μm. Individual particle tracks (yellow lines) for membrane curvatures k=0.4 μm^{-1} and k=0.67μm^{-1}, respectively. Scale bar: 0.25μm. (B) Mean squared displacement as a function of time for single octamers on membrane curvature k=0.4 μm^{-1}. Shades areas highlight the percentage of octamers in a given mobility regime. Dotted red lines indicate the measured anomalous diffusion exponents at the start and end of the track. N> 500 particles. (C) Mean squared displacement as a function of time for single octamers on membrane curvature k=0.67 μm^{-1}. Shades areas highlight the percentage of octamers in a given mobility regime. Dotted red lines indicate the measured anomalous diffusion exponents at the start and end of the track. N> 500 particles. (D) Schematic of multiple attachment model. (E) Anomalous diffusion exponent as a function of detachment / attachment rate.

To develop a more physical understanding of this sub-diffusive behavior we develop a simple model of interactions of the bound octamers with the lipid packing defects (Figure 4.2D). We assume that the AH domains of octamers can form multiple attachments with the surrounding membrane compositions especially on curved membranes. Once octamers are attached, they can no longer diffusive and remain trapped. While when all the attachments are detached, octamer restarts its Brownian motion until it is trapped again. The kinetics of attachment and detachment is modeled by a pair of antagonistic rates: k^{att} and k^{det}, respectively. For simplicity, we assume k^{att} and k^{det} are independent of number of attachments. We also consider an upper-bound for the number of attachments, n and surface fraction of lipid packing defects, s. Furthermore we assume that octamers status follow a Markov chain which the probability of next time step status depend only on the current states. We then compute the time dependent probabilities of being in trapped and diffusive states by solving the involved differential equations. These probabilities are used to compute the time-dependent mean square displacement as a function of k^{att} and k^{det} and n. Thus, the mean square displacement can be calculated as

$$MSD = \frac{4DT}{1+s\left(1+\frac{k^{att}}{k^{det}}\right)\ln\left(1+\frac{k^{att}}{k^{det}}\right)n\left(sk^{att}+k^{det}\right)T} \qquad \text{(Eq. 9)}$$

where MSD is mean square displacement, D is diffusion coefficient, T is the elapsed time, k^{det} and k^{att} is detachment and attachment rate, s is surface fraction of defects, n is maximum number of attachments. This shows a linear scaling of mean square displacement at initial time, and a nearly zero slope at longer times which is consistent with our experimental observations (Figure 4.2B,C).

Building on our analytical model, we also developed a simulation to characterize the relationship between anomalous diffusion exponent, detachment/attachment rates, as well as the number of attachments. We find that by allowing septins to bind the membrane with a single attachment shows Brownian diffusion, whereas septins with multiple membrane attachment sites show sub-diffusive behavior when the ratio of detachment and attachment is lower than 0.2. These data suggest that when the number of attachments increases, the anomalous diffusion exponent decreases and finally decays to zero. Additionally, as the number of attachments increases, the ratio of detachment to attachment decreases, resulting in a longer lifetime of octamers on the membrane. This is consistent with our experimental data showing that as the dwell time of single octamers increases, the alpha exponent decreases. Therefore, diffusion would be much slower for a filament than an octamer as the number of attachments is roughly linear to length of filament. We speculate that the lower diffusivity of filaments could be used as a means to concentrate octamers coming from the bulk to areas on the membrane where polymerization has already occurred to further filament formation. This leads to the prediction that longer filaments may be found on optimum curvatures.

4.3.4 Septin filament length is influenced by membrane geometry

Filament formation is required for stable septin-membrane interactions in vitro and essential for septin function in vivo. Polymerization of octamers into filaments stabilizes septins'

interaction with the membrane, thereby dramatically extending their lifetime to ensure the absorption goes beyond octamer level equilibrium. Conversely, septin filaments can break into smaller filaments or individual octamers in a process termed fragmentation, thereby reducing the dwell time on the membrane (Figure 4.3A). To understand how polymerization and fragmentation might be influenced by curvature, we formulated an expression that links the activation energy of filament formation on a membrane to the elastic energy of the filament per bond using Arrhenius law

$$\Delta G = \Delta G_0 + k_b T l_p l_s \delta K^3 \qquad \text{(Eq. 10)}$$

where ΔG is the activation energy, ΔG_0 is the activation energy of polymerization on the membrane, $k_b T$ is Boltzmann's constant, l_p is the persistence length of septin filaments, l_s is the length of septin filaments, δ is the elastic force working distance, and K is curvature. This relationship predicts that as curvature increases, septin filament length should decrease due to fragmentation. To test this experimentally, we turned to an assay we previously developed to examine septin filament length and curvature at nanometer resolution. This approach uses scanning electron microscopy to image rods of various curvatures, coated with lipids and incubated with septins (Figure 4.3A). Consistent with our previous results, septin filament alignment on the rod is dependent on membrane curvature. Interestingly, we found that as curvature decreases, the filament length distribution shifts to longer filaments (Figure 4.3B), whereas at higher curvature (k >8 μm^{-1}), only octamers are present (Figure 4.3C), consistent with our prediction.

Next, we developed an analytical model to examine the relationship between, dwell time on the membrane, filament length, and fragmentation. Our dissociation model closely follows our multi-step sub-diffusion model (Figure 4.2D,E). Specifically, we assume that: i) the number

of attachments of septins are twice as the number of octamers in that filaments (two per octamer). We also assume that detachment rate of each site is given by the octamer's detachment rate. ii) Septin filaments will dissociate only when all these attachments are released. iii) We take into account that during its dwell time on the membrane a septin filament can fragment into shorter filaments and hence effectively reduce its dwell time and increase its dissociation rate. We can, then write down the probability distribution of these states and calculate the average dwell time as a function of the number of attachments and the ratio of octamer dissociation rate to fragmentation rate.

We find that when no fragmentation is allowed, the dwell time on the membrane increases exponentially with septin length (number of attachments). In the opposite limit of large frag- mentation rates, filaments break into octamers, thus, their dwell time is simply given by the product of the dwell time of a single octamers and logarithm of the number of attachments. These data show that filaments are much more stably associated to the membrane than single octamers which is consistent with our sub-diffusion model (Figure 4.2D,E) and experimental observations. We speculate that membrane curvature influences septin filament length by tuning the fragmentation rate of filaments either through an changing in interaction strength between joined septin octamers (potentially through a conformational change) or by causing septin filaments to bend unfavorably (if the curvature is too high).

4.3.5 Septin filament curvature is not influenced by membrane geometry or filament length

Next, we examined filament curvature on membrane-coated rods of different diameters. Interestingly, we found that filament curvature is independent of the membrane geometry with values between 2-3 μm^{-1} along the entirety of the rod. (Figure 4.3D). In contrast, the curvature of septin octamers is widely disturbed, suggesting that thermal fluctuations prevent the octamer

from stably orienting itself such that it does not have a preferred curvature. This results in the cumulative curvature distribution for the octamer to be much larger than for longer filaments (Figure 4.3D). Moreover, we find that septin filaments will take on a curvature between 2-3 μm^{-1} no matter what their filament length is. These data suggest that septin filaments of any length will align themselves such that their curvature is always the same, regardless of the membrane geometry

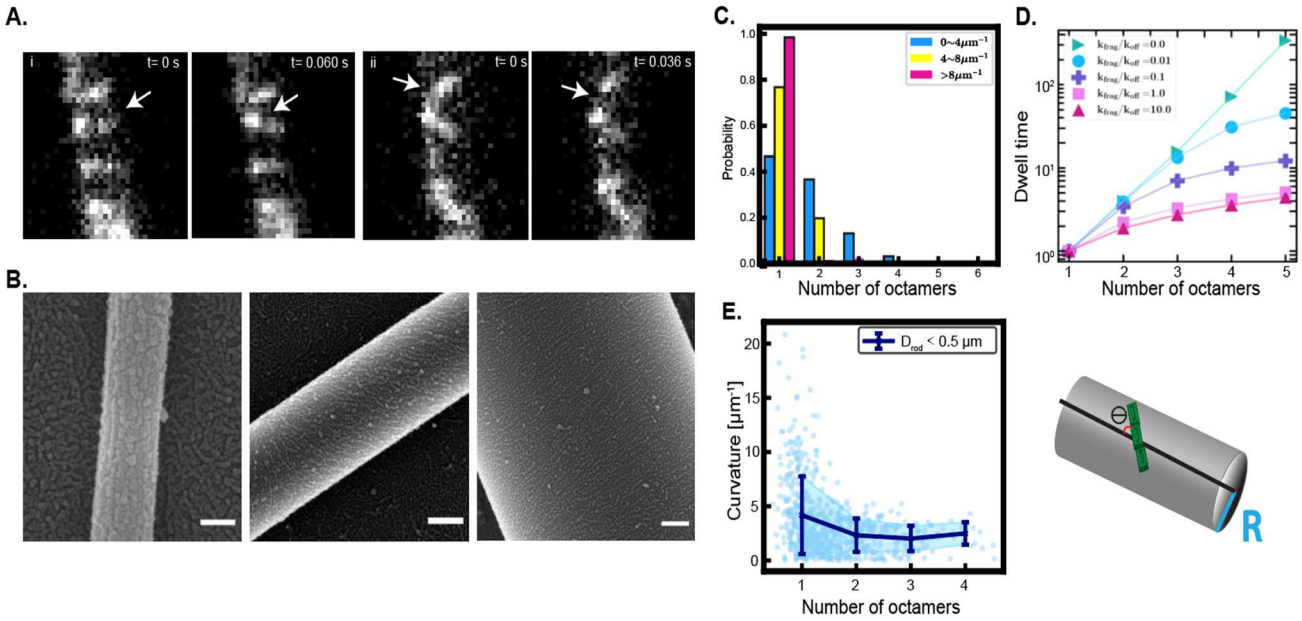

Figure 4.3 Septin filament length, but not curvature is influenced by membrane geometry (A) Representative TIRF images of septins undergoing fragmentation and annealing events on a membrane coated rod. (B) Representative scanning electron micrographs showing septin filaments bound to membrane-coated rods of different curvatures. Scale bars are 100nm, 200nm, and 200nm, respectively (C) Filament length distribution on rods of different membrane curvatures. Blue bars represent membrane curvatures ranging from k=0-4 μm^{-1}; yellow bars represent membrane curvatures ranging from k=4-8 μm^{-1}; Pink bars represent membrane curvatures greater than 8 μm^{-1}. (D) Disassociation rate of filaments as a function of filament length and fragmentation rate. From light-green to red-violet, the ratio between fragmentation and disassociation rate increases from zero to ten. The dwell time of one octamer is represented as one unit. (E) Septin filament curvature as a function of filament length (octamer number) on membrane coated rods with curvatures greater than k=4 μm^{-1}.

4.3.6 Septin assembly onto membranes is a multi-step process

Single octamer binding, diffusion, and filament formation are tightly linked reactions that work together to give rise to curvature sensitivity by septins. To integrate all of these steps into an ensemble reaction. We measured septin adsorption (assembly) onto beads of different membrane curvatures over time using confocal microscopy. Interestingly, plotting the adsorption of septins over time shows a sigmoidal behavior for all curvatures (Figure 4.4). This curve can be divided into three discrete stages: 1) flat domain 2) growth; 3) plateau. In the regime of the flat domain, adsorption is constant at a low level and represents the balance between association and dissociation of the octamer. Knowing that the time scale for the absorption of oligomers to reach the steady state is dissociation rate, and the dwell time of octamers is around 40 ms, the adsorption of octamers is quick to reach steady-state. If octamers were unable to polymerize into filaments, adsorption would stay at this low-level equilibrium indefinitely. Interestingly, septin assembly onto $k=2\mu m^{-1}$ beads shows a shorter lag phase before growth than septins assembling onto $k=0.4\ \mu m^{-1}$ beads at all tested concentrations (Figure 4.4A,B), suggesting that the "seeds" required for septin assembly form faster on $k=2\mu m^{-1}$. During the growth phase, septin adsorption exponentially grows until it reaches the inflection point. During this phase octamers bound to the membrane gradually polymerize, sharply increasing the dwell time on the membrane. As dissociation rate dramatically decreases, absorption starts to grow exponentially which implies that beyond the normal association flux, septins could grow through cooperativity, emerging from filament formation by providing more binding sites via septin-membrane and septin-septin interactions to recruit octamers from bulk onto the membrane. We find no difference in growth rates between the two membrane curvatures tested (Figure 4.4B), suggesting that the polymerization process from $k=2\ \mu m^{-1}$ and below might not be affected by curvature. However, we speculate that on higher

membrane curvaures $k > 2\mu m^{-1}$, we might see changes in growth rates due to higher fragmentation rates. Lastly, at the plateau phase, adsorption has reached steady state, as the beads are either fully occupied or the septins have run out of lipid packing defects for which to bind. Interestingly, we see higher adsorption values for membrane curvatures where $k=0.4\ \mu m^{-1}$ (Figure 4.4A,B) over $k=2\ \mu m^{-1}$, which is in contrast to what we have previously observed. However, these kinetic experiments were performed in the absence of competition (septins were exposed to only one membrane curvature at a time). We speculate that curvature preference for $k=2\ \mu m^{-1}$ emerges during competition through faster seeding events, such that the bulk septin concentration depletes leaving fewer septins to interact with other membrane geometries. However, the data presented here also suggests that the number of septins that can pack onto a given surface can be an important factor in driving adsorption, especially in high concentration regimes.

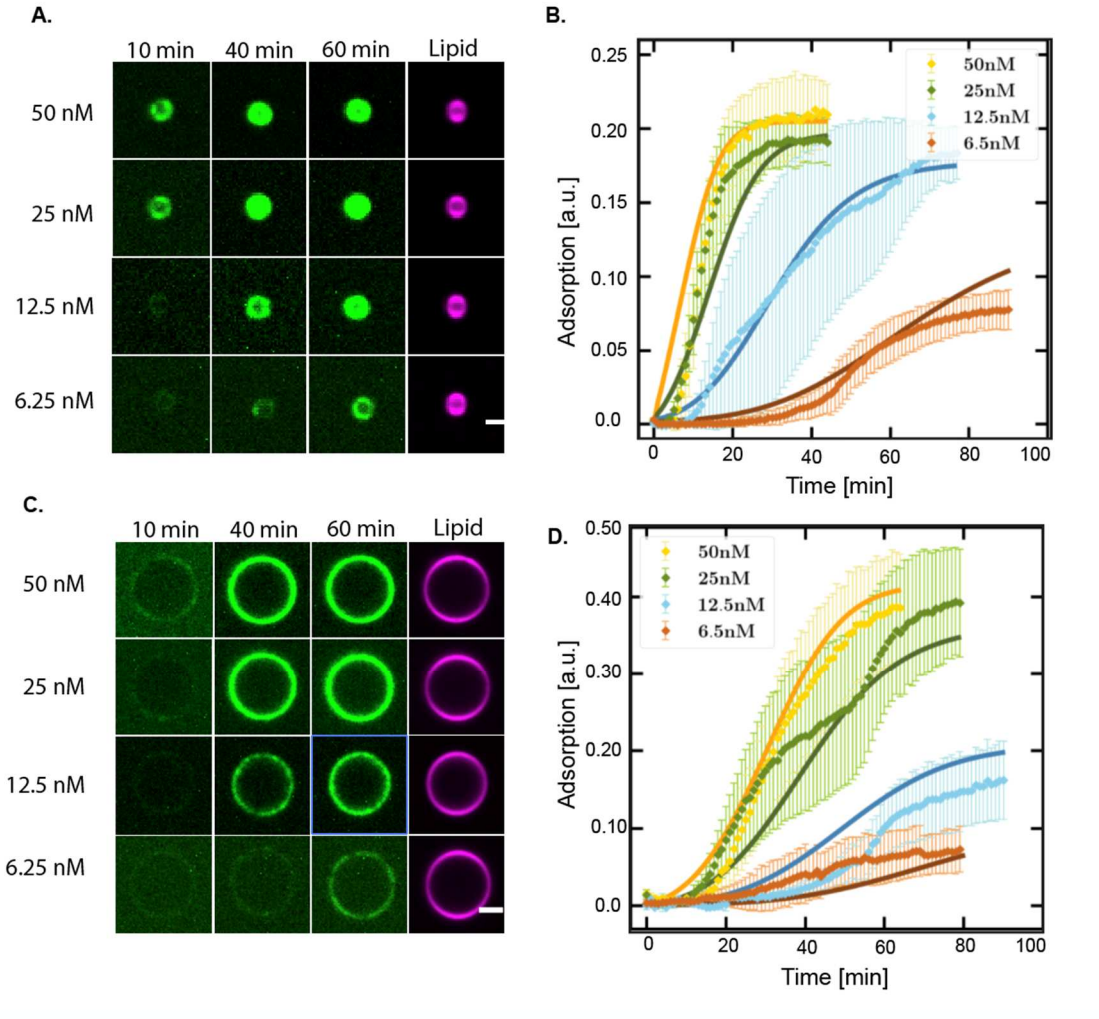

Figure 4.4 Septin assembly kinetics are influenced by membrane curvature
(A) Representative focal slices of septin (green) adsorption at various concentrations onto k=2μm^{-1} membrane coated beads as a function of time. Lipid channel in magenta. Scale bar 2μm. (B) Quantification of images shown in A. Blue line: 50 nM; Red line: 25 nM; Green line: 12.5 nM; Yellow line: 6.25 nM. Error bars highlight the standard deviation. (C) Representative focal slices of septin (green) adsorption at various concentrations onto k=0.4 μm^{-1} membrane coated beads as a function of time. Lipid channel in magenta. Scale bar 2μm. (D) Quantification of images shown in A. Blue line: 50 nM; Red line: 25 nM; Green line: 12.5 nM; Yellow line: 6.25 nM. Error bars highlight the standard deviation.

4.4 Conclusion and future work

In this study, we combined both experiment, modeling, and simulation approaches to understand how septins preferentially assemble on micrometer-scale membrane curvatures. We

find that many steps on the septin-membrane reaction coordinate are sensitive to changes in membrane geometry, however, all of these steps seem to change differently as the membrane bends. For example, single septin octamers where shown to increase their association rate superlinearly with membrane curvatures, suggesting that they would bind more frequently to membranes as the curvature becomes increasing more deformed (bent). In contrast, septin filaments are longer on micrometer-scale curvature, suggesting that these filaments are more stable on membrane geometries of this magnitude. Collectively, our data suggests that septin assembly regulated by individual, successive equilibria that work together to give a monotonic preference for membrane curvature. Future work will aim to integrate all of these steps into a model (analytically and simulation based) to explain the complete adsorption process that we observe in Figure 4 of this work.

CHAPTER 5

THE HIERARCHICAL ASSEMBLY OF SEPTINS REVEALED BY HIGH-SPEED AFM

Published in the *Nature Communications*, October 2020

AUTHORS: Fang Jiao, Kevin S. Cannon, Yi-Chih Lin, Amy S. Gladfelter, Simon Scheuring

Note: Experiments were performed by Fang Jiao. I helped prepare samples. Yi-Chih Lin performed simulations. The paper was written by all authors.

5.1 Introduction

Septins are a family of cytoskeletal GTP-binding proteins, conserved from fungi through humans (Pan, Malmberg and Momany, 2007) that have key roles in cell division, cell polarity, membrane scaffolding and remodeling (Gilden and Krummel, 2010; Mostowy and Cossart, 2012; Marquardt, Chen and Bi, 2019). Due to their diverse and crucial involvement in physiological processes, misregulation of septins has been related to cancers (Peterson and Petty, 2010), neurodegenerative diseases (Hall and Russell, 2004), microbial infections (Torraca and Mostowy, 2016; Van Ngo and Mostowy, 2019), and infertility (Hall, Russell and Pringle, 2008). All septins share a globular core consisting of a polybasic domain that has been suggested to function in lipid binding, a central GTP-binding domain (G-domain), and a septin unique element (Pan, Malmberg and Momany, 2007). The core is flanked by variable C- and N-terminal extensions, with a notable exception in yeast being Cdc10, which has only a very short C-terminus (alike other mammalian septins of the SEPT3 group) (John *et al.*, 2007; Sirajuddin *et*

al., 2007; A. Bertin *et al.*, 2008). Septins assemble into non-polar filaments through interactions between either adjacent G-domains (G-interface) or through N- and C-terminal helices from the globular core (NC-interfaces) (Sirajuddin *et al.*, 2007). The four essential septins in Saccharomyces cerevisiae form a linear palindromic hetero-octamer with the following organization: Cdc11-Cdc12-Cdc3-Cdc10-Cdc10-Cdc3-Cdc12-Cdc11 (A. Bertin *et al.*, 2008). We define this octamer unit as the unitary septin rod, which has a length of ~32 nm, and refer to it as rod in the remainder of the manuscript. These rods further assemble into filaments, filament pairs, and other higher-order structures (A. Bertin *et al.*, 2008; Oh and Bi, 2011). In vivo, higher-order structures form at sites of cell division (Haarer and Pringle, 1987; Bridges and Gladfelter, 2015), and act as scaffolds to recruit and interact with the actomyosin network that drives membrane ingression (Wloka and Bi, 2012; Finnigan, Booth, *et al.*, 2015). Septin function is often associated with filament formation (McMurray *et al.*, 2011), yet the mechanism of assembly is still unclear. Insights into the septin polymerization process have come from in vitro reconstitution methods using recombinantly expressed fluorescently tagged septins, planar supported lipid bilayers, and total internal reflection microscopy (TIRF) or FRET-based measurements in solution (Bridges *et al.*, 2014; Booth and Thorner, 2016). These microscopy-based data led to a model of diffusion-driven annealing for septin assembly, where septins first associate with the membrane, and through diffusion, collide endon to form linear polymers (Bridges *et al.*, 2014). Based on observations including filament length distribution, fragmentation events along the polymer, and the non-helical crystal structure of the human septin complex, it was proposed that septin assembly follows an isodesmic growth process. However, due to the limitations in lateral resolution, it was not possible to follow the earliest stages of septin filament formation from single rods. Thus, the fundamental mechanisms initiating septin

polymerization remain poorly understood. Although septin filaments are found associated with lipid membranes and the cytoskeleton, only the unitary rod is found in the cytosol of fungi and mammals (Sellin *et al.*, 2011; Bridges *et al.*, 2014). How septin rods associate with membranes and the cytoskeleton to promote filament formation is unclear. Up until recently, the septin polybasic domain had been suggested to be responsible for septin-membrane interactions (Aurelie Bertin *et al.*, 2010). However, the yeast septin Cdc12 contains a conserved amphipathic helix (AH) within its C-terminal extension (CTE) that binds membranes and is necessary for curvature sensing of septins (Cannon *et al.*, 2019). Interestingly, the polybasic and AH domains are located on opposite faces of the septin complex, raising questions as to how septins align on the membrane to promote septin-membrane and septin-protein interactions that give rise to the array of higher-order septin structures (Aurelie Bertin *et al.*, 2010; Garcia *et al.*, 2011b; Ong *et al.*, 2014). Understanding the fundamental mechanism of polymerization has been critical for understanding the biophysical properties and functions of the actin and microtubule cytoskeletons and thus the question how septins polymerize is a critical unsolved problem. Here, we investigate, using high-speed atomic force microscopy (HS-AFM) with molecular resolution, how septins polymerize and assemble into filaments and higher-order structures. We show that septin filament assembly is sensitive to environmental pH and ionic strength. The process is diffusion-driven, further favored by filament-alignment and -pairing. Pairing, mediated by the filament face exposing the N-termini, displays structural variability which is likely important in the formation of higherorder structures of varying shape. The filament face exposing the C-termini, notably the C-terminal of Cdc12, is evidenced to interact with lipids. Finally, septin assembly into higher-order structures involves templating by the underlying septin architecture.

5.2 Materials and Methods

Septin expression and purification.

Plasmids encoding either 6-His-TEV siteCdc12/Cdc10 or Cdc11/Cdc3 (Supplementary Table S3)19, we co-transformed into BL21 (DE3) Escherichia coli cells and selected for using chloramphenicol and ampicillin. Positive cultures were grown overnight in Luria-Bertani broth, chloramphenicol, and ampicillin. Cultures were then inoculated into one liter of Terrific Broth with chloramphenicol and ampicillin and grown to an O.D.600nm between 0.6–0.8. Cells were induced with 1 mM of isopropyl- β-D-1-thiogalactopyranoside for 24 h at 22 degrees Celsius. Cells were pelleted at 13,689 xg relative centrifugal force for 15 min. The pellet was re-suspended in lysis buffer (1 M KCl, 50 mM Hepes pH 7.4, 20 mM Imidazole, 1 mM MgCl2, 10% glycerol, 1% Tween-20, 1x protease inhibitor tablet, and 1 mg/ml lysozyme) on ice through vortexing every 5 min for 30 min. The lysate was sonicated twice on ice for 10 s with 2 min between sonication steps. The lysate was clarified through centrifugation in an SS-34 rotor at 47,807 g for 30 min. The supernatant was harvested, passed through a 0.44 μm filter, and incubated with 2 mL of equilibrated HisPur cobalt resin at 4 degrees Celsius for 1 h. The resin-lysate slurry was added to a gravity flow column. The resin was washed 4 times in 5 column volumes in wash buffer (1 M KCl, 50 mM Hepes pH 7.4, and 20 mM Imidazole). Septin complexes were eluted using elution buffer (300 mM KCl, 50 mM Hepes pH 7.4, and 500 mM Imidazole) and subject to two-step dialysis for 24 h into septin storage buffer (300 mM KCl, 50 mM Hepes, 1 mM β-mercaptoethanol) using a 100 K molecular weight cut off dialysis cassette. 60 μg of Tobacco Etch Virus protease was added to the cassette cleave the polyhistidine tag on Cdc12. After 24 h, purified septin complexes were run over a second HisPur cobalt resin and the

flow through was collected. Protein purity and concentration were assessed using SDS-PAGE and Bradford assay, respectively.

Sample preparation.

The purified protein was diluted to 100 nM septin with buffer containing 25 mM HEPES-NaOH, pH7.5, 600 mM (or 150 mM, and other concentrations of) KCl and 0.5 mM BME. Then 3 µl septin solution was immediately deposited on a 1.5 mm-diameter freshly cleaved mica (clean epoxy or silicon) and incubating for 5–50 min. Sample was gently rinsed with incubating buffer and imaging buffer. In situ assembly experiments were performed through subsequent addition of septin into the HS-AFM fluid cell during operation, to reach 60 nM final concentration. Lipid clusters were co-purified with septin, their observation and subsequent bilayer formation was performed in buffer containing 25 mM HEPES-NaOH, pH7.5, 750 mM KCl, 0.5 mM BME. To image filament pairing details with high contrast, setpin filaments were assembled in buffer containing 25 mM HEPES-NaOH, pH 7.5, 600 mM KCl, 0.5 mM BME, and imaged in high salt buffer conditions 750 mM KCl.

High-speed atomic force microscopy (HS-AFM)

All images in this study were taken using HS-AFM (SS-NEX; RIBM, Japan) operated in amplitude modulation mode using optimized scan and feedback parameters. The HS-AFM was steered using operation packages in IgorPro (WaveMetrics, USA). Ultra-short (8-µm) cantilevers (USC, NanoWorld, Switzerland) with nominal spring constant of 0.15 N/m, resonance frequency of ~0.6 MHz, and a quality factor of ~1.5 in imaging buffer (25 mM HEPES-NaOH, pH7.5, 150 mM KCl and 0.5 mM BME). Single septin subunit dissociation and association experiments s were performed in 25 mM HEPES-NaOH, pH 7.5, 2 mM CaCl2, 0.5 mM BME.

Negative-stain electron microscopy

Septin samples were prepared by pipetting ~5 µl of complex (following 10 min incubation of 100 nM septin in 25 mM HEPES-NaOH, pH 7.5, 600 mM (or 150 mM) KCl and 0.5 mM BME) onto carbon-coated glow-discharged electron microscopy grids. After 7 min grids were rinsed and negative staining was performed through addition of 2% phosphotungstic acid which was removed with a filter paper after 1 min. TEM was conducted on a 100- kV JEOL 1400 TEM microscope.

Data analysis

HS-AFM images and movies were drift corrected using a dedicated plugin in ImageJ52. Filaments angle distribution data (alignment) was extracted using the OrientationJ plugin in ImageJ, written by Daniel Sage and available at http:// bigwww.epfl.ch/demo/orientation/. Surface coverage of in situ experiments was determined by dividing the area covered by filaments with the total area (following thresholding between the mica surface and the thickness of a filament layer). In Figs. 1, 4 and 6, the angular distribution values are the average of the full width at half height (FWHH) of Gaussian fits of the filament orientation vector distributions of 3 images under each condition. The error bars of these values are ±1 standard deviation (SD) of the mean of the values from each image. In Figs. 1, 2, 4 and 6, the filament pairing values are the percentage of total filament length that is paired in each image from 3 images under each condition. The error bars of these values are ±1 standard deviation (SD) of the mean of these percentages from each image. The filament length was manually measured in ImageJ with edge enhancement.

Numerical simulation

The evolution of the septin filaments was calculated in MATLAB using a leapfrog algorithm based on the recurrence relation (Eq. 3) with $\Delta t = 1$ s and $j = 1–12$ (Schreck and Yuan, 2013).

$$f\ (t + \ \Delta t, j) + \frac{\Delta f(t,j)}{\Delta t}\ X\ \Delta t \qquad (3)$$

Here, we estimate the different septin adsorption rates from the surface coverage curve (Supplementary Table 5S1) to simulate the evolution of length histograms under varying experimental condition. At the end of the simulation, the population of j-mers at various times was normalized to 1, and then compared with the normalized experimental length histograms to calculate the sum of square error (SSE). The reported SSE was scaled to the number of experimental length histograms to eliminate the bias from different sampling size.

5.3 Results

5.3.1 HS-AFM allows detection of single septin molecules

Highspeed atomic force microscopy (HS-AFM) is a powerful tool for the investigation of biomolecular structures and dynamics such as protein assembly at high spatio-temporal resolution, ~1 nm lateral, ~0.1 nm vertical and ~100 ms temporal resolution, in physiological buffer and at ambient temperature and pressure (Kodera *et al.*, 2010; Igarashi *et al.*, 2011; Chiaruttini *et al.*, 2015; Miyagi *et al.*, 2016, 2018; Munguira *et al.*, 2016; Shibata *et al.*, 2017). Here, we took advantage of HS-AFM to visualize the assembly process of recombinantly-expressed septins from the budding yeast, Saccharomyces cerevisiae. We began by sampling different surfaces conducive for HS-AFM to evaluate if and how septins assemble. First, we deposited septin rods on hydrophobic epoxy or silicon surfaces and acquired highresolution data in which individual septin subunits were clearly resolved along rods and filaments (Fig. 5.1a). These filaments were rather short, with length ~100 nm, thus composed of only ~3 rods. We

tested a range of KCl-concentrations (from 150 mM to 600 mM) but did not succeed to visualize filaments of increased length or in higher-order assemblies on such hydrophobic surfaces. In contrast, on mica, which shares some properties of the yeast inner membrane leaflet surface such as hydrophilicity and negative charge, septin rods readily assembled into long filaments with lengths up to several micrometers (Fig. 5.1b, c), under certain conditions filaments readily paired (Fig. 5.1c, inset). This suggested that the mica support allowed septin filaments to assemble into higher-order structures. Thus, while future experiments on close-to-native bilayers will allow to decipher the details of the protein-membrane interactions, we decided to use this experimental platform to investigate septin filament formation and supramolecular assembly as a function of environmental factors such as monovalent ion (KCl) concentration, bulk septin concentration and pH (Fig. 5.1c, d). Note that in all experiments the filament orientation does not coincide with either the fast- (horizontal) or the slow- (vertical) scan axis of the HS-AFM scanning, and thus is not influenced by the imaging mechanism. According to previous studies, septin rods are stable in both high and low salt solutions (Frazier *et al.*, 1998; A. Bertin *et al.*, 2008; Weems and McMurray, 2017); in agreement, we rarely found objects smaller than the septin rod in our in situ HS-AFM frames (Fig. 5.1). Only in absence of monovalent ions, rod fragments and single septin subunits (300 mM) and elongated filaments were visualized from preparations dialyzed against low-salt buffers (<100 mM) (A. Bertin *et al.*, 2008). However, this discrepancy can be explained by the fact that we image septin assemblies on the mica surface and not in solution. Our control experiment using negative stain EM corroborate that in high salt concentration no filaments were found in bulk, while they formed at lower salt concentration either in bulk or were able to assemble during the negative staining procedure on the EM grid (Supplementary Fig. 5S3). In our HS-AFM experiments filaments formed on the surface, and as salt concentrations were

raised, electrostatic shielding of repulsive charges on the surface and/or between adjacent septin filaments likely promoted polymerization and pairing. While these conditions are higher ionic strengths than physiological bulk concentrations, we suggest that the relative charge between bulk and the surface is likely what is relevant and thus the high salt favors assembly on the mica, which is more negatively charged than the plasma membrane.

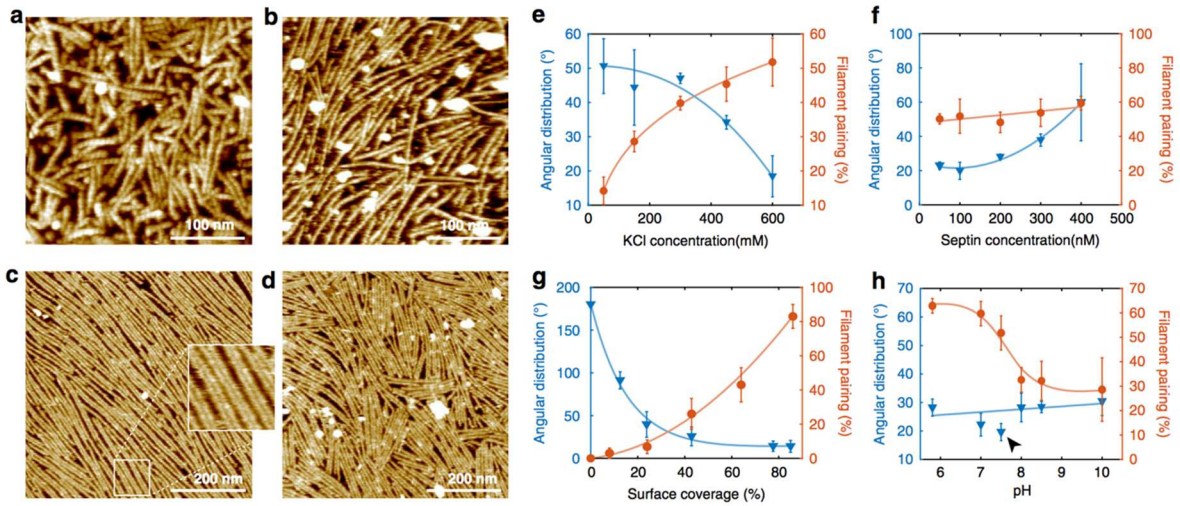

Figure 5.1 Septin filament assembly, alignment and pairing revealed by HS-AFM.
(a) Disordered septin filaments formed using 100 nM septin incubated for 10 min on a hydrophobic epoxy surface in presence of 600 mM KCl. (b) Septin filaments formed using 100 nM septin incubated for 10 min on mica in presence of 150 mM KCl.(c) Septin filaments formed using 100 nM septin incubated for 10 min on mica in presence of 600 mM KCl. Filaments display high packing order and pair formation. (d) Septin filaments formed using 400 nM septin incubated for 10 min on mica in presence of 600 mM KCl. Filaments pair but display limited orientation alignment. (e–h) Filaments higher-order analysis, filament alignment (i.e., angular distribution, where a low angular distribution corresponds to a highly ordered packing) and filament pairing as a function of KCl concentration (e), septin concentration (f), surface coverage (g) and pH (h). The standard condition of all data collection was 600 mM KCl, 100 nM septin, pH 7.5 and at a surface coverage of ~70%. The solid lines in panels e–h are spline fits (except for the linear fit of the angular distribution in h) to show the general trends of the data within the measurement conditions ranges). Data presented in e–h are mean ± s.d. from ≥3 different experiments.

5.3.2 Diffusion-driven septin filament assembly

We next investigated how changing the concentration of septins influences the organization of higher-order assemblies (Fig. 5.1f). We found that increasing septin bulk

concentration leads to decreased filament alignment, i.e., increased angular distribution (Fig. 5.1d), while it had no significant effect on filament pairing. This finding is typical for a diffusion-limited elongation process at a solid-liquid interface, where the increased availability of rods in the bulk to form seeds on a surface results in growth of locally aligned filaments without overall long-range order within the boundaries of a diffusion-driven annealing process. Thus, the degree of order within a large-scale higher-order septin assembly can be influenced by the surface deposition rate and molecular diffusivity, which are critical for the ensemble organization of septin structures. We next assessed the relationship between septin surface coverage, i.e., the encounter probability, and filament alignment and pairing. We hypothesized that pairing of filaments should be enhanced by the abundance of rods and filaments. We performed these experiments at 100 nM septin because higher bulk concentrations reduced long-range filament order. Pairing was limited at initial low surface coverage, where septin rods or short filaments formed at early stages of polymerization deposit in all orientations on the surface. However, with increasing surface coverage, filaments aligned and frequently paired (Fig. 5.1g). This suggests that long and aligned filaments sample more efficiently and find neighboring filaments for pairing, likely through avidity, where the engagement in many interactions favors further pairing. Additionally, individual septin filaments can serve as a template for the growth of a new filament, thereby creating paired filaments de novo (Fig. 5.2a, green arrows). Thus, the ability to pair is enhanced at higher septin filaments density through increased encounter frequency, engagement in bonds and/or templated assembly.

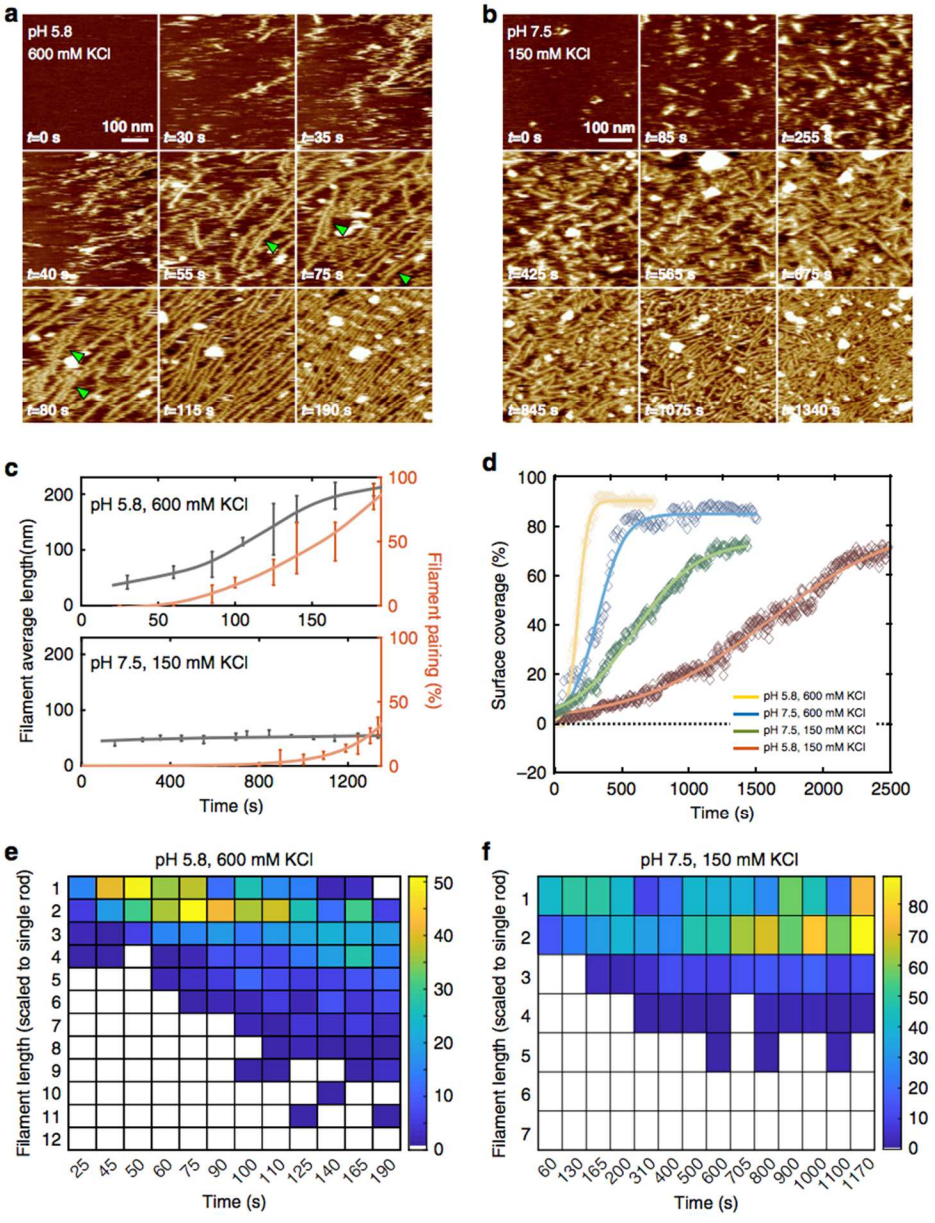

Figure 5.2. Kinetics of septin assembly imaged by HS-AFM.
(a) In situ HS-AFM frames in pH 5.8, 600 mM KCl (top left: imaging conditions; bottom left: image acquisition times) of the septin filaments assembly process. Filament alignment and pairing (green arrows) are established simultaneously. (b) In situ HSAFM frames in pH 7.5, 150 mM KCl (top left, imaging conditions; bottom left: image acquisition times) showing a much

slower assembly process resulting in shorter and less well aligned filaments. (c) Filaments higher-order analysis for (top: a) and (bottom: b), respectively. Data are presented as mean ± s.d. (d) Surface coverage as a function of time under varying conditions (150 mM or 600 mM KCl in pH 5.8 or pH 7.5 buffer). The solid lines are fitted sigmoidal curves. (e, f) Length histograms of septin assemblies as a function of time under conditions (a) shown in (e), and (b) shown in (f). Filament lengths were scaled to the rod length, 32 nm. False color bar: Filament count at each time point.

5.3.3 Septin filament pairing is sensitive to physiological pH

The presence of pairs (Fig. 5.1c, inset) rather than variable-sized filament bundles suggests that pairing is not simply due to crowding and alignment but is mediated by specific interfaces, as has been suggested by EM (Aurélie Bertin *et al.*, 2010). When changing the pH in the HS-AFM fluid chamber, we noticed that septin filament alignment was roughly pH-independent. In contrast, filament pairing was strongly pH-dependent (Fig. 5.1h). Pairing was favored at slightly acidic pH and disfavored at basic pH, with an inversion point around physiological pH. In addition, the only data point that is a notable outlier in the filament alignment analysis is also at pH 7.5, where best packing homogeneity was found (Fig. 5.1h, arrow). These results suggest that below pH 7.5 protonation of amino acids on the septins surface promoted filament pairing, thus suggesting that regions involved in pairing are protein moieties rich in Asp, Glu, and His. Moreover, the pH-dependence of filament pairing was not affected by the density of septins on the surface as we observed a lower frequency of filament pairs at higher pH despite high surface coverage (Fig. 5.1g, h). The fact that the pairing propensity is sensitive around pH 7.5 leads us to hypothesize that minor, physiologically-relevant pH changes might be a means to regulate higher-order septin assembly in cells. Altogether, the results indicate that septin filament assembly, stability, packing and pairing are modulated by charge and kinetics. Protein surfaces that contain negatively charged amino acids may engage in filament pairing and be charge-neutralized through protonation (at lower pH, Fig. 5.1h) and/or electrostatic shielding

(at high KCl, Fig. 5.1e). Filament alignment occurs through two-dimensional orientational adjustments, whereas filament pairing and the ultimate long-range order in the assemblies depend on the number of initial molecular deposition sites and the assembly kinetics (Fig. 5.1f, g).

5.3.4 Septin assembly kinetics

We next investigated the assembly kinetics in time-lapse HS-AFM experiments. Based on the results of the experiments shown in Fig. 5.1, we monitored assembly at pH 5.8 or pH 7.5 and in the presence of 150 mM KCl or 600 mM KCl (Fig. 5.2; Supplementary Fig. 5S4). As a reminder, lower pH and higher salt concentration favored filament assembly and pairing. The septin concentration was kept constant at 60 nM in all experiments, which is in the same order of magnitude as physiological concentrations (Bridges *et al.*, 2014). In elevated ionic strength buffer at slightly acidic pH, filament elongation and pairing occurred basically concomitantly with the rapid surface-binding of septins (Fig. 5.2a). Once filaments were assembled, additional filaments grew in their vicinity and formed pairs (Fig. 5.2c, top). The entire process was completed within ~3 min and led to the formation of long, well aligned filaments (Fig. 5.2a, c). The assembly process critically depended on the surface coverage rate (Fig. 5.2d, yellow trace) and the subsequent filament growth through surface diffusion (Fig. 5.2e), as we never observed filaments in solution under similar conditions when investigating the bulk by negative stain EM (Supplementary Fig. 5S3a). The length histogram (Fig. 5.2e) highlights several features in the evolution of septin assembly. First, the most populated septin filament length rapidly shifts from single rod (25–60 s) to short filaments with length ≥100 nm (a detailed filament length analysis of t = 190 s is shown in Supplementary Fig. S5). Notably, septin single rods are not found anymore on the surface at the end of the growth experiment (Fig. 5.2e, right of first row),

indicating that new rod adsorption directly advances growth of preexisting filaments. Second, longer filaments, >100 nm, develop mainly after the most populated size was larger than two rods (t = ~75–90 s), and their existence distorts the shape of the length distribution with a positive skewness for a long tail, where the longest filaments exceed 300 nm (limited by the scan area for high-resolution HSAFM movie acquisition). The length-distribution skewness provided evidence that the mechanism of septin surface self-assembly comprised not only diffusion-driven end-on annealing of rods to filaments, but also annealing of filaments to preexisting filaments37. In these conditions, the average growth rate peaks at t = ~80 s (Fig. 5.2d), concomitant with the onset of filaments alignment and pairing (Fig. 5.2a, c, orange trace). Thus, we propose that well-aligned filaments promote growth of other filaments by reducing the dimensionality of diffusion from two to one in the confined space and through pairing (Fig. 5.2a, green arrowheads). Finally, the septin filaments on the surface were stable and no fragmentation events were observed after the surface was fully covered. Given the enhanced surface coverage under conditions that promote filament pairing (low pH and/or high salt), we speculate that pairing may influence assembly kinetics by serving as polymerization templates for new septin filaments (Fig. 5.2a, green arrows). These analyses were also performed on septin assembly movies in low salt buffer and neutral pH conditions, where septin surface recruitment and assembly was much slower and final filaments were shorter and not well aligned (Fig. 5.2b). Filament average length was nearly constant and remained very short during the entire assembly process and pairing only occurred after ~15 min incubation and only to a minor extent (Fig. 5.2c, bottom). The low ionic strength buffer critically delays the surface coverage rate (Fig. 5.2d, green trace), and the length histograms (Fig. 5.2f) display filament growth rate is slow and only few medium-long filaments ~120 nm (~4 rods) develop in such conditions. In the final state, the observed filaments lie in all

orientations and are short, the most populated length is ~60 nm (~2 rods) and isolated septin rods are still abundant. Polymerization is clearly minimized, leading to surface coverage with non-ordered short filaments and rods which in turn likely further confine lateral diffusivity of adsorbents and thus the elongation of septin filaments is limited. Similar phenomena were observed in low ionic strength buffer at slightly acidic pH (Supplementary Fig. 5S4), supporting the same idea that decreased salt concentrations lead to slower surface coverage rate (Fig. 5.2d, orange trace) and decreased assembly (Supplementary Fig. 5S6), associated with diminished filament order. Surface coverage versus time traces displayed a sigmoidal shape (Fig. 5.2d), indicating a saturation of the available surface for adsorption was reached. Thus, electrostatics influence the rate of adsorption and subsequent order that emerges in a population of filaments, which in turn impacts the length-scale of filaments and the higher-order assembly.

5.3.5 Simulations support that filament alignment promotes diffusion-driven annealing

Leveraging the high spatial and temporal resolution of HS-AFM, we observed septin assembly dynamics from rod surface adsorption to the growth of filaments of various lengths (Fig. 5.2, Supplementary Fig. S4). The resulting septin length histograms over assembly time (Fig. 5.2e, f) displayed signatures, i.e., the skewness with a tail corresponding to long filaments, indicative of the balance between molecular adsorption and diffusion-driven annealing (Shibata *et al.*, 2017). Therefore, we investigated if the observed assembly kinetics data could be modeled within the framework of a diffusion-driven annealing model comprising two elementary growth steps, single rod addition and filament-filament elongation (Fig. 5.3a). The mass balance equation can be expressed as Eq. 1 (Lin, Li and Fakhraai, 2018)

$$\frac{\partial f(t,j)}{\partial t} = \frac{\partial}{\partial t}\left[\frac{a}{1+e^{-b(t-c)}}\right] \cdot \delta_{j,1}$$

$$+2K(1,j-1)f(t,1)f(t,j-1) - 2K(1,j)f(t,1)f(t,j) \qquad (1)$$

$$+\sum_{i=2}^{j-2} K(i,j-i)f(t,i)f(t,j-i) - \sum_{k=2}^{\infty} K(j,k)f(t,j)f(t,k)$$

where f(t, j) denotes the surface density (unit: μm−2) of septin assemblies of size j-rods at time t. K(r, s) is a size-dependent, diffusion-driven annealing rate constant for two septin reactants with sizes r-rods and s-rods, respectively. Equation 1, line 1, describes the adsorption rate of septin rods as depicted by the slope of surface coverage traces (Fig. 5.2d) fitted by a sigmoidal curve with three parameters, a, b, and c (Supplementary Table S1). Given the known dimensions of the septin rod and the HS-AFM scanning area, we can estimate the rod surface density at any time point as the molecular input for diffusion-driven filament growth steps. Concurrently, septin filament growth is governed by K(r, s) and the surface density of two septin reactants (r-rods and s-rods) via, single rod addition (Eq. 1, line 2); r = 1 and s = j−1; Fig. 5.3a, red arrows), and filament-filament elongation (Eq. 1, line 3); r = i, s = j−i, and i, j ≥ 2; Fig. 5.3a, blue arrows). The negative sign of second terms indicates the decrease of the j-rod population through the growth steps. The diffusion-driven annealing rate, K(r, s), can be referred to as a generalized sum kernel and expressed as in Eq. 2 (Krapivsky, Redner and Ben-Naim, 2011; Schreck and Yuan, 2013; Lin, Li and Fakhraai, 2018):

$$K(r,s) = k_P(r^{-\alpha} + s^{-\alpha}) \qquad (2)$$

where k_P (unit: $\mu m^2 s^{-1}$) is a composite factor and related to the diffusivity of septin assemblies for self-assembly, and the changing diffusivity due to alignment of surface reactants, during polymerization. The negative exponent, −α, of the size parameters can be considered as a mobility exponent of septin assemblies of different size. This generalized sum kernel suggests that septin rods and short filaments contribute more to K(r, s) due to their larger effective

diffusivity (Fig. 5.3a, green circle regions), and it simplifies the free fitting parameters to α and k_P in our proposed model.

Using a leapfrog algorithm (see Methods) we simulated the evolution of length histograms under different experimental conditions with various combinations of α and k_P values based on Eqs. 1 and 2. We then calculated the sum of square error (SSE) between simulation results and experimental data to determine the goodness of the simulations, and thus determine the best-fit parameters. In the conditions of elevated ionic strength and slightly acidic pH, the SSE map readily indicates a global minimum SSE of 0.19 when $\alpha = 5.6$ and $k_P = 1.8 \times 10^{-5}$ μm^2 s^{-1} (Fig. 5.3b, red star). With the best-fit parameters, simulated length histograms (Fig. 5.3c, red lines) describe well the growth of the most populated septin filament length, and reproduce the positive skewness with a long tail in experimental length histograms (Fig. 5.3c, colored bars, after 90 s). Herein, the negative size exponent terms in K(r, s) in Eq. 2 plays a critical role to modulate the skewness of the length distributions and enhances the growth of leading length away from the most populated length via filament-filament elongation (Eq. 1, line 3).

At low salt and neutral pH, the SSE map also shows a semiglobal minimum SSE of 0.32 when $\alpha = 5.6$ and $k_P = 9.1 \times 10{-}7$ μm^2 s^{-1} (Fig. 5.3d, red star). The relatively large SSE is attributed to the differences between simulation and data where the first predicts the growth of longer filaments after 600 s that are missing in the experimental data (Fig. 5.3e, color bars). This disparity can be explained by the fact of that our model only considers an ideal case without the impacts of crowding of rods and short filaments of varying orientation in the diffusion-driven annealing rate. Thus, the k_P in the low pH/high salt conditions is ~20 times larger than in neutral pH/low salt, which indicates that the good alignment of surface reactants in the first case promotes the polymerization process. We performed the same numerical simulations for the low

pH/low salt and neutral pH/high salt conditions (Supplementary Fig. 5S6), which exhibited different degrees of filament alignment disorder (Supplementary Fig. 5S4), and received kP values that are proportional to the filament alignment in these conditions and are between the values obtained for the low pH/high salt and neutral pH/low salt conditions (Supplementary Table 5S2). Therefore, we concluded that the filament alignment order, effectively reducing the diffusive dimension in the diffusion-driven annealing process, has strong influence on polymerization.

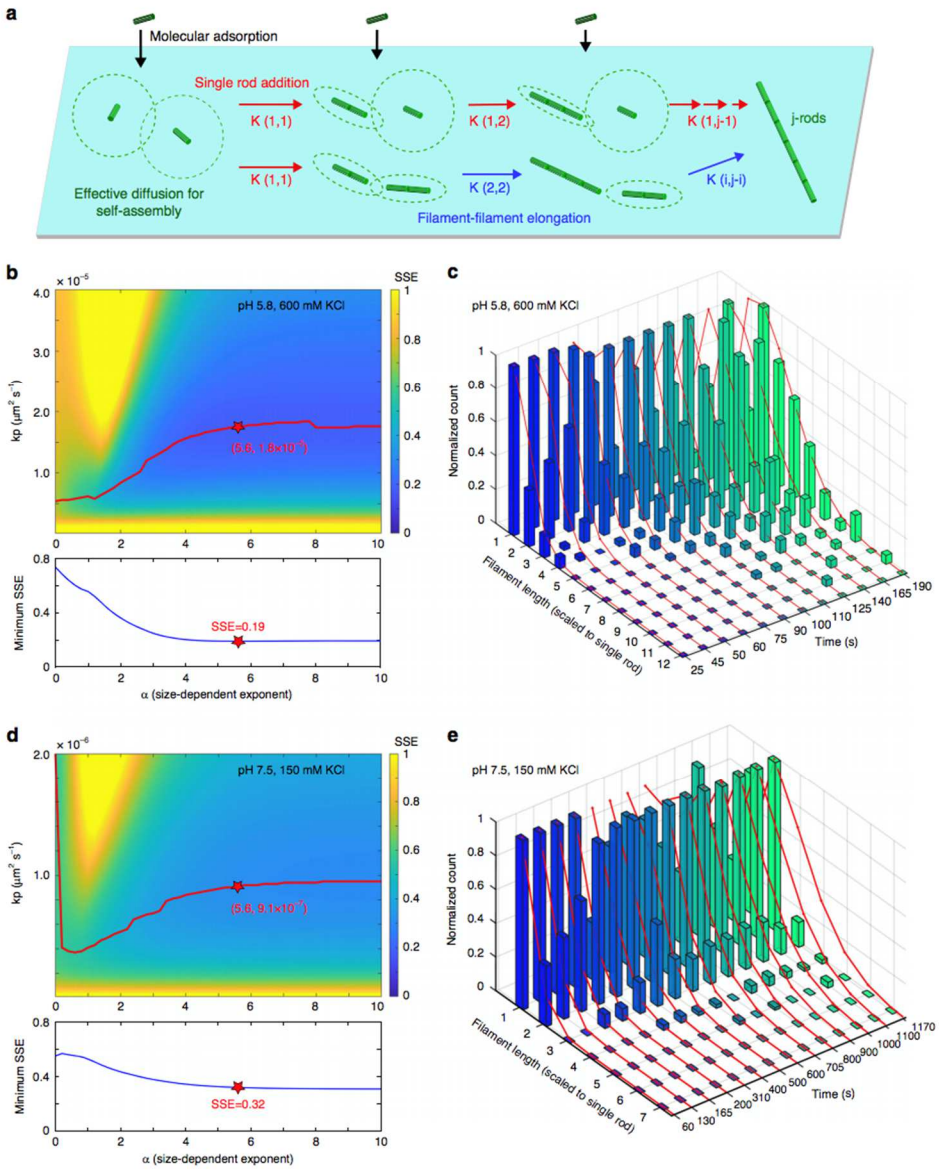

Figure 5.3 Simulated length histograms based on a diffusion-driven annealing model
(a) Schematic of the diffusion-driven annealing model through single rod addition (red arrows) and filament-filament elongation (blue arrows). The diffusion-driven annealing rate, K, depends on the effective diffusion of surface reactants (illustrated by the size of the green dashed circles) for anisotropic self-assembly based on Eq. 1 & 2. (b), (d) (top) Sum of squared error (SSE) maps between experimental and simulated length histograms, the latter simulated using various k_p (a diffusion-related constant) and α (a size-dependent factor) values, to fit the experimental data at different conditions (600 mM KCl in pH 5.8 buffer (b), 150 mM KCl in pH 7.5 buffer (c)). The red trace depicts the path of kp at different α values with minimum SSE. Bottom: The minimum SSE at each α value. The red star indicates the best-fit parameters at α = 5.6 that offer the global minimum SSE in all conditions. (c, e) The comparison between the experimental (bars) and simulated length histograms (red curves), which are calculated by the best-fit parameters at α = 5.6.

5.3.6 Evidence for interaction of the Cdc12 C-terminal domain with lipids

When septin filament assembly was imaged at high resolution in high KCl concentrations, periodic dots could be observed at the filament sides (Fig. 5.4a, white arrowheads). These clusters always occurred on the same side of a given filament and located on the outside of both filaments in paired filaments (Fig. 5.4a, yellow arrowheads). To our surprise, we also found small lipid clusters in the negative stain EM of the same septin sample (Supplementary Fig. 5S7), thus we concluded that lipids, its natural binding partner, were co-purified with septins(Palsdottir and Hunte, 2004; Akil *et al.*, 2016; Gupta *et al.*, 2018). The fact that the lipid clusters located on the outer faces of paired filaments suggested that membrane binding sites and filament pairing sites were mediated by different protein moieties on opposing faces of the septin filaments. To evaluate what part of the septins interacted with lipids, we analyzed the periodicity of the initial lipid clusters, and septin filaments composed of deletion mutants of the C-terminal extensions of Cdc11, Cdc12 or Cdc3 (Cdc11- ΔCTE, Cdc12-ΔCTE, Cdc3-ΔCTE). Similar to wild-type rods (Fig. 4a), only Cdc11-ΔCTE filaments exhibited the clusters, while filaments with Cdc12-ΔCTE or Cdc3-ΔCTE showed bare filaments (Fig. 5.4b). The periodicity of lipid clusters on wild-type septin filaments was ~32 nm (i.e., the length of the rod), while filaments of Cdc11-ΔCTE revealed an average of ~20 nm between clusters with a somewhat wider distribution (Fig. 4c). We cannot interpret this difference with certainty, but note that a periodicity of ~20 nm in the Cdc11-ΔCTE filaments is consistent with the distance between Cdc12s and/or Cdc3s (both having inter-subunit distances of 16 nm and 24 nm in the palindromic filaments). A recent work identified an amphipathic helix in the CTE of Cdc12 (Cannon *et al.*, 2019), consistent with lipid binding capacity. The lipid clusters appear very close to the filaments in the HS-AFM images, while the amphipathic helix in the CTE could possibly

be distant. This is explained with the AFM-tip convolution that gives the filaments a wider appearance and/or with the flexibility of the CTEs and the lipid clusters.

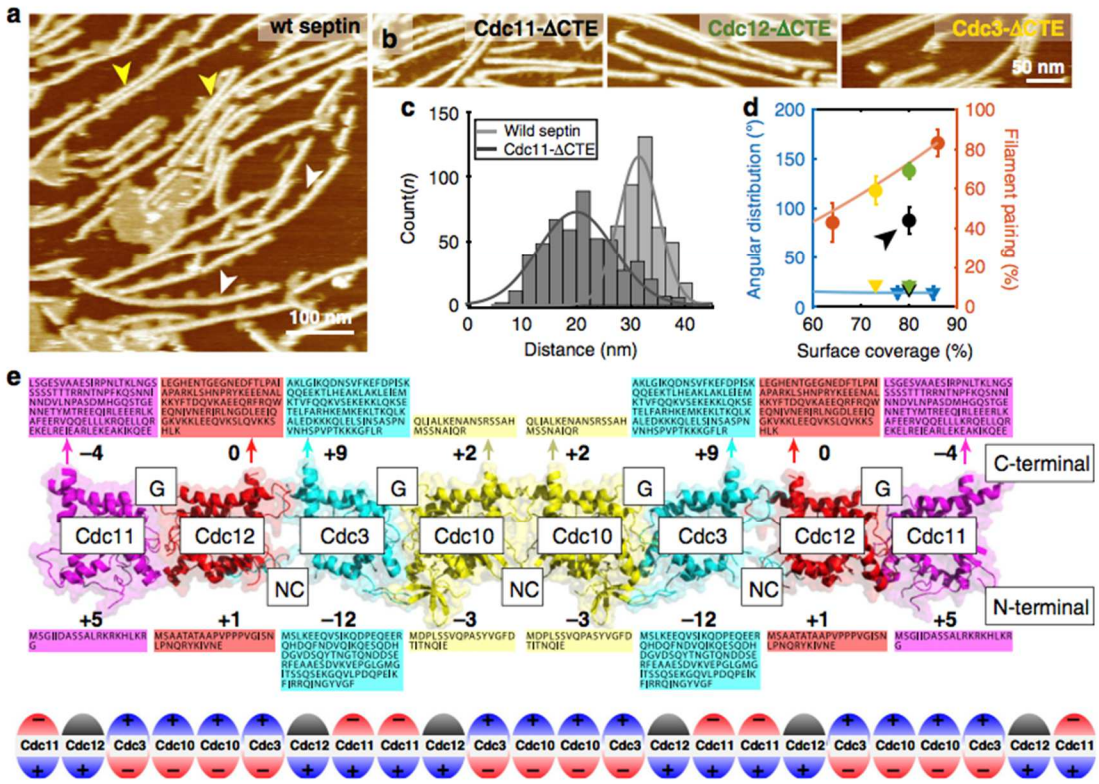

Figure 5.4 Septin filaments bind lipid with the C-terminal face and pair on the N-terminal face

(a) Wild-type septin filaments periodically recruit small lipid clusters on one side of individual septin filaments (white arrowhead), and on both outer faces of paired filaments (yellow arrowheads). Occasionally, these lipid clusters fused on the surface (center of the image). (b) Septin filaments with C-terminal deletion mutants Cdc11-ΔCTE, Cdc12-ΔCTE or Cdc3-ΔCTE septins: Only filaments containing Cdc11-ΔCTE recruit lipid clusters, but display slightly diminished pairing. (c) Distance distribution between lipid clusters recruited by wild-type septins (~32 nm), and Cdc11-ΔCTE (~20 nm). (d) Filament alignment (triangles) and pairing (circles) containing Cdc11-ΔCTE (black), Cdc12-ΔCTE (green) and Cdc3-ΔCTE (yellow), compared to wild-type filaments. Data are presented as mean ± s.d. from ≥ 3 different experiments. (e) Structural model of the yeast septin hetero-octamer rod generated by aligning of the crystal structure of Cdc11 (PDB: 5AR1), and models of Cdc12, Cdc3, and Cdc10 to the crystal structures of in the human hetero-hexamer rod septin-9 (PDB ID: 5CYP), septin-7 (PDB ID: 2QAG), and septin-3 (PDB ID: 4Z54). Boxes display N- and C-terminal sequences, respective (arrows indicate where C-termini protrude from α6 of the respective subunits). The bold numbers indicate the net charges of the surface exposed structurally unresolved termini. Bottom: Schematic of the charge distribution along a septin filament

5.4.7 Septin filaments have a patterned charge distribution

The polarity of lipid association and pairing to opposite faces of the septin filament, along with the conclusions provided by the condition-dependent assembly data shown in Fig. 5.1, prompted us to build a structural model of the yeast septin rod, including the charge properties of the terminal extensions that are not resolved in the X-ray structures (Fig. 5.4e). First, we aligned the structures of yeast Cdc3, Cdc10, and Cd12 with the human septins septin-7, -3, and -9 (PDBs: 2QAG, 4Z54, 5CYP), of which the structures were solved in the context of the hexameric human rod (Supplementary Fig. 5S8a). Adding to this hexameric rod model the yeast Cdc11 (PDB: 5AR1) (Brausemann *et al.*, 2016) through structural propagation of the G-interface as in between Cdc10 and Cdc3, we built a full yeast septin rod structural model and investigated the surface exposed charges and found that the modeled yeast septin hetero-octameric rod showed nearly neutral surface charges on all faces (Supplementary Fig. 5S8b). However, all these structures lack the N- and C-terminal extensions. Thus, we analyzed the N- and C-terminal sequences extending from the structural model and calculated the net charges of these unresolved structural elements (Fig. 5.4e). We found that Cdc3 and Cdc11 had very interesting charge distributions of the N- and C-termini with −12/+9 for Cdc3 and +5/−4 for Cdc11 (and to a lesser extent Cdc10 with −3/+2). Importantly, if these charge distributions along the rod are considered in the context of a long palindromic filament, an alternating pattern of inverted charge distributions is to be expected (Fig. 5.4e, bottom). In such a filament context, positive charges dominate around Cdc3-Cdc10-Cdc10-Cdc3 intercalated by negative charges around Cdc11-Cdc11 on the C-terminal side, and inverted charges on the N-terminal face.

From the experiments varying environmental pH and ion concentration shown in Fig. 5.1, we know that regions involved in filament pairing are protein moieties rich in negatively charged

amino acids, which are found in the N-termini of Cdc10 and Cdc3. On the other hand, filaments comprising C-terminal deletions of Cdc12 or Cdc3 could not recruit lipid clusters. These data suggest the filament pairing face is the N-terminal and the membrane binding is the C-terminal face. Note, the overall net charge of the C-terminal face is positive and thus favorable to bind to negatively charged lipids of the inner membrane leaflet. This arrangement places the strongly negatively charged N-termini of the Cdc3-Cdc10-Cdc10-Cdc3 stretch on the other face, ideally to engage into filament-filament interactions. The flexibility of the CTE of Cdc11 may contribute to inter-filaments contacts, as its absence weakens filament paring ability (note, it is also slightly negatively charged).

5.3.8 Variability of filament pairing interactions

Given that filament pairing occurred early and should therefore be an important step in the formation of higher-order septin structures, we next investigated molecular-level details of the inter-filament interaction (Fig. 5.5a). As expected, we found a uniform length periodicity of ~32 nm along all filaments, representative of the length of the hetero-octameric rod (Fig. 5b). In agreement with previous EM studies (A. Bertin *et al.*, 2008), we found filament pairs where the subunit periodicity of the two interacting filaments matched (Fig. 5.5a, vertical dashed line; Fig. 5.5c), while other filaments paired with a phase shift, i.e., subunits of interacting filaments were mismatched (Fig. 5.5a, tilted dashed line, Fig. 5.5d). The mismatch distance was about 4 nm, corresponding to the length of one septin subunit, i.e., half of the distance between NC-interfaces. Based on these observations, we propose alternative models where septin filament pairing is mediated by N-terminal domains precisely facing each other or in a configuration where they intercalate at the NC-interface locations. The HS-AFM resolution is however only molecular, and we cannot distinguish which subunits face each other. Indeed, given that Cdc10

and Cdc11 have opposite charges on the N-terminal faces, it is appealing to suggest that these subunits pair in the matched filament pairs (Fig. 5.5c, d, molecular models). While isolated filaments may appear enlarged due to AFM-tip convolution, the precise inter-filament distance can be assessed when measuring the top-to-top distance of closely associated filament pairs. These distances were always little (if any) space between paired filaments (Fig. 5.5e). This is different from previous EM observations where neighboring filaments exhibited a railroad track-like appearance with a 15- to 25-nm gap (A. Bertin *et al.*, 2008) The variability of filament pairing interactions is likely of importance in the formation of higher-order structures, especially those that are bent. In any bent higher-order structure the filament positioned in an outermore location (with larger radius of curvature) will have a longer path than a filament located closer to the center of a curved structure. Thus, pairing variability may be a prerequisite for septins to accommodate to curved structures.

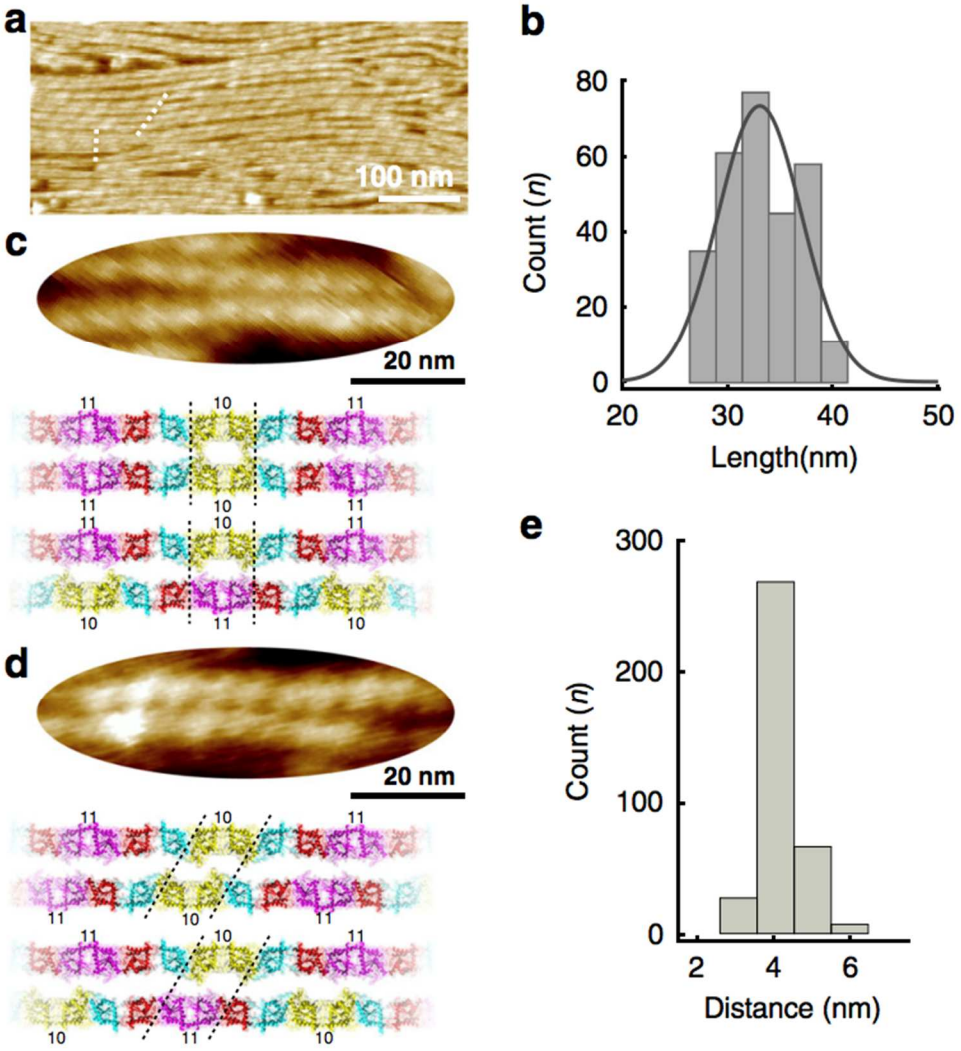

Figure 5.5 Variability of filament pairing
(a) Septin filament pairing exhibit subunit interaction match and mismatch in the same field of investigation.(b) Periodicity length distribution of interacting elements peaking at ~32 nm, i.e., the length of the hetero-octameric septin rod. High-resolution images of (c) matched and (d) mismatched filament pairs. Bottom in (c) and (d): Structural models of matched and mismatched rod interactions. The HSAFM resolution does not allow to distinguish the precise nature of the septin subunit, cases where Cdc10 (label 10) and/or Cdc11 (label 11) face each other are illustrated. (e) Histogram analysis of the top-to-top distance of the filaments in filament-pairs peaking at ~4 nm

5.3.9 Template-controlled 3D-growth of septin filaments

Once a surface was fully covered with aligned and paired septin filaments, we detected additional topographic features on top of the layer of filaments (Fig. 5.6a). These blurry surface features had a periodicity of ~30 nm (Fig. 5.6b), coinciding well with the length of single septin rods, evidence that either Cdc11 or Cdc10 was involved in the recruitment of an additional protein layer (as a reminder, the repetitive palindromic rod sequence is Cdc11-Cdc12-Cdc3-Cdc10-Cdc10-Cdc3-Cdc12-Cdc11). We interpret these protrusions associated to the base septin filament layer as initial septins that may serve to template a second septin layer. Thus, we next investigated how septins assembled into 3Dstructures using HS-AFM experiments of long duration (Fig. 5.6c). First, based on our experiments as displayed in Figs. 5.1 and 5.2, we let a single layer of highly orientated filaments form as a template (Fig. 5.6c, t = 0 min). Then, fresh septin in low salt buffer was added to the template layer to allow assembly of a second layer. We observed that septin filaments started to assemble on top of the first layer (Fig. 5.6c, t = 70 min), until full surface coverage was reached again (Fig. 5.6c, t = 310 min). After establishment of the second layer, filaments initiating a third layer were observed (Fig. 5.6c, t = 310 min, arrowhead). We found that, in contrast to the formation of the first layer that formed on mica under a variety of conditions but most efficiently at high KCl (600 mM), only a narrow window of low salt concentration (<200 mM) permitted the formation of multilayered hierarchical structures (Fig. 6d). The assembly rate of additional layers was fastest in buffer containing ~85 mM KCl. In general, the assembly rate of the second layer was always lower than that of the first layer. We interpret these findings in the following way: The conditions for the second layer growth is based on native-like protein-protein interactions and performs best under physiological conditions, while the assembly on the mica (that also works under such physiological ion concentrations) is

faster under higher ionic strength due to the high surface charge of the mica surface. The templating relationship between first- and second-layer filaments is quantitatively assessed with an ~80% angular correlation (i.e., 80% of filaments in second layer align with the bottom layer), independent of the surface coverage of the second layer (Fig. 6.6e). Interestingly, we found that the second layer has better angular alignment at low surface coverage than the template layer had during formation (Fig. 6f, left), evidence that the first layer readily serves as an alignment template for a more dispersed second layer of filaments. Upon full second layer coverage, the packing orientation is relatively homogeneous, but not as tight as that of the first septin layer (Fig. 5.6f, right), and filament pairing is much less pronounced in the second compared to the first layer, likely a signature of establishing vertical interactions at the price of lateral interactions (Fig. 5.6f, right).

These experiments suggest that the assembly of multilayered architectures is a complex process that is strongly influenced by lateral and vertical interactions between septin layers. While the first layer aligns and pairs almost perfectly, the higher-order assembly is guided by the underlying layer but is overall less ordered, likely leading to a more and more complex and possibly disordered network as more layers are added. The decrease of filament pairing in the second layer indicates that the filament-filament interaction surface between layers and between filaments within one layer are likely the same, thus already occupied by second-layer filaments with their partners underneath not allowing lateral pairing. This concept raises the question, which we cannot answer, whether first-layer filaments remain paired upon growth in 3D.

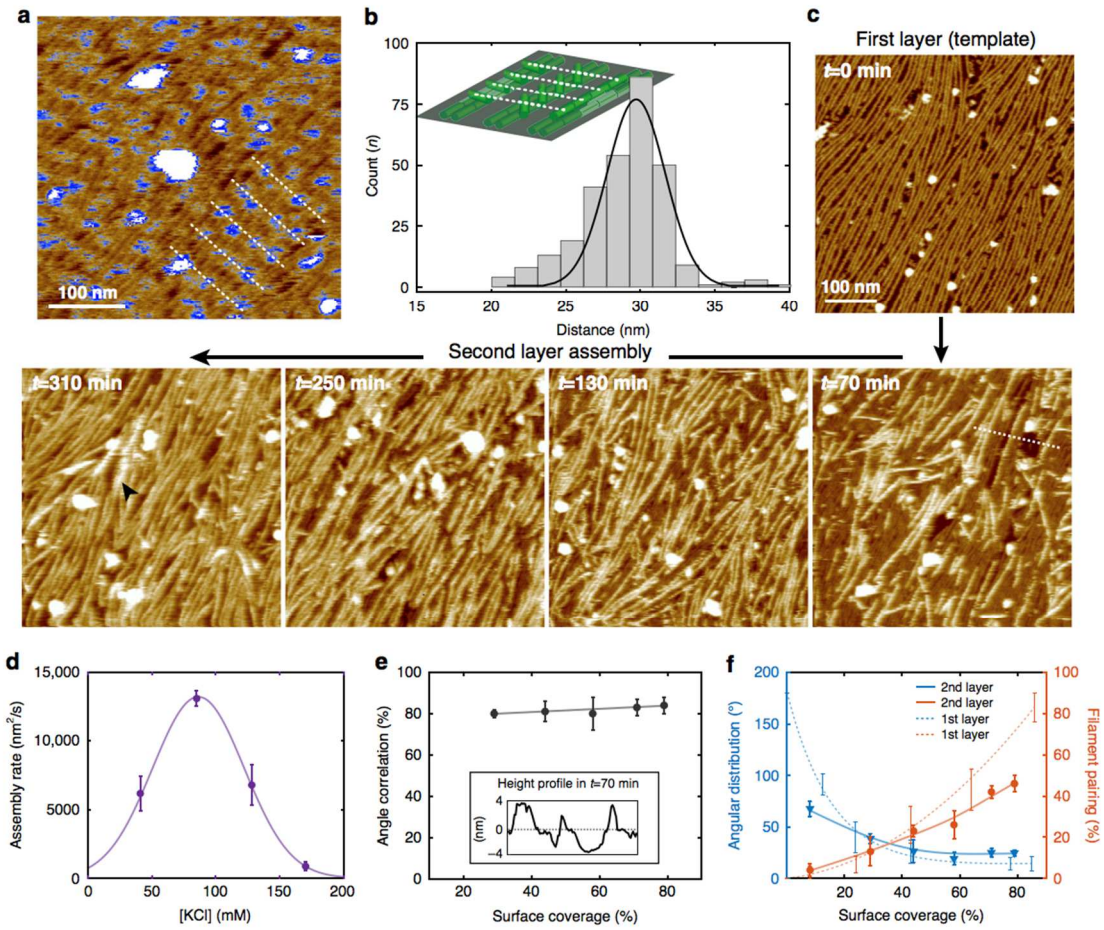

Figure 5.6 Multilayered septin filament assembly observed by HS-AFM
(a) Contrast adjusted HS-AFM frame of septin filaments on which second layer septin molecules start to adhere on the first layer filaments (false-color scale is adapted to enhance the strongly protruding features in blue; the dashed white the periodicity of the features, roughly perpendicular to the aligned first layer filaments). (b) Distance distribution of recruited second layer septins. Peaking at ~30 nm periodicity, matching the septin rod length and thus suggestive of an interaction with Cdc11 or Cdc10 (Inset: cartoon of second layer septin rods on the first layer filaments). (c) HS-AFM image sequence of a second-layer septin filaments assembly on top of a first layer by injection of fresh septin solution (in low salt buffer: 85 mM KCl). Following second-layer formation initiation of filament assembly for the formation of a third layer was observed (arrowhead in t = 310 min). (d) Septin multilayer assemblies can only be established within a rather narrow window of KCl concentration (50 mM to 150 mM KCl). Data are represented as mean ± s.d from ≥3 different experiments. (e) Second layer assembly is guided by the first layer serving as a template: ~80% of the second layer filaments align with the sub-layer filaments, independent of the second-layer filament surface coverage. Inset: Height section profile (along the dashed line in image t = 70 min) showing the two layers of ~4 nm in height, where the surface of the first layer is set to 0 nm. Data are represented as mean ± s.d from ≥3 different imaging areas from 1 representative time-lapse experiment. (f) Both packing orientation and filament pairing are strongly influenced by the first septin layer serving as template. Data are presented as mean ± s.d. from ≥3 different imaging areas from 1 representative time-lapse experiment.

5.4 Discussion

In this work, we employed high-speed atomic force microscopy (HS-AFM) to investigate the assembly process and structure of septins from single subunits to higher-order 3D-structures. HSAFM has formerly proven powerful to study assembly, structure and dynamics of membrane associated proteins (Chiaruttini *et al.*, 2015; Miyagi *et al.*, 2016; Colom *et al.*, 2017; Mierzwa *et al.*, 2017). Our experiments provide insights into the role of pH and ions in modulating assembly, the mechanism of polymerization, first level higher-order structure formation through filament pairing, and growth into 3D multi-layer architectures. We also provide evidence about the faces of the filaments and how they are involved in lipid interactions and protein-protein interactions. The temporal and spatial resolution of HS-AFM has revealed never before detected features of septin assembly from the scale of the single molecule to layers of filaments in higher-order assemblies. In the reconstituted setting, electrostatic interactions played a significant role in filament alignment and pairing, where increased shielding of surface charges through the higher abundance of monovalent ions favored aligned packing and pairing. The average length of filaments increased with salt concentration and long-range ordering of assemblies. We suspect that in cells this shielding occurs due to the large network of interacting proteins that are known to associate with septins, some of which are known to impact the integrity of the higher-order assembly. Alternatively, one could speculate that gated transmembrane channels may locally modulate ion conditions at sites where septins are active in certain cell types and conditions. What is clear is that the degree of short-range order in the form of pairing and long-range order amongst associated filaments can be tuned electrostatically

Another striking control of higher-order assembly can be seen in the pH sensitivity of filament pairing. The sensitivity has an inversion point around physiological pH, which suggests

that regions involved in filament pairing are protein moieties rich in Asp, Glu or His. A structural model further indicates that the N-terminal extensions, especially in Cdc3, contain numerous of Asp and Glu, indicative that the face of the septin rod comprising the N-termini engages into filament-filament interactions. Interestingly, the C-terminal extensions of Cdc11 also contains Asp and Glu residues, consistent with our data that show reduced pairing and filament stability in Cdc11-ΔCTE septin complexes. Together these data point to a mechanism by which cells may be able to control septin assemblies using small changes in pH. We hypothesize that pH changes in addition to phosphorylation could potentially play roles in the rapid rearrangements of septins at cytokinesis and could contribute to asymmetry of septin ring disassembly that can sometimes be seen as there is a mother-daughter asymmetry in pH in budding yeast (Kozubowski, Larson and Tatchell, 2005; Henderson, Hughes and Gottschling, 2014)

Understanding the growth mechanism of polymer formation has been central to the study of actin and microtubule cytoskeletons as well as bacterial cytoskeletal polymers such as FtsZ. To this point, there has been very little known about the dynamics of assembly mechanisms of septins aside from what has been gleaned from TIRF-based assays (Bridges *et al.*, 2014), which have limitations due to the resolution of the light microscope. Our previous work suggested an isodesmic assembly process where low protein concentrations were sufficient for polymerization (Bridges *et al.*, 2014). Here we see evidence for a diffusion-driven annealing process in the fast self-assembly of septin filaments depending on the order of filament alignment. A subtle interplay between the molecular adsorption rate and the diffusion-driven annealing process has a great impact on long-range ordering, and could be a key for controlling size and patterns within higher-order septin assemblies. We suspect that molecular crowding in a real cell membrane setting could fine-tune the dynamics of septin polymerization, through the interaction with other

proteins and/or changing the environmental electrostatics and pH, and post-translational modifications that modulate surface charge.

In many systems, septins are closely associated with and thought to modulate lipids including the plasma membrane, the ER, membranes of intracellular bacteria, and lipid droplets (Akil *et al.*, 2016). Notably, we saw what appear to be droplets of lipid associated with septin rods. Remarkably, the lipid clusters displayed periodicity of rod-length and were recruited and remained on the same face of a given filament, the outside of both filaments when they were paired. This strongly suggests that at least one region for membrane-binding and filament-filament interaction are on the two opposite faces of septin filaments.

In the conditions of our experiments, we show that filament pairing is guided by the N-terminal face. Furthermore, we only see tightly paired filaments, while by negative stain EM both tightly and loosely paired filaments were observed. Several studies have suggested that the CTEs in several septins participate in both homo-/heterotypic protein interactions, thereby providing a mechanism to regulate higher-order septin structures, including filament pairing (Booth *et al.*, 2015; Brausemann *et al.*, 2016; Sala *et al.*, 2016) Tight filament pairs were shown to be independent of CTEs. However, loosely paired filaments have been suggested to be dependent on CTE-CTE interactions (A. Bertin *et al.*, 2008; Finnigan, Takagi, *et al.*, 2015). Subsequent studies have also shown that the septin interacting protein, Bni5, interacts with the CTE of Cdc11 generating structures reminiscent of loosely paired filaments (Booth *et al.*, 2015). In our experiments, analysis of various C-terminal deletion mutations identified membrane-binding to the C-terminal extensions of Cdc3 and Cdc12, while filament-filament interactions are mediated primarily by the N-terminal extensions. A possible explanation for the CTE-dependent formation of loosely paired filaments of Bertin et al. (A. Bertin *et al.*, 2008) may be that by

virtue of flexible linkers between the globular domain and the predicted coil of Cdc11, this extension may be reached by other septins for loose interactions.

HS-AFM also revealed key features about layered, higher-order assembly. In particular, high-resolution images revealed that filament pairing could occur with subunits facing each other or with subunits offset by one protein, thus placing N-termini of one filament into the groove of the NC-interface of the other filament. Variability of filament interface contacts are likely important for the formation of curved septin assemblies such as gauzes, and rings (Rodal *et al.*, 2005; Ong *et al.*, 2014). Multilayered septin filaments can only be established in physiological conditions (<200 mM KCl). Interactions between layers dominate the packing orientation of multilayer filaments, thus lower layers serve as templates for growth into the third dimension. The observation of alignment and pairing within layers and templating between layers may be at the origin of the formation of thick bundles. In cells, the cytoplasmic septin concentration was measured to be 100–200 nM (Bridges *et al.*, 2014) and the KCl concentration is 100–300 mM, thus the observed mechanism may well be representative of the formation of higher-order structures in cells.

The application of HS-AFM to the septin cytoskeleton has enabled the first dynamic analysis of septin assembly from single subunits to higher-order structures, the morphologies of the hierarchical assemblies and the environmental factors that influence assembly. The data provide important insights at the many-molecules level too large for high-resolution structural techniques and too small for optical approaches typically used for in vivo investigations.

5.5 Supplementary Material

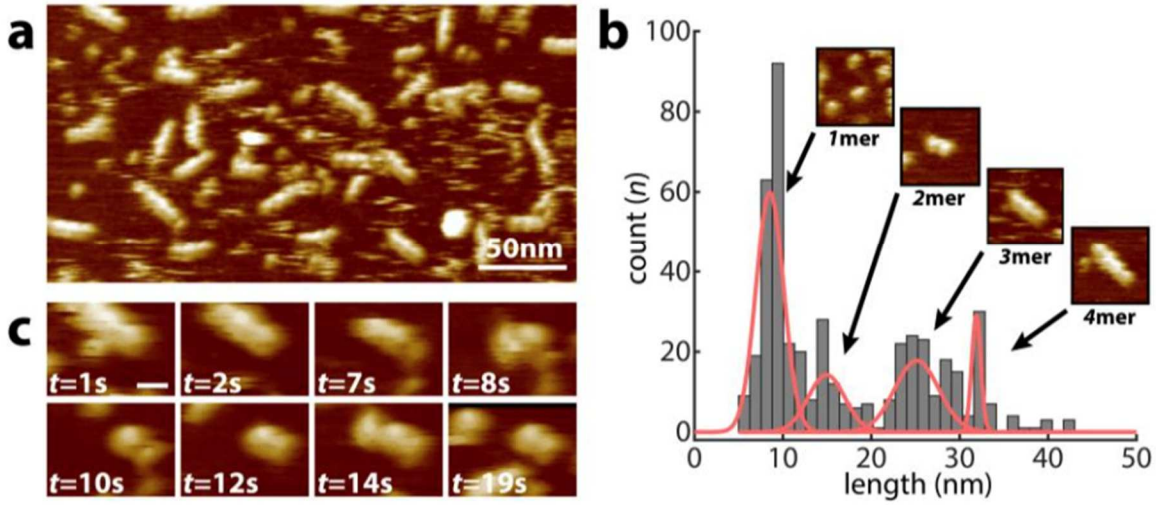

Figure 5S1. **Association of septin monomers into rods in absence of monovalent ions**. (a) Septin subunit assembly in KCl-free buffer: The assembly of the hetero-octameric rod is characterized by 4 topographic units, each of ~8 nm in length. (b) Septin dimers, tetramers, hexamers and octamers with roughly 8, 16, 24, and 32 nm in length, are represented by rods of 1, 2, 3 or 4 topographic features, where topographic monomers, dimers and trimers correspond to 2, 4 and 6 Cdc and the tetramers to 8 Cdc, i.e. the septin rod. Note, the septin rod gave the sharpest length distribution, while the monomers, dimers and trimers gave wider distributions and may comprise assemblies of 1 to 3, 3 to 5 and 5 to 7 Cdc, respectively. (c) HS-AFM movie frames (time points are indicated in the bottom left corner) showing septin subunit association and dissociation events (scale bar: 10 nm)

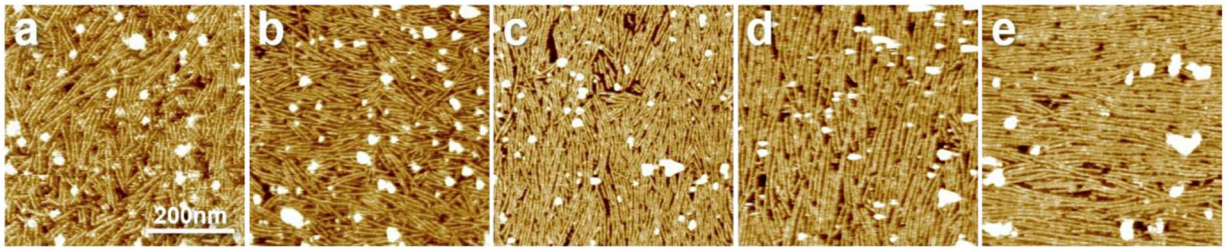

Figure 5S2. Septin assembly under varying KCl concentrations revealed by HS-AFM
(a-e) Septin filaments formed and fully covered the surface using 100 nM septin incubated on mica in presence of 50 mM KCl (a), 150 mM KCl (b), 300 mM KCl (c), 450 mM KCl (d), 600 mM KCl (e).

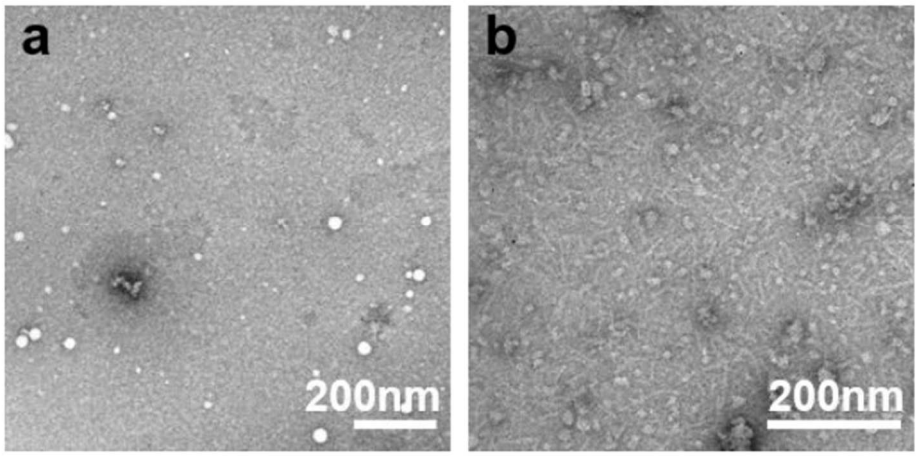

Figure 5S3. Negative stain EM of septin in varying KCl concentrations
(a) No septin filaments were found in solution when incubated in high salt buffer. (b) Septin filamenst were found from lower salt concentration solution (150 mM KCl).

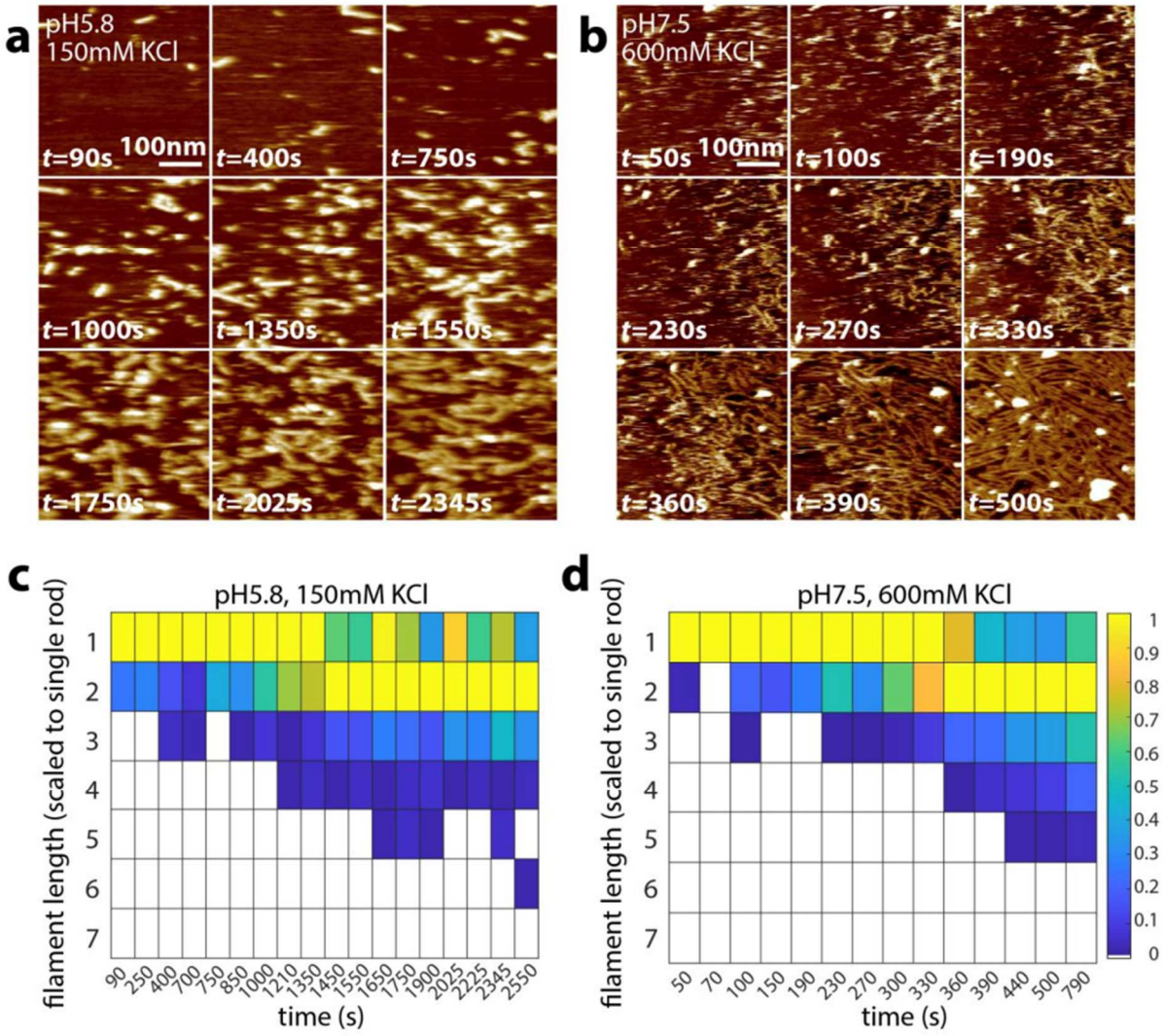

Figure 5S4. Septin assembly imaged by HS-AFM
(a, b) In situ HS-AFM frames (top left: imaging conditions; bottom left: time points) of the septin filaments assembly process. (c, d) Normalized length histograms of septin assemblies as a function of time. The filament length was scaled to the length of single rod, 32 nm. False color bar: Normalized filament count at each time point

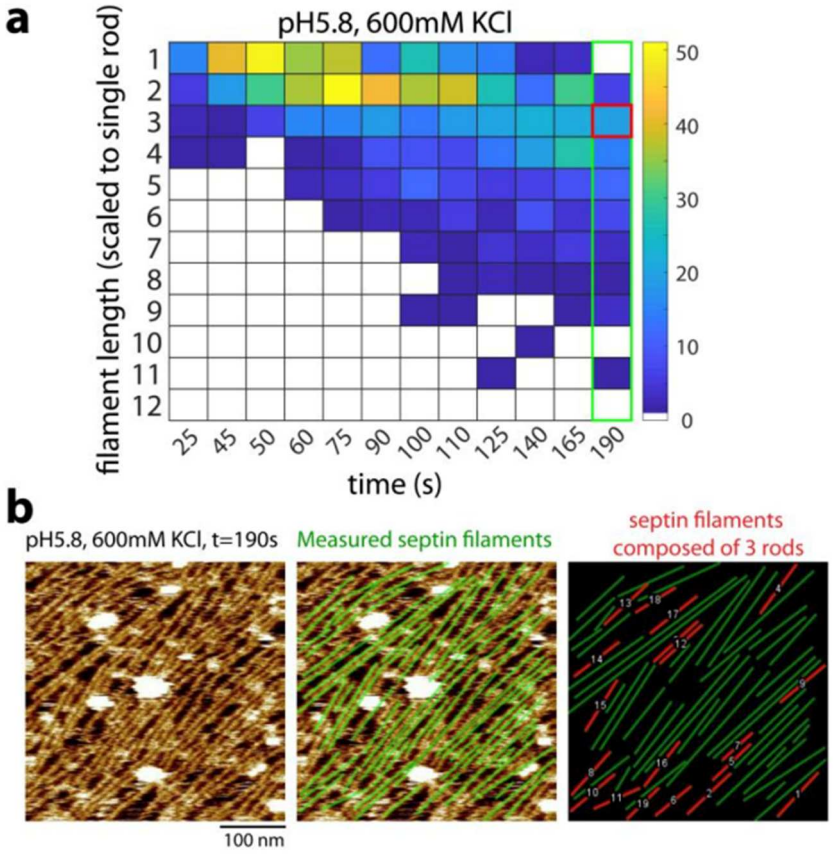

Figure 5S5 Filament analysis
(a) Enlarged length histograms of septin assemblies measured at pH 5.8 and 600 mM KCl (see Figure 2 in the main manuscript). (b) The In situ HS-AFM frame imaged at t=190s (left), the measured septin filaments (middle, green color overlays), and the most populated septin filaments composed of 3 rods highlighted by red color.

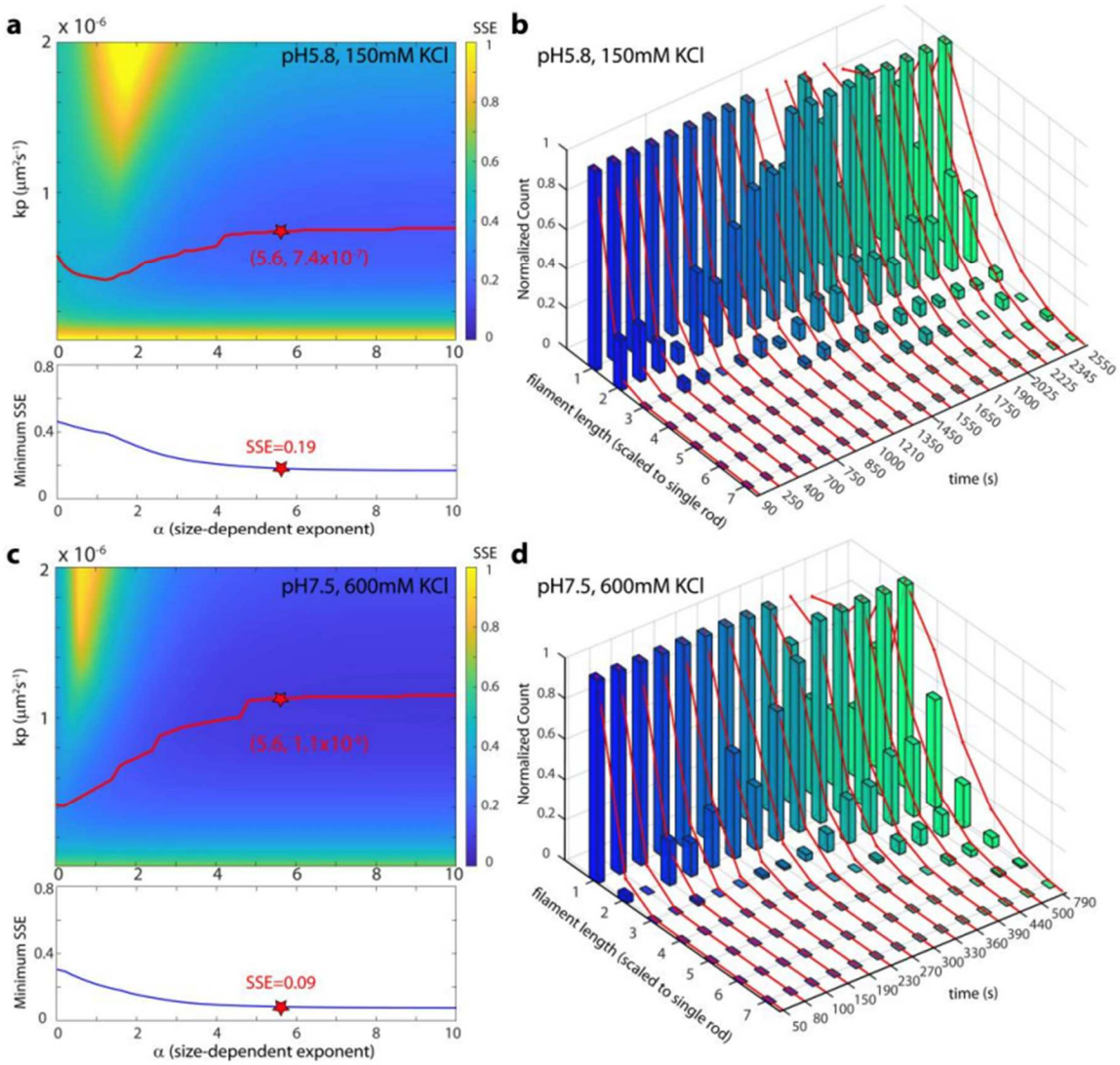

Figure 5S6. Simulated length histograms based on a diffusion-driven annealing model
(a, c) (top) The sum of squared error (SSE) map between experimental and simulated length histograms, which are predicted by using various *kp* (a diffusion-related constant) and α (a size-dependent factor) values at different conditions (150 mM KCl in pH 5.8 buffer (a), 600 mM KCl in pH 7.5 buffer (b)). The red curve highlights the path of *kp* at different α values with minimum SSE. (bottom) The minimum SSE at each α value. The red star indicates the best-fit parameters at α=5.6 that offer the global minimum SSE in both conditions. (b, d) The comparison between the experimental (color bars) and simulated length histograms (red curves), which are calculated by the best-fit parameters at α=5.6.

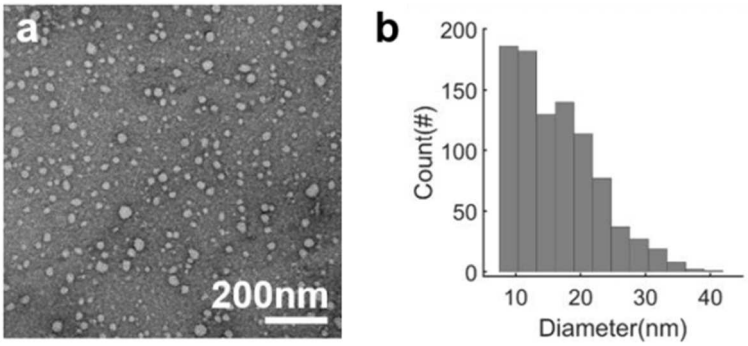

Figure 5S7. Small lipid clusters co-purified with septins
(a) Negative stain EM showed small lipid clusters in the septin sample (see Figure 4 in main text). (b) Lipid clusters diameter distribution with average diameter ~15 nm.

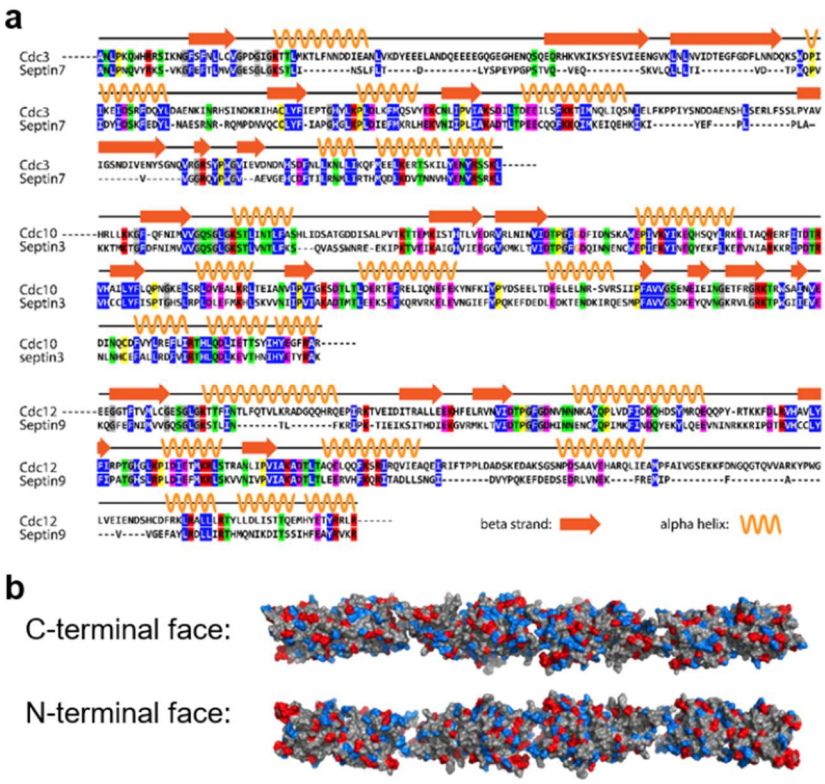

Figure 5S8. Yeast septin structure prediction and surface charge
Cdc3, Cdc10, and Cd12 were predicted and aligned against the known structure of human septin 7 (PDB ID: 2QAG), septin 3 (PDB ID: 4Z54), and septin 9 (PDB ID: 5CYP), all of the alignment proteins show around 50% of sequence identity. (b) The yeast septin hetero-octamer structure by aligning of the crystal structure of Cdc11 (PDB ID: 5AR1), and models of Cdc12, Cdc3, and Cdc10, to the crystal structures of human septin 9 (PDB ID: 5CYP), septin 7 (PDB ID: 2QAG), and septin 3 (PDB ID: 4Z54) show nearly neutral surface charges on both the C-terminal and N-terminal faces

Supplementary Table 5S1 Septin surface density under varying experimental conditions

Condition	a (%)	a (surface density, μm^{-2})	b	c (s)	R-square
pH5.8, 600mM KCl	90.1±0.4	7038±31	0.027±0.001	107±2	0.998
pH5.8 150mM KCl	82.4±1.0	6438±78	0.002±0.0001	2082±25	0.992
pH7.5, 600mM KCl	84.7±0.9	6619±70	0.010±0.0001	311±7	0.988
pH7.5 150mM KCl	73.6±0.8	5749±63	0.004±0.0001	587±8	0.995

Septin surface coverage fitted by a sigmoidal curve ($\frac{\alpha}{1+e^{-b\,(t-c}}$) within 95% confidence of bounds) under varying experimental conditions. Given the dimensions of single septin rod (32nm x 4nm, occupied surface area) and the HS-AFM scanning area (400nm x 400nm), we can further estimate the saturated septin surface density (μm-^{2}) from the septin surface coverage (%).

Supplementary Table 5S2. Best-fit parameter summary

Condition	α	k_P (μm^{2}s^{-1})	Minimum SSE
pH5.8, 600mM KCl	5.6	1.8×10^{-5}	0.19
pH5.8 150mM KCl	5.6	7.4×10^{-7}	0.18
pH7.5, 600mM KCl	5.6	1.1×10^{-6}	0.09
pH7.5 150mM KCl	5.6	9.1×10^{-7}	0.32

Summary of the best-fit parameters at α=5.6 that offers the global/semi-global minimum SSE in all conditions

CHAPTER 6

A GENE DUPLICATION WITHIN A TERMINAL SEPTIN SUBUNIT PROVIDES A DEVELOPMENTALLY REGULATED FILAMENT LENGTH CONTROL MECHANISM

To be submitted for publication

AUTHORS: Kevin S. Cannon, Jose M. Vargas-Muniz, Tsung-Yu Ho, Neil Billington, Ian Seim, James Sellers, Peter Philippsen, Amy. S. Gladfelter

6.1 Introduction

Septins are a family of filament-forming, GTP-binding proteins that function in many cell processes including cytokinesis (Hartwell *et al.*, 1974), cell polarity (Amy S Gladfelter *et al.*, 2005), and membrane organization (Luedeke *et al.*, 2005; Yamada *et al.*, 2016). Although septins are highly conserved from yeast through humans, the number of septin genes between organisms can vary greatly, from 1 in *Chlamydomonas* to 13 humans (Pan, Malmberg and Momany, 2007) . This variable number of septin genes within organisms has been suggested to result from multiple gene duplications. Additionally, alternative splicing in mammalian cells has the potential to produce a wide array of variability in septin gene-products both between different tissues and even within a single cell (Hilary Russell and Hall, 2011; Sellin, Stenmark and Gullberg, 2014). Despite this well appreciated complexity in subunit composition, how the pool of septin proteins available in a cell contributes to septin properties and functions is poorly understood.

Septin proteins self-assemble into hetero-oligomeric complexes that are rod shaped, generally 32 nm long in fungi and are the soluble, minimal subunit of septins (A. Bertin *et al.*,

2008; Bridges *et al.*, 2014). These oligomers then polymerize into filaments by concentrating on either membrane surfaces or other cytoskeletal networks (in animals) and elongate through annealing such that the terminal subunits of the oligomers interact to create filaments (Field *et al.*, 1996b; Aurélie Bertin *et al.*, 2010; Bridges *et al.*, 2014). These filaments are highly flexible however their mechanical properties can be modulated through pairing and interacting proteins to form a variety of higher-order structures such as lattices, bundles and rings (Aurélie Bertin *et al.*, 2010; Garcia *et al.*, 2011b; Ong *et al.*, 2014). The process of oligomeric assembly and polymerization has been studied in most detail in the budding yeast *S. cerevisiae*, where 5 mitotic septins are expressed and arranged in the following order: X-Cdc12-Cdc3-Cdc10-Cdc10-Cdc3-Cdc12-X, where the terminal subunit X can be either Cdc11or Shs1 (Garcia *et al.*, 2011b). Cdc11 and Shs1 impart different properties on complexes and filaments; however, they are only 36 % identical, making it difficult to dissect the molecular basis for the different properties. The interface between terminal subunits is critical to many parameters relevant to septin assembly and could influence properties such as polymerization and fragmentation rates and propensity for bundling and crosslinking.

We set out to address here how sequence variations in the terminal subunit can impact septin filament properties by taking advantage of a duplication of the gene encoding *CDC11* in the genome of the filamentous fungus *A. gossypii*. This results in a situation with two versions of Cdc11, namely Cdc11a and Cdc11b, which show 91% sequence identity. We show that small numbers of changes in the primary sequence in terminal septin subunits can alter fundamental biophysical features of septin filaments, which leads to distinct lengths of septin filaments and sizes of higher-order assemblies both *in vitro* and *in vivo*. Moreover, we show that Cdc11a and Cdc11b localize to septin structures in A. gossypii in a development-specific manner and that

deletion of either CDC11A or CDC11B results in distinct morphological phenotypes in *A. gossypii.* Collectively, these data suggest that despite their high sequence similarity, Cdc11a and Cdc11b proteins exhibit discrete functions during the development of *A. gossypii*.

6.2 Materials and Methods

Ashbya strain construction

Ashbya gossypii strains used in this study can be found in Table S6.1. Description of the plasmids and oligos used to generate the different strains can be found in Table S6.2 and Table S6.3, respectively. For generating the AGB1320, we cloned the GFP:GEN into AGB124 via Yeast Recombination. AGB1320 was then used to transform AG280 to generate AG968, which expresses Cdc11a-mCherry from the endogenous locus, and Cdc11b-GFP from a plasmid under the control of *CDC11b* native promoter. All plasmids generated in this study underwent Sanger sequencing to confirm the fidelity of the target gene sequence

Generation of Phylogenetic Tree

We utilized Treehouse to generate a subtree of the *Ashbya* lineage (Steenwyk and Rokas, 2019). This tree was based on a previously described Saccharomycotina yeast phylogeny (Shen *et al.*, 2018). NCBI Blast was used to identify homologs of *CDC11* in the different species.

Microarray analyses

Transcription data was obtained from the Ashbya Genome Database. In short, highly purified spores from the ΔlΔt laboratory strain were used and all the data was obtained in duplicate. For the time course experiment, spores were inoculated into AFM broth and samples were acquired at each timepoint.. The center represents a region enriched for sporulation, while the rim represents a region of high speed hyphal growth via tip-splitting.

Generation of Ashbya gossypii septin expression plasmids

Plasmid AGB1281 was obtained by restriction enzyme-dependent cloning. CDC11b was amplified from AGB124 using primers AGO2823 and AGO2824. AGB119 and PCR products were digested with XhoI and NdeI. Then the digested products were ligated and transformed into *E. coli* DH5-α. C terminal extension (CTE) swaps were achieved via fusion PCR followed by restriction enzyme-dependent cloning. Cdc11a N terminus was amplified using AGO3069 and AGO3103, Cdc11a CTE was amplified using AGO3070 and 3102, Cdc11b N-terminus was amplified with AGO2825 and AGO3103, and Cdc11b CTC was amplified using AGO2826 and AGO3102. To generate the Cdc11a-Cdc11bCTE construct, we performed Phusion PCR using AGO2825 and AGO3070. For the Cdc11b-Cdc11aCTE we used the AGO3069 and AGO2826 oligos. AGB and fusion PCR products were digested with NdeI and XhoI. Then ligated and transformed into *E. coli* DH5-alpha Cdc11a T62A was generated using the Q5-Site directed mutagenesis kit (NEB).

Septin complex purification

Bl21 (DE3) E. coli cells were transformed using a duet construct expression system using ampicillin and chloramphenicol selection (Bridges *et al.*, 2014). Selected transformants were then grown overnight in 25 mL of luria broth with ampicillin and chloramphenicol selection at 37 degrees Celsius while shaking. 1/60 of LB liquid cultures were added to 1 liter of terrific broth with ampicillin and chloramphenicol selection and were grown to an O.D.600nm between 0.6 and 0.8. Upon reaching the appropriate O.D.600nm, 1 mM of isopropyl-B-D-1-thiogalactopyranoside was added to the cultures to begin induction. Induced cultures were grown for 18 hours at 18 degrees Celsius while shaking before harvesting by centrifugation at 10,000 RCF for 15 minutes. Pellets were resuspended in lysis buffer (1M KCl, 50 mM hepes pH 7.4, 40 mM imidazole, 1 mM

MgCl2, 10% glycerol, 0.1 % Tween-20, 1mg/ml lysozyme, and a 1x protease inhibitor tablet (Roche) at 4 degrees Celsius for 30 mins to generate cell lysates. Cell lysates were then sonicated on ice for 10 seconds every two minutes. Lysates were clarified by spinning at 20,000 RPM for 30 minutes using an SS-34 rotor at 4 degrees Celsius. The supernatant was passed through a 0.44 um filter and then incubated with 2 mL of equilibrated cobalt resin at 4 degrees for 1 hour. The lysate-resin mixture was then added to a gravity flow column. Following the initial flow-through of unbound lysate, the resin was washed 4x (50 mL each wash) using wash buffer (1M KCl, 50 mM hepes pH 7.4, 40 mM imidazole, 5% glycerol). Bound protein was then eluted using elution buffer (500 mM imidazole, 300 mM KCl, 50mM hepes pH 7.4, 5% glycerol) and then dialyzed into septin storage buffer (300mM KCl, 50 mM hepes pH 7.4, 1mM BME, and 5 % glycerol) for 24 hours using two steps. Protein purity was determined via SDS-PAGE and protein concentration was determined using a Bradford assay. To achieve a stoichiometric septin complex of Ashbya septins, we use Cdc12 with primary sequence derived from *S. cerevisiae* while all other subunits were Ashbya-derived sequences.

Electron microscopy and Image processing

Proteins were diluted to 50 nM (in buffer containing 10 mM MOPS, 2 mM $MgCl_2$, 0.1 mM EGTA (pH 7.0) with 50 mM or 300 mM NaCl as indicated in the text. 3 hours after dilution, samples were applied to UV treated, carbon coated EM grids and stained using 1% uranyl acetate. Micrographs were recorded on a JEOL 1200EX microscope using and AMT XR-60 CCD camera at a nominal magnification of 40000x. Rod shaped particles were picked manually for each dataset (n=2300 for CDC11a, n=1777 for CDC11b. Reference-free image alignments and classifications were conducted using SPIDER software. Each aligned dataset was classified into 100 classes using K-means classification and 30 example class averages were selected to produce each montages

shown in Figure S1. The whole micrographs shown in Figure S1 are bandpass filtered between 2 and 40 pixels for clarity (FIJI FFT bandpass filter).

Preparation of small unilamellar vesicles for seeding onto supported lipid bilayers

75 mole percent of dioleoylphosphatidylcholine (DOPC) and 25 mole percent phosphatidylinositol (soy) were mixed in chloroform in a glass cuvette. For bead assays, 0.05 mole percent of rhodamine-phosphotitdyl-ethanolamine (Rh-PE) was added to the above mixture. Lipid films were made by evaporating the chloroform using argon gas followed by an overnight incubation under negative vacuum pressure. The following day, the lipid films were hydrated using an aqueous supported lipid bilayer (SLB) buffer (150 mM KCl, 20 mM hepes pH 7.4, and 1 mM $MgCl_2$) to a final concentration of 5 mM. Hydrated lipid films were vortexed for 10 seconds and allowed to sit at 37 degrees Celsius for 5 minutes. This process of vortexing and incubation at 37 degrees Celsius was repeated five more times (or until the lipid film was hydrated). The hydrated film was subject to water bath sonication at 2-minute intervals until the opaque solution became transparent (vindication of small unilamellar vesicle formation).

Preparation of supported lipid bilayers onto planar and curved surfaces

Planar supported lipid bilayers were prepared by plasma (oxygen) treatment of glass coverslips (PE25-JW, Plasma Etch) on high power for 15 minutes. Reaction chambers were prepared onto the plasma treated glass using a previously established method (Bridges and Gladfelter, 2016). 1 mM of small unilamellar vesicles was added to the reaction chamber (using SLB buffer) followed by the addition of 1 mM $CaCl_2$, followed by incubation at 37 degrees Celsius for 20 minutes as to promote bilayer formation. After bilayer formation, excess small unilamellar vesicles were washed vigorously with 150 µL of SLB buffer six times. It is essential not to touch the cover glass during this step as bilayer continuity can be affected. Prior to adding

septins to the membrane, the bilayers are washed again with 150 µL of reaction buffer to lower the salt as to promote septin binding (50 mM hepes pH 7.4, 0.13 mg/mL bovine serum albumin (BSA) , 1 mM β-mercaptoethanol). This step is repeated 5 more times. On the last wash, remove 125 µL of the reaction buffer. 25 µL of septins at the desired concentration were added to the bilayer and imaged by total internal reflection fluorescence microscopy using a Nikon TiE TIRF system equipped with a solid-state laser system (15 mW, Nikon LUn-4), a Nikon Ti-82 stage, a 100x Plan Apo 1.49 NA oil lens, and Prime 95B CMOS camera (Photometrics).

Supported lipid bilayers on silica microspheres were generated as previously reported by (Bridges *et al.*, 2016). 50 nM of small unilamellar vesicles (75 mole percent DOPC, 25 mole percent Soy PI, 0.05 mole percent Rh-PE) were added to silica microspheres of various membrane curvatures at a total surface area of 440 mM^2. Note: The total surface area of each bead size is equal. SUVS were incubated with the microspheres for 1 hour at room temperature on a rotator to induce bilayer formation. After bilayer formation, the microspheres were spun down each bead size at the minimal sedimentation velocity for each bead (It is important not to exceed this number as bilayer continuity can be affected). 50 µL of the supernatant was removed and discarded. 200 µL of pre-reaction buffer (33.3 mM KCl and 50 mM hepes pH 7.4) was used to resuspend / wash the beads. The microspheres were spun down again (at the appropriate sedimentation velocity) and 200 µL of supernatant was removed. 200 µL of fresh pre-reaction buffer was added to resuspend / wash the microspheres. This process was repeated three more times. Washed microspheres were then mixed at a 1:1 ratio. 29 µL of this mixture was added to 721 µL of reaction buffer (33.3 mL KCl, 50 mM hepes pH 7.4, 0.1% methyl cellulose, 0.13 mg/ml BSA, 1 mM β-mercaptoethanol). 75 µL of this mixture was added to a reaction chamber glued to a poly-ethylene glycol coated coverslip ((Bridges *et al.*, 2016; Cannon *et al.*, 2019). 25

μL of septins at a desired concentration were added to the reaction chamber and allowed to reach steady state (1 hr) and were imaged using spinning disc confocal microscopy.

Measuring protein adsorption on lipid bilayers supported on silica microspheres

Images of fluorescent-tagged septins adsorbed onto curved supported bilayers on microspheres were acquired using a spinning disc (Yokogawa W1) confocal microscope (Nikon Ti-82 stage) using a 100x Plan Apo 1.49 NA oil lens and a Prime 95B CMOS camera (Photometrics). Images were analyzed using Imaris 8.1.2 software (Bitplane AG) as previously described (Bridges *et al.*, 2016; Cannon *et al.*, 2019).

Analysis of septin surface coverage onto planar supported lipid bilayers

10 locations on a given lipid bilayer were blindly selected to form 10 separate images. Each image was background subtracted. The total number of pixels with septin signal were divided by the total number of pixels in the image to get the fraction of septins bound to the surface. This number was multiplied by 100 to get a percent surface coverage.

Filament length distribution measurements and exponential fit analysis

Filament lengths were measured by uploading raw images to FIJI and using the Ridge detection (Steger, 1998) plugin.. After image segmentation and processing, septin length distributions are extracted from each field of view. We are unable to resolve the frequencies of the smallest septin filaments due to the diffraction limit of light (~200nm) and the small size of septin octamers (~32nm) and are thus left with an incomplete length distribution. Therefore, an arithmetic average of the observed lengths will not be an accurate estimate of the true mean length of the population, and we must use a model to extrapolate to the true length distribution. Observation, physical models of septin polymerization, and robust model fits suggest that this distribution is a left-truncated exponential. Since we have incomplete data, we utilize a

convenient property of exponential distributions to obtain model fits and estimate the population mean length.

An exponential length distribution has the following PDF: $f(x) = \lambda \exp(-\lambda x)$, where $1/\lambda$ is the mean length. If we let X be an exponentially distributed random variable, i.e. $X \sim \text{Exp}(X)$, then X is *memoryless*, which means that: $P(X > x + a \,|X > a) = P(X > x)$, for some cutoff value a. In practice, this implies that if the true septin length population is exponentially distributed with some mean length $1/\lambda$, then our left-truncated data will be described by the same λ. To fit, we simply choose a cutoff value a below which data is ignored, subtract this value from the observed lengths, and obtain the fit parameter λ. To ensure robustness of fits, fit quality for a small range of cutoff values is assessed, and the smallest cutoff value that corresponds to a stable value of the fit parameter, λ, is the one used for the final model fit. Cutoff values are close to 200nm. The true length distribution is related to the left-truncated data by the scaling factor, $\exp(\lambda a)$.

Persistence length measurements

Persistence length measurements were calculated from raw TIRF microscopy images of septin filaments seeded onto planar supported lipid bilayers using a previously published MATLAB GUI method (Graham *et al.*, 2014)

Ashbya cell growth and imaging

Ashbya spores were inoculated into full medium at 30 °C for either 12, 16, 18,or 24 hours before harvesting mycelial cells. Harvested cells were washed 3x using low fluorescence media. Cells were subsequently mounted onto low fluorescence medium based agar pads (2% agar). Images were acquired using a spinning disc (Yokogawa) confocal microscopy (Nikon Ti-82 stage), a 100x 1.49 NA oil lens, and a 95B Prime sCMOS camera (Photometrics). Ashbya deletion and replacement strain images were acquired using a wide-field microscope equipped for differential

interference contrast imaging. (Nikon Ti-82 stage, a 40x air Plan Apo 0.95 NA objective using a 95B Prime sCMOS camera (Photometrics).

Branch point, inter-region ring filament length, and ratio measurements

We measured filament length of branch points by merging both Cdc11a and Cdc11b channels using ImageJ. Measurements of filament lengths were made manually. For ratiometric analysis, images were background subtracted (in both channels individually). Summed fluorescence intensity was exacted at each of these sites. The summed fluorescence intensity sum of the Cdc11a channel was then divided by the summed fluorescence intensity of the Cdc11b channel. Measurements from all structures was plotted using PlotsofData (Postma and Goedhart, 2019).

Fluorescence recovery after photobleaching of Ashbya septin structures

Fluorescent images of Ashbya expressing Cdc11a and Cdc11b were acquired as previously described above. Regions of interested were made using Nikon elements software. These regions were laser ablalated using a 405 nm laser, followed by standard confocal imaging (as described above) to monitor fluorescence recovery. Fluorescence intensity recovery was monitored (following background subtraction of individual channels) using the Time Series analyzer plugin in FIJI.

6.3 Results

6.3.1 Tandem duplication of the CDC11 locus in the Ashbya gossypii lineage

The *Ashbya gossypii* genome encodes eight septin genes, all of which have homologs in *S. cerevisiae* (Gattiker *et al.*, 2007). Interestingly, in *Ashbya* there are two copies of the *CDC11* gene on two different chromosomes. *CDC11a* (AER445C) is on chromosome V while *CDC11b* (AFR436C) is on chromosome VI. The 411 amino acids of AgCdc11a share 91% identity (95%

similarity) to the 408 amino acids of Cdc11b. We predict that these two paralogs originated from an ancestor that had a tandem duplication of the *CDC11* locus (Figure 6.1A). Based on the current synteny of the loci, after the duplication event in the *Ashbya* ancestor, a DNA double-strand break presumably occurred between the two *CDC11* copies that were repaired through a complex gene fusion event. This duplication was followed by the complex double-strand repair presumably occurred relatively recently in the *Ashbya gossypii* evolutionary history because the only other sequenced species closely related to A. gossypii, with a second copy of *CDC11* that is in synteny with the *A. gossypii* homolog is *A. aceri* (Figure 6.1B). The *A. aceri* Cdc11a protein is 100% identical to Cdc11a from *A. gossypii* Cdc11a while the *A. aceri* Cdc11b shares 95% identity with *A. gossypi*i Cdc11b. *A. aceri* Cdc11b is also more similar to *A. gossypii* Cdc11a (94% identity) than *A. gossypii* Cdc11b (Figure 6.1C). Thus, a duplication and rearrangement has preserved a lineage of closely related *Ashbya* species with an additional Cdc11 protein. We therefore set-out to examine the biophysical and cellular significance of having a second Cdc11 protein of similar but not identical sequence.

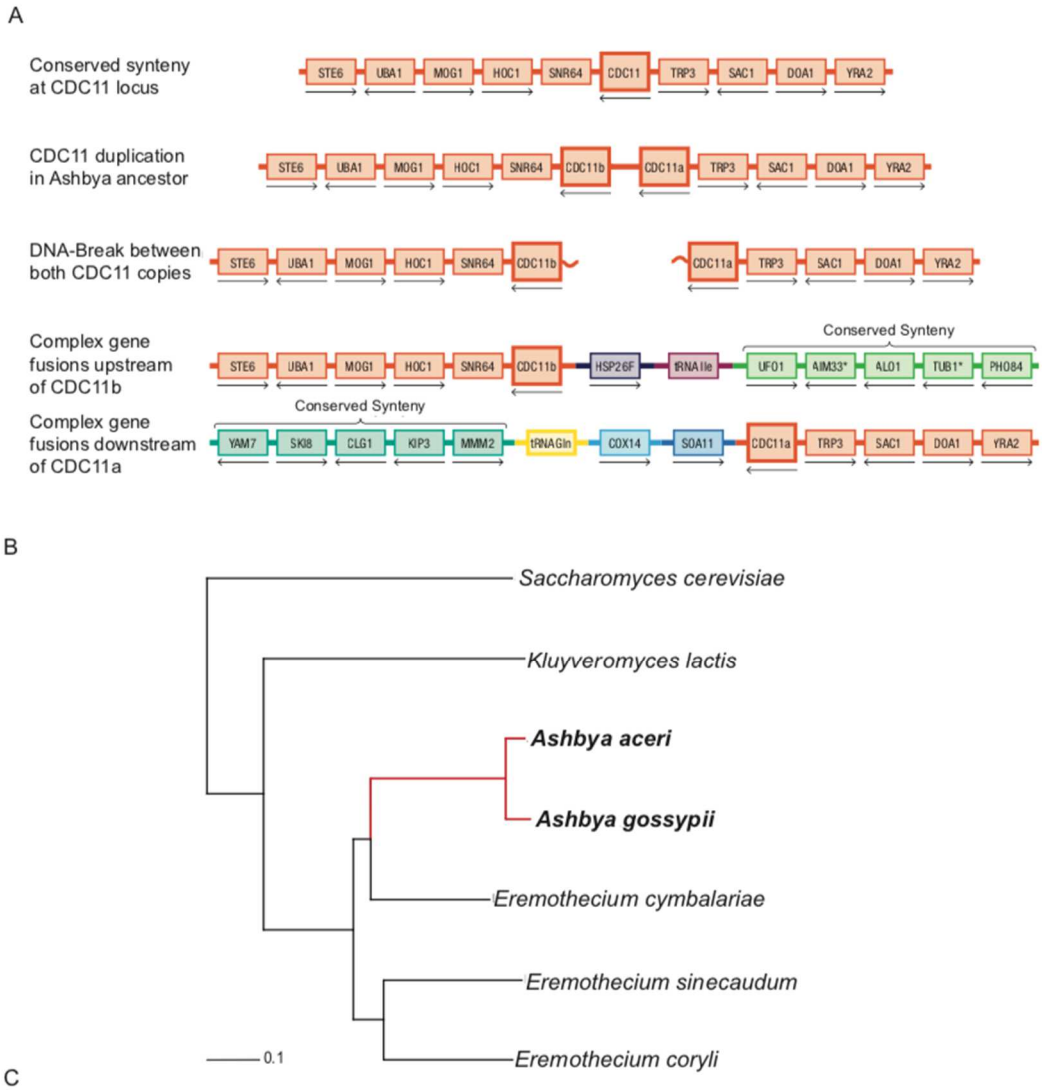

C

Species	*Ashbya gossypii*		*Ashbya Aceri*	
Locus	AER445C	AFR436C	AER445C	AFR436C
Protein	Cdc11a	Cdc11b	Cdc11a	Cdc11b
Length (aa)	411	408	411	405
% identity	100	91	100	94.1

Figure 6.1. *Ashbya* genome encodes 2 copies of *CDC11*. (A) Schematics of the molecular origin of *CDC11a* and *CDC11b*. The two copies originated from a tandem duplication followed by a complex double-strand break repair. (B) This duplication occurred only in the *Ashbya* lineage (red line) and both *Ashbya gossypii* and *Ashbya aceri* genomes contain the *CDC11b* gene. (C) Comparison of the different Cdc11 peptides in *A. gossypii* and *A. aceri*. Percent identity was determined by comparing each peptide to *A. gossypii* Cdc11a.

6.3.2 Identity of terminal subunit changes the biophysical properties of septin filaments

We set out to determine if capping septin octamers with either Cdc11a or Cdc11b could confer distinctive filament properties such as length, polymerization rate, and rigidity. To do this, we purified recombinant *Ashbya*(from *A. gossypii)* septins from *E. coli*. Septin complexes capped with either AgCdc11a or AgCdc11b form hetero-octamers and are capable of filament formation in solution (Figure 6.2A,B). Although septins can polymerize in solution *in vitro*, in fungal cells septin filament formation is dependent on septin-membrane interactions (Bridges *et al.*, 2014, 2016). We therefore reconstituted septin assembly with recombinant proteins and planar supported lipid bilayers (SLBs) (Figure 6.2C). The distribution of filament lengths for both Cdc11a and Cdc11b-capped octamers at steady state could be approximated by a single exponential function, consistent with isodesmic polymer growth models (Figure 6.2D) (Romberg, Simon and Erickson, 2001; Skillman *et al.*, 2013). Fitting to a single exponential function also allowed us to calculate an average filament length despite the diffraction limit of the light microscope and for Cdc11a complexes was 0.72 μm (~23 octamers) and for Cdc11b complexes 0.52 μm (~16 octamers) (Figure 6.2D). This suggests that the affinity for "end-on" Cdc11a-Cdc11a interactions is stronger than Cdc11b-Cdc11b interactions.

We hypothesized that differences in affinity between neighboring Cdc11-capped complexes could influence the rate at which septins form filaments on the membrane. To test this hypothesis we adsorbed septin complexes containing either Cdc11a- or Cdc11b-capped septin complexes onto planar supported lipid bilayers and monitored change in fluorescence intensity over time to measure rates of assembly. Interestingly, we observed similar increase in fluorescence intensity through time for both Cdc11a- and Cdc11b-capped octamers, suggesting septin assembly rates on the membrane are not dependent on the Cdc11 polypeptide that

occupies the terminal position within the hetero-octamer (Figure 6.2E). Surprisingly, when we examined the surface coverage for both complexes at steady-state, we found that Cdc11b complexes occupy approximately 2-fold greater space on the membrane (Figure 6.2F). We speculate that the observed higher surface coverage by Cdc11b-capped filaments could result from a shorter average filament length, as shorter filaments might be able to more efficiently pack together on the membrane than longer filaments. Additionally, having a higher density of bound septins with shorter filaments would increase the number of available binding sites (free filament ends) for which septin octamers coming from the bulk could interact, thereby potentially increasing amount of septin bound to the membrane.

The mechanical properties of cytoskeletal filaments are intimately tied to their functions. As Cdc11a or Cdc11b are the terminal subunits for filament formation, they are uniquely poised to influence the intrinsic flexibility of a septin filament. Therefore, next we characterized the persistence length (Graham *et al.*, 2014), the average length over which filaments stay straight, for septin filaments composed of either Cdc11a- and Cdc11b-capped complexes. Interestingly, the persistence length of both classes of filaments is similar (1.38 and 1.13 μm, Cdc11a and Cdc11b complexes, respectively) (Figure 6.2G), suggesting that despite apparently different affinities, that Cdc11a and Cdc11b generate filaments with similar flexibilities. When combined these data show that the identity of septin protein in the terminal position of the oligomer can produce septins with different average lengths and packing densities on membranes, indicating that relatively small changes in the protein sequence can produce substantially different polymer behaviors.

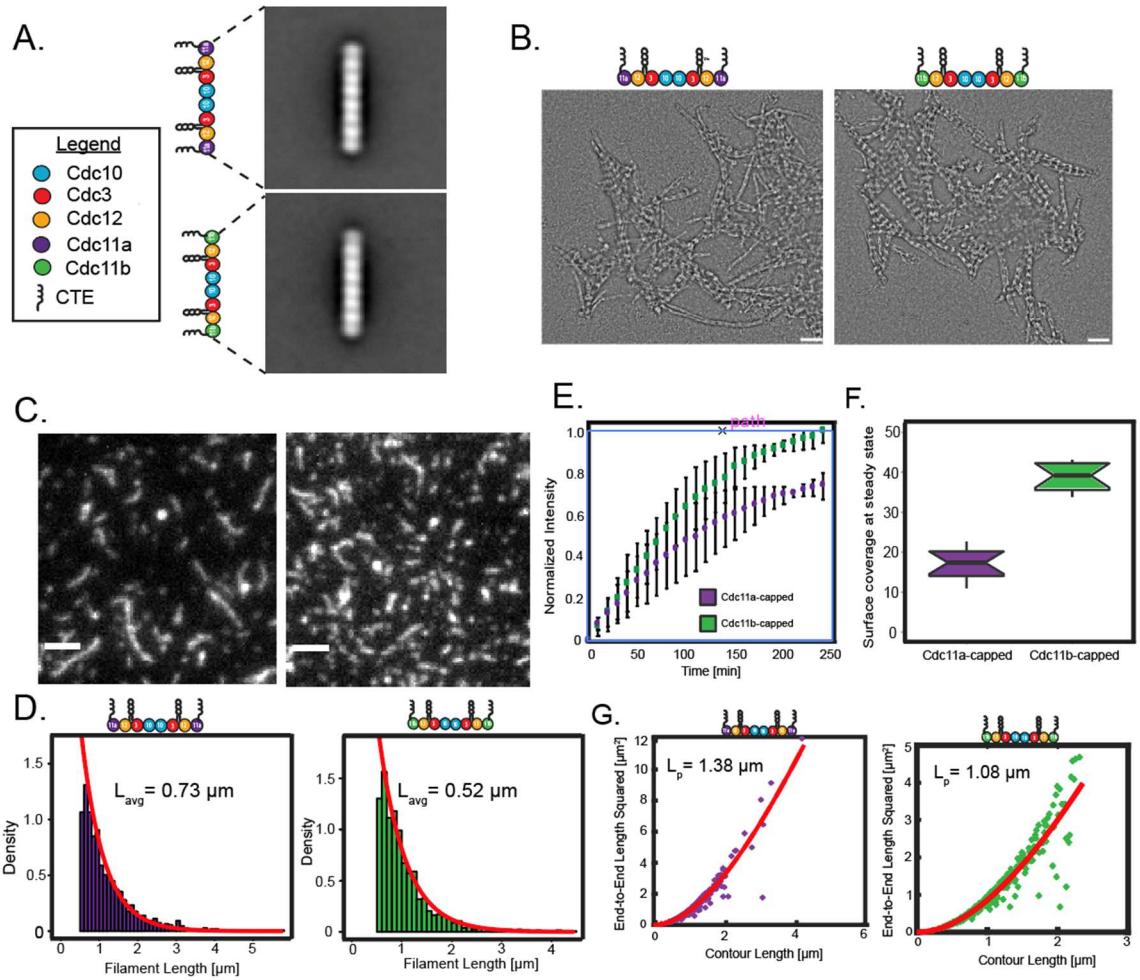

Figure 6.2 Cdc11a- and Cdc11b-capped octamers have distinct biochemical properties. (A) Global averages and montages of class averages showing the predominant octameric structure of Cdc11a- and Cdc11b-capped complexes in high salt (300 mM KCl). Scale bars, 10 nm. Cartoon of septin octamers highlighting individual polypeptides. (B) Transmission electron micrographs of Cdc11a- and Cdc11b-capped octamers forming filaments in solution at low salt (50 mM KCl), respectively. Scale bars, 100nm. (C) Representative TIRF image of 0.5 nM Cdc11a- (left panel) or Cdc11b (right panel) -capped filaments formed on a planar supported lipid bilayers (SLBs) (75% DOPC and 25% PI) at steady-state. Scale bar 2µm. (D) Steady-state filament length distributions for Cdc11a- (left panel) and Cdc11b (right panel)-capped octamers**.** Distributions were fit to a single exponential (red) from which the average filament length was determined. (E) 1nM of either Cdc11a- or Cdc11b-capped octamers were seeded onto planar SLBs (75% DOPC and 25% PI) and imaged by TIRF microscopy through steady-state. Normalized fluorescence intensity is plotted as a function of time relative to Cdc11b-capped octamer intensity. (F) Violin plot showing the percent surface coverage for Cdc11a- and Cdc11b-capped filaments at steady-state on planar SLBs. Horizontal black bars represent the mean, vertical black bars represent the deviation from the mean. n=10 different locations on the bilayer. (G) End-to-end distance analysis was used to calculate the persistence length of Cdc11a-(left

panel) and Cdc11b- (right panel) capped filaments. Filled black dots represent individual filaments. Red lines represent the best fit to equation 1. N > 80 filaments for each sample

6.3.3 Cdc11a and Cdc11b septin complexes display the same curvature

Septins are the only identified sensor of positive micron-scale membrane curvature in eukaryotes. Previous work in our lab has utilized an in vitro reconstitution system to measure septin adsorption using positively curved SLBs, fluorescently-tagged, recombinant protein, and quantitative fluorescence microscopy (Bridges *et al.*, 2016). Recombinant septins from budding yeast were shown to preferentially assemble onto spherical SLBs with a curvature , $\kappa = 2\ \mu m^{-1}$ (corresponding to a diameter of 1 μm) when mixed with SLBs of various curvatures. We used the spherical SLB system to examine the curvature-sensing ability of *Ashbya* septins containing either Cdc11a or Cdc11b-capped septin complexes. When we measured adsorbance for both complexes at steady state, we found that both Cdc11a and Cdc11b have preference for beads where $\kappa = 2\mu m^{-1}$(Figure 6.3A,B), consistent with the curvature preference for budding yeast septins. Interestingly, we noticed that Cdc11b complexes show a higher absorption value, (0.8 and 1.0 for Cdc11a and Cdc11b, respectively) (Figure 6.3B), indicating that more of this septin complex is bound to the bead. This is consistent with our previous data where Cdc11b-capped complexes occupy a higher surface coverage on planar membranes relative to Cdc11a at steady state(Figure 6.2E). Higher absorbance values onto beads ($\kappa = 2\mu m^{-1}$) at steady state could be explained through at least two hypotheses. The first being that Cdc11b-capped complexes have a stronger affinity (Kd) for curved membranes than Cdc11a-capped octamers. The second possibility is that a curved membrane provides a higher number of binding sites for Cdc11b-capped octamers. Previously you said shorter filaments higher packing is this = or different from what you said before? Unfortunately, we cannot easily distinguish between these scenarios because due to low protein yield in

purification we were unable to generate the saturation binding isotherms to calculate the precise Kd and maximum binding values.

Collectively, these data suggest that Cdc11b-capped complexes have a higher affinity for membranes with a curvature of $\kappa = 2\mu m^{-1}$ than Cdc11a-capped complexes. Additionally, more Cdc11b-capped complexes are bound to the membrane surface at this concentration regime. However, we cannot distinguish between whether the membrane is providing more binding sites for Cdc11b-capped octamers, and/or if the filament length distribution and packing are also driving faster and more septin adsorption onto curved membranes.

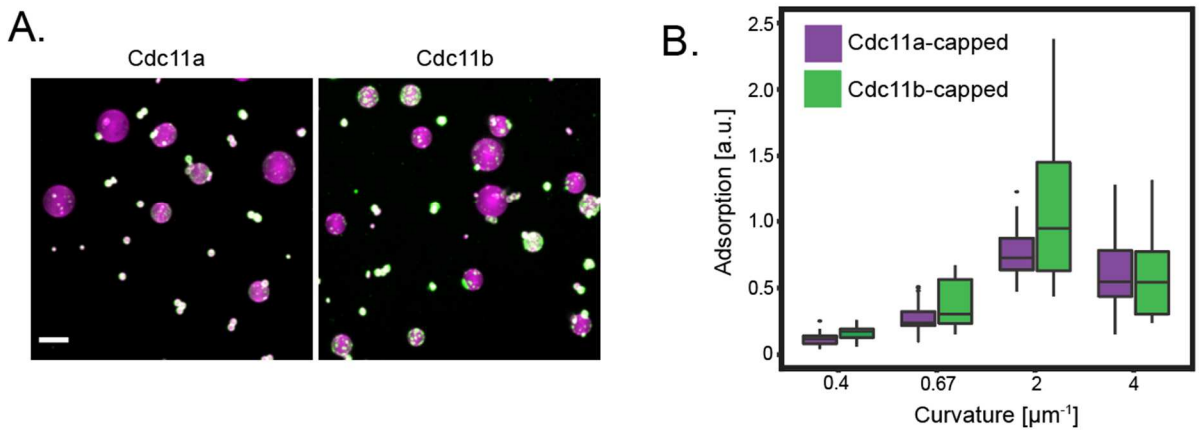

Figure 6.3 Cdc11a- and Cdc11b-capped octamers display the same curvature preference

(A) SLBs (75% DOPC, 25% PI, 0.05% Rh-PE) were formed onto silica microspheres with different curvatures (k= 0.4, 0.67, 2, and 4 µm-1). 15 nM of Cdc11a- or Cdc11b septin complexes were added to the microspheres and images were collected at steady state (1 hour). Representative images are maximum intensity projections. Magenta (lipid), green (septin). Scale bar 5 µm. (B) Box and whisker plot quantifying septin adsorption onto silica microspheres. Horizontal black bars represent the median. Vertical black bars represent the spread of the data. n> 50 beads for each curvature.

6.3.4 Cdc11a and Cdc11b complexes co-assemble into filaments

We next investigated if recombinant septin complexes containing either Cdc11a or Cdc11b could co-assemble into filaments *in vitro* in the absence of other cellular factors. First, we mixed

equal amounts of Cdc11a- and Cdc11b-capped septin complexes onto planar SLBs and examined filaments using two color TIRF microscopy. We observed filaments that contained both Cdc11a and Cdc11b septin complexes (Figure 6.4A,B), demonstrating that both classes of septin complexes are capable of co-assembling into filaments. However, we did notice that there appeared to be a higher density of Cdc11b-capped complexes on the membrane, despite adding equal concentrations of both septin octamers which was consistent with our previous results (Figure 6.2E). Interestingly, when we measured the steady-state filament length distribution of co-assembled polymers, we found that the average filament length was shorter than either Cdc11a or Cdc11b filaments alone (Figure 6.4C, and Figure 6.2A,B). Moreover, we observed an increase in filament persistence length (from ~1μm to ~2μm), suggesting that a "mismatch" interaction between Cdc11a-Cdc11b can influence filament rigidity (Figure 6.4D). Collectively, these data show that co-assembly of these different septin complexes can lead to polymers of distinct length and flexibility compared to either type of homopolymer.

Next, we measured septin adsorption onto SLBs of various curvatures after mixing equal concentrations of Cdc11a and Cdc11b together (Figure 6.4E,F). Unsurprisingly, we saw a curvature preference for beads where $\kappa = 2\mu m^{-1}$ for both Cdc11a- and Cdc11b-capped complexes, consistent with our previous observations (Figure 6.3A,B). Moreover, Cdc11b complexes showed a higher adsorption than Cdc11a complexes (Figure 6.4F). Interestingly, we observed less total adsorption of protein onto all tested curvatures when we mixed Cdc11a and Cdc11b complexes (Figure 6.4F) than we saw with either Cdc11a or Cdc11b alone (Figure 6.3B).

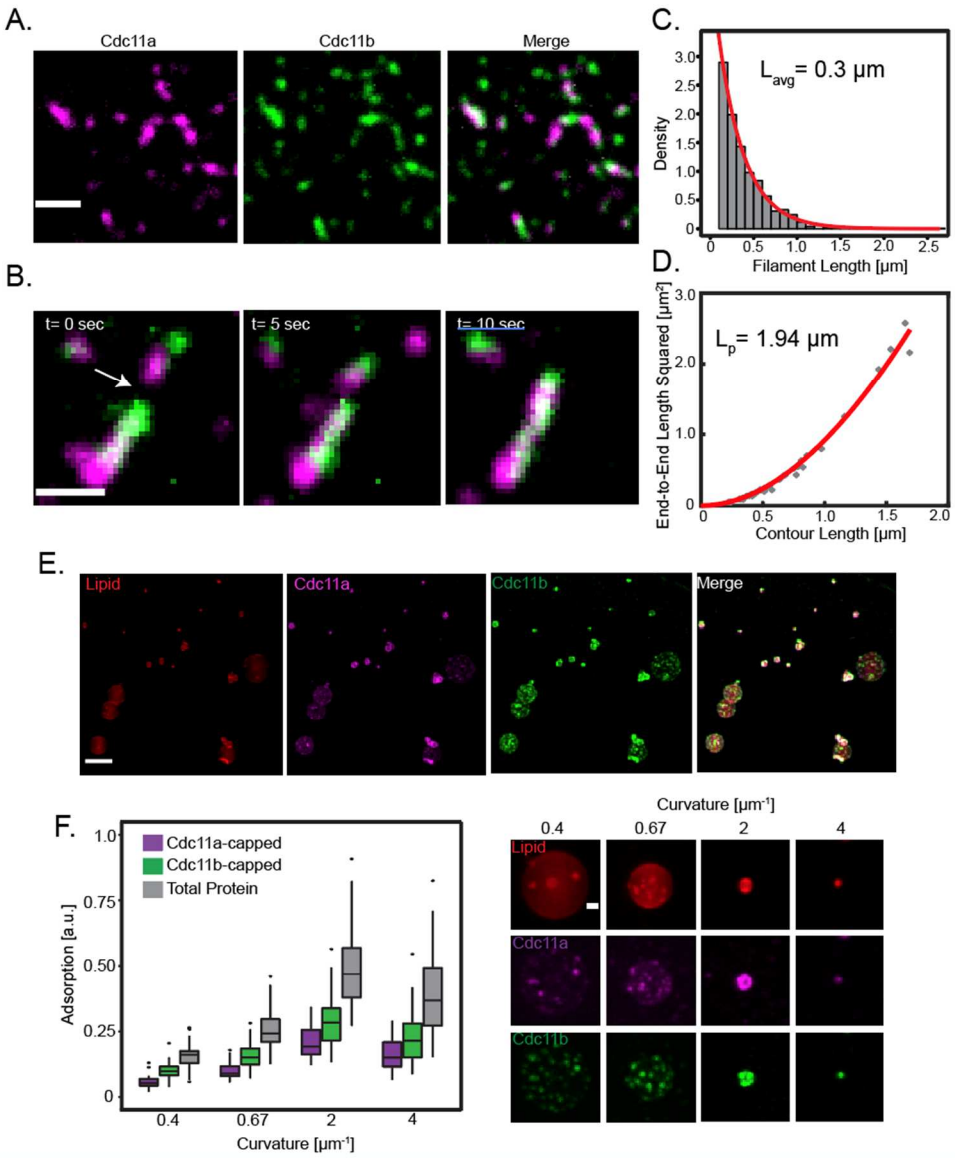

Figure 6.4 Cdc11a and Cdc11b complexes co-assemble into filaments on planar and curved membranes (A) Representative TIRF image of filaments assembled from 0.25 nM of Cdc11a- (magenta) and Cdc11b- (green) capped complexes (total 0.5 nM protein) on planar SLBs at steady state. Scale bar 5 µm. (B) Image montage highlighting an annealing event. Scale bar 1 µm. (C) Steady state fIlament length distribution. Red line is a single exponential fit from which the average filament length was determined. (D) End-to-end distance analysis was used to calculate the persistence length of co-assembled filaments. Filled black dots represent individual filaments. Red lines represent the best fit to equation 1. N > 60 filaments. (E) SLBs (75% DOPC, 25% PI, 0.05% Rh-PE) were formed onto silica microspheres with different curvatures (k= 0.4, 0.67, 2, and 4 µm-1). 7.5 nM of Cdc11a- and Cdc11b septin complexes (15 nM total protein) were added to the microspheres and images were collected at steady state (1 hour). Representative images are maximum intensity projections. Red (lipid), magenta (Cdc11a-capped complexes), green (Cdc11b-capped complexes). Scale bar 5 µm. (F) Box and whisker plot quantifying septin adsorption onto silica microspheres. Cdc11a-capped complex (purple) , Cdc11b-capped complex

(green) , and total protein (pink) are shown separately. Horizontal black bars represent the median. Vertical black bars represent the spread of the data. n> 30 beads for each curvature. Below are maximum intensity projections of single lipid-coated beads (red) of various curvature showing Cdc11a (magenta) and Cdc11b (green) adsorption. Scale bar 1 μm.

6.3.5 C-terminal extension chimeras do not phenocopy wild-type Cdc11a or Cdc11b filament or curvature sensing properties

Much of the sequence variation between Cdc11a and Cdc11b occurs within the C-terminal extension (CTE) region of the protein (Supplemental Figure 6S1). Therefore, we generated Cdc11 chimeras through swapping the CTE's of Cdc11a and Cdc11b to test if the CTE sequence was sufficient to impart the properties particular to either Cdc11a or Cdc11b. Using planar SLBs, we found that Cdc11a-Cdc11bCTE and Cdc11b-Cdc11aCTE-capped complexes had an average steady state filament length of 0.94 μm (~29 octamers) and 0.55 μm (~17 octamers), respectively (Figure 6.5B,D). Interestingly, Cdc11a-Cdc11bCTE-capped complexes are longer than Cdc11a-capped complexes, whereas there is no difference in average filament length between Cdc11b-Cdc11aCTE- and Cdc11b-capped septin complexes. Most surprisingly, we observed equal surface coverage for both types of polymers, despite their unequal average filament lengths (Figure 6.5C). Additionally, we observed that swapping the CTE's does not alter filament rigidity, as we calculated similar persistence length values for these complexes (Figure 6.5E). Next, we examined if swapping the CTE's would result in any differences in curvature sensitivity. We found that both chimeras still showed a curvature preference for 1 μm beads (Figure 6.5F,G). However, we did notice an increase in total adsorption onto the beads for both chimeras relative to their wild-type Cdc11a and Cdc11b-capped complexes (Figure 6.5F,G). Collectively, these data show that despite the CTE sequences harboring most of the sequence variation between the two Cdc11 paralogs, they are insufficient to recapitulate the biochemical/biophysical features of each Cdc11 polypeptide.

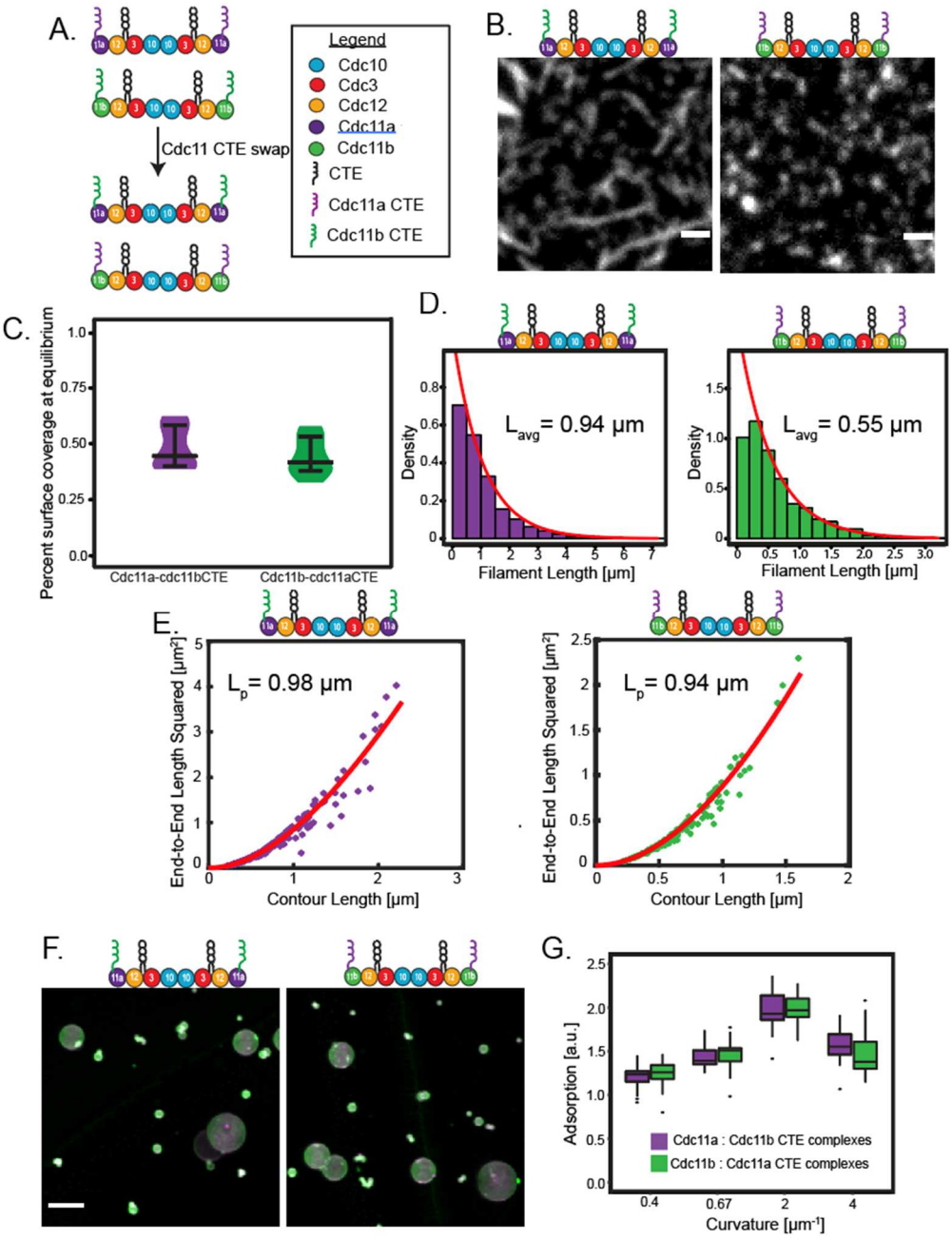

Figure 6.5 C-terminal extension chimeras do not phenocopy wild-type Cdc11a- or Cdc11b-capped octamer filament or curvature sensing properties. (A) Cartoon of septin octamers highlighting CTE swaps. (B) Representative TIRF image of 0.5 nM Cdc11a-Cdc11bCTE (left panel) and Cdc11b-Cdc11aCTE (right panel) capped filaments formed on a planar supported lipid bilayers (SLBs) (75% DOPC and 25% PI) at steady-state. Scale bar 1µm. (C)Violin plot showing the percent surface coverage for Cdc11a-Cdc11bCTE- and Cdc11b-Cdc11aCTE -capped filaments at steady-state on planar SLBs. Horizontal black bars represent the mean, vertical black bars represent the deviation from the mean. n=5 different locations on the bilayer. **(D)** Steady-state filament length distributions for Cdc11a-Cdc11bCTE- (left panel) and Cdc11b-Cdc11aCTE (right

panel) apped complexes. Distributions were fit to a single exponential (red) from which the average filament length was determined. (E) End-to-end distance analysis was used to calculate the persistence length of Cdc11a-(left panel) and Cdc11b- (right panel) capped filaments. m 1. N > 90 filaments for each sample. (F) SLBs (75% DOPC, 25% PI, 0.05% Rh-PE) were formed onto silica microspheres with different curvatures (k= 0.4, 0.67, 2, and 4 μm-1). 15 nM of Cdc11a-Cdc11bCTE- and Cdc11b-Cdc11aCTE-capped complexes were added to the microspheres and images were collected at steady state (1 hour). Representative images are maximum intensity projections. , Magenta (lipid), green (septin). Scale bar 5 μm. (G) Box and whisker plot quantifying septin adsorption onto silica microspheres. Horizontal black bars represent the median. Vertical black bars represent the spread of the data. n> 30 beads for each curvature.

6.3.6 A single point mutation can tune the filament length distribution of Cdc11a-capped complexes.

Given that the CTEs were not sufficient to interconvert the function of the different Cdc11 proteins, we examined the predicted structure of the globular portion of the protein to search for any differences between these two proteins. We threaded both Cdc11a and Cdc11b through Phyre 2 (L. A. Kelley *et al.*, 2015) and overlaid the predicted structures (Figure 6.6A). Despite most of the globular core being highly conserved among both gene products, we found a single sequence variation located just before a prominent difference in predicted structure. Specifically, Cdc11a contains a threonine at position 62, whereas Cdc11b contains an alanine. Interestingly, the Cdc11a sequence flanking this substitution is predicted to be more helical, whereas the structure within this region of the Cdc11b polypeptide is predicted to be disordered. With these potential structural differences in mind, we purified Cdc11a T62A and examined the steady-state filament length distribution on planar supported bilayers. Remarkably, we observed that the average filament length of these complexes was dramatically reduced when compared to wild-type Cdc11a-capped complexes, and much closer to the average filament length of wild-type Cdc11b-capped complexes (Figure 6.6B,C). Moreover, the surface coverage of Cdc11aT62A-capped complexes was similar to Cdc11b-capped filaments (Figure 6.6D). Interestingly, this portion of the polypeptide is not located at the surface of the canonical polymerization interface (N-C interface). However, as Cdc11 polypeptides are mirror images of one another, we speculate that when neighboring Cdc11-

capped octamers oligomerize this region of the protein could participate in interactions that drive polymerization. Alternatively, by altering this residue, we've induced conformational changes at the polymerization interface. In sum, these data show that even a single amino acid difference can alter the degree to which septins form filaments, which is a fundamental feature of the septin cytoskeleton.

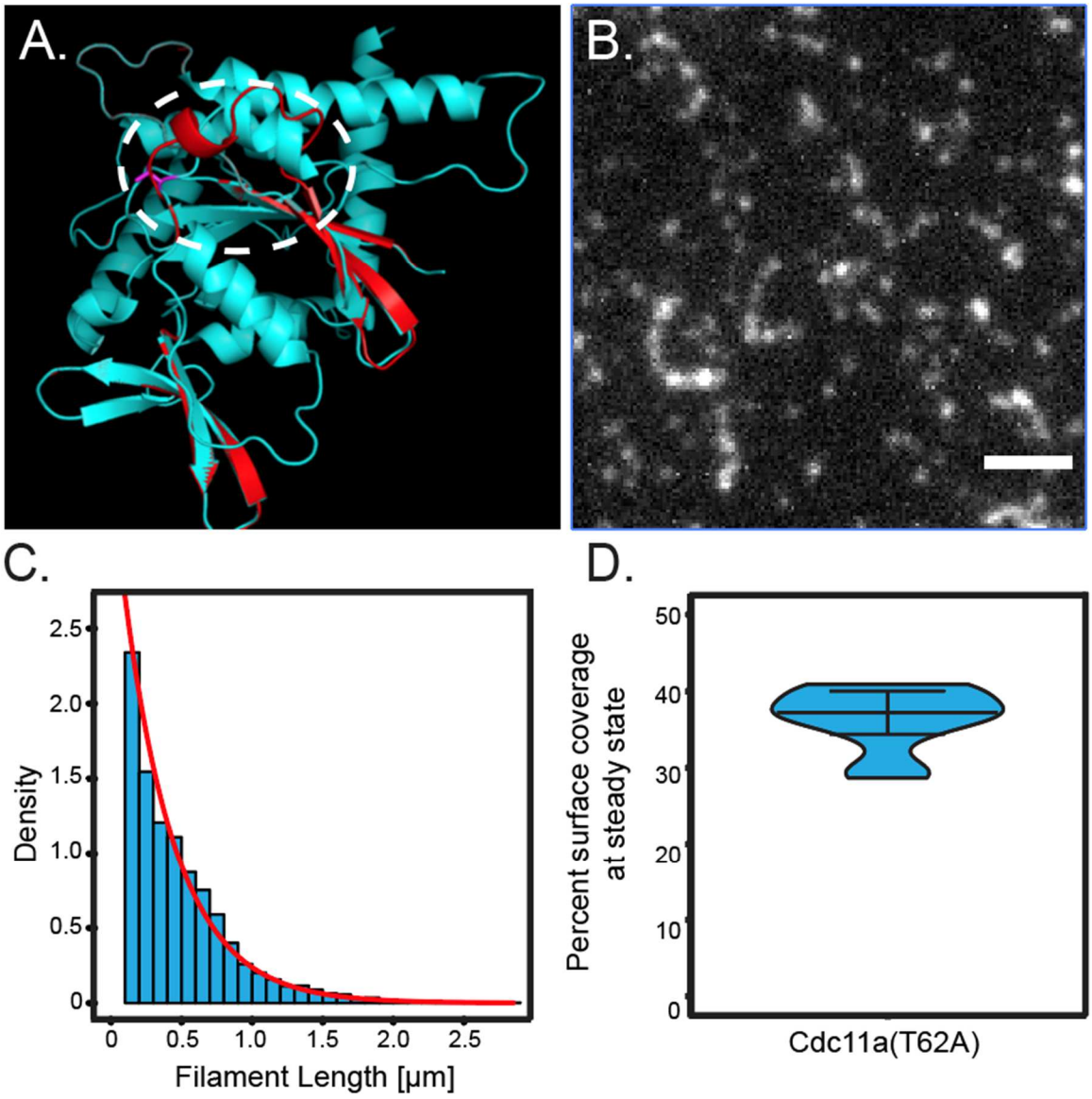

Figure 6.6 A single point mutation within a novel polymerization interface can tune the filament length distribution of Cdc11a-capped complexes. (A) Cdc11a (cyan) and Cdc11b (red)

primary sequences were threaded through the structural prediction algorithm Phyre and overlayed through Pymol. The site of structural divergence is circled and is preceded by a single amino acid difference (magenta). (B) Representative TIRF image of 0.5 nM Cdc11aT62A- capped filaments formed on a planar supported lipid bilayers (SLBs) (75% DOPC and 25% PI) at steady-state. Scale bar 2μm. (C) Steady-state filament length distributions for Cdc11aT62A- capped complexes**.** Distributions were fit to a single exponential (red) from which the average filament length was determined. (D) Violin plot showing the percent surface coverage for Cdc11aT62A-capped complexes at steady-state on planar SLBs. Horizontal black bars represent the mean, vertical black bars represent the deviation from the mean. n=10 different locations on the bilayer for 3 different bilayers.

6.3.7 Cdc11b is expressed in vivo and colocalizes with Cdc11a-capped octamers.

We next examined the expression timing and localization of Cdc11a- and Cdc11b-capped octamers in cells. As the *CDC11b* locus could encode a pseudogene that is not expressed, we examined transcript levels of *CDC11b* over time. We found that both *CDC11a* and *CDC11b* transcripts are regulated throughout the life cycle of *A. gossypii.* Specifically, *CDC11b* transcripts are abundant inside spores and following germination, the number of transcripts is reduced until 18 hours, where the *CDC11b* transcript begins to increase in abundance, whereas we see a steady increase in *CDC11a* expression over time through 18 hours (Supplemental Figure 6S2),

Next, we wanted to visualize the localization of Cdc11 polypeptides over time in *A. gossypii*. During hyphal growth, septins can assemble into several major structures: 1) Thin filaments, which run along the cell cortex; 2) Inter-region rings, that consist of bundles of septin filaments aligned parallel to the long axis of the hyphal tube; 3) Branch point structures, where septins localize to sites of micron-scale curvature at the base of emergent hyphae that extend perpendicular to the main hyphal axis; 4) Symmetrical tip-splitting structures where septins localize to the micron-scale curvature at the bases of bifurcated tips (Helfer and Gladfelter, 2006; DeMay *et al.*, 2009; Bridges *et al.*, 2016). To examine the localization of Cdc11a and Cdc11b-capped octamers at these various structures through time, we generated a strain

that co-expressed Cdc11a-mCherry and Cdc11b-eGFP under the control of their native promoters and imaged using confocal microscopy. We observed robust Cdc11a localization at all septin structures from 12 to 24 hours (Figure 6.7B). When we measured the ratio of Cdc11a- to Cdc11b-capped octamer fluorescence intensity at branch point and IR-ring structures from 12 to 18 hours, we find a consistently higher level of Cdc11a relative to Cdc11b (Figure 6.7C,D). Only at 24 hours do we observe Cdc11b localization at septin structures and a reduction in the ratio of Cdc11a- to Cdc11b-capped octamers, suggesting at 24 hours Cdc11b-capped octamers become the dominant Cdc11 species (Figure 6.7C,D). However, there is still remnant Cdc11a-capped octamer present at this time at all septin structures, suggesting that these two Cdc11-capped octamers are capable of co-assembling *in vivo* (Figure 6.7B-D). These data show that expression of Cdc11a and Cdc11b proteins are regulated in a temporal fashion.

Given that mixed Cdc11a and Cdc11b-capped complexes had different septin filament lengths compared to homopolymers *in vitro*, we next examined how increasing levels of Cdc11b influenced the length of septin filaments incorporated into branch points and inter-region rings. We find that at branch points, the average filament length decreases over time, with the shortest filament occurring at 24 hours, consistent with Cdc11b localization to these structures (Figure 6.7D). Interestingly, when we examined septin filament length at IR rings, we found that the average filament length increases over time, with the longest filaments occurring at 24 hours. However, inter-region rings are known to be regulated by the kinases Elm1 and Gin4 (DeMay *et al.*, 2009), suggesting that post-translational modification of septins could be another means to regulate filament length in higher-order structures. To examine if this length change was associated with differences in filament dynamics by monitoring the recovery of Cdc11a- and Cdc11b-capped complexes after photobleaching after 24 hr growth at both branch points and IR-

rings. We observed similar $t_{1/2}$ for both proteins, suggesting that the both types of septin complex are incorporating with similar rates within the time resolution of the acquisition (Figure 6.7E,H). Collectively, these data show that Cdc11b expression affects filament length both positively and negatively depending on the type of septin structure in *A. gossypii*.

Next, we investigated if Cdc11a and/or Cdc11b could functionally compensate for one another. To do this, we generated deletion strains (where either *CDC11A* OR *CDC11B* were deleted from the genome) and examined *A. gossypii* cell morphologies using DIC microscopy. We find that cells lacking *CDC11A* exhibit multiple morphology phenotypes at both 18 and 24 hours, including hyper-branched hyphae, long, persistent hyphae where no lateral branches emerge, and aberrant tip-spliting events (Figure 6.7J). Cells lacking *CDC11B* exhibit no observable morphological defects at 18 hours, however at 24 hours we observe aberrant tip-splitting events (Figure 6.7K). Interestingly, the tip-splitting defects observed in cells lacking *CDC11A* are different than those in cells lacking *CDC11B*. Tip-splitting hyphae in *cdc11aΔ* are asymmetric and appear to undulate in a wave-like pattern and are thicker than those in *cdc11bΔ* tip-splitting hyphae. Moreover, *cdc11bΔ* tip-splitting hyphae are both asymmetric and symmetric, and were observed to undergo tri- and quadfurcations (Figure 6.7K). This is in contrast to wild-type cells where tip-spliting events are always bifurcation events (Figure 6.7I). This data suggests that Cdc11a and Cdc11b have distinct, developmentally regulated functions. To further verify that these phenotypes are loss of function alleles we generated replacement strains, (where either the *CDC11A* or *CDC11B* gene would replaced the other) such that *A. gossypii* would either express two copies of *CDC11A* or *CDC11B*. We find that cells with two copies of *CDC11B* still show hypherbranching and tip-splitting phenotypes reminiscent of *cdc11aΔ* cells (Figure 6.7L). However, the tip-splitting phenotype is less severe than *cdc11aΔ*

cells, suggesting that *CDC11B* can partially functionally compensate for *CDC11A*. In cells with two copies of *CDC11A*, we observe normal growth relative to that of wild-type at 18 hours, however, at 24 hours we observe a high frequency of tip-splitting events, moreso relative to wild-type cells. Interstingly, these tip-splits appear to be morphologically indistinguishable from that of wild-type cells, suggesting that *CDC11A* can functionally compensate for *CDC11B* with respect to hyphal morphology, however it cannot properly compensate in regulating the number of tip-splitting events. Collectively, these data suggest that despite their high sequence similarity, Cdc11a and Cdc11b proteins exhibit discrete functions during the course of the growth cycle of *A. gossypii*.

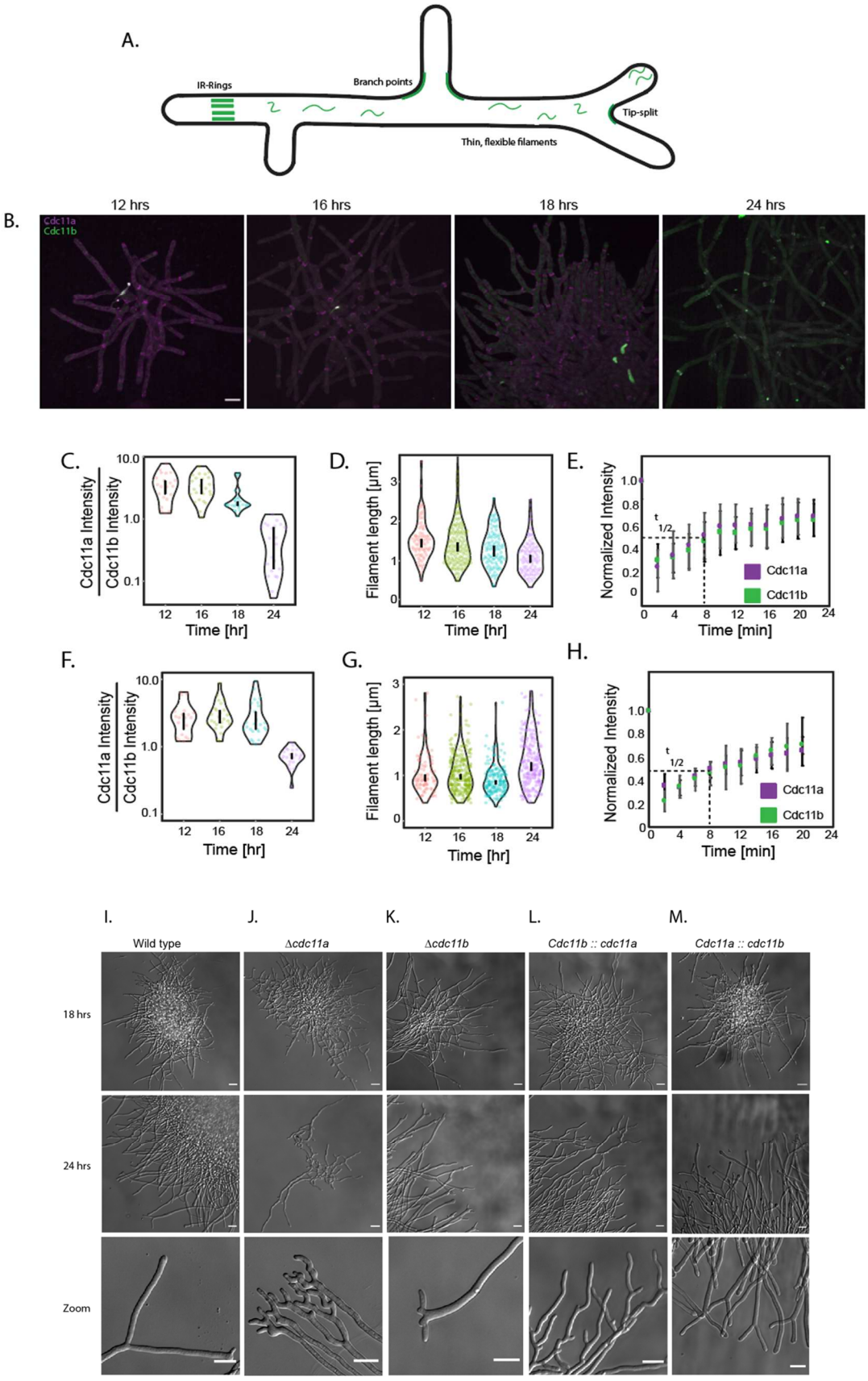
A.
IR-Rings
Branch points
Tip-split
Thin, flexible filaments
B.
12 hrs
16 hrs
18 hrs
24 hrs
Cdc11a
Cdc11b
C.
Cdc11a Intensity / Cdc11b Intensity
Time [hr]
D.
Filament length [µm]
Time [hr]
E.
Normalized Intensity
t 1/2
Cdc11a
Cdc11b
Time [min]
F.
Cdc11a Intensity / Cdc11b Intensity
Time [hr]
G.
Filament length [µm]
Time [hr]
H.
Normalized Intensity
t 1/2
Cdc11a
Cdc11b
Time [min]
I.
J.
K.
L.
M.
Wild type
Δcdc11a
Δcdc11b
Cdc11b :: cdc11a
Cdc11a :: cdc11b
18 hrs
24 hrs
Zoom

Figure 6.7 Cdc11a and Cdc11b localization to septin structures is temporally regulated. (A) Cartoon of a simplified *A. gossypii* to highlight to variety of septin structure (B) Maximum intensity projections of A. gossypii cells expressing integrated Cdc11a-mCherry (magenta) and Cdc11b-GFP (green) at different time points. Scale bar 10 μm. (C) Violin plot of the ratio of Cdc11a to Cdc11b sum intensities at branched structures over time. Vertical bars represent the 95% confidence interval. N > 20 septin structures analyzed in > 7 different cells. (D) Violin plot showing measured septin filament lengths at branched structures over time. Vertical bars represent the 95% confidence interval. N > 100 septin filaments analyzed in > 7 different cells. (E) Recovery curve of Cdc11a (magenta) and Cdc11b (green) at curved structures. Dahsed lines represent the time of half-maximal recovery. Error bars represent the standard error. N= 10 cells. (F) Violin plot of the ratio of Cdc11a to Cdc11b sum intensities at IR-ring structures over time. Vertical bars represent the 95% confidence interval. N > 20 septin structures analyzed in > 7 different cells. (G) Violin plot showing measured septin filament lengths at branched structures over time. Vertical bars represent the 95% confidence interval. N > 100 septin filaments analyzed in > 7 different cells. (H) Recovery curve of Cdc11a (magenta) and Cdc11b (green) at curved structures. Dahsed lines represent the time of half-maximal recovery. Error bars represent the standard error. N= 10 cells.
(I-M) Representative DIC images of *A. gossypii* cells imaged on agar pads after either 18 or 24 hours in liquid culture. Zoomed in image highlights tip-splitting events. All scale bars 20 μm.

6.4 Discussion

In this study we investigated the effects of having two similar, but distinct terminal subunits (Cdc11a and Cdc11b) on septin filament properties using in vitro reconstitution and in vivo imaging. Our data demonstrates that small changes in individual septin subunits can alter septin filament length, which in turn can influence the kinetics of septin assembly onto membranes. Collectively, our data highlight how cells might utilize different pools of available septin polypeptides to alter their biochemical/biophysical properties of the septin cytoskeleton to best suit downstream functions.

Our *in vitro* data show that when Cdc11a- and Cdc11b-capped complexes were seeded onto planar SLBs, Cdc11a-capped complexes formed filaments ~2x longer than Cdc11b-capped complexes. These data suggest that the affinity between Cdc11a-Cdc11a subunits is stronger than Cdc11b-Cdc11b subunits. However, we were surprised when we saw that Cdc11b-capped complexes showed a higher density of membrane-bound septin than Cdc11a-capped complexes.

Our previous data showing that single septin octamers are unable to stay bound (high off rate) to the membrane suggesting that septins must form filaments (to effectively lower the off rate) to remain associated with the membrane (Bridges *et al.*, 2016; Cannon *et al.*, 2019). Thus, we thought that septin complexes that could form longer filaments would show a higher density of septins on the membrane. In contrast, we see that Cdc11b-capped complexes, despite forming shorter filaments, show a higher degree of membrane binding than Cdc11a-capped complexes. We speculate that the interaction strength of Cdc11b-Cdc11b interactions is strong enough to form filaments that are capable of staying bound to the membrane (an effective off rate that is low). Furthermore, because the affinity of Cdc11b-Cdc11b interactions is weaker than Cdc11a-Cdc11a interactions, this could allow a higher number of shorter, but stably bound filaments to form on the membrane, effectively increasing the number of binding sites (free filament ends) for which single octamers, either coming from the bulk solution, or diffusing on the membrane could interact. This, in turn, would increase the density of septins on the membrane (Figure 6.8). Thus, the shorter filaments formed by Cdc11b have essentially a comparable and very low off rate as the filaments formed from Cdc11a, but by being shorter, there are more binding sites at the ends to enhance recruitment of new subunits, yielding a higher density of septins bound to the membrane. However, this might not be due to filament length alone as Cdc11a-Cdc11bCTE-capped complexes show similar membrane binding density despite having different filament lengths. Interestingly, CTE regions of septins has been shown to influence septin filament pairing (Aurélie Bertin *et al.*, 2010). We speculate that these difference is surface coverage may also be due to filament pairing, however we were unable to detect any differences in fluorescence intensity or filament width by light microscopy methods (data not shown). Future work will have to use higher resolution methods to test this hypothesis.

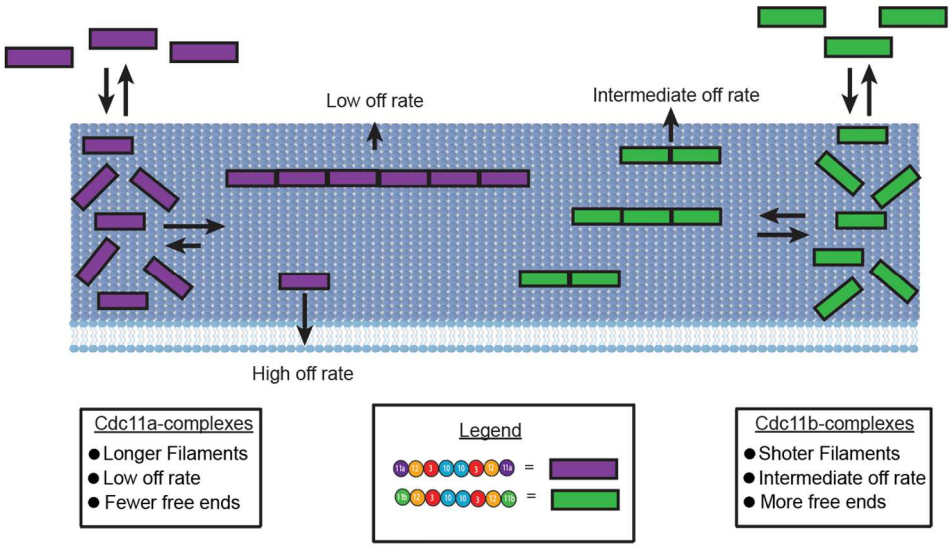

Figure 6.8 Kinetic argument for how short filaments promote higher membrane adsorption by septins Single septin octamers from the bulk initially bind to the membrane with the same on and off rates. Through diffusion, septin octamers will collide to form filaments. The overall length of the filaments depends on the strength of the Cdc11 interaction, such that Cdc11a-capped complexes form longer filaments than Cdc11b-capped complexes. However, not all septin octamers will get incorporated into filaments before dissociating from the membrane (high off-rate). Although, Cdc11b-capped filaments are shorter than those with Cdc11a, there is a greater number of filaments on the membrane. This in turn provides more binding sites (free filament ends) for nearby complexes on the membrane / in bulk solution to interact leading to an increase in adsorption for Cdc11b-capped complexes.

Interestingly, we found that Cdc11a- and Cdc11b-capped complexes are capable of co-polymerizing into filaments that show different biochemical/biophysical properties than filaments arising from either type of complex alone. We saw that co-polymerized filaments showed an increase in filament rigidity relative to filaments capped with either complex alone, highlighting the importance of the terminal subunit in controlling filament flexibility. It should be noted, however, that the persistence length values reported here are lower than those previously reported for septins. However, we are confident in our values as we have measured a higher number of filaments than in our previous reports ((Bridges *et al.*, 2014; Khan, Newby and Gladfelter, 2018) and used both the end-to-end and cosine correlation analysis (data not shown) methods to calculate persistence length (Graham *et al.*, 2014), which yielded similar values.

When Cdc11a- and Cdc11b-capped complexes are mixed at a 1:1 ratio the average filament length at steady-state and total adsorption onto membrane curvature is decreased relative to Cdc11a or Cdc11b-capped complexes. Consistent with this, the average filament length at branch points decreases as Cdc11b expression increases. In contrast, as Cdc11b expression increases, we observe longer filaments at IR-rings. However, IR-rings are known to be regulated by the kinase Elm1 (DeMay *et al.*, 2009), suggesting that septin filament length can be further regulated by post-translational modifications. As a major function of septins is to serve as a scaffold, we suspect that by controlling the local concentration of septins (through regulating filament formation) at the membrane, the cell can subsequently tune the concentrations of septin-interacting proteins that promote processes such as polarized growth and mitotic progression. Future work should determine the precise stoichiometry between Cdc11a- and Cdc11b-capped complexes and how these relative levels regulate the total septin concentration on the membrane.

All known fungi with budding yeast-like genomes, even those which underwent a genome duplication event carry a single copy for each septin. Interestingly, *Ashbya* species are the excepton by carrying two copies of *CDC11* (Gattiker *et al.*, 2007). What then makes *Asbhya* unique? *Ashbya* has evolved a life style of a filamentous fungus with continuously growing and branching hyphae. The closely related *E. cymbalariae*, *E. sinecaudum* and *E. coryli* carry one *CDC11* gene, yet also form hyphae. However, none of these three species exhibit two branching patterns, namely lateral branching (low speed growth, 0.2 μm/min for emergant germling hyphae) and symmetrical tip-splitting events (faster growth, 3.5 μm/min within 24 hours) (Köhli *et al.*, 2008). It is important to note that lateral branches are the predominant mode of growth early in *Ashbya* development (Knechtle, Dietrich and Philippsen, 2003), whereas tip-splitting events begin later stages of growth (around ~18 hours) (Ayad-Durieux *et al.*, 2000). Our deletion and replacement data suggest that

Cdc11a is important in lateral branching and tip-splitting. In contrast Cdc11b plays a minor role in lateral branching, potentially just to limit the local concentration of septin-interacting proteins at these sites by having shorter filaments, however, it is more important for tip-splitting events. Interestingly, cells with two copies of *CDC11B* still show asymmetric tip-splitting events, suggesting that *CDC11A* and *CDC11B* either have distinct functions at these sites or the length distribution/number of septins at tip-splits must be precisely regulated as to control the localization of polarity proteins required for symmetry breaking including Cdc42 and Bni1 (Seiler and Plamann, 2003; Schmitz *et al.*, 2006).

The septin superfamily is thought to have emerged from ancient gene duplications that gave rise to the different classes of septins shared across many eukaryotes (Pan, Malmberg and Momany, 2007; Auxier *et al.*, 2019). This recent duplication of a terminal septin subunit reveals how small changes in the primary sequence can lead to substantial biophysical differences for the polymer providing a glimpse at how functional diversification may have occurred in this gene family.

6.5 Supplemental material

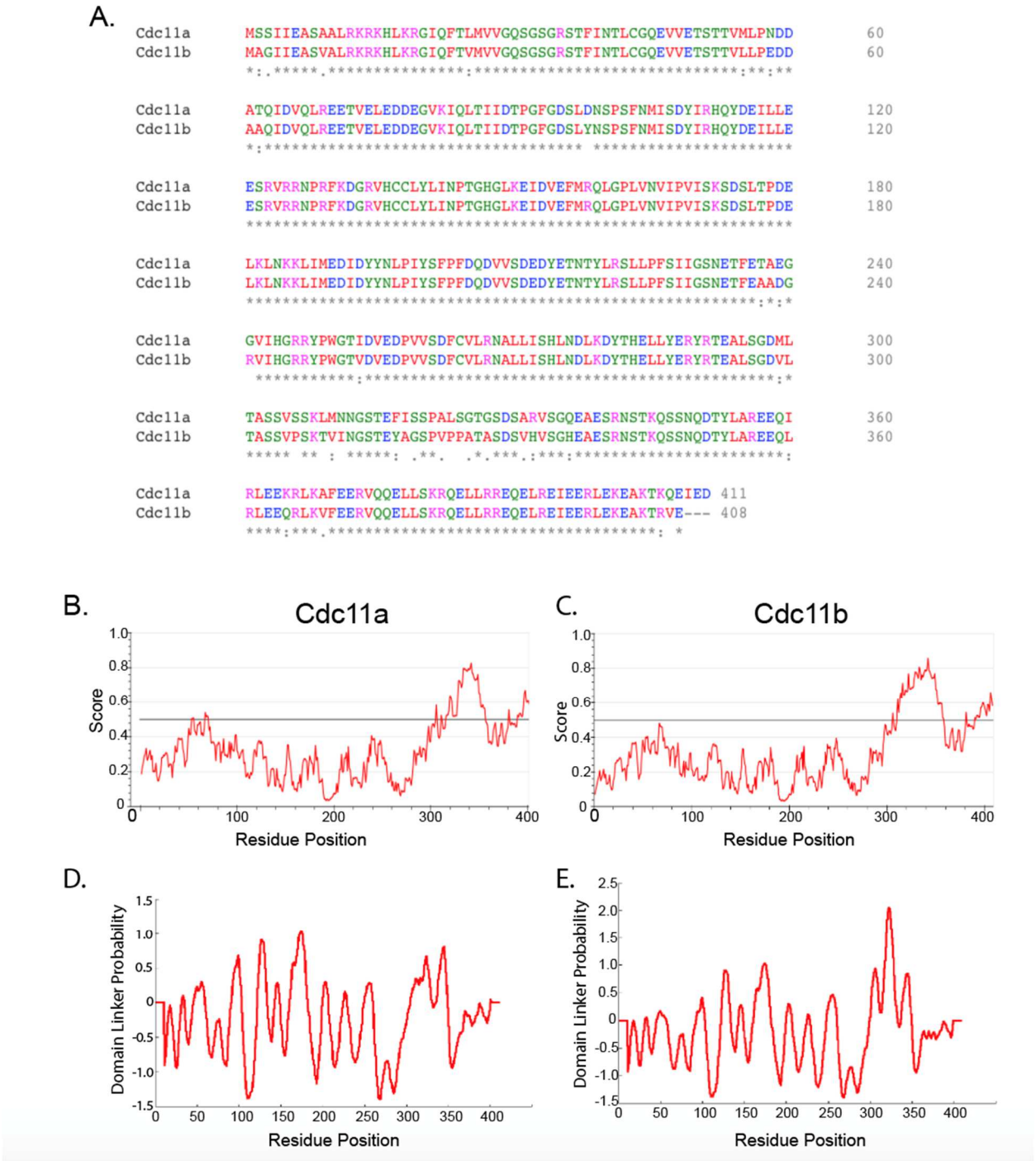

Figure 6S1 The highest degree of sequence variation between Cdc11a and Cdc11b is within the C-terminal extension (A) Primary sequence alignment of Cdc11a and Cdc11b. (B,C) IUPRED output of predicted intrinsically disordered regions within Cdc11a (panel 1) and Cdc11b (panel 2) polypeptides. (D,E) Loop-length-dependent support vector machine prediction of protein domain linkers in Cdc11a and Cdc11b polypeptides, respectively.

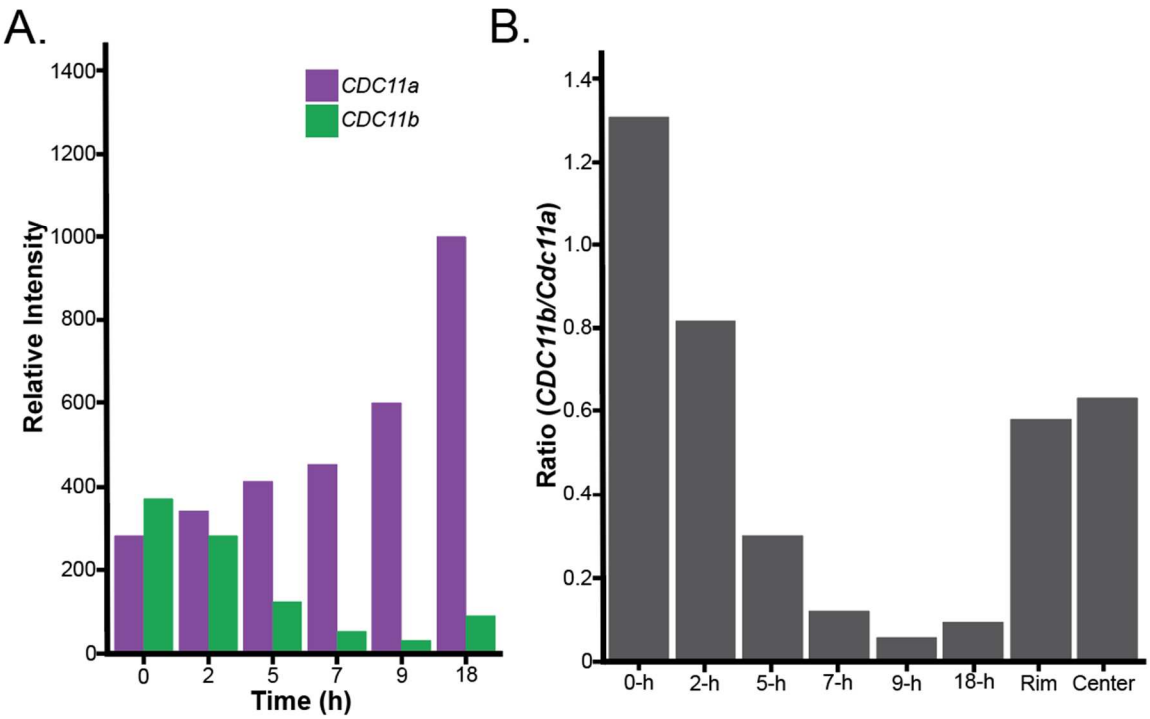

Figure 6S2. *CDC1b* transcription is regulated over time. (A) *CDC11b* transcription is repressed in early time points in liquid media. *CDC11b* transcript is relatively abundant in the spores (0-h), and repressed after germination. (B) Spores contain a higher ratio of *CDC11B/CDC11a* transcript. After germination, *CDC11a* transcripts are more abundant. In mature mycelia, the ratio of *CDC11a*:*CDC11b* is closed to 2:1

CHAPTER 7

DISCUSSION AND FUTURE WORK

This thesis provides insight into the mechanisms used by septins to preferentially assemble onto micrometer-scale membrane curvatures. First, we showed that septins contain a highly conserved amphipathic helix, which is necessary for preferential assemble onto curved membranes. We have extended these studies to show that the amphipathic helix might also be involved in regulating septin bundling, suggesting their might be an interplay between membrane binding and septin-septin interactions. Next, we utilized several *in vitro* reconstitution and physical modeling approaches to determine the scale(s) by which curvature sensing by septins operates; at the level of single octamers to filaments. Although the work done in this theisis has shed new light on how septins assemble onto curved membranes, there are two infinitely deep rabbit holes for the next graduate student/post doc to jump into: i.) the structural basis of curvature sensing by septins and ii.) the kinetic and thermodynamic processes that drive this micrometer-scale curvature preference. In the following sections I will elaborate on what we know about each of these rabbit holes and my perspective on their future.

7.1 The structural basis of curvature sensing by septins

For proteins that sense nanometer-scale membrane curvature, amphipathic helices utilize the increased space between lipid headgroups (lipid packing defects) that results from the highly bent membrane as binding sites (Drin and Antonny, 2010). This

mechanism of AH binding, refered to as the “wedge model”, postulates that the shallow AH insertion alleviates the stress of the membrane induced by membrane curvature. This suggests that these AH’s interact mostly with the lipid head groups of the membrane, although there are most certainly interactions with the hydrophobic portion of the AH domain with the hydrocarbon tails of the fatty acyl chains of the lipid molecules. Interestingly, in prokaryotes, the protein SpoVM utilizes an insertional amphipathic helix to sense micrometer-scale membrane curvature. However, through experiment and simulation, the AH of SpoVM was observed to penetrate deep into the membrane, coming into contact mostly with the acyl chains of lipids (Gill, J.-P. Castaing, *et al.*, 2015). This is an interesting observation and leads me to wonder how if the penetration depth of septin AH domains is similar to that of SpoVM. Perhaps micrometer-scale curvature sensors operate at the level of the fatty acyl chain of the lipid rather than the polar head group of lipids. Why then would micrometer-scale curvature sensors need to insert deep into the bilayer to feel membrane geometry? I don’t think we really have a good answer for this. We speculate that it could have something to do with how curvature influences fatty acyl chain packing within the membrane, which in turn can influence the interaction landscape (i.e. hydrophobic interactions) between the membrane and the AH. This in turn might alter the structure of the AH in the membrane, such that we might expect an ensemble of helical structures (i.e. length of the AH helix) each with unique binding strengths thereby leading to preferential assembly onto membranes in a geometry depenent manner. Another interesting hypothesis is that the membrane environment provides a platform for which AH domains can oligomerize. It was speculated that SpoVM molecules oligomerize in

the membrane (Gill, J.-P. Castaing, *et al.*, 2015), and preliminary single molecule TIRF images of recombinant septin AH domains on membranes give some creedence to this theory. Interestingly, although our recombinantly purified AH domains sense micrometer-scale curvature, single septin octamers (containing the same number of AH domains), were found to have higher association rates for nanometer-scale curvature.. It is possible that in the context of the septin, AH domains might only be able to oligomerize once filaments have formed and septins become stably bound to the membrane through avidity. If one decides to pursue these experiments, be sure to use a variety of different lipid mixtures with different physicochemical properties include acyl chain length and charge, as these properties may control penetration depth of the AH domain, oligomerization potential, and even curvature sensitivity.

An interesting feature of the septin complex is the spacing of AH domains within a single septin heteromer. As the number of polypeptides and length within a septin heteromer change depending on the organism of interest, so does the distance between neighboring AH domains. For example, the distance between AH domains in budding yeast and mammalian septins is ~24 and ~16 nm, respectively. Interestingly, experiments from our lab show that there is a difference in curvature sensitivity between these two septin complexes (Bridges *et al.*, 2016). These observations lead us to hypothesize that the spacing between AH might function as a "molecular ruler", effectively setting the scale for curvature sensitivity by septins. We have preliminary data showing how the spacing of AH domains impacts curvature sensitivity in the context of septin complexes as well as the AH alone (Figure 7.1 and Appendix), however it is incomplete and requires further experimental evidence. One must ask

then, what the structural basis for shift in curvature sensitivity? Is the distance between AH domains serving as a "ruler", and if so, what is it measuring? It could be the distance between lipid packing defects (binding sites), which would scale with membrane curvature (higher curvature = higher frequency of lipid packing defects). Additionally, by having AH domains spaced further apart, the septin complex could explore more physical space on the membrane, potentially to find defects over long distances. As the defects on the micron-scale are much less frequent (and thus probably spaced further apart) than those on the nanometer scale, increased space between AH domains could promote an increased probability of fruitful interact with the membrane. To test this hypothesis, it will be important to finish the experiments started in Appendix 5 and 6. Additionally, it might be fruitful to purify recombinant septin heteromers from different organisms with differently spaced AH's to show their curvature preference gain more insight into this interesting hypothesis.

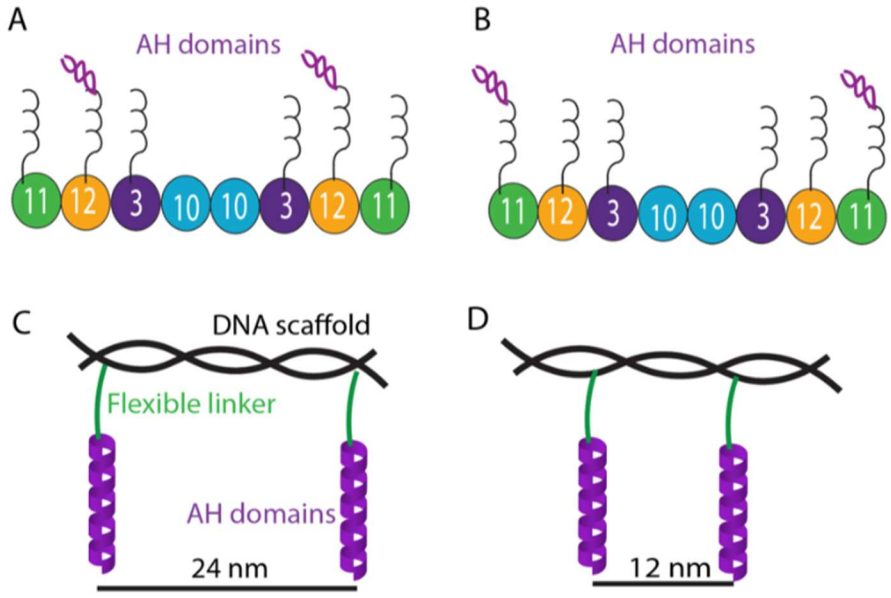

Figure 7.1 Construct designs to test the role of AH spacing in curvature sensing. (A) Cartoon of a wildtype septin complex where the AH domains (purple) are located on the C-terminus of Cdc12. (B) Example of an chimera where the AH domain (purple) has been moved

to the C-terminus of Cdc11, effectively changing the distance between AH domains compared to wildtype. (C) Cartoon of synthetic AH constructs we can generate with collaborator Ronit Freeman. The AH domains (purple) can be tethered to a flexible linker (green) which can be linked to a DNA scaffold (black). (D) An example of another synthetic construct where the distance between AH domains has been shortened.

7.2 Kinetic and thermodynamic basis of curvature sensing by septins

In this thesis, we showed that membrane curvature influences single septin octamer binding kinetics, diffusion, and filament formation. This is clear evidence that curvature sensing by septins operates throughout the entire septin-membrane interaction coordinate (Figure 1.2A and Figure 4.1A). Our observations showing single octamers show an enchanced association rate that scales superlinearly with membrane curvature (thus, octamers do not have a micrometer-scale curvature preference), but that septin filaments are longer on micrometer scale curvatures suggests that there must be a fine balance between each of these steps such that septins preferentially assemble onto curved membranes in a geometry-dependent manner. However, the limitations of light and electron microscopy make it difficult or impossible to measure several of the kinetic and thermodynamic process in the septin assembly process including coopertivity, annealing / fragmentation rates, and how the dissociation rate of septin filaments from the membrane scales with length. To circumvent this, we have established two different approaches through collaboration: 1.) Simulation and modeling (Preliminary work is described in Chapter 4 of this thesis). 2.) High-speed atomic force microscopy (Preliminary work is described in Chapter 5 of this thesis). Future work should aim to use simulation and modeling approaches to predict the importace of specific kinetic and thermodynamic steps within the septin-membrane reaction coordinate for curvature sensing. For example, if we simulate septin binding to

curved membranes by enhancing the rate of annealing (filament formation) with curvature, while keeping all other parameters (i.e. octamer association rate or fragmentation rate) constant, can we change the preferential assembly of septins onto a given membrane curvature? With these predictions in mind, we can then turn to high-speed atomic force microscopy to measure these processes in (i.e. assembly / fragmentation rates, and filament bending energy) in a curvature-dependent manner in real time with nanometer-scale resolution (Figure 7.2).

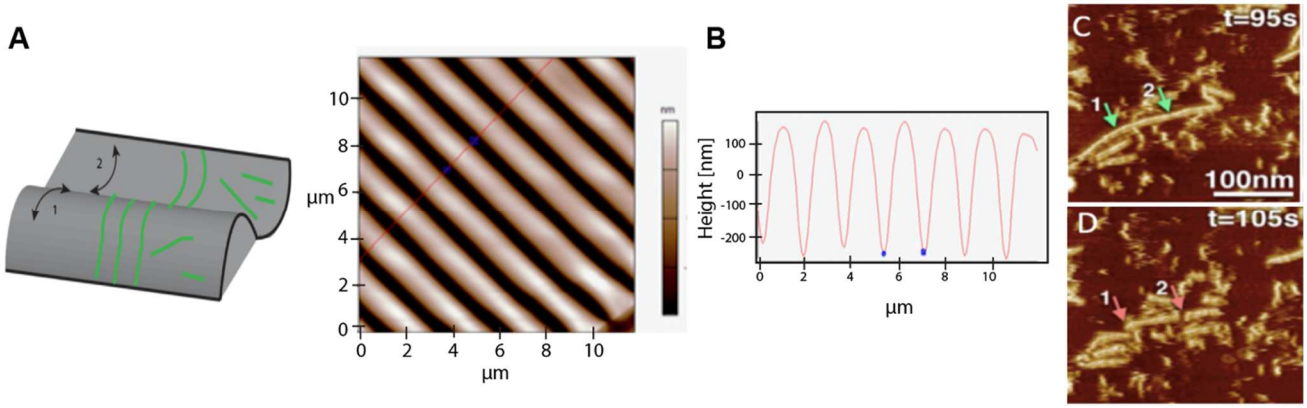

Figure 7.2 Experimental design for imaging septins on curved surfaces using high speed atomic force microscopy
(A) Panel I: Schematic of solid-support undulating surface. Both positive (1) and negative (2) curvatures can be fabricated and tuned. Examples of potential orientations of septin filaments of varying lengths (green) can be imaged with nanometer resolution using HS-AFM. Panel II: Example of a curved substrate via AFM. (Image courtesy of Ronit Freeman lab). (B) Height profile of the undulating surface shown in A, panel II. (C-D) Imaging of septins on a flat mica surface using high speed AFM. (Image courtesy of Simon Scheurring lab). Red arrow marks point of reference. Green arrow marks fragmentation events.

As septins have been shown to recruit upwards of sixty proteins to the bud-neck in *S. cerevisiae* (Gladfelter, Pringle and Lew, 2001), it will be exciting to see if/how the above kinetic processes change in response to interaction with the large suite of septin binding proteins. Work done in the Gladfelter lab by Ben Woods has shown that septins polymerized from budding yeast extracts exhibit differences in flexural rigidity and

filment length depending on the genetic background of the extract (Personal communication). However, the curvature sensitivity in the presence / absence of septin interacting proteins has yet to be tested. This will be an exciting avenue of future research.

APPENDIX I

PRELIMINARY DATA: ASSESSING THE ROLE OF ELECTROSTATICS IN SPETIN-MEMBRANE AND SEPTIN-SEPTIN INTERACTIONS

Rationale

We are only beginning to understand how septins interact with membranes. The current dogma in the field is that septins interact with membranes through several polybasic patches (2-3 amino acid stretches) present near the N-termini in several septin polypeptides. Lacking structural data within these regions, and over-interpretation of data (in my opinion!), it is difficult to say whether or not these stretches of basic residues actually participate in membrane binding. Work from this thesis has shown that septins possess a highly conserved amphipathic helix, which is both necessary and sufficient for sensing membrane curvature. However, truncation of the AH domain in the context of the budding yeast hetero-octamer shows that although septins fail to preferentially assemble onto membrane curvature, they still do bind membranes. It is clear from these data that either: 1.) the polybasic domain is a real membrane binding domain, or 2.) there is a yet another unidentified septin-membrane interaction motif. However, before the AH domain was identified, it was important to see if the binding of septins to curved membranes was electrostatic by nature.

Methods and Results

To test if the septin-membrane interaction is driven by electrostatic interactions, septins were allowed to bind to beads of various membrane curvatures under normal binding conditions (100 mM KCl and pH 7.4). Increasing amounts of KCl concentrations (100 mM, 500 mM, 1000 mM) were added to the septin-membrane bead mixture. To my surprise, after adding KCl concentrations of either 500 mM or 1000

mM, septins were still bound to the beads. It is important to note that there was a large drop in fluorescence intensity upon adding higher KCl concentrations (500 and 1000 mM). These data suggest that the septin interaction with curved membranes is potentially driven by some other interaction rather than through electrostatics alone. We will discuss the relative contribution of septin electrostatic interactions with the membrane below.

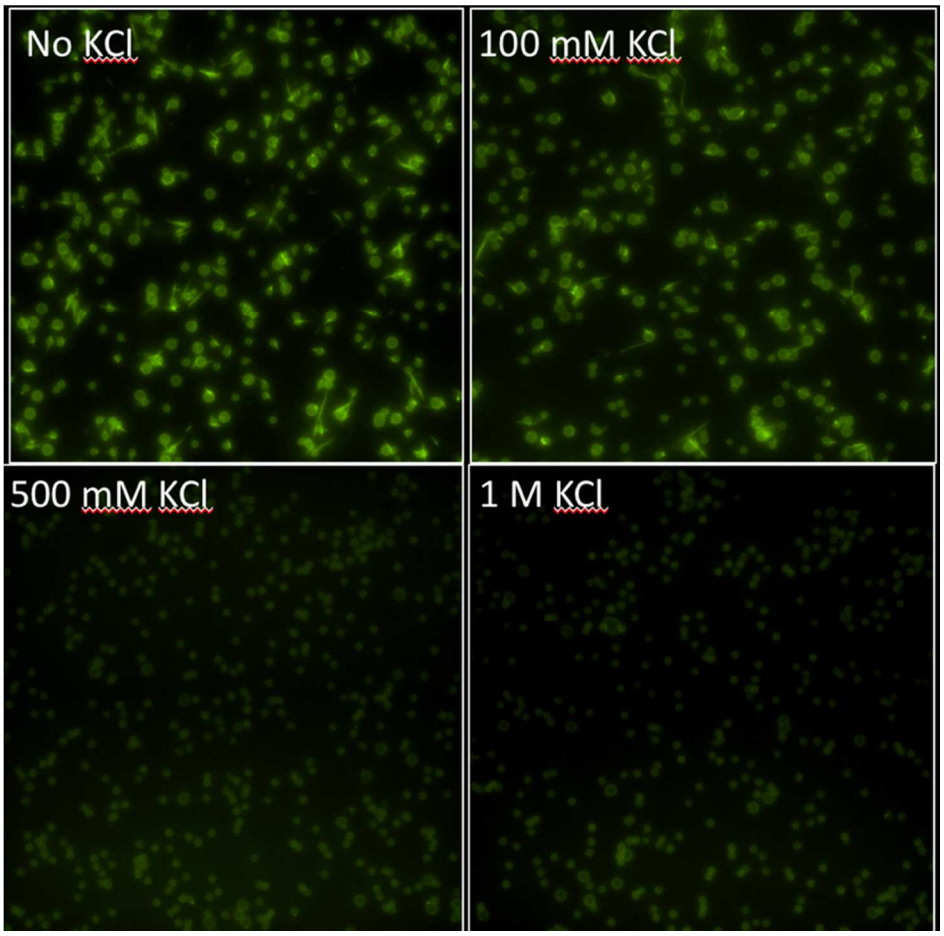

Figure A1. Septin binding to curved membranes may not be driven entirely by electrostatic interactions. (A-D) 100 nM of recombinant yeast septins were added to 3 and 5 µm diameter beads and the reaction was allowed to reach steady state. Exogenous KCl was added to the reaction mixture and the remaining septin population bound to the beads was visualized using wide-field fluorescence microscopy.

Discussion

Here we show that septin binding to curved membranes is a combination of electrostatic and some other mechanism. Interestingly, data from Andrew Bridges and myself (independently) show that septins will not bind membranes if the salt concentration exceeds 200 mM or if there is an absence of anionic lipid within our membrane mixtures. These data highlight the importance of electrostatics in septin-membrane binding. The observation that a population of bound protein to the beads after titrating in 1M KCl suggests that septins have another, non-electrostatic means to interact with membranes. Data presented in this thesis suggests that this other non-electrostatic motif is the amphipathic helix domain, which is heavily influenced by hydrophobic interactions. This is not to say that the amphipathic helix is not in part dependent on electrostatic interactions, as the polar face of the helix is lined with charged amino acid residues including lysine and glutamate. We speculate that initial recruitment to curved membranes is actually dependent on the charges present on the polar face of the helix. Only after recruitment, can the helix fold as it inserts itself into the membrane to utilize hydrophobic contacts, thereby stably anchoring septins to the membrane. As septins were allowed to reach steady state before high KCl concentrations were added, we suspect that the septin (helix)- membrane interaction was stable and therefore unaffected by the addition of high ionic strength.

Another interesting observation made from the work done in this thesis as well as others, is that septin filaments are capable of stacking on top of one another to form layers. At 100nM septin concentration we are in a concentration regime where all the septin that can be bound to a population of beads (at our controlled surface area of 440mm^2), are bound (See Figure 2.1). This and electron microscopy data from this

thesis suggests that septin-septin layers are also present in the experiment above. We speculate that the loss of a subset of septins from the beads following exposure to high ionic strength is due to the electrostatic nature of septin-septin layering interactions.

APPENDIX II

PRELIMINARY DATA: MUATIONS OF CDC12 AH DOMAIN IMPACTS FILAMENT FORMATION AND MEMBRANE BINDING

Rationale

Amphipathic helices are as diverse as they are frequent. All AH domains have distinct physicochemical properties with respect to charge, hydrophobicity, and length. These characteristics lead to alterations in membrane affinity, curvature sensitivity, and lipid-packing sensitivity. For example, amphipathic lipid packing sensor (ALPS) motifs are amphipathic helices, however, the polar face of these amphipathic helices are typically void of charged residues, rendering these motifs insensitive to the electrostatic landscape of the membrane. This in turn, allows the helix to be more perceptive to the lipid packing defects present in curved membranes via hydrophobic interactions. After observing that the amphipathic helix within Cdc12 played a role in curvature sensing, the next step was to make mutations within this domain in hopes to reveal important residues for either membrane binding, curvature sensitivity, and/or lipid packing sensitivity.

The mutations that were made and their rationale where A.) Replacement of the glutamate and lysine residues present at the interface of the hydrophilic and hydrophobic faces of the helix with uncharged serine residues. According to the "snorkel model" having charged residues located at this interface (particularly lysine) are uniquely poised to promote both hydrophilic and hydrophobic interactions with the membrane. Namely, the positively charged ammonium group interacts with anionic lipid headgroups, while the four-carbon chain of the R-group contributes to

hydrophobic interactions with the hydrocarbon tails of the lipid. We speculated that by replacing these charged interfacial residues with small, uncharged residues we would either see 1.) A reduction in membrane binding and/or 2.) A more drastic shift in curvature preference by septins for higher membrane curvatures. The second mutant that was made was B.) An extended interface mutant. The logic for the design of this mutant follows what was mentioned above. The third mutant was C.) A charge void mutant, where all charged residues were replaced with the uncharged, but polar residue serine. This mutant would allow us to test if the electrostatic component of the amphipathic helix of Cdc12 aids in septin-membrane recruitment and/or curvature sensitivity. Lastly, we made a mutant, D) where the hydrophobic region of the amphipathic helix was replaced with positively charged lysine residues. This mutant would allow us to assess the contribution of the hydrophobic face of the helix with respect to septin-membrane interactions and curvature sensitivity. It is important to note that all of these mutations were made in the Cdc12 amphipathic helix and purified in the context of the budding yeast septin hetero-octamer (Cdc11,Cdc12,Cdc3,Cdc10 polypeptides). These mutations were not tested in context of the amphipathic helix alone. However, based on the results below, I would be wary to walk down that path.

Methods and Results

The various mutants were cloned and subsequently purified in the context of the budding yeast septin hetero-octamer. To assess the impact these mutations have on filament formation, membrane binding, and curvature sensitivity, I preformed three experimental assays: 1.) Filament formation in solution using polyethylene-glycol passivated coverslips; 2.) Membrane binding and filament formation on planar

supported lipid bilayers (75 mol% DOPC, 25 mol% Soy PI); 3.) Membrane binding and curvature sensitivity on curved supported lipid bilayers (75 mol% DOPC, 25 mol% Soy PI). The data below is only qualitative (sadly), as I became more quantitative over the course of graduate school. However, there are some important observations.

In solution, wild-type septins form filaments ~2-10 μm in length and are clearly flexibly polymers (Figure A2). In contrast, filaments with the interface mutant B (interfacial lysine and glutamate) are long, appear bundled, and are rigid. Interestingly, filaments with extended interface mutant, C, appear to fall into two subpopulations; one being comparable to wild-type with respect to length and flexibility; the other being bundled filaments, albeit a comparable length to wild-type. The charge-void mutant shows similar filament characteristics to wild-type, although these filaments are much more sparse, suggesting that a large amount of septins are below the diffraction limit and are less capable of forming micron-scale long filaments. Lastly, and unfortunately, the hydrophobic null mutant does not form filaments. Interestingly, when these experiments were performed on a planar supported lipid bilayer, the results are fairly consistent with those done in solution. However, it is important to note that the surface coverage of membrane-bound septins appears to decrease, regardless of the mutant. However, these experiments were performed long before we knew that it takes ~4 hours to reach steady state on planar supported lipid bilayers. These images were taken ~10 - 20 mins upon addition of septins. Thus, rather than viewing this data as reduced surface coverage by septins (and thus membrane binding ability), it is also important to consider that the kinetics of septin binding to membranes could change here, such that if I looked at later timepoints, the surface coverage can either be tantamount to that of

wild-type or even enhanced. Lastly, I examined septin binding to curved surfaces in the context of these various mutations. Although these images were never quantified (for reasons explained below), they are contrasted identically, such that we can infer relative binding propensities. I observed enhanced binding of both interface mutants to membrane-coated beads. Interestingly, it appears further enhanced with the extended interface mutant. Furthermore, we observe what appears to be reduced binding of the charge void mutant and no binding at all to curved membranes in hydrophobic null mutants.

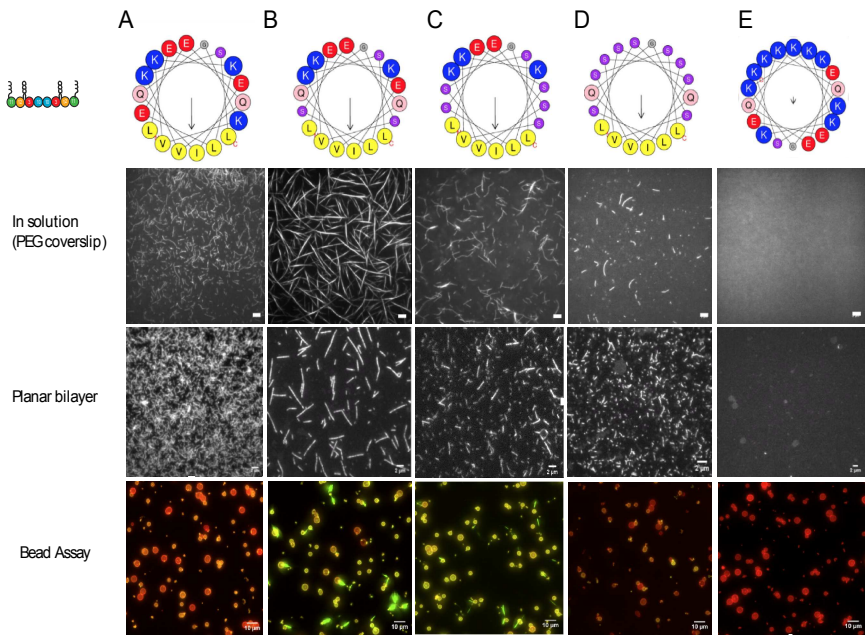

Figure A2 Mutations in the amphipathic helix of Cdc12 alter septin filament properties and membrane binding onto curved surfaces. (A) Helical wheel of the wild-type Cdc12 amphipathic helix. (Column I, panel I) 100 nM wild-type septins on polyethylene-glycol passivated coverslips. Scale bar 4 µm. (Column I, panel II) 2 nM wild-type septins on planar supported lipid bilayers. Scale bar 2 µm. (Column I, panel III) 15 nM wild-type septins on membrane coated beads (1,3,5 µm diameters). Scale bar 10 µm. (B) Helical wheel of interface mutant within the Cdc12 amphipathic helix. (Column II, panel I) 100 nM interface mutant septins on polyethylene-glycol passivated coverslips. Scale bar 4 µm. (Column II, panel II) 2 nM interface mutant septins on planar supported lipid bilayers. Scale bar 2 µm. (Column II, panel III) 15 nM interface mutant septins on membrane coated beads (1,3,5 µm diameters). Scale bar 10 µm. (C) Helical wheel of the extended interface mutant within the Cdc12 amphipathic helix.

(Column III, panel I) 100 nM extended interface mutant septins on polyethylene-glycol passivated coverslips. Scale bar 4 µm. (Column III, panel II) 2 nM extended interface interface septins on planar supported lipid bilayers. Scale bar 2 µm. (Column III, panel III) 15 nM extended interface mutant septins on membrane coated beads (1,3,5 µm diameters). Scale bar 10 µm. (D) Helical wheel of the charge void mutant within the Cdc12 amphipathic helix. (Column IV, panel I) 100 nM charge void mutant septins on polyethylene-glycol passivated coverslips. Scale bar 4 µm. (Column IV, panel II) 2 nM charge void mutant septins on planar supported lipid bilayers. Scale bar 2 µm. (Column IV, panel III) 15 nM charge void mutant septins on membrane coated beads (1,3,5 µm diameters). Scale bar 10 µm. (E) Helical wheel of the hydrophobic null mutant within the Cdc12 amphipathic helix. (Column V, panel I) 100 nM hydrophobic null mutant septins on polyethylene-glycol passivated coverslips. Scale bar 4 µm. (Column V, panel II) 2 nM hydrophobic null mutant septins on planar supported lipid bilayers. Scale bar 2 µm. (Column V, panel III) 15 nM hydrophobic null mutant septins on membrane coated beads (1,3,5 µm diameters). Scale bar 10 µm.

Discussion

The data presented above shows that even through mutation of the amphipathic helix domain, we can impact septin filament properties including length, flexibility, and membrane binding. Although this is interesting, it is much harder to faithfully deduce if mutations in the AH domain of Cdc12 are directly impacting membrane binding and/or curvature sensitivity by septins or if the observations we see are a function of altering septin filament properties. It will be an interesting endeavor to probe how the AH domain influences septin filament properties.

APPENDIX III

PRELIMINARY DATA: pH CONTROLS SEPTIN FILAMENT LENGTH AND ADSORPTION ONTO MEMBRANES

Rationale

I should be clear that this observation was stumbled upon and never really pursued until I saw drastic differences in septin adsorption on curved membranes when compared to the data Andrew Bridges acquired. Despite septin concentrations and bead surface area being the same, septin adsorption was different. Upon analyzing methods, the only difference between Andrew's data and mine was pH. I had always used pH 7.4 wheras Andrew had used pH 8.0. Therefore, the following set of experiments performed were to test the hypothesis that pH influences septin adsorption onto both planar and curved membranes.

Methods and Results

Budding yeast septins were seeded onto planar supported lipid bilayers in buffers either at pH 7.4 or pH 8.0 (75 mol% DOPC, 25 mol% soy PI). Septins were allowed to reach steady state (~4 hrs) and then imaged using TIRF microscopy from which membrane binding, filament length distributions, and persistence length could be measured. Qualitatively, there appear to be more septins bound to the membrane in solutions at pH 7.4 than at pH 8.0 (Figure A4.1). Interestingly, when we analyzed the filament length distribution of septins at both pH values, filaments were longer at pH 7.4 than those at pH 8.0. Lastly, when we examined septin filament flexibility at different pH values, we found no difference.

Next, we examined if the pH of the solution would impact septin adsorption onto curved membranes. Similar to the experiment above, budding yeast septins were seeded onto cuved membranes (3 µm bead diameter; 75 mol% DOPC, 25 mol% soy PI, 0.05 mol% Rh-PE) in buffers either at pH 7.4 or 8.0. Once steady state was reached (~ 1 hr) septin adsorption onto the beads was measured. Interestingly, ~ 65% more septin was bound to beads in a buffer at pH 7.4 than pH 8.0 (Figure A4.2)

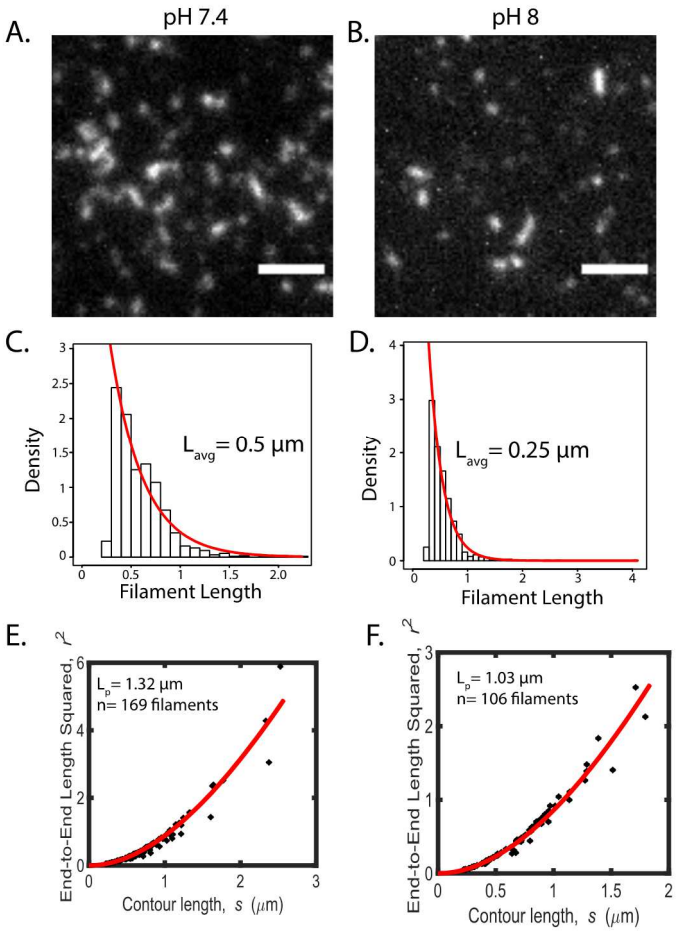

Figure A3.1 pH influences septin adsorption and filament length on onto planar membranes
(A) 0.1 nM budding yeast septins seeded onto a planar supported lipid bilayer in a buffer with Hepes pH 7.4. Images were acquired at steady state (4 hrs) using TIRF microscopy. Scale bar 2 µm. (B) 0.1 nM budding yeast septins seeded onto a planar supported lipid bilayer in a buffer with Hepes pH 8.0 Images were acquired at steady state (4 hrs) using TIRF microscopy. Scale bar 2 µm. (C) Filament length distribution at steady state for budding yeast septins in a buffer

with hepes pH 7.4. Distributions were fit to a single exponential (red) from which the average filament length was determined (D) Filament length distribution for budding yeast septins at steady state in a buffer with hepes pH 8.0. Distributions were fit to a single exponential (red) from which the average filament length was determined. (E) End-to-end distance analysis was used to calculate the persistence length of septin filaments at pH 7.4. Filled black dots represent individual filaments. Red lines represent the best fit to equation. (F) End-to-end distance analysis was used to calculate the persistence length of septin filaments at pH 7.4. Filled black dots represent individual filaments. Red lines represent the best fit to equation.

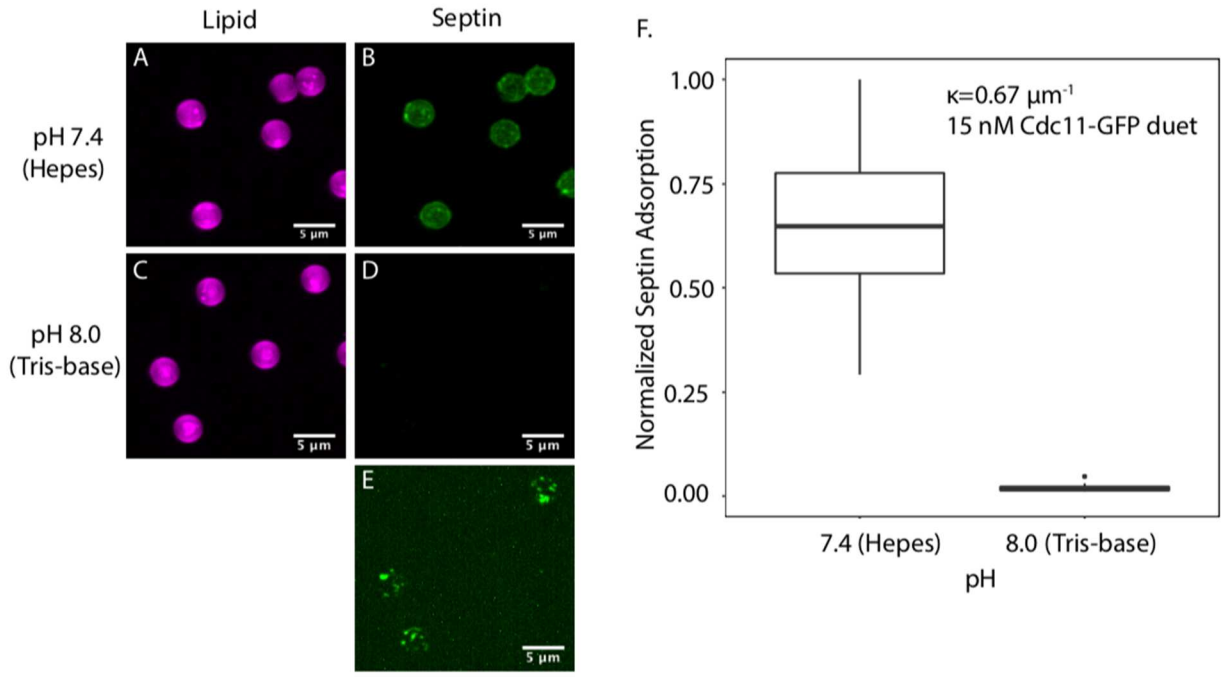

Figure A3.2 pH influences septin adsorption onto curved surfaces
(A) Lipid channel for 3 µm beads in a buffer with Hepes pH 7.4. (B) Septin adsorption onto 3 µm beads at 15 nM septin concentration in a buffer with Hepes pH 7.4. (C) Lipid channel for 3 µm beads in a buffer with Tris-base pH 8.0. (D) Septin adsorption onto 3 µm beads at 15 nM septin conentratin in a buffer with Tris-base pH 8.0. Images from B and D are contrasted identically. (E) Enhanced contrast of 15 nM septin binding to 3 µm beads in a buffer with Tris-base pH 8.0. (F) Quantification of septin adsorption (Normalized) as a -function of pH

Discussion

In this section we highlight the importance of pH in regulating septin-membrane and septin-septin interactions. Interestingly, the work performed in Chapter 5 of this thesis clearly shows that septin filament pairing is pH-dependent. We speculate that the ability of septin filaments to pair with one another on the membrane could be a means to promote cooperative septin assembly to further increase the number of stable septins on the membrane. It will be important for future researchers to either keep their pH values consistent across experiments, as this can drastically change the results obtained. However, it might also be used as a tool to control the binding of septins on the membrane.

APPENDIX IV

PRELIMINARY DATA: PRE-POLYMERIZED SEPTINS ARE CAPABLE OF SENSING MEMBRANE CURVATURE

Rationale

The septin assembly process begins with the binding of short, 32 nm rods to the membrane. Rods bound to the membrane can diffuse and collide with neighboring rods to form filaments and other higher order structures. Does the septin assembly process have to occur for septins to sense curvature? Or can septin filaments formed in solution sense curvature just the same? We decided to test this hypothesis by pre-polymerizing septins into filaments and added them to beads of different membrane curvatures and examined adsorption at steady state.

Methods and Results

25 nM of budding yeast septins were allowed to polymerize in solution for one hour at room temperature. 25 nM of pre-polymerized septins were then added to several membrane curvatures (bead diameters 1,3,5 μm; 75 mol% DOPC, 25 mol% soy PI, 0.05 mol% Rh-PE). After steady state was reached (~1 hr) septin adsorption onto the beads was observed using confocal microscopy. We found that pre-polymerized septins adsorb onto all bead sizes with a preference for 1 μm beads, akin to the curvature preference of septins which are allowed to assemble into filaments on the membrane (Figure A5). Interestingly, we saw equal binding of pre-polymerized septins to both 3 and 5 μm beads. These data suggest that pre-polymerized septin filaments are still able to detect changes in membrane curvature.

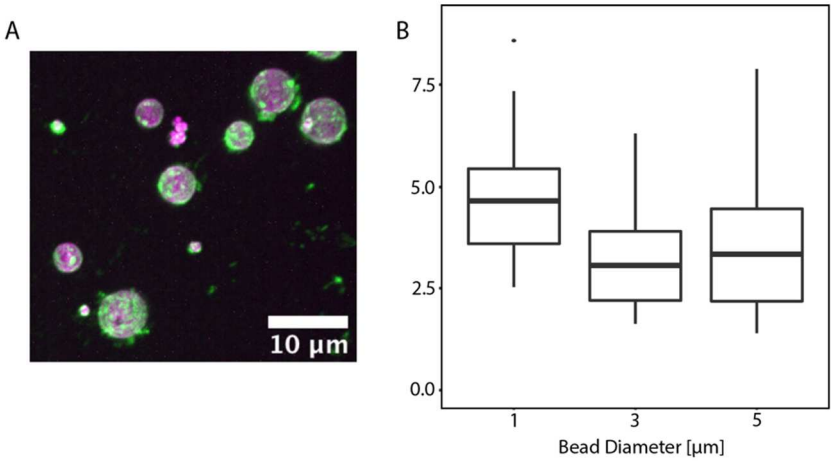

Figure A4 Pre-polymerized septins are capable of sensing membrane curvature
(A) Representative maximum intensity projection of 25 nM pre-polymerized septin (green) bound to curved membranes (magenta). Scale bar 10 µm. (B) Box plot quantifying pre-polymerized septin adsorption onto curved membranes. Thick black line represents the mean. Thin vertical lines represent the standard deviation. N> 34 beads per bead diameter.

Discussion

Here we show that septin filaments are capable of detecting changes in micron-scale membrane curvature. We see the same curvature preference for septins that either assemble on the membrane or septin filaments from the bulk binding to the membrane. Interestingly, however, is the lack of curvature preference for the 3 µm beads over the 5 µm beads. This is not typically the case for septins that assemble onto the membrane, as the preference is usually 1 µm > 3 µm > 5µm. As this experiment was only done once, it is possible that septin filament adosption onto curved membranes is random (but then again if it were random, I'd expect to see equal binding across all curvatures, I think, maybe?) and the results obtained from this experiment are not a true depiction of what normally happens. Alternatively, septin filaments could still have a preference for 1 µm beads, however the ability of a filament to sense the curvatures present on 3 and 5 µm

diameter beads diminishes as the curvature becomes increasingly more shallow. To put this idea into other words, it's as if the septin filaments can sense curvature up until a certain geometry. Once this point is reached and the curvature becomes shallow enough, filaments perceive it as being flat no matter what. This would explain the equal binding onto 3 and 5 μm beads. Another interesting way to think about this is when we form filaments in solution, we have a distribution of filament lengths. Differences in filament length will probably lead to differences in the on and off rates for a filament onto a given membrane curvature. I speculate that this could make interpreting this experiment infinitly complicated. Future work should 1.) repeat this data set. 2.) Extend the number of curvatures available to the septin filaments. 3.) Pre-polymerize filaments at several concentrations.

APPENDIX V

PRELIMINARY DATA: CHANGING THE DISTANCE BETWEEN AMPHIPATHIC HELIX DOMAINS VIA C-TERMINAL EXTENSIONS INFLUENCES MEMBRANE CURVATURE SENSING BY

Rationale

An interesting feature of the heteromeric septin complex is the spacing between amphipathic helix domains. In the context of the budding yeast septin hetero-octamer, the AH domains are approximately spaced 24 nm apart. It's tempting to speculate that the distance between these domains serves as a molecular ruler for septins to sense curvature on the micrometer scale. To test this hypothesis we cloned and purified C-terminal extension swaps to change the distance between amphipathic helix domains within the septin complex and examined how this impacted membrane binding and filament length distributions on planar supported lipid bilayers, as well as septin adsorption onto curved surfaces.

Methods and Results

For these experiments, we swapped the C-terminal extension (CTE) of Cdc12 (the AH-containing CTE) with the CTEs of Cdc11 or Cdc3 such that the distance between AH domains was either increased (Cdc12CTE-Cdc11 CTE swap, ~32 nm spacing) or decreased (Cdc12CTE-Cdc3CTE swap, ~16 nm spacing). These constructs were purified and 0.5 nM of each construct was seeded onto planar supported lipid bilayers (75 mol% DOPC, 25 mol% soy PI) and allowed to reach steady state (~4 hrs). We found that both wild-type and Cdc12CTE-Cdc3CTE swapped septins showed an average steady state filament length of 0.6 μm, whereas Cdc12CTE-Cdc11CTE swapped septins had an average steady state filament length of 0.9 μm (Figure A6A-H)). Interestingly, we observed a population of septin

filaments that appeared longer, potentially bundled, and more rigid when compared to wild-type in Cdc12CTE-Cdc11CTE swapped septins. Moreover, we observed multiple septin rings per field of view in Cdc12CTE-Cdc3CTE swapped septins. These data suggest that the order of the CTE regions and potentially the spacing of the AH domains can alter septin filament properties and membrane binding.

Next, we seeded 15 nM of purified CTE swapped constructs onto beads of various membrane curvatures (75 mol% DOPC, 25 mol% soy PI, 0.05 mol% Rh-PE). As expected, wild-type septins with AH domains spaced ~24 nm apart preferentially assembled onto 1 μm beads. Interestingly, Cdc12CTE-Cdc11CTE swapped septins show an equal preference for both 0.5 and 1 μm beads, whereas Cdc12CTE-Cdc11CTE swapped septins shows near equal binding for 0.5, 1, and 3 μm beads, although the 1 μm bead is shows a slightly higher septin adsorption. Moreover, both CTE swapped septin constructs show higher total adsorption on curved membranes when compared to wild-type. These data suggest the order of the CTE regions and potentially the spacing of the AH domains with the septin heteromer can influence the degree of membrane binding and the sensitivity of septins to membrane curvature.

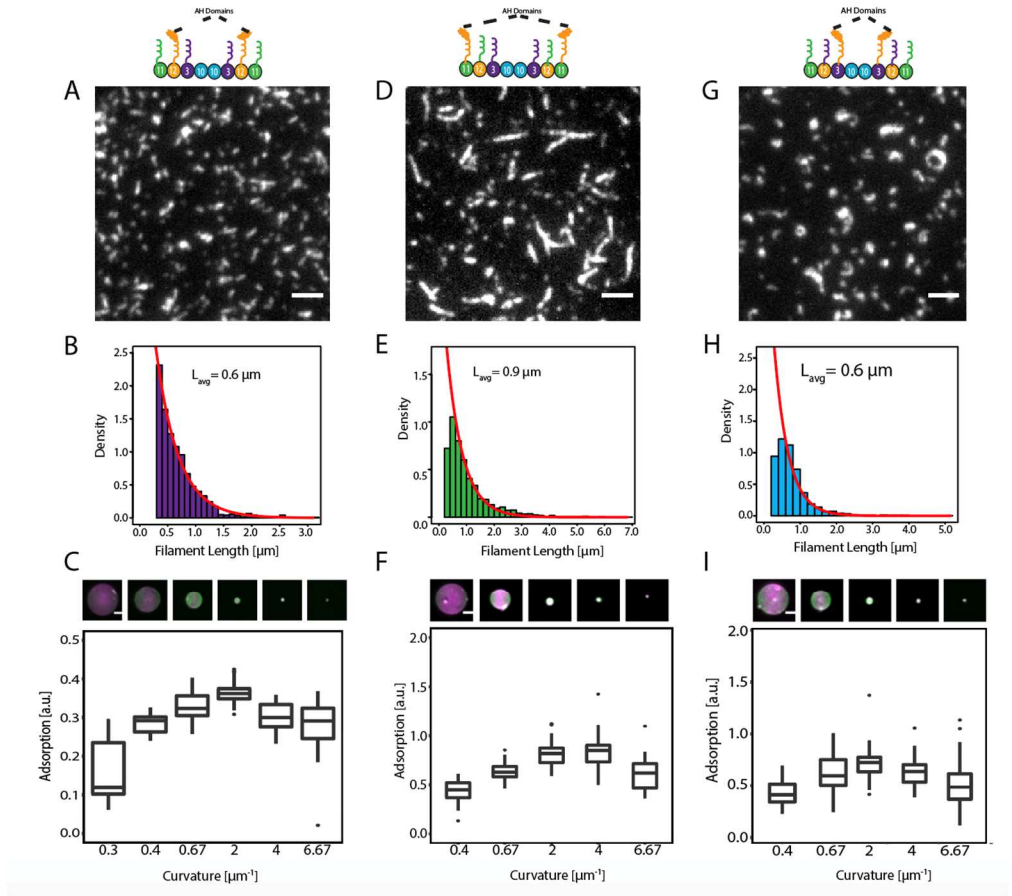

Figure A5 Changing the spacing of AH domains via CTE-swaps alters septin filament properties and curvature sensitivity by septins

(A) Representative TIRF microscopy images of 0.5 nM wild-type septins on a planar supported bilayer at steady state. (B) Filament length distribution at steady state for wild-type septins seeded on planar supported lipid bilayers. Distributions were fit to a single exponential (red) from which the average filament length was determined. (C) Box plot showing wild-type septin adsorption onto several membrane curvatures. Thick black lines represent the mean and vertical lines represent the standard deviation. Representative maximum intensity projections showing 15 nM septin (green) binding to various curved membranes (magenta) are placed above the plot. Scale bar 2 µm. (D) Representative TIRF microscopy images of 0.5 nM Cdc12CTE-Cdc11CTE swapped septins on a planar supported bilayer at steady state. (E) Filament length distribution at steady state for Cdc12CTE-Cdc11CTE swapped septins seeded on planar supported lipid bilayers. Distributions were fit to a single exponential (red) from which the average filament length was determined. (F) Box plot showing Cdc12CTE-Cdc11CTE swapped septin adsorption onto several membrane curvatures. Thick black lines represent the mean and vertical lines represent the standard deviation. Representative maximum intensity projections showing septin (green) binding to various curved membranes (magenta) are placed above the plot. Scale bar 2 µm. (G) Representative TIRF microscopy images of 0.5 nM Cdc12CTE-Cdc3CTE swapped septins on a planar supported bilayer at steady state. (H) Filament length distribution at steady state for Cdc12CTE-Cdc3CTE swapped septins seeded on planar supported lipid bilayers. Distributions were fit to a single exponential (red) from which the average filament length was determined. (I)

Box plot showing Cdc12CTE-Cdc3CTE swapped septin adsorption onto several membrane curvatures. Thick black lines represent the mean and vertical lines represent the standard deviation. Representative maximum intensity projections showing septin (green) binding to various curved membranes (magenta) are placed above the plot. Scale bar 2 μm

Discussion

In this section we show that by moving the AH domain via C-terminal extension swaps, we are able to alter septin filament length on planar surfaces and adsorption / curvature sensitivity. It is interesting that by placing the CTE's onto different septin polypeptides, we can change filament length (at least for Cdc12CTE-Cdc11CTE swaps). It is unclear how the CTE's would control something such as septin filament length, however, our previous data from Appendix II of this thesis shows that by mutating residues in the AH domain of Cdc12 is enough to alter filament properties. Future work should examine how the CTE domains influence septin assembly into filaments.

It's hard to say if the difference in curvature sensitivity we see by moving the AH domains difference distances from one another (via CTE swaps) is the direct cause for a reduction in curvature sensitivity by septins. It's certainly possible that by changing the distance between curvature sensitive binding domains impacts how septins interact with the membrane / detect defects in the membrane. It is also possible that by swapping CTE's we are influencing septin filament pairing interactions. However, I can't say for sure, as there is data suggesting that the CTE's and/or N-termini contribute to filament pairing. Interestingly, these domains are on opposite faces of the septin complex, and I speculate there may be a geometry dependent-pairing mechanism. Additionally, I am usually skeptical to give credence to results that change curvature sensitivity where filament properties are altered, as was the case for the Cdc12CTE-Cdc12CTE swapped septins. However, this difference cannot be traced back to filament length alone, as the

Cdc12CTE-Cdc3CTE swap shows a higher total adsorption value on curved membranes, as well as a wider spread of preferred curvatures than wild-type septins, despite having an equal average filament length.

APPENDIX VI

PRELIMINARY DATA: DESIGNING SYNTHETIC CONSTRUCTS TO ALTER THE SPACING BETWEEN CURVATURE SENSITIVE AH DOMAINS

This work was done as a collaboratin between myself and Maggie Daly of Freeman Lab at UNC Chapel Hill. Maggie designed and synthesized the constructs. I helped with the initial design and performed bead assays.

Rationale:

Similar to the rationale described in the previous appendix we were curious to see if the spacing between AH domains can drive curvature-specific adsorption onto membranes. However, we were curious to see if the spacing of the AH domains alone is sufficient to promote curvature sensitivity.

Methods and Results

To test the hypothesis that the spacing of AH domains alone can drive curvature specific adsorption by septins we synthesized single stranded DNA scaffolds from which AH domains can be covalently conjugated via a flexible PEG linker (Figure A6A). To allow for two AH domains per DNA scaffold, we synthesized complimentary single DNA strands, each conjugated to one AH domain. We then mixed these two constructs and allowed the DNA strands to hybridize via complimentray base pairing (Figure A6B). The complexes were then mixed with beads of various membrane curvatures and adsorption was assessed by confocal microscopy. We find that where the AH domains are spaced ~4 nm apart display no curvature sensitivity, showing equal binding to all tested membrane curvatures (Figure A6C).

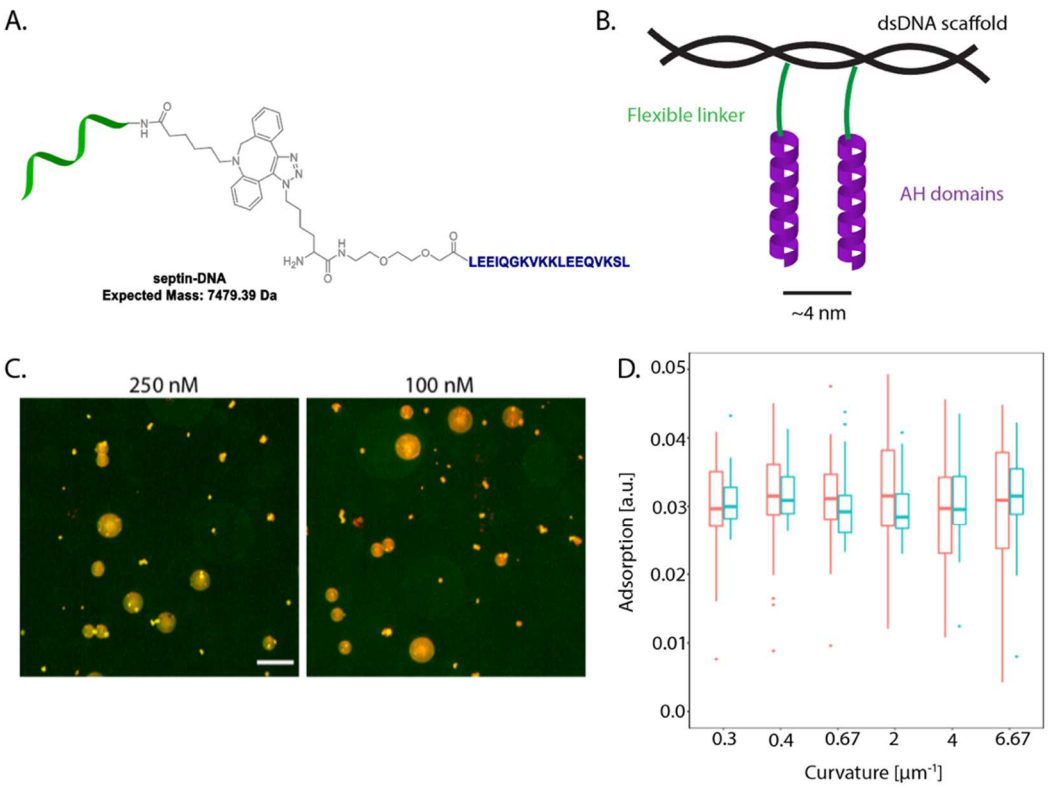

Figure A6. Measuring adsorption of DNA-AH scaffolds onto curved membranes.
(A) Design of single stranded DNA scaffold covalently conjugated to the Cdc12 AH domain by a flexible PEG linker. DNA is colored green and the Cdc12 AH domain is colored blue. (B) Schematic of the double stranded DNA-AH complex formed after allowing complementray single DNA-AH constructs to hybridize. (C)Representative maximum intensity projections showing DNA duplex-AH (green) binding to multiple membrane curvatures (red) at 250 and 100 nM. Scale bar 10 μm. (D)Box and whisker plot quantifying DNA duplex-AH adsorption onto various membrane curvatures. N> 30 beads per bead size. 250 nM

Discussion

The data presented above show that when AH domains are spaced close together ~4 nm, they are unable to distinguish between membrane geometries. This is in contrast to our previous results (Figure 2.5E), where AH domains spaced only 9 amino acids apart show a curvature preference for $k=2\mu m^{-1}$. Interestingly, however, in our synthesized constructs, the AH domains are dangling off perpendicular to the length axis of the DNA scaffold, where as our previous data from Figure 2.5E, the AH

domains are arranged linearly. Collectively, these data hint that both the spacing of AH domains and the geometric configuration of the AH domains might be an important factors in driving curvature specific adsorption.

APPENDIX VII

PRELIMINARY DATA: FILLING IN LIPID PACKING DEFECTS RESULTS IN A LOSS IN CURVATURE SENSITIVITY BY SEPTINS

Rationale

Amphipathic helices operate by using lipid packing defects, or exposed regions of hydrophobicity between lipids, generated by both thermal fluctuations and curvature, as sites to interact with- and binding to the membrane. Simulations have shown that the frequency and size of lipid packing defects scale with membrane curvature. Many nanometer-scale curvature sensors that possess AH domains sense curvature on the basis of the number of available binding sites, rather than through an affinity difference for membrane curvature, such that the preference for proteins containing these domains typically errs on side of higher curvature. This does not appear to be the case for septins, as chapter two of this thesis showed that both affinity and the number of available binding sites are important factors in regulating curvature sensing by septins (Figure 2.1). Moreover, where the number of binding sites are concerned, we observe higher Bmax values at lower curvatures (Figure 2.1). This is the opposite case for nanometer-scale curvature sensors that posses AH domains. Collectively, these data suggest that septins might utilize amphipathic helices differently on the micrometer-scale membrane curvatures on which they preferentially assemble.

As budding yeast septins have an amphipathic helix within the Cdc12 polypeptide (in the context of a septin hetero-octamer with Cdc11,Cdc12,Cdc3, and Cdc10 polypeptides), we tested if lipid packing defects are essential for septin-mediated curvature sensing. To test this hypothesis we utilized a fluorescent fatty acid, BODIPY-FL-C16 as a chemical agent to "occupy" the available packing defects present on curved membranes. If septin AH domains are

utilizing lipid packing defects to sense membrane curvature, we expected to see a loss in curvature sensitivity by septins as the number of available binding sites (lipid packing defects) was dimished by addition of the BODIPY-FL-C16 agent.

Methods and Results

Increasing concentrations of BODIPY-FL-C16 were added to a mixed solution of 1 and 5 μm membrane-coated beads (75 mol% DOPC, 25 mol% soy PI, 0.05 mol% Rh-PE) 1 hour prior to adding the septins. 25 nM of budding yeast septins were added to the beads and protein adsorption was measured using confocal microscopy. We found that increasing concentrations of BODIPY-FL-C16 resulted in equal binding by septins on both 1 and 5 μm beads. These results suggest that septins are reliant on lipid packing defects present in curved membranes to sense membrane geometry.

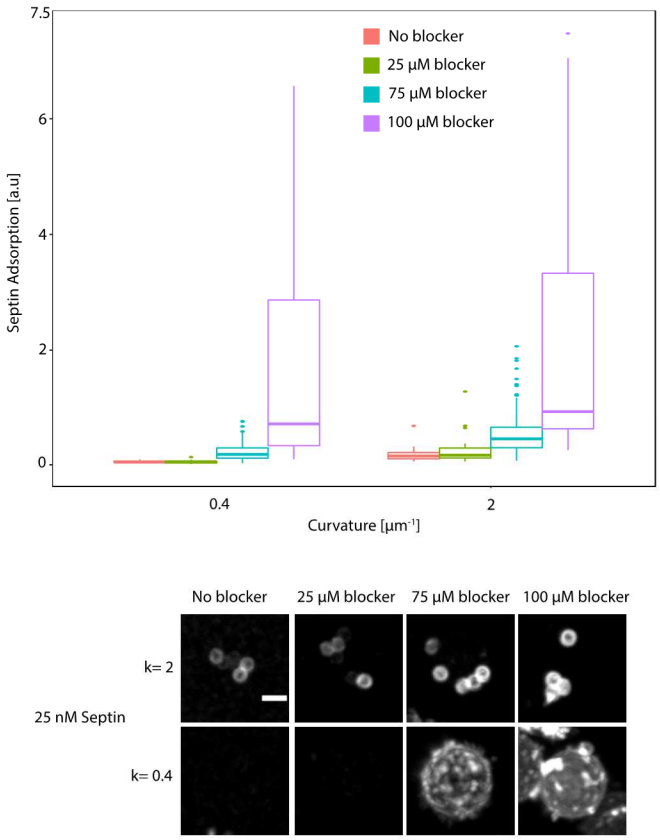

Figure A7 Filling lipid packing defects results in a loss in curvature sensitivity by septins
(A) Box plot quantifying adsorption of 25 nM septin onto membrane curvatures in the presence of increasing amounts of BODIPY-FL-C16. Thick horizontal lines represent the mean. Vertical lines represent the standard deviation. (B) Representative maximum intensity projection of bound septins (grey) to membrane curvatures in the presence of BODIPY-FL-C16. Scale bar 2 µm.

Discussion

The data presented here suggest that lipid packing defects are important for regulating preferential assembly onto curved membranes. However, it should be noted that as we approached equal binding by septins onto 1 and 5 µm beads (100 µM BODIPY-FL-C16), we were beginning to see a disruption of the membrane around the beads, especially the 5 µm bead. If I was to repeat this experiment, I would only add the BODIPY-FL-C16 to the 1 µm bead (which in theory should have a larger number of

lipid packing defects) at different concentrations and subsequently measure adsorption onto both membrane curvatures, that way one could potentially equalize the number of defects present on both membranes. Alternatively, one could test the hypothesis that lipid packing defects are important for septin adsorption by utilizing different lipid mixtures in our biomimetic membranes. For example, if one wanted to increase the number of lipid packing defects, one either increase the amount of phosphotidyl-ethanolamine lipid content and/or increase the number of unsaturated fatty acyl chains. Utilizing different lipid mixtures has been partially explored in the Gladfelter lab, and it would it would be fruitful to identify how membrane composition influences septin membrane binding and potentially curvature sensitivity.

REFERENCES

Adams, A. E. M. and Pringle, J. R. (1984) 'Relationship of actin and tubulin distribution to bud growth in wild-type and morphogenetic-mutant Saccharomyces cerevisiae', *Journal of Cell Biology*. doi: 10.1083/jcb.98.3.934.

Ajat, M. *et al.* (2017) 'Hepatic stellate cells retain the capacity to synthesize retinyl esters and to store neutral lipids in small lipid droplets in the absence of LRAT', *Biochimica et Biophysica Acta - Molecular and Cell Biology of Lipids*. doi: 10.1016/j.bbalip.2016.10.013.

Akil, A. *et al.* (2016) 'Septin 9 induces lipid droplets growth by a phosphatidylinositol-5-phosphate and microtubule-dependent mechanism hijacked by HCV', *Nature Communications*. doi: 10.1016/0021-8502(80)90042-7.

Altmann-Jöhl, R. and Philippsen, P. (1996) 'AgTHR4, a new selection marker for transformation of the filamentous fungus Ashbya gossypii, maps in a four-gene cluster that is conserved between A. gossypii and Saccharomyces cerevisiae', *Molecular and General Genetics*. doi: 10.1007/BF02191826.

Arasada, R. and Pollard, T. D. (2015) 'A role for F-BAR protein Rga7p during cytokinesis in S. pombe', *Journal of Cell Science*. doi: 10.1242/jcs.162974.

Asano, S. *et al.* (2005) 'Concerted mechanism of Swe1/Wee1 regulation by multiple kinases in budding yeast', *EMBO Journal*. doi: 10.1038/sj.emboj.7600683.
Auxier, B. *et al.* (2019) 'Diversity of opisthokont septin proteins reveals structural constraints and conserved motifs 06 Biological Sciences 0604 Genetics', *BMC Evolutionary Biology*. doi: 10.1186/s12862-018-1297-8.

Ayad-Durieux, Y. *et al.* (2000) 'A PAK-like protein kinase is required for maturation of young hyphae and septation in the filamentous ascomycete Ashbya gossypii', *Journal of Cell Science*.
Baba, M. *et al.* (1997) 'Two distinct pathways for targeting proteins from the cytoplasm to the vacuole/lysosome', *Journal of Cell Biology*. doi: 10.1083/jcb.139.7.1687.

Barral, Y. *et al.* (2000) 'Compartmentalization of the cell cortex by septins is required for maintenance of cell polarity in yeast', *Molecular Cell*. doi: 10.1016/S1097-2765(00)80324-X.
Beber, A. *et al.* (2018) 'Septin-based readout of PI(4,5)P2 incorporation into membranes of giant unilamellar vesicles', *Cytoskeleton*. doi: 10.1002/cm.21480.

Beber, A. *et al.* (2019) 'Membrane reshaping by micrometric curvature sensitive septin filaments', *Nature Communications*. doi: 10.1038/s41467-019-08344-5.

Bendezú, F. O. *et al.* (2015) 'Spontaneous Cdc42 Polarization Independent of GDI-Mediated Extraction and Actin-Based Trafficking', *PLoS Biology*. doi: 10.1371/journal.pbio.1002097.

Bertin, Aurelie *et al.* (2008) 'Saccharomyces cerevisiae septins: Supramolecular organization of heterooligomers and the mechanism of filament assembly', *Proceedings of the National Academy of Sciences of the United States of America*. doi: 10.1073/pnas.0803330105.

Bertin, A. *et al.* (2008) 'Saccharomyces cerevisiae septins: Supramolecular organization of heterooligomers and the mechanism of filament assembly', *Proceedings of the National Academy of Sciences*. doi: 10.1073/pnas.0803330105.

Bertin, Aurélie *et al.* (2010) 'Phosphatidylinositol-4,5-bisphosphate Promotes Budding Yeast Septin Filament Assembly and Organization', *Journal of Molecular Biology*. doi: 10.1016/j.jmb.2010.10.002.

Bertin, Aurelie *et al.* (2010) 'Ultrastructural Organization of Budding Yeast Septin Filaments Both in vitro and in situ, Analyzed by Electron Microscopy', *Biophysical Journal*. doi: 10.1016/j.bpj.2009.12.2069.

Bigay, J. *et al.* (2005) 'ArfGAP1 responds to membrane curvature through the folding of a lipid packing sensor motif', *EMBO Journal*. doi: 10.1038/sj.emboj.7600714.

Boettcher, B. *et al.* (2012) 'Nuclear envelope morphology constrains diffusion and promotes asymmetric protein segregation in closed mitosis', *Journal of Cell Biology*. doi: 10.1083/jcb.201112117.

Booth, E. A. *et al.* (2015) 'A förster resonance energy transfer (FRET)-based system provides insight into the ordered assembly of yeast septin hetero-octamers', *Journal of Biological Chemistry*. doi: 10.1074/jbc.M115.683128.

Booth, E. A. and Thorner, J. (2016) 'A FRET-based method for monitoring septin polymerization and binding of septin-associated proteins', *Methods in Cell Biology*. doi: 10.1016/bs.mcb.2016.03.024.

Brausemann, A. *et al.* (2016) 'Crystal structure of Cdc11, a septin subunit from Saccharomyces cerevisiae', *Journal of Structural Biology*. doi: 10.1016/j.jsb.2016.01.004.

Bretscher, A. (2003) 'Polarized growth and organelle segregation in yeast: The tracks, motors, and receptors', *Journal of Cell Biology*. doi: 10.1083/jcb.200301035.

Bridges, A. A. *et al.* (2014) 'Septin assemblies form by diffusion-driven annealing on membranes', *Proceedings of the National Academy of Sciences*. doi: 10.1073/pnas.1314138111.

Bridges, A. A. *et al.* (2016) 'Micron-scale plasma membrane curvature is recognized by the septin cytoskeleton', *Journal of Cell Biology*. doi: 10.1083/jcb.201512029.

Bridges, A. A. and Gladfelter, A. S. (2015) 'Septin form and function at the cell cortex', *Journal of Biological Chemistry*. doi: 10.1074/jbc.R114.634444.

Bridges, A. A. and Gladfelter, A. S. (2016) 'In vitro reconstitution of septin assemblies on supported lipid bilayers', *Methods in Cell Biology*. doi: 10.1016/bs.mcb.2016.03.025.

Brown, M. F. (2012) 'Curvature forces in membrane lipid-protein interactions', *Biochemistry*. doi: 10.1021/bi301332v.

Budvytyte, R. *et al.* (2013) 'Structure and properties of tethered bilayer lipid membranes with unsaturated anchor molecules', *Langmuir*. doi: 10.1021/la401132c.

Byers, B. and Goetsch, L. E. (1976) 'A highly ordered ring of membrane-associated filaments in budding yeast', *Journal of Cell Biology*. doi: 10.1083/jcb.69.3.717.

Cannon, K. S. *et al.* (2019) 'An amphipathic helix enables septins to sense micrometer-scale membrane curvature', *Journal of Cell Biology*. doi: 10.1083/jcb.201807211.

Cannon, K. S., Woods, B. L. and Gladfelter, A. S. (2017) 'The Unsolved Problem of How Cells Sense Micron-Scale Curvature', *Trends in Biochemical Sciences*. doi: 10.1016/j.tibs.2017.10.001.

Casamayor, A. and Snyder, M. (2003) 'Molecular dissection of a yeast septin: distinct domains

are required for septin interaction, localization, and function.', *Molecular and cellular biology*. doi: 10.1128/MCB.23.8.2762.

Caudron, F. and Barral, Y. (2009) 'Septins and the Lateral Compartmentalization of Eukaryotic Membranes', *Developmental Cell*. doi: 10.1016/j.devcel.2009.04.003.
Chao, J. T. *et al.* (2014) 'Polarization of the endoplasmic reticulum by ER-septin tethering', *Cell*. doi: 10.1016/j.cell.2014.06.033.

Chiaruttini, N. *et al.* (2015) 'Relaxation of Loaded ESCRT-III Spiral Springs Drives Membrane Deformation', *Cell*. doi: 10.1016/j.cell.2015.10.017.

Cho, S. J. *et al.* (2011) 'Septin 6 regulates the cytoarchitecture of neurons through localization at dendritic branch points and bases of protrusions', *Molecules and Cells*. doi: 10.1007/s10059-011-1048-9.

Cid, V. J. *et al.* (2001) 'Dynamic localization of the Swe1 regulator Hsl7 during the Saccharomyces cerevisiae cell cycle', *Molecular Biology of the Cell*. doi: 10.1091/mbc.12.6.1645.

Clay, L. *et al.* (2014a) 'A sphingolipid-dependent diffusion barrier confines ER stress to the yeast mother cell', *eLife*. doi: 10.7554/eLife.01883.

Clay, L. *et al.* (2014b) 'A sphingolipid-dependent diffusion barrier confines ER stress to the yeast mother cell', *eLife*. doi: 10.7554/eLife.01883.

Colom, A. *et al.* (2017) 'Dynamic remodeling of the dynamin helix during membrane constriction', *Proceedings of the National Academy of Sciences of the United States of America*. doi: 10.1073/pnas.1619578114.

Dagdas, Y. F. *et al.* (2012) 'Septin-mediated plant cell invasion by the rice blast fungus, Magnaporthe oryzae', *Science*. doi: 10.1126/science.1222934.

DeMay, B. S. *et al.* (2009) 'Regulation of distinct septin rings in a single cell by Elm1p and Gin4p kinases.', *Molecular biology of the cell*. doi: 10.1091/mbc.E08-12-1169.

DeMay, B. S., Noda, N., *et al.* (2011) 'Rapid and quantitative imaging of excitation polarized

fluorescence reveals ordered septin dynamics in live yeast.', *Biophysical journal*. doi: 10.1016/j.bpj.2011.07.008.

DeMay, B. S., Bai, X., *et al.* (2011) 'Septin filaments exhibit a dynamic, paired organization that is conserved from yeast to mammals', *Journal of Cell Biology*. doi: 10.1083/jcb.201012143.

Dolat, L. *et al.* (2014) 'Septins promote stress fiber-mediated maturation of focal adhesions and renal epithelial motility', *Journal of Cell Biology*. doi: 10.1083/jcb.201405050.

Dolat, L. and Spiliotis, E. T. (2016) 'Septins promote macropinosome maturation and traffic to the lysosome by facilitating membrane fusion', *Journal of Cell Biology*. doi: 10.1083/jcb.201603030.

Drin, G. *et al.* (2007) 'A general amphipathic α-helical motif for sensing membrane curvature', *Nature Structural and Molecular Biology*. doi: 10.1038/nsmb1194.

Drin, G. and Antonny, B. (2010) 'Amphipathic helices and membrane curvature', *FEBS Letters*. doi: 10.1016/j.febslet.2009.10.022.

Egelhofer, T. A. *et al.* (2008) 'The septins function in G1 pathways that influence the pattern of cell growth in budding yeast', *PLoS ONE*. doi: 10.1371/journal.pone.0002022.

Estey, M. P. *et al.* (2010) 'Distinct roles of septins in cytokinesis: SEPT9 mediates midbody abscission', *Journal of Cell Biology*. doi: 10.1083/jcb.201006031.

Ewers, H. *et al.* (2014) 'A septin-dependent diffusion barrier at dendritic spine necks', *PLoS ONE*. doi: 10.1371/journal.pone.0113916.

Fares, H., Goetsch, L. and Pringle, J. R. (1996) 'Identification of a developmentally regulated septin and involvement of the septins in spore formation in Saccharomyces cerevisiae', *Journal of Cell Biology*. doi: 10.1083/jcb.132.3.399.

Fengsrud, M. *et al.* (2000) 'Ultrastructural characterization of the delimiting membranes of isolated autophagosomes and amphisomes by freeze-fracture electron microscopy', *European Journal of Cell Biology*. doi: 10.1078/0171-9335-00125.

Field, C. M. *et al.* (1996a) 'A purified Drosophila septin complex forms filaments and exhibits GTPase activity', *Journal of Cell Biology*. doi: 10.1083/jcb.133.3.605.

Field, C. M. *et al.* (1996b) 'A purified Drosophila septin complex forms filaments and exhibits GTPase activity', *Journal of Cell Biology*. doi: 10.1083/jcb.133.3.605.

Finnigan, G. C., Takagi, J., *et al.* (2015) 'Comprehensive genetic analysis of paralogous terminal septin subunits Shs1 and Cdc11 in Saccharomyces cerevisiae', *Genetics*. doi: 10.1534/genetics.115.176495.

Finnigan, G. C., Booth, E. A., *et al.* (2015) 'The carboxy-terminal tails of septins Cdc11 and Shs1 recruit myosin-II binding factor Bni5 to the bud neck in Saccharomyces cerevisiae', *Genetics*. doi: 10.1534/genetics.115.176503.

Ford, S. K. and Pringle, J. R. (1991) 'Cellular morphogenesis in the Saccharomyces cerevisiae cell cycle: Localization of the CDC11 gene product and the timing of events at the budding site', *Developmental Genetics*. doi: 10.1002/dvg.1020120405.

Frazier, J. A. *et al.* (1998) 'Polymerization of purified yeast septins: Evidence that organized filament arrays may not be required for septin function', *Journal of Cell Biology*. doi: 10.1083/jcb.143.3.737.

Fujimoto, T. and Parton, R. G. (2011) 'Not just fat: The structure and function of the lipid droplet', *Cold Spring Harbor Perspectives in Biology*. doi: 10.1101/cshperspect.a004838.

Gallop, J. L. *et al.* (2006) 'Mechanism of endophilin N-BAR domain-mediated membrane curvature', *EMBO Journal*. doi: 10.1038/sj.emboj.7601174.

Garcia, G. *et al.* (2011a) 'Subunit-dependent modulation of septin assembly: Budding yeast septin Shs1 promotes ring and gauze formation', *Journal of Cell Biology*. doi: 10.1083/jcb.201107123.

Garcia, G. *et al.* (2011b) 'Subunit-dependent modulation of septin assembly: Budding yeast septin Shs1 promotes ring and gauze formation', *Journal of Cell Biology*. doi: 10.1083/jcb.201107123.

Garrenton, L. S. *et al.* (2010) 'Pheromone-induced anisotropy in yeast plasma membrane phosphatidylinositol- 4,5-bisphosphate distribution is required for MAPK signaling', *Proceedings of the National Academy of Sciences of the United States of America*. doi: 10.1073/pnas.1005817107.

Gattiker, A. *et al.* (2007) 'Ashbya Genome Database 3.0: A cross-species genome and transcriptome browser for yeast biologists', *BMC Genomics*. doi: 10.1186/1471-2164-8-9.
Gautier, R. *et al.* (2008) 'HELIQUEST: A web server to screen sequences with specific α-helical properties', *Bioinformatics*. doi: 10.1093/bioinformatics/btn392.

Gehlen, L. R. *et al.* (2011) 'Nuclear geometry and rapid mitosis ensure asymmetric episome segregation in yeast', *Current Biology*. doi: 10.1016/j.cub.2010.12.016.

Gilden, J. K. *et al.* (2012) 'The septin cytoskeleton facilitates membrane retraction during motility and blebbing', *Journal of Cell Biology*. doi: 10.1083/jcb.201105127.

Gilden, J. and Krummel, M. F. (2010) 'Control of cortical rigidity by the cytoskeleton: Emerging roles for septins', *Cytoskeleton*. doi: 10.1002/cm.20461.

Gill, R. L., Castaing, J.-P., *et al.* (2015) 'Structural basis for the geometry-driven localization of a small protein', *Proceedings of the National Academy of Sciences*. doi: 10.1073/pnas.1423868112.

Gill, R. L., Castaing, J. P., *et al.* (2015) 'Structural basis for the geometry-driven localization of a small protein', *Proceedings of the National Academy of Sciences of the United States of America*. doi: 10.1073/pnas.1423868112.

Giot, L. and Konopka, J. B. (1997) 'Functional analysis of the interaction between Afr1p and the Cdc12p septin, two proteins involved in pheromone-induced morphogenesis', *Mol Biol Cell*. doi: 10.1091/mbc.8.6.987.

Gladfelter, Amy S *et al.* (2005) 'Interplay between septin organization, cell cycle and cell shape in yeast.', *Journal of cell science*. doi: 10.1242/jcs.02286.
Gladfelter, Amy S. *et al.* (2005) 'Interplay between septin organization, cell cycle and cell shape in yeast', *Journal of Cell Science*. doi: 10.1242/jcs.02286.

Gladfelter, A. S., Pringle, J. R. and Lew, D. J. (2001) 'The septin cortex at the yeast mother-bud

neck', *Current Opinion in Microbiology*. doi: 10.1016/S1369-5274(01)00269-7.

Gopalakrishnan, G. *et al.* (2009) 'Supported bilayers formed from different phospholipids on spherical silica substrates', *Langmuir*. doi: 10.1021/la9006982.

Graham, J. S. *et al.* (2014) 'Multi-platform compatible software for analysis of polymer bending mechanics', *PLoS ONE*. doi: 10.1371/journal.pone.0094766.g001.

Gupta, K. *et al.* (2018) 'Identifying key membrane protein lipid interactions using mass spectrometry', *Nature Protocols*. doi: 10.1038/nprot.2018.014.

Haarer, B. K. and Pringle, J. R. (1987) 'Immunofluorescence localization of the Saccharomyces cerevisiae CDC12 gene product to the vicinity of the 10-nm filaments in the mother-bud neck.', *Molecular and cellular biology*. doi: 10.1128/mcb.7.10.3678.

Hall, P. A. and Russell, S. E. H. (2004) 'The pathobiology of the septin gene family', *Journal of Pathology*. doi: 10.1002/path.1654.

Hall, P. A., Russell, S. E. H. and Pringle, J. R. (2008) *The Septins*, *The Septins*. doi: 10.1002/9780470779705.

Harbury, P. B. *et al.* (1993) 'A switch between two-, three-, and four-stranded coiled coils in GCN4 leucine zipper mutants', *Science*. doi: 10.1126/science.8248779.

Hartwell, L. H. *et al.* (1973) 'Genetic control of the cell division cycle in yeast: V. Genetic analysis of cdc mutants', *Genetics*.

Hartwell, L. H. *et al.* (1974) 'Genetic control of the cell division cycle in yeast', *Science*. doi: 10.1126/science.183.4120.46.

Hatzakis, N. S. *et al.* (2009) 'How curved membranes recruit amphipathic helices and protein anchoring motifs', *Nature Chemical Biology*. doi: 10.1038/nchembio.213.

Heasley, L. R. and Mcmurray, M. A. (2016) 'Roles of septins in prospore membrane morphogenesis and spore wall assembly in saccharomyces cerevisiae', *Molecular Biology of the*

Cell. doi: 10.1091/mbc.E15-10-0721.

Heid, H. *et al.* (2014) 'On the formation of lipid droplets in human adipocytes: The organization of the perilipin-vimentin cortex', *PLoS ONE*. doi: 10.1371/journal.pone.0090386.

Helfer, H. and Gladfelter, A. S. (2006) 'AgSwe1p regulates mitosis in response to morphogenesis and nutrients in multinucleated Ashbya gossypii cells', *Molecular Biology of the Cell*. doi: 10.1091/mbc.E06-03-0215.

Henderson, K. A., Hughes, A. L. and Gottschling, D. E. (2014) 'Mother-daughter asymmetry of pH underlies aging and rejuvenation in yeast', *eLife*. doi: 10.7554/eLife.03504.

Henriques, A. O. and Moran, C. P. (2007) 'Structure, assembly, and function of the spore surface layers', *Annual Review of Microbiology*. doi: 10.1146/annurev.micro.61.080706.093224.

Higgins, D. and Dworkin, J. (2012) 'Recent progress in Bacillus subtilis sporulation', *FEMS Microbiology Reviews*. doi: 10.1111/j.1574-6976.2011.00310.x.

Hilary Russell, S. E. and Hall, P. A. (2011) 'Septin genomics: A road less travelled', in *Biological Chemistry*. doi: 10.1515/BC.2011.079.

Hofbauer, H. F. *et al.* (2018) 'The molecular recognition of phosphatidic acid by an amphipathic helix in Opi1.', *The Journal of cell biology*. doi: 10.1083/jcb.201802027.

Hu, J. *et al.* (2012) 'Septin-driven coordination of actin and microtubule remodeling regulates the collateral branching of axons', *Current Biology*. doi: 10.1016/j.cub.2012.04.019.

Hu, Q. *et al.* (2010) 'A septin diffusion barrier at the base of the primary cilium maintains ciliary membrane protein distribution', *Science*. doi: 10.1126/science.1191054.

Huang, K. C. and Ramamurthi, K. S. (2010) 'Macromolecules that prefer their membranes curvy.', *Mol Microbiol*. doi: 10.1111/j.1365-2958.2010.07168.x.

Hussain, S. *et al.* (2018) 'MreB filaments align along greatest principal membrane curvature to orient cell wall synthesis', *eLife*. doi: 10.7554/eLife.32471.

Igarashi, K. *et al.* (2011) 'Traffic jams reduce hydrolytic efficiency of cellulase on cellulose surface', *Science*. doi: 10.1126/science.1208386.

Jiao, F. *et al.* (2020) 'The hierarchical assembly of septins revealed by high-speed AFM', *Nature Communications*. doi: 10.1038/s41467-020-18778-x.

John, C. M. *et al.* (2007) 'The Caenorhabditis elegans septin complex is nonpolar', *EMBO Journal*. doi: 10.1038/sj.emboj.7601775.

Johnson, C. R. *et al.* (2015) 'Cytosolic chaperones mediate quality control of higher-order septin assembly in budding yeast', *Molecular Biology of the Cell*. doi: 10.1091/mbc.E14-11-1531.

Joo, E., Surka, M. C. and Trimble, W. S. (2007) 'Mammalian SEPT2 Is Required for Scaffolding Nonmuscle Myosin II and Its Kinases', *Developmental Cell*. doi: 10.1016/j.devcel.2007.09.001.

Kaback, D. B. and Feldberg, L. R. (1985) 'Saccharomyces cerevisiae exhibits a sporulation-specific temporal pattern of transcript accumulation.', *Molecular and Cellular Biology*. doi: 10.1128/mcb.5.4.751.

Kang, H., Tsygankov, D. and Lew, D. J. (2016) 'Sensing a bud in the yeast morphogenesis checkpoint: A role for Elm1', *Molecular Biology of the Cell*. doi: 10.1091/mbc.E16-01-0014.

Kanki, T. *et al.* (2009) 'Atg32 Is a Mitochondrial Protein that Confers Selectivity during Mitophagy', *Developmental Cell*. doi: 10.1016/j.devcel.2009.06.014.

Kelley, J. B. *et al.* (2015) 'RGS proteins and septins cooperate to promote chemotropism by regulating polar cap mobility', *Current Biology*. doi: 10.1016/j.cub.2014.11.047.

Kelley, L. A. *et al.* (2015) 'The Phyre2 web portal for protein modeling, prediction and analysis', *Nature Protocols*. doi: 10.1038/nprot.2015.053.
Khan, A., Newby, J. and Gladfelter, A. S. (2018) 'Control of septin filament flexibility and bundling by subunit composition and nucleotide interactions', *Molecular Biology of the Cell*. doi: 10.1091/mbc.E17-10-0608.

Kim, E. Y. *et al.* (2017) 'Dash-and-Recruit Mechanism Drives Membrane Curvature Recognition by the Small Bacterial Protein SpoVM', *Cell Systems*. doi:

10.1016/j.cels.2017.10.004.

Kim, S. W. *et al.* (2017) 'Genetic incorporation of Nε-acetyllysine reveals a novel acetylation-sumoylation switch in yeast', *Biochimica et Biophysica Acta - General Subjects*. doi: 10.1016/j.bbagen.2017.02.002.

Kinoshita, M. *et al.* (2002) 'Self- and actin-templated assembly of mammalian septins', *Developmental Cell*. doi: 10.1016/S1534-5807(02)00366-0.

Knechtle, P., Dietrich, F. and Philippsen, P. (2003) 'Maximal polar growth potential depends on the polarisome component AgSpa2 in the filamentous fungus Ashbya gossypii', *Molecular Biology of the Cell*. doi: 10.1091/mbc.E03-03-0167.

Kodera, N. *et al.* (2010) 'Video imaging of walking myosin v by high-speed atomic force microscopy', *Nature*. doi: 10.1038/nature09450.

Köhli, M. *et al.* (2008) 'Growth-speed-correlated localization of exocyst and polarisome components in growth zones of Ashbya gossypii hyphal tips', *Journal of Cell Science*. doi: 10.1242/jcs.033852.

Kozubowski, L., Larson, J. R. and Tatchell, K. (2005) 'Role of the septin ring in the asymmetric localization of proteins at the mother-bud neck in Saccharomyces cerevisiae', *Molecular Biology of the Cell*. doi: 10.1091/mbc.E04-09-0764.

Kraft, C. *et al.* (2008) 'Mature ribosomes are selectively degraded upon starvation by an autophagy pathway requiring the Ubp3p/Bre5p ubiquitin protease', *Nature Cell Biology*. doi: 10.1038/ncb1723.

Krapivsky, P. L., Redner, S. and Ben-Naim, E. (2011) *A kinetic view of statistical physics*, *A Kinetic View of Statistical Physics*. doi: 10.1017/CBO9780511780516.

Krokowski, S. *et al.* (2018) 'Septins Recognize and Entrap Dividing Bacterial Cells for Delivery to Lysosomes', *Cell Host and Microbe*. doi: 10.1016/j.chom.2018.11.005.

Lai, C. L. *et al.* (2012) 'Membrane Binding and Self-Association of the Epsin N-Terminal Homology Domain', *Journal of Molecular Biology*. doi: 10.1016/j.jmb.2012.08.010.

Lenarcic, R. *et al.* (2009) 'Localisation of DivIVA by targeting to negatively curved membranes', *EMBO Journal*. doi: 10.1038/emboj.2009.129.

Levin, P. A. *et al.* (1993) 'An unusually small gene required for sporulation by Bacillus subtilis', *Molecular Microbiology*. doi: 10.1111/j.1365-2958.1993.tb01736.x.

Lew, D. J. (2003) 'The morphogenesis checkpoint: How yeast cells watch their figures', *Current Opinion in Cell Biology*. doi: 10.1016/j.ceb.2003.09.001.

Lew, D. J. and Reed, S. I. (1995) 'A cell cycle checkpoint monitors cell morphogenesis in budding yeast', *Journal of Cell Biology*. doi: 10.1083/jcb.129.3.739.

Lewis, B. A. and Engelman, D. M. (1983) 'Lipid bilayer thickness varies linearly with acyl chain length in fluid phosphatidylcholine vesicles', *Journal of Molecular Biology*. doi: 10.1016/S0022-2836(83)80007-2.

Lin, Y. C., Li, C. and Fakhraai, Z. (2018) 'Kinetics of Surface-Mediated Fibrillization of Amyloid-β (12-28) Peptides', *Langmuir*. doi: 10.1021/acs.langmuir.7b02744.

Liu, M. *et al.* (2019) 'Glucose starvation triggers filamentous septin assemblies in an S. Pombe septin-2 deletion mutant', *Biology Open*. doi: 10.1242/bio.037622.

Longtine, MARK S *et al.* (2000) 'Septin-dependent assembly of a cell cycle-regulatory module in Saccharomyces cerevisiae.', *Molecular and cellular biology*.

Longtine, M. S. *et al.* (2000) 'Septin-Dependent Assembly of a Cell Cycle-Regulatory Module in Saccharomyces cerevisiae', *Molecular and Cellular Biology*. doi: 10.1128/MCB.20.11.4049-4061.2000.

Longtine, M. S., Fares, H. and Pringle, J. R. (1998) 'Role of the yeast gin4p protein kinase in septin assembly and the relationship between septin assembly and septin function', *Journal of Cell Biology*. doi: 10.1083/jcb.143.3.719.

Low, C. and Macara, I. G. (2006) 'Structural analysis of septin 2, 6, and 7 complexes', *Journal of Biological Chemistry*. doi: 10.1074/jbc.M605179200.

Luedeke, C. *et al.* (2005) 'Septin-dependent compartmentalization of the endoplasmic reticulum during yeast polarized growth', *Journal of Cell Biology*. doi: 10.1083/jcb.200412143.

Lupas, A. N. and Bassler, J. (2017) 'Coiled Coils – A Model System for the 21st Century', *Trends in Biochemical Sciences*. doi: 10.1016/j.tibs.2016.10.007.

Maddox, A. S. *et al.* (2007) 'Anillin and the Septins Promote Asymmetric Ingression of the Cytokinetic Furrow', *Developmental Cell*. doi: 10.1016/j.devcel.2007.02.018.

Marquardt, J., Chen, X. and Bi, E. (2019) 'Architecture, remodeling, and functions of the septin cytoskeleton', *Cytoskeleton*. doi: 10.1002/cm.21475.

Mata, J. *et al.* (2002) 'The transcriptional program of meiosis and sporulation in fission yeast', *Nature Genetics*. doi: 10.1038/ng951.

Mavrakis, M. *et al.* (2014) 'Septins promote F-actin ring formation by crosslinking actin filaments into curved bundles', *Nature Cell Biology*. doi: 10.1038/ncb2921.

Mckenney, P. T., Driks, A. and Eichenberger, P. (2013) 'The Bacillus subtilis endospore: Assembly and functions of the multilayered coat', *Nature Reviews Microbiology*. doi: 10.1038/nrmicro2921.

McMillan, J. N. *et al.* (2002) 'Determinants of Swe1p degradation in Saccharomyces cerevisiae', *Molecular Biology of the Cell*. doi: 10.1091/mbc.E02-05-0283.

McMurray, M. A. *et al.* (2011) 'Septin Filament Formation Is Essential in Budding Yeast', *Developmental Cell*. doi: 10.1016/j.devcel.2011.02.004.

Meitinger, F. *et al.* (2011) 'Phosphorylation-dependent regulation of the F-BAR protein Hof1 during cytokinesis', *Genes and Development*. doi: 10.1101/gad.622411.

Meseroll, R. A., Occhipinti, P. and Gladfelter, A. S. (2013a) 'Septin phosphorylation and coiled-coil domains function in cell and septin ring morphology in the filamentous fungus Ashbya gossypii', *Eukaryotic Cell*. doi: 10.1128/EC.00251-12.

Meseroll, R. A., Occhipinti, P. and Gladfelter, A. S. (2013b) 'Septin phosphorylation and coiled-coil domains function in cell and septin ring morphology in the filamentous fungus Ashbya gossypii', *Eukaryotic Cell*. doi: 10.1128/EC.00251-12.

Mierzwa, B. E. *et al.* (2017) 'Dynamic subunit turnover in ESCRT-III assemblies is regulated by Vps4 to mediate membrane remodelling during cytokinesis', *Nature Cell Biology*. doi: 10.1038/ncb3559.

Mim, C. *et al.* (2012) 'Structural basis of membrane bending by the N-BAR protein endophilin', *Cell*. doi: 10.1016/j.cell.2012.01.048.

Miyagi, A. *et al.* (2016) 'High-speed atomic force microscopy shows that annexin V stabilizes membranes on the second timescale', *Nature Nanotechnology*. doi: 10.1038/nnano.2016.89.

Miyagi, A. *et al.* (2018) 'High-Speed Atomic Force Microscopy Reveals the Inner Workings of the MinDE Protein Oscillator', *Nano Letters*. doi: 10.1021/acs.nanolett.7b04128.

Mortensen, E. M. *et al.* (2002) 'Cell cycle-dependent assembly of a Gin4-septin complex', *Molecular Biology of the Cell*. doi: 10.1091/mbc.01-10-0500.

Mostowy, S. *et al.* (2010) 'Entrapment of intracytosolic bacteria by septin cage-like structures', *Cell Host and Microbe*. doi: 10.1016/j.chom.2010.10.009.

Mostowy, S. and Cossart, P. (2012) 'Septins: The fourth component of the cytoskeleton', *Nature Reviews Molecular Cell Biology*. doi: 10.1038/nrm3284.

Munguira, I. *et al.* (2016) 'Glasslike Membrane Protein Diffusion in a Crowded Membrane', *ACS Nano*. doi: 10.1021/acsnano.5b07595.
Neiman, A. M. (2011) 'Sporulation in the budding yeast Saccharomyces cerevisiae', *Genetics*. doi: 10.1534/genetics.111.127126.

Van Ngo, H. and Mostowy, S. (2019) 'Role of septins in microbial infection', *Journal of Cell Science*, 132(9), p. jcs226266. doi: 10.1242/jcs.226266.

Nguyen, N., Shteyn, V. and Melia, T. J. (2017) 'Sensing Membrane Curvature in Macroautophagy', *Journal of Molecular Biology*. doi: 10.1016/j.jmb.2017.01.006.

Nishihama, R., Onishi, M. and Pringle, J. R. (2011) 'New insights into the phylogenetic distribution and evolutionary origins of the septins', in *Biological Chemistry*. doi: 10.1515/BC.2011.086.

Nölke, T. *et al.* (2016) 'Septins guide microtubule protrusions induced by actin-depolymerizing toxins like Clostridium difficile transferase (CDT)', *Proceedings of the National Academy of Sciences of the United States of America*. doi: 10.1073/pnas.1522717113.

Oh, Y. and Bi, E. (2011) 'Septin structure and function in yeast and beyond', *Trends in Cell Biology*. doi: 10.1016/j.tcb.2010.11.006.

Ong, K. *et al.* (2014) 'Architecture and dynamic remodelling of the septin cytoskeleton during the cell cycle', *Nature Communications*. doi: 10.1038/ncomms6698.

Onishi, M. *et al.* (2010) 'Role of Septins in the Orientation of Forespore Membrane Extension during Sporulation in Fission Yeast', *Molecular and Cellular Biology*. doi: 10.1128/mcb.01529-09.

Onishi, M. and Pringle, J. R. (2016) 'The nonopisthokont septins: How many there are, how little we know about them, and how we might learn more', *Methods in Cell Biology*. doi: 10.1016/bs.mcb.2016.04.003.

Palsdottir, H. and Hunte, C. (2004) 'Lipids in membrane protein structures', *Biochimica et Biophysica Acta - Biomembranes*. doi: 10.1016/j.bbamem.2004.06.012.

Pan, F., Malmberg, R. L. and Momany, M. (2007) 'Analysis of septins across kingdoms reveals orthology and new motifs', *BMC Evolutionary Biology*. doi: 10.1186/1471-2148-7-103.
Peter, B. J. *et al.* (2004) 'BAR Domains as Sensors of Membrane Curvature: The Amphiphysin BAR Structure', *Science*. doi: 10.1126/science.1092586.

Peterson, E. A. and Petty, E. M. (2010) 'Conquering the complex world of human septins: Implications for health and disease', *Clinical Genetics*. doi: 10.1111/j.1399-0004.2010.01392.x.

Postma, M. and Goedhart, J. (2019) 'Plotsofdata—a web app for visualizing data together with their summaries', *PLoS Biology*. doi: 10.1371/journal.pbio.3000202.

Pranke, I. M. *et al.* (2011) 'α-Synuclein and ALPS motifs are membrane curvature sensors whose contrasting chemistry mediates selective vesicle binding', *Journal of Cell Biology*. doi: 10.1083/jcb.201011118.

Ramamurthi, K. S. *et al.* (2009) 'Geometric cue for protein localization in a bacterium', *Science*. doi: 10.1126/science.1169218.

Ramamurthi, K. S., Clapham, K. R. and Losick, R. (2006) 'Peptide anchoring spore coat assembly to the outer forespore membrane in Bacillus subtilis', *Molecular Microbiology*. doi: 10.1111/j.1365-2958.2006.05468.x.

Raspelli, E. *et al.* (2011) 'Budding yeast Dma1 and Dma2 participate in regulation of Swe1 levels and localization', *Molecular Biology of the Cell*. doi: 10.1091/mbc.E11-02-0127.

Rodal, A. A. *et al.* (2005) 'Actin and septin ultrastructures at the budding yeast cell cortex', *Molecular Biology of the Cell*. doi: 10.1091/mbc.E04-08-0734.
Romberg, L., Simon, M. and Erickson, H. p. (2001) 'Polymerization of FtsZ, a bacterial homolog of tubulin. Is assembly cooperative?', *Journal of Biological Chemistry*. doi: 10.1074/jbc.M009033200.

Roux, A. *et al.* (2010) 'Membrane curvature controls dynamin polymerization', *Proceedings of the National Academy of Sciences of the United States of America*. doi: 10.1073/pnas.0913734107.

Sadian, Y. *et al.* (2013) 'The role of Cdc42 and Gic1 in the regulation of septin filament formation and dissociation', *eLife*. doi: 10.7554/eLife.01085.

Sakchaisri, K. *et al.* (2004) 'Coupling morphogenesis to mitotic entry.', *Proceedings of the National Academy of Sciences of the United States of America*. doi: 10.1073/pnas.0400641101.

Sala, F. A. *et al.* (2016) 'Heterotypic Coiled-Coil Formation is Essential for the Correct Assembly of the Septin Heterofilament', *Biophysical Journal*. doi: 10.1016/j.bpj.2016.10.032.

Schmitz, H. P. *et al.* (2006) 'From function to shape: A novel role of a formin in morphogenesis of the fungus Ashbya gossypii', *Molecular Biology of the Cell*. doi: 10.1091/mbc.E05-06-0479.

Schreck, J. S. and Yuan, J. M. (2013) 'A kinetic study of amyloid formation: Fibril growth and length distributions', *Journal of Physical Chemistry B*. doi: 10.1021/jp401586p.

Seiler, S. and Plamann, M. (2003) 'The Genetic Basis of Cellular Morphogenesis in the Filamentous Fungus Neurospora crassa', *Molecular Biology of the Cell*. doi: 10.1091/mbc.E02-07-0433.

Sellin, M. E. *et al.* (2011) 'Deciphering the rules governing assembly order of mammalian septin complexes', *Molecular Biology of the Cell*. doi: 10.1091/mbc.E11-03-0253.

Sellin, M. E., Stenmark, S. and Gullberg, M. (2014) 'Cell type-specific expression of SEPT3-homology subgroup members controls the subunit number of heteromeric septin complexes', *Molecular Biology of the Cell*. doi: 10.1091/mbc.E13-09-0553.

Shen, X. X. *et al.* (2018) 'Tempo and Mode of Genome Evolution in the Budding Yeast Subphylum', *Cell*. doi: 10.1016/j.cell.2018.10.023.

Shen, Y. R. *et al.* (2017) 'SEPT12 phosphorylation results in loss of the septin ring/sperm annulus, defective sperm motility and poor male fertility', *PLoS Genetics*. doi: 10.1371/journal.pgen.1006631.

Shibata, M. *et al.* (2017) 'Real-space and real-Time dynamics of CRISPR-Cas9 visualized by high-speed atomic force microscopy', *Nature Communications*. doi: 10.1038/s41467-017-01466-8.

Shulewitz, M. J., Inouye, C. J. and Thorner, J. (1999) 'Hsl7 Localizes to a Septin Ring and Serves as an Adapter in a Regulatory Pathway That Relieves Tyrosine Phosphorylation of Cdc28 Protein Kinase inSaccharomyces cerevisiae', *Molecular and Cellular Biology*. doi: 10.1128/mcb.19.10.7123.

Sia, R. A. L., Bardes, E. S. G. and Lew, D. J. (1998) 'Control of Swe1p degradation by the morphogenesis checkpoint', *EMBO Journal*. doi: 10.1093/emboj/17.22.6678.

Sia, R. A. L., Herald, H. A. and Lew, D. J. (1996) 'Cdc28 tyrosine phosphorylation and the morphogenesis checkpoint in budding yeast', *Molecular Biology of the Cell*. doi: 10.1091/mbc.7.11.1657.

Simunovic, M. *et al.* (2015) 'When Physics Takes Over: BAR Proteins and Membrane Curvature', *Trends in Cell Biology*. doi: 10.1016/j.tcb.2015.09.005.

Simunovic, M. *et al.* (2016) 'How curvature-generating proteins build scaffolds on membrane nanotubes', *Proceedings of the National Academy of Sciences of the United States of America*. doi: 10.1073/pnas.1606943113.

Simunovic, M., Srivastava, A. and Voth, G. A. (2013) 'Linear aggregation of proteins on the membrane as a prelude to membrane remodeling', *Proceedings of the National Academy of Sciences*. doi: 10.1073/pnas.1309819110.

Singer, S. J. and Nicolson, G. L. (1972) 'The fluid mosaic model of the structure of cell membranes', *Science*. doi: 10.1126/science.175.4023.720.

Sirajuddin, M. *et al.* (2007) 'Structural insight into filament formation by mammalian septins', *Nature*. doi: 10.1038/nature06052.

Sirianni, A. *et al.* (2016) ' Mitochondria mediate septin cage assembly to promote autophagy of Shigella ', *EMBO reports*. doi: 10.15252/embr.201541832.

Skillman, K. M. *et al.* (2013) 'The unusual dynamics of parasite actin result from isodesmic polymerization', *Nature Communications*. doi: 10.1038/ncomms3285.

Sorre, B. *et al.* (2012) 'Nature of curvature coupling of amphiphysin with membranes depends on its bound density', *Proceedings of the National Academy of Sciences of the United States of America*. doi: 10.1073/pnas.1103594108.

Spiliotis, E. T., Kinoshita, M. and Nelson, W. J. (2005) 'A mitotic septin scaffold required for mammalian chromosome congression and segregation', *Science*. doi: 10.1126/science.1106823.
Stachowiak, J. C. *et al.* (2012) 'Membrane bending by protein-protein crowding', *Nature Cell Biology*. doi: 10.1038/ncb2561.

Steenwyk, J. L. and Rokas, A. (2019) 'Treehouse: A user-friendly application to obtain subtrees from large phylogenies', *BMC Research Notes*. doi: 10.1186/s13104-019-4577-5.

Steger, G. (1998) 'An unbiased detector of curvilinear structures', *IEEE Transactions on Pattern*

Analysis and Machine Intelligence. doi: 10.1109/34.659930.

Suetsugu, S., Kurisu, S. and Takenawa, T. (2014) 'Dynamic shaping of cellular membranes by phospholipids and membrane-deforming proteins', *Physiological reviews*. doi: 10.1152/physrev.00040.2013.

Szule, J. A., Fuller, N. L. and Peter Rand, R. (2002) 'The effects of acyl chain length and saturation of diacylglycerols and phosphatidylcholines on membrane monolayer curvature', *Biophysical Journal*. doi: 10.1016/S0006-3495(02)75223-5.

Takeda, T. *et al.* (2013) 'Drosophila F-BAR protein Syndapin contributes to coupling the plasma membrane and contractile ring in cytokinesis', *Open Biology*. doi: 10.1098/rsob.130081.

Takemura, K. *et al.* (2017) 'Salt Bridge Formation between the I-BAR Domain and Lipids Increases Lipid Density and Membrane Curvature', *Scientific Reports*. doi: 10.1038/s41598-017-06334-5.

Tan, I. S. and Ramamurthi, K. S. (2014) 'Spore formation in Bacillus subtilis', *Environmental Microbiology Reports*. doi: 10.1111/1758-2229.12130.

Tan, X. *et al.* (2016) 'PtdIns(4,5)P2 signaling regulates ATG14 and autophagy', *Proceedings of the National Academy of Sciences of the United States of America*. doi: 10.1073/pnas.1523145113.

Tanaka-Takiguchi, Y., Kinoshita, M. and Takiguchi, K. (2009) 'Septin-Mediated Uniform Bracing of Phospholipid Membranes', *Current Biology*. doi: 10.1016/j.cub.2008.12.030.

Tinevez, J. Y. *et al.* (2017) 'TrackMate: An open and extensible platform for single-particle tracking', *Methods*. doi: 10.1016/j.ymeth.2016.09.016.

Torraca, V. and Mostowy, S. (2016) 'Septins and bacterial infection', *Frontiers in Cell and Developmental Biology*. doi: 10.3389/fcell.2016.00127.

Trimble, W. S. and Grinstein, S. (2015) 'Barriers to the free diffusion of proteins and lipids in the plasma membrane', *Journal of Cell Biology*. doi: 10.1083/jcb.201410071.

Tsui, F. C., Ojcius, D. M. and Hubbell, W. L. (1986) 'The intrinsic pKa values for phosphatidylserine and phosphatidylethanolamine in phosphatidylcholine host bilayers', *Biophysical Journal*. doi: 10.1016/S0006-3495(86)83655-4.

Ursell, T. S. *et al.* (2014) 'Rod-like bacterial shape is maintained by feedback between cell curvature and cytoskeletal localization', *Proceedings of the National Academy of Sciences*. doi: 10.1073/pnas.1317174111.

Vanni, S. *et al.* (2014) 'A sub-nanometre view of how membrane curvature and composition modulate lipid packing and protein recruitment', *Nature Communications*. Nature Publishing Group, a division of Macmillan Publishers Limited. All Rights Reserved., 5, p. 4916. Available at: https://doi.org/10.1038/ncomms5916.

Versele, M. and Thorner, J. (2004) 'Septin collar formation in budding yeast requires GTP binding and direct phosphorylation by the PAK, Cla4', *Journal of Cell Biology*. doi: 10.1083/jcb.200312070.

Walker, R. G., Willingham, A. T. and Zuker, C. S. (2000) 'A Drosophila mechanosensory transduction channel', *Science*. doi: 10.1126/science.287.5461.2229.

Weems, A. and McMurray, M. (2017) 'The step-wise pathway of septin heterooctamer assembly in budding yeast', *eLife*. doi: 10.7554/eLife.23689.

Westfall, P. J. and Momany, M. (2002) 'Aspergillus nidulans septin AspB plays pre- and postmitotic roles in septum, branch, and conidiophore development', *Molecular Biology of the Cell*. doi: 10.1091/mbc.

Wloka, C. and Bi, E. (2012) 'Mechanisms of cytokinesis in budding yeast', *Cytoskeleton*. doi: 10.1002/cm.21046.

Wolf, E., Kim, P. S. and Berger, B. (1997) 'MultiCoil: A program for predicting two- and three-stranded coiled coils', *Protein Science*. doi: 10.1002/pro.5560060606.

Yamada, S. *et al.* (2016) 'Septin Interferes with the Temperature-Dependent Domain Formation and Disappearance of Lipid Bilayer Membranes', *Langmuir*. doi: 10.1021/acs.langmuir.6b03452.

Yang, P. L. *et al.* (2016) 'Lipid droplets maintain lipid homeostasis during anaphase for efficient cell separation in budding yeast', *Molecular Biology of the Cell*. doi: 10.1091/mbc.E16-02-0106.
Yoshikawa, Y. *et al.* (2009) 'Listeria monocytogenes ActA is a key player in evading autophagic recognition', *Autophagy*. doi: 10.4161/auto.5.8.10177.

Youn, J. Y. *et al.* (2010) 'Dissecting BAR domain function in the yeast amphiphysins Rvs161 and Rvs167 during endocytosis', *Molecular Biology of the Cell*. doi: 10.1091/mbc.E10-03-0181.

Zhang, X. *et al.* (2011) 'Membrane cholesterol modulates the fluid shear stress response of polymorphonuclear leukocytes via its effects on membrane fluidity', *American Journal of Physiology - Cell Physiology*. doi: 10.1152/ajpcell.00458.2010.

Zimmerberg, J. and Kozlov, M. M. (2006) 'How proteins produce cellular membrane curvature', *Nature Reviews Molecular Cell Biology*. doi: 10.1038/nrm1784.